INTERFACIAL PROPERTIES OF GRAFTED ZWITTERIONIC POLYMERS AND INTERACTION WITH PROTEINS AT THE NANOSCALE

BY

SYEDA TAJIN AHMED

DISSERTATION

Submitted in partial fulfillment of the requirements
for the degree of Doctor of Philosophy in Chemical and Biomolecular Engineering
in the Graduate College of the
University of Illinois Urbana-Champaign, 2021

Urbana, Illinois

Doctoral Committee:

Professor Deborah E. Leckband, Chair
Professor Martin Gruebele
Professor Hyunjoon Kong
Assistant Professor Simon A. Rogers

ABSTRACT

Zwitterionic polymers are considered to be great candidate for surface modifications of biosensors and implantable materials because of their super hydrophilicity and ability to prevent non-specific protein adsorption or 'fouling'. They also provide steric and electrostatic stabilization for colloid or nanoparticles in electrolytes, protein/drug stabilization and prevent marine fouling. Their functional performance as biocompatible, non-fouling coatings in different environment such as salt concentration in medium, types of salt, temperature etc. affect their solubility, swelling behavior and molecular level surface properties. In this thesis, the design parameters of grafted polysulfobetaine thin films- one of the commonly known polyzwitterions, are identified to be- grafted chain densities, polymer molecular weight, and/or film thickness and demonstrated how these parameters tune protein adsorption and surface forces at varying ionic strength of the surrounding medium and at different grafting densities. The first part of this study address the research question- why do grafted zwitterionic polymers display excellent non-fouling properties but directly interact with proteins in solution? The results of the study reported that proteins do adsorb on this so-called non-fouling polysulfobetaine grafted chains. The amount of adsorbed proteins follow a bell shaped curve, with the maximum adsorption happening at low (non-overlapping mushrooms) grafting densities and a low adsorption high (dense brush) grafting densities. This adsorption profile is a signature of ternary adsorption of proteins on weakly attractive grafted polymer chains is well described by theory, and it allows us to both test our hypothesis that the polysulfobetaines form segment-protein attractive interactions by overcoming the osmotic repulsion of insertion into the grafted chain layer as well as identify design parameters to tune protein adsorption on such zwitterionic thin films.

In the second part of the study, the surface forces between grafted polysulfobetaine chains and mica were measured as a function of distance in order to investigate the influence of ionic strength, polymer molecular weight and surface density on the range of interactions and the amplitude of interfacial forces. The repulsive forces generated by thin films were quantified with sub nanometer resolution in distance by using a Surface Force Apparatus (SFA). SFA, based on multiple beam interferometry, can directly inform us of the efficacy of polysulfobetaines as entropic barriers in colloid or nanoparticle stabilization in salt solutions. The results from this study highlighted the potential for using sparsely grafted chains for developing non-fouling coatings and/or particle stabilization, whereas previous reports only focused on densely grafted brushes of polysulfobetaines.

Next, surface force measurements were performed between a statistical copolymer consisting of non-ionic oligoethylene glycol and zwitterionic polysulfobetaine polymers at high and low grafting densities and testing surface mica at varying zwitterionic composition. Here, we tested the hypothesis that although the monomer constituents are chemical structurally different, they are well-mixed and non-interacting and thus, their influence on steric repulsive forces depend on the zwitterionic content in the copolymer chains. The ionic strength dependence of the chain extension and repulsive forces increased proportionally with the sulfobetaine content, reflecting the increasing influence of charged monomers and their interactions with ions in solution. These results suggested that ethyene glycol and sulfobetaine behave as non-interacting, miscible monomers that contribute independently to the polymer extension and chain interactions with ions. These findings have important practical implication in stabilizing proteins/drugs by differential interactions of zwitterionic and non-ionic counterparts in the copolymer chains.

Prior to beginning my research project in surface science, I had investigated protein mediated binding kinetics by using Micropipette Aspiration Assay (MPA), the results of which are included in the fifth chapter of this thesis.

Finally in the last chapter of my thesis, I discussed future directions of the project. Here I elaborated on using thin films of polyzwitterions to tune surface interactions with proteins for direct, in-situ measurements of protein folding dynamics of immobilized, high value proteins or drugs at the interface.

ACKNOWLEDGMENTS

I am truly grateful to my father and mother for encouraging me all these years and allowing me to push forward in my career. Despite living almost 8000 miles away from home, they have been a driving force for me, and I have always felt their presence beside me. Thank you Abbu, Ammu.

I treasure my immediate and extended family for their continuing support, especially my siblings Bhaiya and Rukmi, Bhabi, Nisha and all my nephews and nieces. I love you all so much and thank you for being there for me.

I am grateful to my Ph.D. advisor Prof. Deborah Leckband who has helped me grow as an independent researcher. She has always pushed me to achieve my full potential. I am greatly indebted to her for guidance, advice, and all the interactions we have had over the years. I also thank my dissertation committee members, Prof. Martin Gruebele, Prof. Hyunjoon Kong and Dr. Simon Rogers, for their valuable feedback and insightful discussions. I am appreciative of Prof. Paul Braun in opening his laboratory and resources for my work.

I had a great time as a graduate student at University of Illinois thanks to its huge and engaging Bangladeshi community. This community has always welcomed me with open arms, and I could not go through this difficult stage of life without the love and support of my Bangladeshi brothers and sisters here at UIUC. They made me feel like Urbana-Champaign was my second home.

I also want to acknowledge my fellow lab members in the Leckband group for their camaraderie, for their inputs on my research as well as life outside of work. Special thanks to my ChBE cohort and Sunday trivia group: Shekhar, Giri, Mai, and Ritwika for helping me keep my sanity! I am truly grateful to my friends: Matt, Mashiat, Garima, Fariz, Shadman, my cohort from the thesis

writing group and people I have met and got to know better during the pandemic; they gave me so much support in the last mile of this journey.

I would also like to acknowledge Dr. Poonam Sehgal, Dr. Lydia Kisley and Dr. Roberto Andresen Eguiluz for being great post doc mentors, Mr. John Roscheck for fixing the instruments as they often fell apart (!), and my school friends: Aniqua, Fariha, Enora, Amreen and Parisa for being my cheerleaders throughout these years.

Last, but not least, I want to thank the previous graduate coordinator in the ChBE Dept Maggie Metzger Chappell for being there for me like a mother.

Thank you everyone for believing in me.

To Abbu and Ammu

TABLE OF CONTENTS

CHAPTER 1: INTRODUCTION

1.1 Overview of research problem

Developing platform that resists non-specific protein adsorption or fouling is a long standing problem. In biomedical applications, where artificial surfaces are in contact with blood are susceptible to fouling. Eventually fouling leads to degradation of the performance of biosensors, surface-based diagnostic devices, artificial implants and this further invokes the immune response and subsequently results in rejection of the device or platform.[1,2] Moreover, adhesion or attachment of cells, bacteria, other microorganisms on surfaces like-ship hulls, causing marine fouling, are also undesirable. Even a small amount of proteins on surface can lead to the adhesion and propagation of unwanted fouling. For example, to ensure that a surface is biocompatible, less than 5 ng/cm^2 fibrinogen adsorption is required to inhibit platelet adhesion.[3] Platforms that satisfy such criteria are called 'ultra-low fouling surfaces.'[4]

Neutral, water soluble polymers are used for a wide range of biological applications, including nanoparticle stabilization and the fabrication of non-fouling surface coatings. The development of antifouling coatings is particularly important for many applications, such as ship paints,[5, 6] separation membranes,[3, 8] enzyme immobilization,[9] blood-contacting medical materials such as-biosensors,[10] medical implants,[11] contact lenses,[12] and drug delivery carriers.[13, 14] The first-generation of blood contacting polymer coatings were 2-hydroxyethyl methacrylate (polyHEMA)-based polymers and poly(ethylene glycol) or PEG.[15, 16] However, these and similar polymers show varying degrees of non-specific protein adsorption in undiluted human blood serum and plasma,[4] as well as chemical instability in presence of oxygen and transition metal ions found in most biological solutions.[14, 15]

Zwitterionic thin films have been studied as a potential alternative, due to their facile synthesis via Atom Transfer Radical Polymerization (ATRP),[19–21] hemocompatibility,[22] improved chemical stability, controlled composition,[23] and antifouling properties.[21, 22] Zwitterionic polymers (ZI) are a family of polymers with equal number of positively charged and negatively charged moieties in the side-chain.[26] Thus they are overall charge neutral. Zwitterionic polymers are different from polyelectrolytes (polyanions or polycations), where only monomers of the same charge are present in the polymer. Interestingly, zwitterionic coatings with distinctly different chemistries reportedly exhibit strikingly similar ultra-low protein adsorption and apparent protein compatibility.[4]

Despite being regarded as 'ultra-low fouling' materials, the grafted zwitterionic polymers show film thickness dependent adsorption.[27] In recent studies it has been showed that they directly interact with proteins in solution.[28] So why do these polymers interact directly with proteins in solution, but repel proteins when they are grafted on substrates? In this thesis I tested the hypothesis that polysulfobetaine chains behave like weakly-attractive polymers that interact with proteins and identified design parameters to tune protein adsorption.

Surfaces modified with grafting polysulfobetaines, which is one of the most commonly studied polyzwitterions, have been shown to very effective against colloid or nanoparticle aggregation is harsh environment, high salt concentration, and elevated temperatures for example. In these applications, surface forces play an important role in maintaining steric and electrostatic stabilization against particle aggregation. [29, 30] Molecular level details of the interfacial force fields and the impact of ionic strength on those forces are central to understanding the efficacy of these materials in different application. Previous studies focus mostly on swelling behavior of polyzwitterions in solution or at surfaces, especially at high grafting densities. In this thesis, surface forces were measured between polysulfobetaine chains and a testing surface mica at

different ionic strength of the solution and at varied grafting density. The force measurements and quantitative comparisons with polymer models constitute the major difference from prior studies. Moreover, the range and amplitude of surface forces of dilute chains also directly inform of the efficacy of using thin polysulfobetaines as non-fouling coatings and steric barriers for stabilizing colloids and/or nanoparticles.

For development of non-fouling coatings and biomaterials, in addition to homopolymers, segment-segment immiscibility and differences in solvent-segment interactions in statistical or random copolymers are also explored to modulate interfacial energies between polymer-modified surfaces or two immiscible polymers. Do these 'chemically heterogeneous' materials behave as two miscible components within the copolymers or do they phase separate affecting the thin film structure and resulting in change in interfacial properties? Previous studies have informed on the potential of adding zwitterionic components to copolymers in order to develop biomaterials with better non-fouling properties and biocompatibility, but the molecular level information is not studied in details. Using Surface Force Apparatus, surface force measurements of grafted copolymers as a function of composition of the sulfobetaine content was carried out in this work. The results of this study inform how compositions also play important role in tuning the osmotic repulsive barrier generated by such thin films in electrolyte solution, in addition to design parameters like- chain grafting density, polymer molecular weight. Such 'chemically heterogeneous' copolymers have potential in developing platform to study protein folding dynamics, stabilization of high value proteins and drug delivery.

1.2 Introduction to zwitterionic polymers

Structures of zwitterionic polymers for developing non-fouling coatings are inspired by naturally occurring substances and as such they are very biocompatible. For example- phosphorylcholine (PC), the side chains of which contains phosphate anions and quaternary ammonium cations, mimics the zwitterionic phospholipids found in red blood cell membranes.[31] Also, polysulfobetaines are analogues of Taurine, which is distributed in human at 0.1% of total body weight.[32] The structure of carboxybetaine is similar to that of glycine betaine, which is one of the compatible and essential solutes for osmotic regulation of living organisms.[33] The chemical structures of commonly used zwitterionic polymers are given in Figure 1.1.

Current research on polymer coatings involves mostly zwitterion materials for developing (1) biocompatible materials and (2) preventing fouling or non-specific protein adsorption at interfaces. A brief literature review on the numerous applications of zwitterionic polymers at interfaces is discussed in *Appendix G*. Although the concept of biocompatibility is often linked to non-biofouling, the two are not synonymous, even though there is strong overlap in the technology used to implement them.[34] Zwitterionic polymer coated substrates demonstrate ultra-low fouling or non-specific adsorption <5 ng/cm^2 , the acceptable amount of fibrinogen adsorption which is required to prevent platelet adhesion, and subsequent immune response.[3] Zwitterionic brushes grown from surfaces have been extensively reported by Jiang's group.[4] Studies reported that polysulfobetaines[35, 20], and polycarboxybetaines[20, 30, 31] and polyphosphorylcholines[38] meet such criteria.

For surface modifications by zwitterionic polymers, both 'grafting from'[39–41] and 'grafting to' [36, 37] methods have been employed, with varying degree of success in developing 'ultra-low fouling' coatings. With the 'graft from' method, polymers can be initiated by immobilized initiators, like

initiators used in Atom Transfer Radical Polymerization (ATRP).[18, 38–40] The initiators, themselves are grafted on various surfaces by adhesive linkers; for example-thiols for gold surfaces,[47, 48] silanes for glass surfaces,[49] mussel-inspired bioadhesive known as 3,4-dihydroxyphenylalanine (DOPA) groups[42] for various surfaces. On the other hand, 'graft to' method requires the direct attachment of pre-prepared polymers onto the surfaces via the above-mentioned linkers. The ''graft-from'' method via surface-initiated ATRP is able to produce coatings with high packing densities while the ''graft-to'' method via DOPA linkage is conveniently implemented for practical applications.[2, 44] These coated substrates are then challenged with complex biological media such as protein,[20] cells,[37] platelets,[51] 10 and 100% human serum and plasma,[22, 52] bacteria,[42, 53, 54] and in the in vivo environments[55] for assessing the anti-fouling properties of the polymer coatings. Zwitterions have been utilized in a variety of structures designed for biological applications (Figure 1.2).[56] For example, zwitterionic polymers are used as protein chaperones and stabilizers,[50, 51] for making zwitterionic polymer-protein conjugates,[59, 60] zwitterion-conjugated surfaces,[20, 29, 43, 48] , zwitterion-conjugated membranes,[61–63] zwitterionic nanoparticles,[64–66] hydrogels,[67–70] and liposomes.[71]

These studies report phenomenology without any understanding of the mechanisms of protein adsorption on grafted polymer chains. In Chapter 2 of this thesis, we identified design parameters that tune protein adsorption on polysulfobetaine grafted at various grafting densities and described the mechanism of adsorption based on theory of colloid interactions with weakly-attractive grafted chains. In the next section this theory is described in details.

1.3 Theory of protein adsorption on weakly attractive grafted brush

Theoretical studies analyzed different modes of protein adsorption to end-grafted polymers under both good and poor solvent conditions, as a function of molecular weight and grafting density.[93, 151, 152, 75] Proteins can adsorb to brushes by three modes, depending on the protein dimensions, the protein–surface attraction, the polymer molecular weight (MW) and the grafting density Γ (chains per area)[92, 94] (Figure 1.3). When $2R_P \ll s$, primary adsorption occurs when proteins can diffuse through the brush to adsorb to the grafting substrate, and the adsorbed amount will depend on the brush properties and magnitude of the protein–surface attraction (Figure 1.3a; primary adsorption). At densities where $2R_P \gg s$, proteins may adsorb at the outer edge of the brush (Figure 1.3b; secondary adsorption) via attractive interactions with the polymer or long-range attraction to the grafting surface. At intermediate grafting densities, reduced osmotic repulsion enables protein insertion into the brush (Figure 1.3c; ternary adsorption).[52, 55, 56] However, the osmotic and steric repulsion disfavors ternary adsorption under good solvent conditions where proteins do not bind the polymer.[52, 53] In good solvent, where there is negligible protein-polymer attraction, protein adsorption decreases monotonically with increasing grafting density.[54, 57] However, if the chains weakly attract proteins, then proteins can penetrate the brush and bind the polymer. Under the latter conditions, Kröger and Halperin predicted that protein adsorption versus the grafting density would exhibit a bell-shaped profile (Figure 1.4) with a maximum at intermediate grafting densities and negligible adsorption on either dense or sparse chains).[73] Indeed, such a bell-shaped profile was reported for weakly attractive, grafted poly (N-isopropyl acrylamide) above the lower critical solution temperature.[57, 58] The predicted adsorption profiles for non-interacting versus weakly attractive grafted polymers are thus distinct signatures for both testing the hypothesis that ZI polymers universally repel proteins and identifying conditions that tune protein adsorption.

Polymer models of protein interactions with grafted chains provide a theoretical framework for identifying material properties that suppress or promote protein adsorption.[72, 74, 77, 78, 80] Halperin predicted mechanisms by which proteins adsorb to surfaces displaying end-grafted chains in good solvent, as a function of the molecular weight and grafting density.[77] Halperin and Kröger developed a model to describe interactions between proteins and neutral brush segments like polyethylene glycol (PEG) considering two ternary adsorption modes,[73] such as (1) weak, nonspecific adsorption due to weak attraction between protein and brush segments (for example: interactions between PEG and serum albumin protein surface) and (2) strong, site specific adsorption (e.g. binding of PEG with antibodies). Ternary adsorption affects the capacity of brushes to repress protein adsorption and it can happen two ways- (1) backbone and (2) terminal adsorption. In terminal adsorption, the protein binds only to free ends whereas in backbone adsorption it binds to interior chain segments. For backbone adsorption, the protein adsorption per chain, Γ exhibits a maximum around $\Sigma \approx \Sigma_{osm}$ and tends to be zero for both $\Sigma \sim 0$ (densely grafted chains) or at $\Sigma \rightarrow \infty$ (dilute chains), where $1/\Sigma$ is the grafting density of chains. This is illustrated in Figure 1.4.

Proteins contain polar groups on surface, so it is puzzling that ZI polymers are considered to be general ultra-low fouling materials. A recent report indeed demonstrated that proteins bind zwitterionic poly(sulfobetaine) in solution, and that the polymer can alter the protein folding stability.[81] In this study, the tryptophan fluorescence of proteins with different isoelectric points (i.e. surface charges) was measured in the presence of polysulfobetaine chains in solution and it was shown that the melting temperature of the proteins is shifted, indicating that soluble pSB chains change both the local polarity near tryptophan residues and the protein conformation. Other reports also documented protein adsorption on some ZI polymer coatings.[69, 82] A limited number

of studies of poly(zwitterion) interactions with proteins reported that poly(zwitterions) can inhibit antibody binding or substrate recognition, suggesting a direct protein− polymer association.[58] Taking advantage of the weak protein-segment interactions, polyzwitterions are also studied as potential protein stabilizer and chaperones. [39, 40] A challenge is to reconcile these findings with reports of the super low fouling properties of these materials when grafted on substrates.

In chapter 2 we showed that the adsorption profile of proteins on grafted polysulfobetaine films follow a bell-shaped curve which was predicted by theory for weakly attractive grafted neutral polymers and thus, we provided a description of the adsorption mechanism. Moreover, the amount of polymer adsorption was measured in various salt concentration or ionic strength because the solubility of polyzwitterions is affected by salt type and salt concentration. The effect of salt concentration on the solubility of zwitterionic polymers is elaborated in the following section.

1.4 Zwitterionic polymer solubility

The solubility of zwitterionic polymers is dependent on solution ionic strength, temperature, type of ions present in solution. Their use as non-fouling materials and colloid stabilizers require polyzwitterions to be in a well-extended conformation upon grafting on substrates. Also, in hydrogel form the solubility of polyzwitterions also dictate the degree of swelling, and thus its mechanical or structural properties. Therefore, it is an interesting problem to look at solubility of these polymers in different environment at varying ionic strength, in presence of mono and multivalent ions, as well as temperatures, which is discussed in details below-

1.4.1 Effect of ionic strength and nature of inorganic salt on solubility of zwitterionic polymers

The addition of small molar mass inorganic salt has been shown to have a nuanced influence on swelling and solubility of polysulfobetaines. In the bulk, ions are needed to prevent strong

electrostatic intra-polymer associations of pSBMA (also known as self-association) and solubilize the polymer given the similar charge density of the cationic and anionic groups.[117, 118] Grafted poly(carboxybetaine) brush extension increased according to the order of $Li^+ > Na^+ > K^+$, but there is no influence of the anion species along the Hoffmeister series. On the other hand, the swelling of poly(sulfobetaines) in solution depended on the anion species in the series: $SO_4^{2-} < Cl^- < Br^- < NO_3^- < I^- < ClO_4^- < SCN^-$. Likewise, swelling depended on the cation species in the following order: $Li^+ < Na^+ < K^+ < Ca^{2+}$. [85, 86] In contrast, dynamic light scattering measurements showed that increasing salt concentration does not change swelling or hydration of poly(phosphorylcholine) brushes at all. [87]

The cloud temperature of such polyzwitterions has strong influence on the chemical structure of spacer group separating the anion and cation groups,[88] the nature of salt ions added (i.e. position in the Hoffmeister series) [111, 127, 140, 91] and polymer geometry.[92] For example- 3-((2-methacryloyloxyethyl) dimethylammonio)propane-1-sulfonate (SPE) and its analogues, similar to the pSBMA studied in this thesis, display decreasing cloud points with increasing amount of added salt, and the influence followed the order of the Hoffmeister series of anions: $SO_4^{2-} < Cl^- < Br^-$.[93] Interestingly, this behavior cannot be generalized for all polysulfobetaines due to various different chemical structures that are possible. [94]

Additionally, influence of salt concentration and salt types on the swelling behavior of grafted poly(sulfobetaine) chains are also not consistent. Some reports suggested that poly(sulfobetaines) in solution swell with increasing salt concentration, from 10^{-2} M to 1 M NaCl,[95] while other findings suggested that the chains contract.[96] Given these different results, it is important to establish how the ionic composition of the medium influence the interfacial properties of grafted, zwitterionic polymer films. These studies reveal the importance of knowledge of surface level

properties influenced by polymer chemistries in developing design rules for using polyzwitterions in various applications. This is addressed in this thesis in Chapter 3 and 4.

1.4.2 Modulating solubility by temperature

Zwitterionic polymers typically display upper critical solubility temperature (UCST),[1,79, 86, 56, 97] the temperature above which the constituents are completely soluble. This solubility behavior has been exploited for drug delivery applications employing polymers or copolymers as vectors. The UCST of the polymer can be used to release the drug only within in areas that temperature exceeds the UCST.[98] Studies showed that the UCST can be manipulated by changing the length of spacer group between the cationic and anionic charges of the betaine moiety,[99] the structure of the spacer group , as well as the nature and the amount of inorganic salt added to the polymer solution. For example, polySBP or poly(4-((3-methacrylamidopropyl)dimethylammonio)-butane-1-sulfonate), a polysulfobetaine has a higher cloud point than that of polySPP or poly(3-((3-methacrylamidopropyl)dimethylammonio) propane-1-sulfonate); the former has one more carbon in the chain spacer separating the charges.[88] The cloud point of polySBP also decreased with addition of salt. In subsequent studies it was discovered that the influence of length of chain spacer is more complex. For example, increasing the spacer length from three to four carbon increased the phase transition temperatures significantly for polysulfobetaines, but increasing the length of spacer from two to three for polycarboxybetaines the reverse effect was observed.[93] Moreover, the UCST can be manipulated by polyionic cosolutes. With pSB for instance, addition of polyanions have shown to decrease the UCST while addition of polycations have increased the UCST.[100]

1.4.3. Anti-polyelectrolyte effect of polyzwitterions in solution

The effective use of polymer coatings requires knowledge of their interfacial properties and dependence on polymer chemistry, chain density, and solution composition. Salts affect the phase behavior and excluded volume of zwitterionic polymers, but previous studies showed that the effects of ionic strength or salt composition on solutions of polyzwitterions are by no means universal.[101] The phase behavior of aqueous solutions of poly(sulfobetaine) in inorganic salts, for example, depends on the identity and amount of the salt, as well as the spacer group separating the anionic and cationic groups of the betaine moiety.[92, 88] This salt-dependent behavior sets this family of polymers apart from other neutral polymers like PEG.[102, 103] The salt-dependent behavior also differs from classical polyelectrolytes, whose hydrodynamic radii decrease with increasing ionic strength. By contrast, zwitterionic polymers often exhibit 'antipolyelectrolyte' behavior—that is, the solubility and hydrodynamic radii increase with increasing monovalent salt concentrations.[84,89,104] For example, the equilibrium thickness of zwitterionic poly(sulfobetaine) brushes in pure water is less than the Flory radius, but the chains swell with increasing monovalent salt concentration.[85,105,106] This anti-polyelectrolyte behavior has demonstrated functional benefits. Studies attribute the anti-fouling properties of zwitterionic coatings, in part, to the increased entropic barrier associated with greater polymer swelling in concentrated salt solutions.[107, 108] The anti-polyelectrolyte behavior is also exploited to sterically stabilize colloidal particles in concentrated salt solutions, such as physiological saline or brine.[29,65,109,110] In contrast to polyelectrolytes, which shrink and fail as steric stabilizers in concentrated salt solutions, the efficacy of zwitterionic polymers increases with increasing salt concentration. This is discussed in details in the following section. The swelling behavior of grafted brushes,[111] as well the hydrodynamic radius of phosphorylcholine polymers in aqueous solutions,[112, 105] reportedly

decreased or showed no change with increasing monovalent salt concentration. Conversely, reports of carboxybetaine zwitterionic brushes showing 'anti-polyelectrolyte' behavior, similar to polysulfobetaines in our case, are prevalent.[137, 139] These studies focused on salt dependent swelling behavior in solution or at interfaces. However, for development of non-fouling coating surfaces, or nanoparticle/colloid stabilizers, we need to understand how the solubility affects the surface forces or the repulsive entropic barrier generated by the polyzwitterionic thin films. Therefore, in this thesis we showed systematically the influence of ionic strength on interfacial forces of grafted polysulfobetaine brushes at varying grafting densities, as a model polyzwitterion.

1.4.4 Swelling behavior of polyelectrolytes

Charged polymers are known as polyelectrolytes, which can be divided into two major classes- univalent polyelectrolytes, where all charges have the same sign (either positive or negative) and multivalent polyelectrolytes, also known as polyampholytes, where the molecules contain both negative or anionic and positive or cationic groups. When overall net charge on the polyampholytes is zero, that is, it consists of equal number of positive and negatively charged groups it is known as polyzwitterions. Example of biological univalent polyelectrolyte is hyaluronic acid, which consists of negatively charged carboxylic acid group. Cationic polyelectrolytes often consist of positively charged ammonium groups such as: $-N^{+}(CH_3)_3$

The segments of univalent polyelectrolytes usually repel each other, but they can be attracted in physisorbed form or repelled in depleted form, from surfaces depending on the relative strengths of van der Waals and electrostatic forces. The forces between surfaces grafted with polyelectrolytes are very interesting because in addition to the excluded volume effects, the segment length, Kuhn length, l_K, degree of association, α, pH, type and concentration of electrolyte ions, c_s in the bulk solution come into play.

Pincus explained the interactions between grafted polyelectrolytes into two regimes: (1) the dilute 'osmotic brush' regime when the mean separation between the counterions within each layer, $s_c < c_s^{1/3}$, and in this case, the length of the brush is independent of salt concentration in the bulk and the brush thickness is given by, $L = \alpha^{1/2} L_c$; L_c= countour length of the polymer; and (2) the concentrated 'salted brush' regime where the brush thickness is given by, $L = \alpha^{1/2} L_c / s_c c_s^{1/3}$, where $s_c c_s^{1/3} > 1$. Therefore, the layer thickness decreases with increasing c_s with weak dependence of $L \propto c_s^{-1/3}$. This means that when the concentration of added salt exceeds the concentration of 'free' mobile counter ions within the brush, a crossover occurs. The osmotic pressure of the counterions decreases and the brush height decreases accordingly.[115]

In brushes containing weak polyelectrolytes (also known as 'annealed brush') the degree of association depends on pH of the solution. For such weak polyelectrolytes, upon the addition of large amounts of salt the brushes shrink in a very similar way as strong polyelectrolyte brushes according to $L \propto c_s^{-1/3}$, however, in presence of low amounts of salt causes the brush height to increase. This is predicted by Lyatskaya et al. and Fleer [116, 117] and the swelling of brush follow a power law of $L \propto c_s^{1/3}$. The salt dependent swelling behavior of strong and weak polyelectrolytes is illustrated in Figure 1.5.

In Chapter 3, we showed that the surface forces and the range of interactions between grafted polysulfobetaine chains and mica increased with increasing ionic strength. The force-distance profile is different from surface force measurements between grafted polyelectrolytes previously measured by Balastre et al.[118] where they demonstrated that at higher salt concentrations the range of the repulsion decreases as $1/c_s^{1/3}$.

The ability to generate steric or osmotic repulsion barrier of polyzwitterionic thin films in high salt solution , as studied in this thesis, is very important aspect of these polymers in biomedical or

marine applications for prevention of non-specific protein adsorption and/or microorganisms attachment on surfaces. The surface forces can be measured at sub nanometer distance resolution by a popular technique called Surface Force Apparatus (SFA) as described in the following section.

1.5 Surface force apparatus for measuring surface forces

SFA measurements are uniquely suited to interrogate molecular level surface properties of zwitterionic polymers. Force measurements quantify the ranges, magnitudes, and origins of interfacial forces that determine polymer interactions. [119, 120] Force measurements are distinct from, but complimentary to, spectroscopic methods that have been applied to zwitterionic polymers,[34, 71] which identify perturbed chemical groups or structural changes, but not the interaction potentials that cause those perturbations. The SFA quantifies molecular scale forces between the surfaces of two macroscopic, curved, transparent silica disks as a function of their separation.[119, 122]. Surface Forces Apparatus (SFA) is used for directly measuring the force-laws between surfaces in liquids or vapors at the Ångstrom resolution level. The technique is developed and described in details by Christenson,[123–126] Israelachvili,[127–129] Horn,[80, 81] Leckband,[132–135] Patel and Tirrell,[136] Claesson,[125, 137] Craig,[138] Kumacheva[139] and many more.

With the SFA technique two atomically smooth and curved surfaces of radius ~1 cm, usually back silvered mica (thickness ~2-3 μm) immersed in a liquid can be brought toward each other in a highly controlled way. The two surfaces are in a crossed cylinder configuration which is locally equivalent to a sphere near a flat surface or to two spheres close together. The distance between the two surfaces is controlled by use of a three-stage mechanism of increasing sensitivity: The coarse control (upper rod), the medium control (lower rod) and a piezoelectric crystal tube allow positioning to within about 1 mm, 1 nm and 0.1 nm respectively. A schematic diagram of our SFA

setup is given in Figure 1.6 and a schematic diagram of the inside of the Mark II SFA is given in Figure 1.7. The steps for preparing mica and details of processing captured images of fringes using a MATLAB program is described in details in *Appendix B and D* respectively.

As the surfaces approach each other, they trap a very thin film of liquid between them, and the forces between the two surfaces (across the liquid film) can be measured. In addition, the surfaces can also be moved laterally past each other for measuring shear forces during sliding. The results on many different liquids have revealed ultrathin film properties that are profoundly different from those of the bulk liquids.

In most SFA experiments, the surfaces are visualized optically with Multiple Beam Interferometry (MBI) using "fringes of equal chromatic order" (FECO) in a spectrophotometer.[69, 90, 91] The MBI theory is discussed in details in *Appendix C*. Briefly, in SFA setup a white light is passed vertically up through the two opposing surfaces and the emerging beam is then focused onto the slit of a grating spectrometer (Jarrell-Ash half-meter grating spectrometer, dispersion: 3.28 nm/mm). The beam emerging from the spectrometer can be viewed by an eyepiece or recorded via a video camera (Figure 1.6). In our study, we used an Andor Zyla 5.5 sCMOS camera (Oxford Instruments), at an exposure time of 0.3 seconds and took snapshots of the FECO fringes using Andor Solis software. From the positions of the colored FECO fringes seen in the spectrogram, the thickness of adsorbed layers and the absolute distance between the two surfaces can be measured, as well as the refractive index of the medium between them. The shapes of the FECO fringes one obtains the shapes of the surfaces and of any thin film trapped between them (Figure 1.7). A great benefit of the FECO optical technique is that thermal drifts of the surfaces can be directly monitored and controlled.

Normal forces between the surfaces are measured by moving the surfaces at the base of the double-cantilever 'force springs' by a distance $\Delta D_{applied}$ using the differential micrometer, motor-driven fine micrometer and/or piezo tube. The actual distance that the surfaces move relative to each other, ΔD_{meas}, is measured by MBI. The changed force ΔF between the surfaces, when they come to rest at a separation D, is therefore-

$$\Delta F(D) = k(\Delta D_{applied} - \Delta D_{meas}) \quad \text{(Equation 1.4)}$$

where k is the spring constant. Then measured surface forces between the cylindrically curved surfaces are normalized by the radius of curvature R in order to directly relate to the interaction energy per unit area between two flat surfaces by applying Derjaguin approximation:

$$F(D)/R = 2\pi E(D) \quad \text{(Equation 1.5)}$$

In Chapter 2 and 3, Surface Forces Apparatus (SFA) measurements were used to quantify the molecular scale forces between end-grafted zwitterionic poly(sulfobetaine) polymers and mica, as a function of the grafting density and molecular weight, at different monovalent salt concentrations. For such an asymmetric system consisting of- (1) the grafted pSBMA chains-thiol thin film and (2) mica in aqueous solution corresponded to a 2 layer asymmetrical interferometer, given by: $D\mu_3^2 = n\Delta\lambda_n\mu_1/2$ for small separation;[119] Here, $\Delta\lambda_n$ is the shift of wavelength λ of the nth fringe, μ_3 is the refractive index of the medium (salt solution in this case), μ_1 is the refractive index of mica and D is the thickness or separation distances between the two surfaces. The two-layer model is a good approximation for our system because the ~2-3 μm thickness of mica is 1-2 orders of magnitude larger than the ~2-20 nm thickness of the organic layers (the details of derivation of equations is given in *Appendix D*).

Mica is a molecularly smooth, birefringent material which means that it has two indices of refraction in the plane perpendicular to the incident light (mica also has a third optical axis, *α*-

component, which is parallel to the incident light and thus not observed in SFA experiments). The optical path with the lower refractive index results in the lower wavelength fringe, the β-component, and the higher refractive index results in the higher wavelength γ -component. Typical values for the refractive index of reddish or brownish mica are

$$\mu_\beta = 1.5794 + 4.76 \times 10^5/\lambda^2 \ \text{Å}^2$$

$$\mu_\gamma = 1.5846 + 4.76 \times 10^5/\lambda^2 \ \text{Å}^2$$

When the optical axes of the two mica surfaces are perfectly aligned, the shift between the β- and γ -components of the fringe will be maximized. Conversely, when the optical axes are at right angles to each other, there will be no shift between the β- and γ -components of the fringes. The mica acts as a polarizer for the light going through the surfaces, and if great care is taken to align the surfaces in a known orientation, it is possible to gain insight into the molecular alignment between the surfaces. In this work, mica was used as a test surface during force measurements.

The discs are coated with metal and using interferometric techniques, the absolute surface separation with Angstrom resolution can be determined. The interferometry is an important advantage for investigating soft, deformable solvent-swollen polymer brushes whose compressibility makes it difficult to establish the true separation distances.[135] The SFA allows accurate force measurements as a function of absolute surface separation, obtaining structural (brush height), behavioral (repulsive, attractive, adhesion), and historical (hysteresis) information. For example, SFA has been previously used to investigate polyelectrolytes brushes in the presence of salts, showing that multivalent ions cause brush adhesion and hysteresis caused by a bridging action of the ions between brush chains, while in the presence of monovalent ions, brushes present purely repulsive forces with no detectable hysteresis.[142] SFA has also been used to show other water soluble polymers such as PEG and PNIPAM fail to follow simple polymer approximations

and antifouling behavior.[143–145] These example works demonstrate the potential SFA has for investigating the structure and behavior of zwitterionic polymer brushes.

Previous Atomic Force Microscopy (AFM) and Neutron Reflectivity studies characterized the swelling behavior of grafted brushes. AFM measurements of the force versus the distance between phosphorylcholine brush grafted surface and a colloidal probe were used to estimate grafting density and degree of polymerization of grafted chains, using Alexander de Gennes theory as a first approximation. [146] However, one of the limitations of AFM is that we cannot accurately predict whether the probe contacted the sample i.e. polymer brush due to possible long range interactions between the probe and the brush, and substrate deformations. [147]

In our studies the resolution of distance measurements were affected by the gold coated substrates (compare sharpness of FECO fringes in Figure 1.8 and Figure 1.9). The estimated surface roughness of gold is ~1 nm (see AFM images in *Appendix A*) and as such, it limits the distance resolution of our measurements to ~1 nm. For better resolution, Klein et al. used macroinitiator coated mica substrates to graft polyzwitterions in surface force measurements, which requires special setup to avoid any contamination on high surface energy mica during the polymer synthesis process. [148] This will be under consideration in preparation of substrates for future surface force measurements.

In Chapter 4 of the thesis, the surface forces were measured between a statistical copolymer consisting of non-ionic oligoethylene glycol and zwitterionic sulfobetaine content at varying compositions and mica. The motivation for this project is described in the following section in details.

1.6 Statistical copolymers

Statistical or random copolymers have a uniform average composition along the contour length of the polymer molecule, which are different from traditional block copolymers, which exhibit a step function change in composition at the junction point between the blocks. Gradient copolymers are intermediate between random and block copolymers, which have a controlled gradient of composition along the backbone of the chain. [149] Statistical copolymers are of great interest because of their ability to reduce the interfacial energy between the two components, which is crucial for achieving good mixing and adhesion between immiscible components. [150] Also, copolymers are used in designing of nanocomposite materials one of the challenges is to tune interfacial energies between particle fillers and the matrices to facilitate dispersion of particles.[151–154] Moreover, diblock polymers are exploited on neutral surfaces (i.e. surfaces with zero interfacial energies) to obtain perpendicular orientation of microdomains of the blocks at the interface, which has important implication in electronic materials application. [155] More recently, proteinlike chains with tunable sequence distributions for applications as compatibilizers have also been studied.[156] One of the ways to tune interfacial energies using copolymers is to vary the composition of the components. Experimental studies have extensively studied the effect of chemical sequence on the efficacies of statistical copolymers for use as 'chemical compatibilizer' between incompatible polymer blends, between polymers and surfaces. [150, 157] These studies demonstrated that random copolymers can strengthen interfaces of incompatible homopolymers much better than diblock copolymers.[150] Also, by changing the composition of styrene of a poly(styrene-co-methylmethacrylate) the interfacial energies between the copolymer and homopolymer melt becomes more favorable when the composition of the grafted copolymer chemically resembles more similar to that of the melt. [158] One interesting study showed the importance of diblock

copolymers to control the orientation of lamellar microdomain at the interface as surface modifiers.[159]

In addition to experimental studies, many theoretical studies have been carried out to quantify the interfacial width of such immiscible polymer blends and copolymers, the interfacial energies, the characteristic length of loop and size of microdomains by Self-Consistent Field Theory (SCFT),[160] Flory theory,[161–163] Monte Carlo Simulations,[164,165] Molecular Dynamics Simulations[166] and scaling and analytical theories.[161,167] One of the important parameter for describing 'blockiness' of chains is f, whose limit is going from the least blocky or alternating copolymers to most blocky or diblock copolymers. These studies report that the copolymers behave like compatibilizer between two immiscible polymer blends by maximizing energetically favorable contact between the favorable components while optimizing entropy by forming loops. [166] Gersappe et al. used Monte Carlo simulations and SCFT to model the behavior of grafted random AB copolymer brushes with solvophobic component B and showed that B monomer, the incompatible segments within the copolymer has a tendency to segregate away from the solvent due to the distribution in the sequence composition, this 'layering effect' or 'vertical segregation' was more prominent with the increasing blockiness of the copolymer. [168] They also showed that 'lateral segregation' or 'rippling effect' for the 'blocky' copolymers with well-defined microdomains of B component, which decreases for the random copolymers and form almost a uniform phase for the alternating copolymer or the least blocky copolymer, indicating that lateral phase separation doesn't occur in this system. The prominent lateral segregation that was observed for 'blocky copolymers' resemble the behavior of a brush that contained 50/50 mixture of incompatible homopolymers of A and B. [169–171] Pickett demonstrated that demixing of AB gradient copolymer brush occurs with a chain-end exclusion zone that is small and located near

the grafting surfaces at high temperatures, but extends throughout the brush layer at lower temperatures by using scaling theories and SCFT. [172] Moreover, Trombly et al. used SCFT to quantify the interfacial properties of random copolymer brushes (AB) in contact with a homopolymer melt A and showed that the interfacial energy increases with increasing grafting density, chemical incompatibility between the components, and the relative size of free chain to the grafted chains.[157] This analysis also showed that it is possible to achieve 'neutral or zero interfacial energy' surfaces by increasing grafting density of the random copolymer brush at a particular effective volume fraction, $f_{eff} \sim 0.5$ in the interfacial zone between the brush and melt. This study reveal the importance of using random or statistical copolymer brushes to reduce interfacial energies or achieve neutral conditions between surfaces and polymer blends.

In Chapter 4 we will discuss the use of a particular random copolymer with oligoethylene glycol and sulfobetaine monomers at high and low grafting densities in biological applications and how its surface energy is affected by the change in composition in the grafted copolymer at varying ionic strength. We find that the component of the grafted copolymer affect the overall swelling behavior of the brush or mushroom like chains independently, in an additive manner i.e. with the increase of the ionic strength dependent component, % sulfobetaine content in the grafted copolymer. This finding has important applications where the homopolymer PEGMA and pSBMA are used to tune interfacial energy with proteins to modulate interaction such as-biocompatible materials in protein drug delivery. Moreover, the weak interactions of the sulfobetaine segments with proteins, and the preferential hydrophobic interactions of OEG with proteins is hypothesized to stabilize immobilized proteins/high value drugs which is discussed in future work in Chapter 6.

1.6.1 Comparison with non-ionic polymer: Polyethylene Glycols (PEG)

Surface modification with PEGs have previously been explored to achieve protein stabilization[4, 5] or reduce non-specific protein adsorption of opsonins.[175] Also, an example of using polyzwitterions to enhance protein stabilization was demonstrated by conjugating a model protein (chymotrypsin enzyme) with zwitterionic poly(carboxybetaine) and compared with the gold-standard PEG. Using urea denaturation assay, and thermostability measurements, they showed that while the stabilizing effect was comparable for both polymers, the mechanism is different.[176] Cleland and coworkers demonstrated that PEG stabilized partially unfolded proteins against aggregation by binding to exposed hydrophobic surfaces.[174] For PEG-lyted proteins, PEG acts as a protective physical barrier around the protein, increasing the local viscosity and eventually reducing the structural dynamics of proteins and thus, making it more difficult to unfold and remain folded.[177] On the other hand, pCB-protein conjugate was found to stabilize globular proteins by drawing water molecules away from hydrophobic regions of proteins, due to its superhydrophilicity, and thus holding the protein together by strengthening its hydrophobic interactions and reducing interaction with water surrounding it.[176]

The head-on-head comparison of PEG and pZI has been performed in terms of surface hydration, water structuring, protein stabilization and/ antifouling mechanism in bulk solution and on grafted conditions. The antifouling mechanism of polymers is often hypothesized to be due to the strong surface hydration where water molecules tightly associated with the polymer that act as physical and energetic barrier for biomolecules to displace water,[102,178–181] but the non-covalent interactions driving the strong hydration depend on the polymer. For PEG, water associates to the oxygen atoms of ether (-R-O-R'-) through hydrogen bonding.[103] On the other hand, evidence of strong hydration in zwitterionic polymers has been demonstrated to occur through electrostatic

interactions.[182–185] Molecular simulation studies reported ethylene glycol$_4$ or EG$_4$ alters the properties of the protein via hydrophobic interactions whereas superhydrophilic carboxybetaine polymers or CB has a minimal effect on the protein due to the shared zwitterionic nature of CB and protein.[186] Furthermore, the number of water molecules associated with side chains of polyzwitterions depends on the differences in charge densities of anions and cations.[88,187] Experiments comparing the two polymer classes showed that surface hydration with PEG was perturbed upon contact with proteins, while no or little influence on water structuring could be seen around pSBMA brushes.[186,188]

These studies show that the underlying molecular signatures of polyzwitterions and PEG-lyted systems are unlikely to be similar. In chapter 4, we systematically varied the zwitterionic content in random copolymers of poly(SBMA-co-OEGMA) and investigated the influence on surface forces at varying ionic strength in the surrounding medium. The research question is- do these chemically different constituents of copolymer chains mix well together or do they phase separate? The differences in ionic strength dependent surface forces with copolymer composition inform us how such 'chemically heterogeneous' material differentially interact with proteins or small molecules in various applications, discussed in the following subsection.

1.6.2 Stabilization of protein-conjugates in chemically heterogeneous environment

Surface modification with copolymers of two different chemical structures of monomers is of great interest to improve functional outcomes. For example-in order to exploit the stimuli-responsiveness of both zwitterionic polymers and non-ionic PNIPAM polymers, copolymers were synthesized and tested for improved and controllable properties, such as phase separation of ionic zwitterionic segments at T<UCST and of non-ionic segments of PNIPAM at T>LCST.[189] Chang and coworkers incorporated zwittterionic blocks in diblock copolymers for surface modifications

to mimic polar/hydrophlic biomaterial surface with controlled surface coverage or packing density and achieved high resistance to fouling from complex media such as whole blood.[190] Moreover, Tethered zwitterionic chains also reportedly stabilize proteins.[191] In recent works by Schwartz et al., copolymer brush consisting of OEGMA and pSBMA was explored to develop chemically heterogeneous substrate that can stabilize proteins by segregating the polar surfaces through interactions with polar groups of SBMA and segregating the hydrophobic regions of protein via interactions with the amphiphilic OEGMA part of the copolymer brush.[192] Interestingly, most stabilization of protein in this study was seen with an intermediate % zwitterionic content in the grafted copolymer brush but the mechanism was unclear. Given the interest in developing biocompatible, non-fouling coatings with superhydrophilic sulfobetaines and amphiphilic oligoethylenes, the interfacial properties of a statistical copolymer with simple variation of its constituents were studied for better and improved functional outcome in Chapter 4.

1.7 Antifouling mechanism of polyzwitterions

The antifouling mechanisms of polyzwitterions are often attributed to surface hydration, association of large number of water molecules and formation of steric barrier. Also, lack of entropy gain due to ions and water molecules release are also discussed in literature.[50] These mechanisms can manifestations of a central concept that can be described by enthalpy and entropy of the system. Large surface hydration of polyzwitterions means increasing effective excluded volume of the monomer layers which form a steric barrier against protein adsorption or fouling. Moreover, the higher the number of water molecules, the larger the enthalpy of hydration for the proteins to overcome. The number of water molecules also depends on the coordination number of the ion spheres in the side chains of the polyzwitterions. Only when the entropy gain due to

counterions (from both proteins and polymers) and water molecules release is higher than the enthalpy of hydration, proteins can bind or adsorb. For polyzwitterions, this is usually not favorable because the enthalpy gain due to hydration on polymer segments is usually very high that prevents water displacement. Moreover, hydrophobic interaction between protein and polymer segments is too small to overcome the large enthalpy of hydration, therefore it is not a driving force for protein adsorption. Therefore, the net entropy gain and the high enthalpy of surface hydration lead to low to negligible non-specific protein adsorption or fouling. The details of the water structure argument, surface hydration argument, water and counter ion release argument are discussed in *Appendix G.*

1.8 Simple polymer theories to explain interactions of grafted brushes in good solvent

When two polymer-covered surfaces approach each other, they experience repulsive force once the outer segments begin to overlap at a separation distance of a few R_g. This interaction is usually called a repulsive osmotic force due to the unfavorable entropy associated with confining the chains between the surfaces. In the case of polymers this repulsion is usually referred to as the steric or overlap repulsion, and it plays an important role in many natural and practical systems. For example, colloidal particles that would normally coagulate in a solvent can often be stabilized by adding a small amount of polymer to the dispersion. Such polymer additives are known as protectives against coagulation, and they lead to the steric stabilization of a colloid. [29,30]

The forces depend on (1) the coverage of polymer on each surface, (2) whether the polymer is simply adsorbed from solution (a reversible process where the coverage depends on the bulk polymer concentration) or irreversibly grafted onto the surfaces, and (3) the quality of the solvent for the polymer. Two limiting situations, corresponding to low and high surface coverage, are

described by Dolan and Edwards theory and Alexander, de Gennes theory and/or Millner-Witten-Cates theory respectively.

In the limit of low surface coverage there is no overlap or entanglement of neighboring chains, and each chain interacts with the opposite surface independently of the other chains. For two such surfaces the repulsive energy per unit area is a complex series, but over the distance regime from D≈ 8Rg down to D≈2Rg, it is roughly exponential and is given by Dolan and Edwards theory [193]

$$\frac{F(D)}{R} \approx Ae^{-\frac{D}{Rg}}$$ (Equation 1.1);

Here, the prefactor, A≈ $\frac{72\pi KT}{\Gamma}$, where Γ is the area per chain, K is the Boltzmann constant and T is absolute temperature. For simple chains in good solvent, the decay length is the radius of gyration of a random coil, R_g. However, with pSBMA chains from the Dynamic Light Scattering (DLS) experiments showed that, the hydrodynamic radius, r_H depend on the salt concentration.[48,85,194,195] We therefore deem the decay constant an "effective R_g" or R_{eff}.

Going from low coverage ($s > R_g$) to high coverage ($s < R_g$), the adsorbed or grafted chains are forced to extend away from the surface much farther than R_g or R_F. In the case of end grafted chains, as might be expected intuitively, the thickness of the "brush" layer L in good solvent, where the segments repel each other, is given by $L=nl^{3/5}/s^{2/3} =R_F(R_F/s)^{2/3}$ [196] ; where s is the distance between two grafted chains, n is the degree of polymerization and l is the monomer length (approximately 0.3 nm). The repulsive pressure between two brush-bearing surfaces is given the Alexander-de Gennes equation [197]

$$P(D)= \frac{KT}{s^3}[(\frac{2L}{D})^{9/4}-(\frac{D}{2L})^{3/4}]$$

The first term in Equation 1.2 comes from the osmotic repulsion between the coils, which favors their expansion and so acts to increase D, while the second term comes from the elastic stretch

energy of the chains, which favors contraction and so acts to decrease D. The energy form of this equation, after some modifications is given by,

$$\frac{F(D)}{R} \approx \frac{16KT\pi L}{35\, s^3}\,[7(\frac{2L}{D})^{5/4}\text{-}(\frac{D}{2L})^{7/4}\text{-}12] \quad \text{(Equation 1.2)}$$

for D<<R and D<2L. [198]

In contrast to the Alexander-de Gennes model (AdG), which assumed a step function for the segment density profile, the self-consistent mean field analysis of Millner-Witten-Cates theory[199] assumes a parabolic concentration profile of chains with normal distance from the grafted substrate and the distance-dependent free energy between end-grafted chains in good solvent is given by-

$$\frac{F(D)}{R} = -\,4\pi P_0\,[(\frac{2L_0}{D}) + (\frac{D}{2L_o})^2 - \frac{1}{5}(\frac{D}{2L_o})^5 - (\frac{9}{5})] \quad \text{(Equation 1.3)}$$

where, D is the distance between mica and the grafted polymer and L_0 is the equilibrium brush extension. In this model, $L_0 \sim N(\sigma w)^{1/3}$ and $P_0 \sim N(\sigma w)^{2/3}(\sigma^2/12)^{1/3}$, where N is the degree of polymerization and w is an excluded volume parameter. Additionally, the compression energy of grafted brush is estimated to vary as the cube of the compression distance, D which is qualitatively weaker than that estimated by AdG theory with a step function of monomer concentration profile. Moreover, this theory assumes that the free ends of the chains are distributed throughout the entire height of the brush, rather than confined to a narrow zone at the outer extremity. The free energy of the compressed brushes is determined by the osmotic repulsion within the brush and by the elastic restoring energy of the chains. The first term of the equation represents the osmotic contribution, and the second and third terms reflect the chain elasticity. This model describes well the energy between grafted chains with narrow polydispersity. It does not account for segment-segment attraction or osmotic contributions from ions within the brush.

To adapt the above equation for our asymmetric system (grafted brush and bare mica surfaces), $2L_o$ is replaced by L_o, as described previously.[200, 132]

$$\frac{F(D)}{R} = -4\pi P_0 \left[\left(\frac{L_0}{D}\right) + \left(\frac{D}{L_o}\right)^2 - \frac{1}{5}\left(\frac{D}{L_o}\right)^5 - \left(\frac{9}{5}\right)\right] \qquad \text{(Equation 1.4);}$$

The use of such theories helps to develop design rules, such as prediction of optimal steric barrier thickness and surface density to effectively repel proteins of known size.

In Chapter 3 and 4, we will discuss how these simple polymer theories to quantitatively compare the salt-dependence of the interfacial forces, the force-distance profiles determined for brushes with Millner-Witten-Cates theory. Data obtained with dilute chains were compared with Dolan and Edwards theory. These simple polymer models do not account for segment-segment attraction prevalent in zwitterionic polymers. However, the dependence of fitted parameters on the salt concentration enabled quantitative comparisons of the amplitudes and ranges of the forces on the monovalent salt concentration. Therefore, simple polymer theories used in our study provided insight on the equilibrium chain extension of the brush, and relevant coil size of weakly overlapping chains or dilute mushroom like chains, and amplitude of surface forces from fitted prefactor values, which is an intrinsic scale of surface forces.

1.9 Research questions

Given the low fouling properties and excellent biocompatibility of zwitterionic materials, and their easy synthesis routes, these polymers of broad practical interests. In my research I attempted to address the following research questions-

a. Do proteins adsorb on grafted zwitterionic polymer chains? If they do, under what conditions do they adsorb? What are the design parameters for tuning the protein adsorption? What is the mechanism of protein adsorption on grafted zwitterionic polymers (**Chapter 2**)?

b. How do the ionic strength dependent swelling behavior influence surface forces of grafted zwitterionic polymers? What are the range of interactions and magnitude of such repulsive forces (**Chapter 3**)?
c. How does chemical composition of copolymers with zwitterionic content affect the surface forces? Do change in copolymer composition affect the miscibility of chemically different non-ionic and zwitterionic polymer? Do they behave independently of one another or do they interact with one another in ways that lead to phase segregation and affect the surface forces? (**Chapter 4**)?
d. What is the role of O-mannosylation in cadherin mediated binding? How do autoimmune antibodies that cause skin blistering diseases influence cell binding kinetics? (**Chapter 5)**.

My findings helped identify protein adsorption mechanism on grafted zwitterionic polymers that is described by the theory of particle interactions with weakly attractive polymer chains. This study helped reconcile solution studies that showed direct interactions of proteins with soluble polysulfobetaine chains with studies that demonstrated ultra-low fouling properties. The surface force measurements with homopolymer of sulfobetaine methacrylates and varied zwitterionic contents in copolymers revealed quantitative differences in chain extension, coil size and range and magnitude of repulsive forces at different ionic strengths. The results from this study show how grafting density, molecular weight and ionic strength cooperate to tune the osmotic repulsion barrier that have important implications in their use as nanoparticle stabilizer or non-fouling coatings in different environment. Moreover, results from the force-distance measurements using SFA reveal that the simple variation of monomer compositions of statistical copolymer with sulfobetaines and oligoethylene methacrylates allow tuning of interfacial forces of polymer grafted surfaces in different salt concentrations of the aqueous solution. Brief discussion on the cell

adhesion molecules-cadherins and their binding affinity under different types of mutations is given in Chapter 5. Finally I discussed future directions to study protein folding stability to test hypothesis that at an intermediate zwitterionic composition of the grafted copolymers, the protein folding is enhanced than that with either homopolymers. This study will help us understand the potential use of such copolymers for designing drug carrier with zwitterionic moieties encapsulating protein/drug of interest.

1.10 Figures

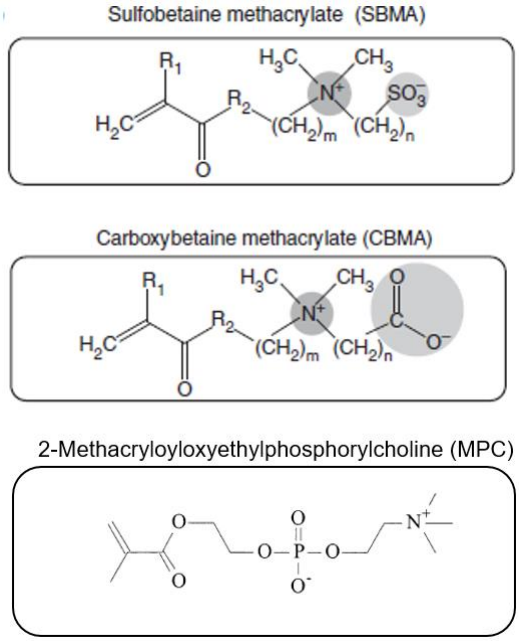

Figure 1.1: Chemical structures of common repeat units of zwitterionic polymers.

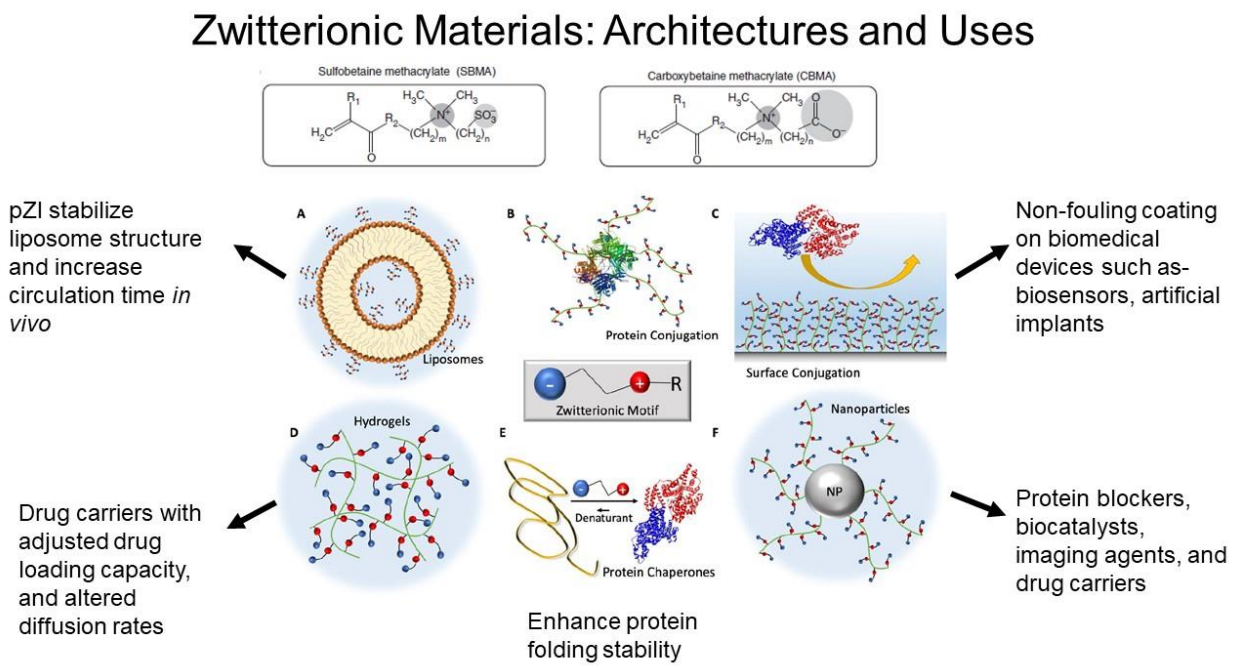

Figure 1.2: Applications of zwitterionic polymers in various forms and microenvironments [Adapted with permission from Erfani et al., *Biomacromolecules* **2020,** 21, 2557–2573. Copyright 2020 American Chemical Society]

.

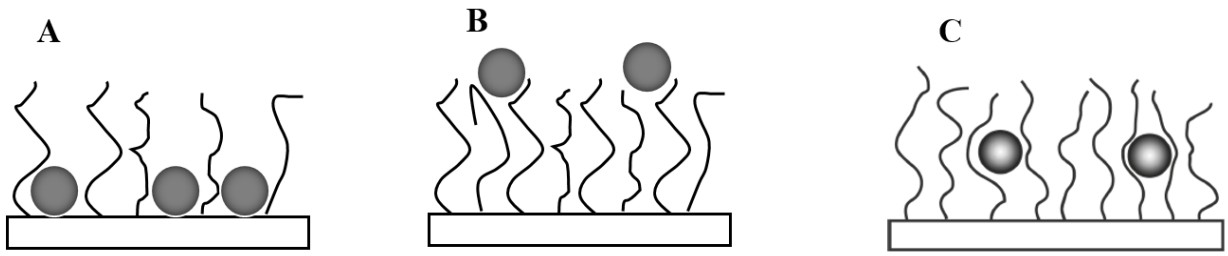

Figure 1.3: Protein adsorption modes on polymer brushes. (A) Primary Adsorption; (B) Secondary Adsorption and (C) Ternary Adsorption.

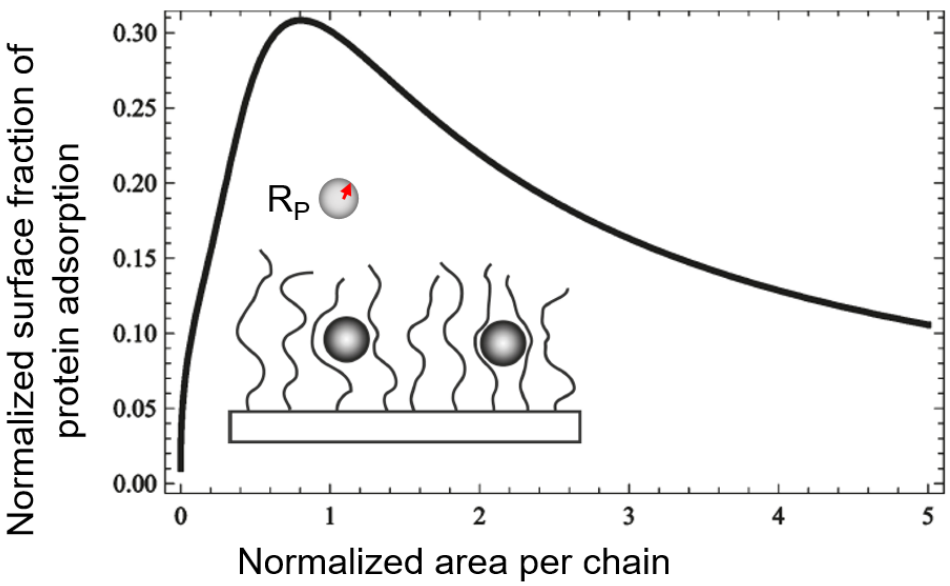

Figure 1.4: Predicted ternary protein adsorption profile for weakly attractive grafted brushes. This is the scenario for intermediate size of protein, R_P<<brush height, H_o so that it avoids compression of the brush, but the protein is large enough to incur a significant insertion penalty, $F_{in} \approx F_{osm} > k_bT$; that affects their ternary adsorption.

[Adapted with permission from: Halperin and Kröger, *Langmuir* 2009, 25(19), 11621–11634. Copyright 2009 American Chemical Society].

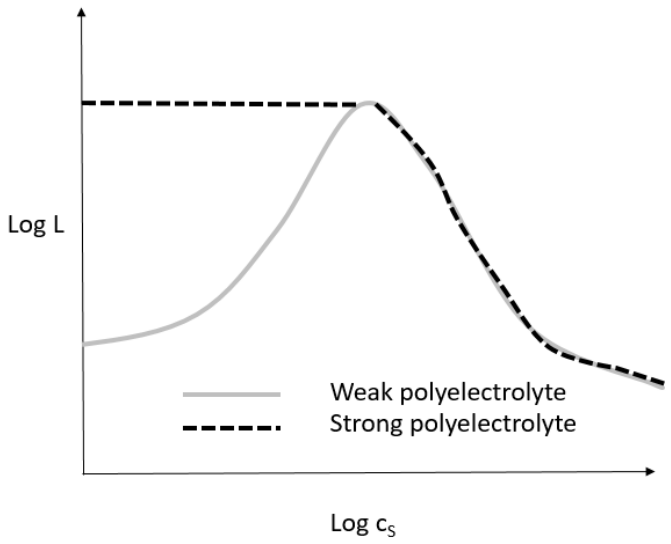

Figure 1.5: Dependence of the brush height L on the external salt concentration c_S. Both the behavior of a strong and a weak polyelectrolyte brush are schematically drawn. At low salt concentrations the thickness of strong polyelectrolyte brushes (dashed line) is independent of the concentration of added salt. Weak polyelectrolyte brushes (solid line) swell upon addition of salt.

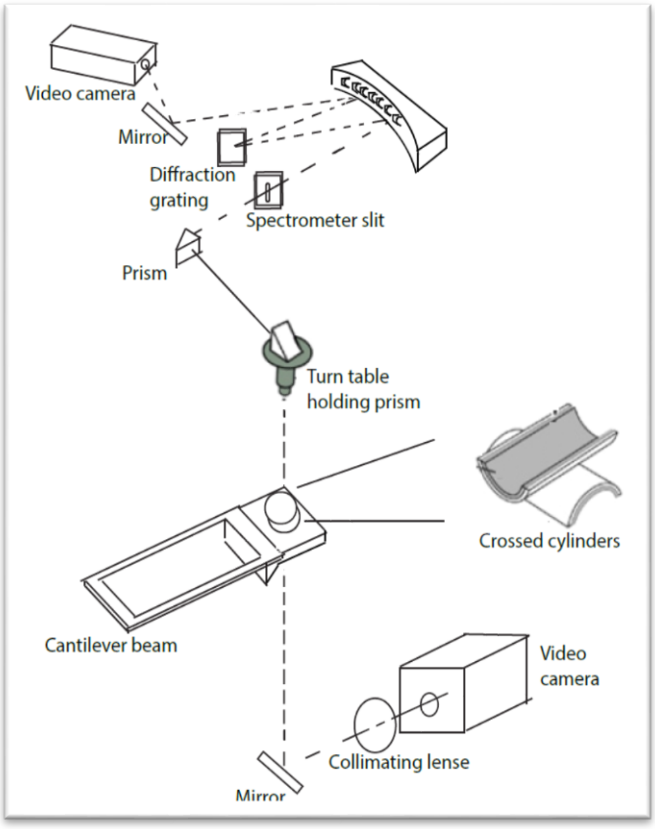

Figure 1.6: Schematic diagram of Surface Force Apparatus setup. The surfaces or the crossed cylinders are illuminated normally by collimated white light (a 150 W tungsten-halogen lamp). An image of the mica-gold surfaces is focused on to the slit of a spectrometer by a microscope objective lens, and the image is centered on the slit by a rotating turn-table. By rotating the turn-table the surfaces may be scanned allowing us to study the surfaces by observing the FECO fringes produced in the spectrometer.

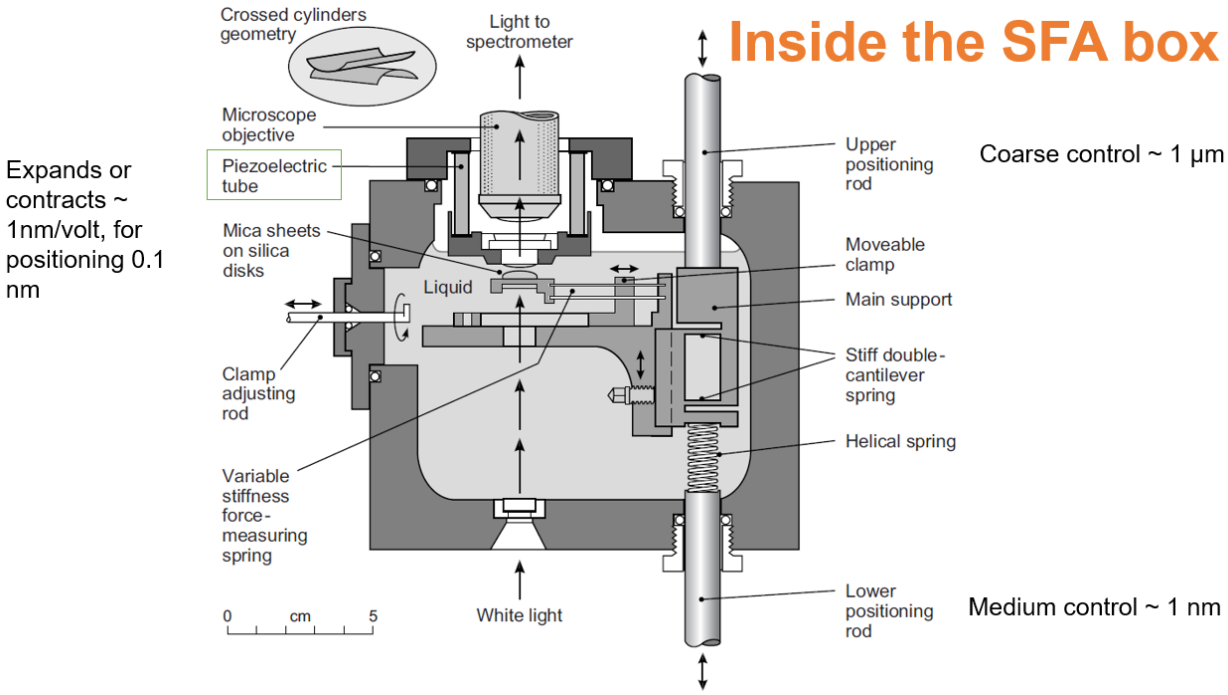

Figure 1.7: Schematic diagram of inside of the SFA box and various controls for separating distances between two crossed cylinders (shown in inset) [Adapted from J. Israelachvili, *Intermolecular and Surface Forces*, 3rd edition, Academic Press, **2011**, ISBN: 978-0-12-375182-9].

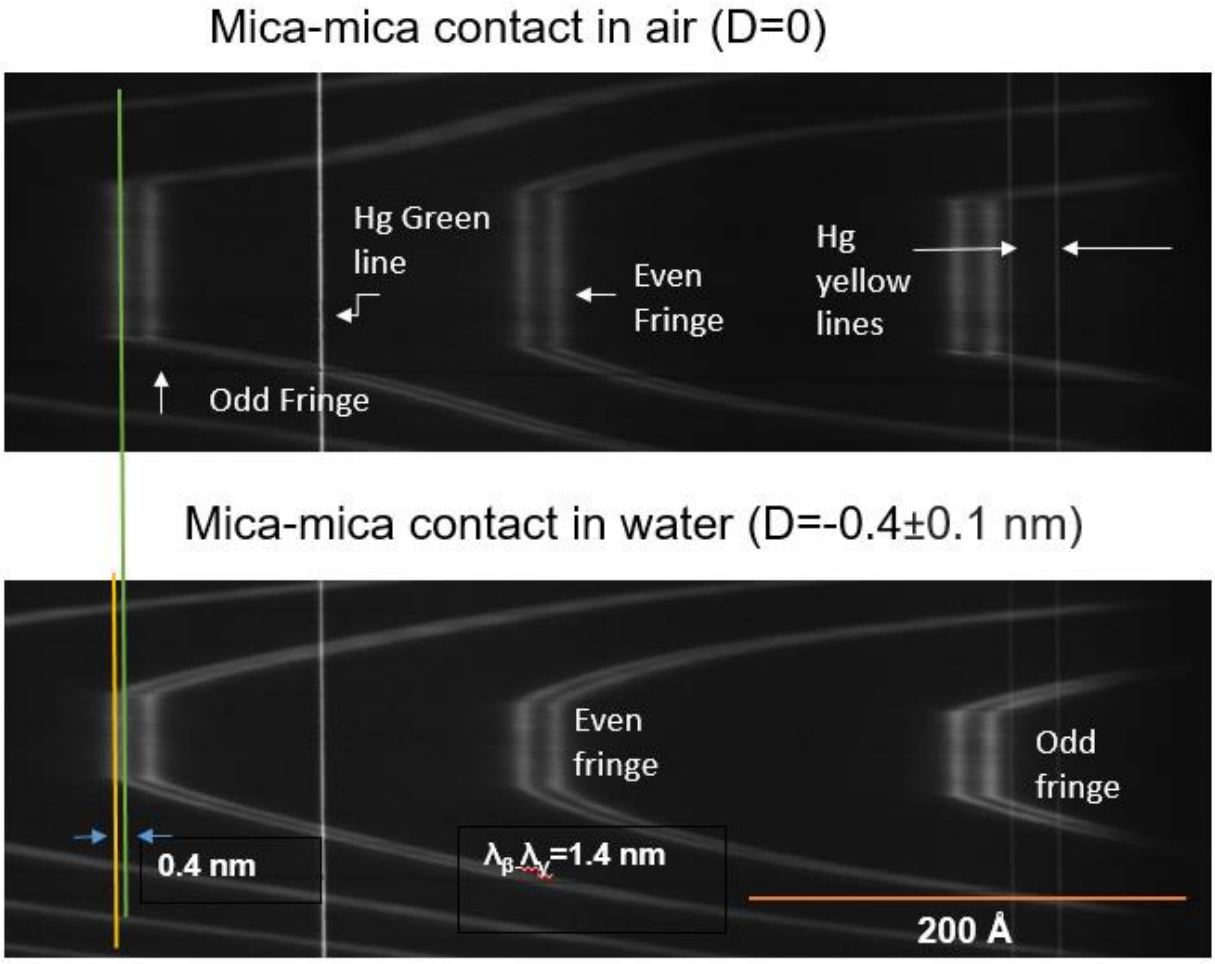

Figure 1.8: FECO of mica surfaces in adhesive contact (D = 0) (a) in air and (b) in water. Note that the odd order fringes appear narrower than the even order fringes. In both cases, the contacting parts of the surfaces flatten due to elastic deformations of the mica and supporting glue. Each fringe appears as a doublet with a β- and a γ -component due to the birefringence of mica. The vertical lines at the edges of the pictures are the green and yellow Hg calibration lines.

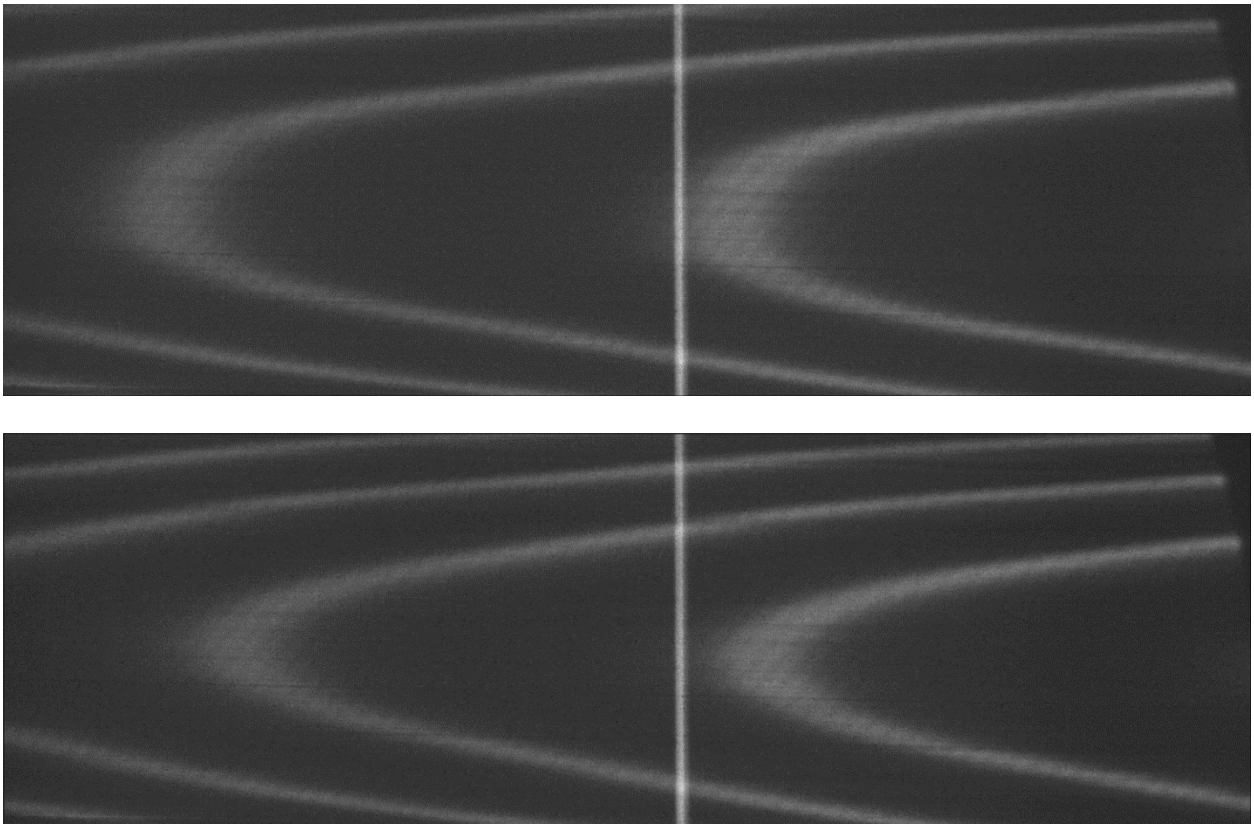

Figure 1.9: FECO of (a) contact between mica and OH-terminated thiol coated gold surfaces (D = 0) and (b) contact between mica and polysulfobetaine grafted gold substrate, in 10 mM sodium nitrate in 20 mM phosphate buffer at pH 7 . Note that the fringes are fuzzier than that for mica-mica system (Figure 1.7). This is because surface roughness of gold (RMS ~1 nm) which forms part of the interferometer. A Gaussian fit was applied to find the peak of the FECO fringes by a matlab program (*Appendix B*). The vertical lines at the edges of the pictures are the green and yellow Hg calibration lines.

CHAPTER 2: PROTEIN ADSORPTION ON GRAFTED ZWITTERIONIC POLYMERS

This chapter is adapted in part from journal article: Ahmed, Syeda Tajin and Leckband, Deborah E. Protein Adsorption on Grafted Zwitterionic Polymers Depends on Chain Density and Molecular Weight. *Adv Funct Mater*. 2020; 2000757:1-10 (doi:10.1002/adfm.202000757) with permission [copyright 2020 John Wily and Sons].

2.1 Introduction

Zwitterionic (ZI) polymers are of broad practical interest, in part due to numerous reports of the ultra-low fouling properties of zwitterionic surface coatings. [4,50,70,201] Zwitterionic polymers contain both cationic and anionic groups and are charge neutral. They are known for having properties such as ultralow non-specific protein adsorption and biocompatibility when grafted on surface. [22,67] Poly(zwitterions) have been exploited for applications that are negatively impacted by non-specific protein adsorption. Examples include biosensors, biomedical devices, targeted drug delivery, and tissue scaffolds. [61,202,203]

The 'ultra-low' fouling properties of ZI polymer coatings have been attributed mainly to polymer solvation, which simulations predict also prevents protein-polymer interactions. [84,187] Although solvation should in principle also prevent segment-segment interactions, under some conditions, zwitterionic polymers exhibit behavior characteristic of both inter-chain and intra-chain association. Specifically, polymer solubility is typically low at low ionic strength where polar groups are not screened. [85] Likewise, the concentration dependence of the viscosity of ZI polymer solutions suggests both inter and intra-chain association. [126, 233, 234] Both the chain solubility and swelling depend on ionic strength, consistent with the ionic strength-dependent regulation of polar,

segment-segment interactions and ion association with the chains. Moreover, the antifouling nature of such materials is very complex and attributed to many factors, including the chemical structure of side chains of polyzwitterionic materials. [24, 235]. In order to diversify the molecular design of grafted zwitterionic polymers, polysulfobetaines are often chosen to study the effect of charged group separations of side chains, chain length, orientation of side chains of polymer on the antifouling property. [24, 236]

Proteins also contain polar groups, so why would they not interact with charged groups on side chains of ZI polymers? A recent report indeed demonstrated that proteins bind zwitterionic poly(sulfobetaine) in solution, and that the polymer can alter the protein folding stability. [81] Other reports also documented protein adsorption on some ZI polymer coatings. [35, 236] A challenge is to reconcile these findings with reports of the super low fouling properties of these materials.

Halperin and Kroger predicted mechanisms by which proteins adsorb to surfaces displaying end-grafted chains in good solvent, as a function of the molecular weight and grafting density.[77] At low grafting densities, when the distance between chains (s) is less than the protein diameter, the proteins can diffuse through polymer layers to adsorb to the underlying surface (primary adsorption). At high grafting densities, proteins cannot penetrate the dense polymers, but may adsorb to the outer edge (secondary adsorption). At intermediate grafting densities, reduced osmotic repulsion enables protein insertion into the brush (ternary adsorption). [72,76,77] However, the osmotic and steric repulsion disfavors ternary adsorption under good solvent conditions where proteins do not bind the polymer [77,78]. In good solvent, where there is negligible protein-polymer attraction, protein adsorption decreases monotonically with increasing grafting density. [159, 237] However, if the chains weakly attract proteins, then proteins can penetrate the brush and bind the polymer. Under the latter conditions, Kröger and Halperin predicted that protein adsorption versus

the grafting density would exhibit a bell-shaped profile with a maximum at intermediate grafting densities and negligible adsorption on either dense or sparse chains. [73] Such a bell-shaped profile was reported for weakly attractive, grafted poly (N-isopropyl acrylamide) above the lower critical solution temperature. [79] The predicted adsorption profiles for non-interacting versus weakly attractive grafted polymers are thus distinct signatures for both testing the hypothesis that ZI polymers universally repel proteins and identifying conditions that tune protein adsorption.

Results from this study reconcile observed protein binding to pSBMA in solution with the reported ultra-low fouling properties of dense, ZI thin films. We investigated protein adsorption on end-grafted poly(sulfobetaine) (pSBMA) thin films, as a function of the grafting density, molecular weight, and ionic strength. Polymers were synthesized from surfaces using atom transfer radical polymerization, which enabled control of both the polymer grafting density and molecular weight. In measurements with both model proteins and full serum, the adsorption profiles exhibit bell-shaped curves, with maxima that depend weakly on the protein size and on the ionic strength. These results confirm protein binding to ZI pSBMA thin films. They also suggest an underlying adsorption mechanism and design rules for blocking protein adsorption.

2.2 Materials and methods

2.2.1 Chemicals

Monomer 2-(Methacryloyloxy) ethyl] dimethyl-(3-sulfopropyl) ammonium hydroxide or SBMA (95%, $H_2C=C(CH_3)CO_2CH_2CH_2N(CH_3)_2(CH_2)_3SO_3$, Molecular Weight 279.35) was purchased from Sigma Aldrich (Product # 537284, St Louis, MO). Bis[2-(2'-bromoisobutyryloxy)ethyl]disulfide or the Br- terminated initiator ($C_{12}H_{20}Br_2O_4S_2$, Molecular Weight 452.22) was purchased from Sigma-Aldrich (Product # 723169, St Louis, MO).

Ligand 1,1,4,7,10,10-Hexamethyltriethylenetetramine or HMTETA (97%, $[(CH_3)_2NCH_2CH_2N(CH_3)CH_2\text{-}]_2$, Molecular Weight 230.39) was purchased from Sigma Aldrich (Product # 366404, St Louis, MO). Copper (I) bromide and Copper (II) Bromide were (Product # 254185 and 221775, respectively) purchased from Sigma Aldrich (St Louis, MO). 11-Mercapto-1-undecanol or the OH- terminated thiol (97%, Linear Formula $HS(CH_2)_{11}OH$, Molecular Weight 204.37) was purchased from Sigma-Aldrich (Product # 447528, St Louis, MO). Ultrapure water (resistance 18.2 MΩ.cm at 25^0C) was obtained using Synergy® UV (Millipore Sigma) water purification system and pure methanol was purchased from Thermo Fisher Scientific. N,N-Dimethylformamide or DMF (calibration solution for Surface Plasmon Resonance) was purchased from Fisher Scientific (99.8%, extra dried over molecular sieves, AcroSeal™, ACROS Organics™, Cat # AC348430025). Sodium phosphate (monobasic, monohydrate) was from Merck (Millipore Sigma, Product # 567545).

2.2.2 Proteins

Lysozyme (white crystalline powder) was purchased from Fisher Scientific (Fisher BioReagents™ Lysozyme, Egg White, Product # L-7651). Bovine Serum Albumin (Product # A2153, lyophilized powder, ≥96%) and Fetal Bovine Serum (Product #12103C, USA origin) were purchased from Sigma-Aldrich.

2.2.3 Protein expression

PGK and PGK-FRET were obtained from bacterial cultures. The detailed protocol for PGK expression and purification is described elsewhere [81]. For protein expression, we used the pET28b (Genscript) that contains a T7 promoter for bacterial cell expression. The cDNAs for the PGK variants each contain a 6X-His tag and thrombin cleavage site. The cDNAs were cloned into the plasmid. E. coli BL21 Codon Plus (RIPL) cells (Agilent Technologies) were transfected with the

resulting constructs by the heat-shock method (60 s in water at 42ºC followed by 120 s on ice). Transformed colonies grown for 12-14 hours at 37ºC on Kanamycin plates. Next, isolated colonies were picked and expanded, first in 15 ml Falcon tubes containing LB broth, followed by growth in 1 L cultures in LB at 37 ºC under shaking. Cells were grown in LB broth (10 mg LB powder/500ml of ultrapure water) until the culture reached an optical density of 0.6 at 620 nm. Then, 1M isopropyl β-D-1-thiogalactopyranoside or IPTG (Inalco) was added to the culture solution to induce protein production. Upon induction, the cells were cultured overnight at 20ºC. Then the cells were pelleted by centrifugation at 4225 RCF for 25 mins (Sorvall RC-5C Plus Superspeed Centrifuge, Rotor-GS3) and resuspended in 10 ml of lysis buffer (500mM NaCl, 20mM Dibasic Na_2HPO_4, 5mM Imidazole at pH: 8.0) with 10 µl of added DNAse (New England Biolabs). Then, the cells were sonicated (Qsonica, at amplitude 70, pulse on for 6 sec and off for 54 sec, process time is 6 mins for a total 60 minutes in 4^0C) and the lysate was collected by centrifugation at 11.925 RCF for 25 mins at 4ºC (Sorvall RC-5C Plus Superspeed Centrifuge, Rotor-SS-34). The collected liquid was filtered through a 0.45 µm and 0.22 µm filters, respectively to remove any aggregates or ruptured bacterial cells. The protein was then affinity purified (GE, Aktapure) by binding to a HisTrap column (GE Healthcare) that was pre-equilibrated with 20mM Na_2HPO_4, 500mM NaCl and 500 mM Imidazole at pH= 7.4 and the protein was eluted with the same buffer. The eluted protein solution was filtered and concentrated in 20 mM sodium phosphate buffer at pH 7 using EMD Millipore™ Amicon™ Ultra-15 Centrifugal Filter Units with a 50MW cutoff. Finally, the concentrated protein solutions were dialyzed into 20 mM sodium phosphate buffer at pH 7, using a 10MW cutoff dialysis tube (Snakeskin™ dialysis tubing, Thermo Scientific, Product # 68100, Lot# TG61631). The purity and molecular weight of the final proteins

used in measurements were assessed by SDS-PAGE. Eluted and purified PGK proteins were stored at -20^{0}C until use.

2.2.4 Substrate and SAM preparation for pSBMA synthesis

To prepare glass substrates for pSBMA synthesis on SPR chips, glass microscope slides (Fisher Scientific, Pittsburgh, PA) were cut into 0.7inch x 0.7inch pieces and cleaned with acetone and water. The cut glass pieces were then dried under a filtered N_2 stream. For ellipsometry measurements, gold coated Si wafers were cut into 1in x1in pieces and rinsed with ethanol and water, and dried under a filtered N_2 stream. Both SPR glass chips and Si wafers were assembled into a sample holder that was placed in a thermal evaporator (Kurt J. Lesker Nano36 Thermal Evaporator System; Seitz Materials Research Laboratory, University of Illinois at Urbana-Champaign), and coated with an adhesion-promoting layer of 2nm chromium, followed by a 55 nm film of gold under vacuum ($5x10^{-6}$ Torr). Prior use, all glassware were cleaned for at least 2 hours in a base bath, which is made of 500 gm of potassium hydroxide dissolved in 1L water and then mixed in approximately 8L of isopropanol.

2.2.5 Fabrication of linear gradients of pSBMA on gold coated substrates

Silicon wafers were cut into 5 x 1 inch pieces, and used for making linear gradients with the linear dipper. The wafers were rinsed with methanol, acetone and water, and then dried under a filtered N_2 stream, before assembling onto a sample holder of the thermal evaporator. Then, the wafers were coated with an adhesion-promoting 2 nm chromium layer followed by deposition of a 55 nm gold layer by thermal evaporation under vacuum ($5x10^{-6}$ torr).

Gradients of Br-terminated alkanethiols were assembled on the gold-coated Si wafers with a homebuilt linear dipper. [209] Briefly, the dipper tool moves the substrate vertically into the solution, at a controlled rate. The programmed dipping profile is controlled with a computer-driven

linear-motion drive. The instrument design and LabView program controlling the dipper (Ver 9.0, National Instruments) were kindly provided by Prof. N. Spencer (ETH, Zürich).

To generate gradients, the gold coated substrates were first dipped into a solution of 5.87 mM solution of 11-Mercapto-1-undecanol (OH-SAM) at a velocity of 5 μm/s, at room temperature. Because the thiol adsorption follows a Langmuir-type adsorption isotherm, the dipping velocity was increased exponentially with time, in order to generate a linear gradient of OH-terminated thiol along the length of the substrate. After dipping, the substrates were removed from thiol solution, rinsed with ethanol, and dried with nitrogen. Next, the linear gradients of OH-terminated thiols were backfilled with a 3.4 mM ethanolic solution of initiator Bis[2-(2′-bromoisobutyryloxy)undecyl]disulfide or SAM-Br by an overnight incubation at 4^{o}C. To generate gradients with the desired initiator density, the initiator and alkanethiol concentrations and dipping program were controlled. After cleaning the two-component linear gradients with ethanol and drying, the substrates were placed in the custom reaction vessel for the ATRP reaction described below, to generate a linear gradient of pSBMA chains of similar molecular weight (Figure 2.6). The grafting density was estimated from the initiator density determined by XPS, and an assumed conversion efficiency of 10%. [210]

2.2.6 Fabrication of uniform pSBMA on gold coated substrates

To synthesize pSBMA chains at uniform grafting densities, gold-coated SPR glass chips and Si wafers were immersed in mixture prepared from stock solution: 3.4 mM ethanolic solution of initiator Bis[2-(2′-bromoisobutyryloxy)undecyl]disulfide (SAM-Br) and 5.87 mM ethanolic solution of 11-Mercapto-1-undecanol (SAM-OH) and the final mixture containing 100, 70, 37 and 13 mol % SAM-Br . The molar ratios of Br-terminated and OH-terminated SAMs in the mixture determine the initiator surface density, which controls the pSBMA grafting density. The molar

ratios of SAM-Br and SAM-OH were chosen so that the grafting densities are within the range of the linear gradients fabricated by linear dipper mechanism (Table 2.5). The substrates were incubated in the alkanethiol solutions for ~8 hours at 4^{o}C, after which the substrates were rinsed with absolute ethanol, and dried in a filtered N_2 stream. Then, pSBMA chains were grafted from these substrates by ATRP. The SAMs were prepared this way because, in order to estimate the thickness of grafted pSBMA chains on a SPR glass chip, a gold coated Si wafer (reflective surface) is needed for ellipsometry measurements. Also, BSA and FBS adsorption was measured on uniformly grafted pSBMA chains.

2.2.7 pSBMA synthesis by ATRP

Polysulfobetaine was synthesized by Atom Transfer Radical Polymerization (ATRP). [211] Briefly, the substrates were sealed in custom, one armed reaction vessel with rubber septum and connected with Schlenk lines for maintaining an inert environment. The substrates in the individual scintillation vials were degassed with three cycles of vacuum and Ar gas. In a round bottom flask, monomer [2-(Methacryloyloxy)ethyl]dimethyl-(3-sulfopropyl)ammonium hydroxide was dissolved in 1:1 volumetric mixture of methanol and water at a final concentration of 0.2 M. The monomer solution was degassed with a glass frit and kept under Ar gas at all time throughout the reaction. Then $CuBr_2$, ligand HMTETA and CuBr were added to the flask at a final concentration of 16.79 mM, 46 mM and 0.56 mM in this order. When the reactants are well mixed, the mixture was transferred into the reaction vessel by a glass syringe. The reaction proceeded in room temperature under Ar atmosphere for 15 mins. After that, the reaction was terminated by removing substrates from the solution and rinsing with methanol and water mixture copiously. Finally, the substrates were rinsed with ultrapure water (resistivity at 18MΩ.cm at 25^{0}C; Millipore, Sigma) and dried off in nitrogen stream and stored under vacuum before use.

2.2.8 Film thickness determinations by ellipsometry

Ellipsometry was performed using a Variable Angle Spectroscopic Ellipsometer (J.A. Woollam VASE). After assembling alkanethiol monolayers or after pSBMA synthesis on alkanethiols on gold coated Si wafers, the dried samples were scanned in three different spots at three different angles of incidence (65, 70 and 75^{o}) in the visible region (300-900 nm). The bare, gold-coated Si wafer and 100 mole% SAM-OH monolayers on gold coated Si wafers were used as references. The resulting curves were fit to a multilayer model consisting of bulk silicon of default thickness 1 mm, a silicon oxide layer of 2 nm, Cr of 2 nm and Au metal layers, and a Cauchy dispersion layer. The thiol and polymer layers were fit to quantify the polymer brush. For the Cauchy dispersion layer, we used a refractive index of 1.46 for the organic layer. [212]

For protein adsorption measurement using VASE, pSBMA grafted on gold coated Si wafers were incubated in protein solutions for 2 hours at 4^{0}C. After incubation, the slides were rinsed with buffer to remove unbound protein, and then dried under a N_2 stream. Then, the dry thickness of the polymer brushes, with and without adsorbed protein were measured. Both the thickness and the refractive index of Cauchy dispersion layer (η) were fitted to quantify the polymer brush. The adsorbed protein Γ (ng/cm^2) was determined from $\Gamma = h\,(\eta - \eta_0)/(d\eta/dc)$, where h is the difference in film thickness after protein adsorption, and η_0 and η are the refractive indices of the layer before and after protein adsorption, respectively. $d\eta/dc$ is the refractive index increment, which is typically 0.19 mL/gm for proteins. [213] Also the value of η_0 =1.334 was measured for the aqueous buffer.

To determine swelling ratios of pSBMA grafted on alkanethiol monolayers on gold-coated Si wafer, measurements of the hydrated polymer layers were carried with samples in a 5 mL vertical liquid cell (5ml Vertical Liquid Cell (TLC-100) with 0-0.1M NaCl, in 20mM sodium phosphate

buffer (at pH= 7.4) at a fixed angle of 75° and 300-900 nm scans in 5 nm steps. Data were fit to the same multilayer model with the addition of a bulk H_2O layer above the film.

2.2.9 X-ray Photoelectron Spectroscopy (XPS)

The density of Br-terminated alkanethiols was determined by XPS (Kratos AxisULTRA spectrometer) and the Br/S ratios. The excitation source was the monochromatic Al K α radiation at 1486.6 eV (225 W, 40 eV pass energy). The samples were loaded on a rectangular metal support, using double-sided adhesive tape, and analyzed at a pressure of 10^{-9} Torr. The C 1s hydrocarbon peak at 285.0 eV was used as the reference peak to measure the binding energy. Surface chemical compositions were determined from the integrated peak areas in the XPS spectra, using CasaXPS software (Version 2.3 19PR1.0). By assuming the maximum packing density of 2.1 bromine initiator/nm^2 and 10% reaction conversion efficiency reported for polystyrene [210], we estimated the grafting densities (Table 2.1). Figure 1B shows the changes in Br 3p/S 2p ratios along the length of the linear gradient. Also, XPS was performed on samples prepared with uniform grafting density (Figure 2.11) to estimate grafting density (Table 2.5).

2.2.10 Protein adsorption measurement by Surface Plasmon Resonance (SPR)

2.2.10.1 Preparation of calibration solutions

The SPR was calibrated with solutions of 0.4 to 50.0 volume % N, N-Dimethylformamide (DMF) in water. Using an Abbe 3L refractometer (Milton Roy Co., Rochester, NY), the refractive index of the solutions was measured in order to determine the slope of bulk refractive index vs. percentage change in reflectance (%ΔR). The slope was found to be 4032% reflected intensity (%ΔR)/ RIU, where RIU represent one refractive index unit, which is used as a sensitivity factor of the SPR and used to convert the intensity changes to effective adlayer thickness or absolute

surface coverages of the proteins [238, 243]. The refractive index range of the solutions encompassed the range of planned protein adsorption experiments.

2.2.10.2 Protein solutions

Phosphoglycerate Kinase (with and without fused fluorescent proteins), lysozyme, BSA and FBS were used for this study. PGK was purified as described, and lysozyme and BSA were used without further purification. For lysozyme adsorption measurements, the carrier buffer contained 20 mM sodium phosphate (prepared from monohydrate, monophosphate $Na_2HPO_4.H_2O$ in ultrapure water) at pH 7.4. The final lysozyme solutions contained 140 µM lysozyme in carrier buffer with 0, 50 mM, 100 mM or 300mM NaCl. WT PGK and PGK-FRET were purified from bacterial cultures as described below. We prepared 6.50 µM PGK solutions in 20 mM sodium phosphate buffer at pH 7.4 that contained 0, 50, 100 and 300 mM NaCl in buffer. Bovine Serum Albumin was prepared at 30 µM in Phosphate Buffered Saline (1X Solution containing 137 mM NaCl, 2.7 mM KCl, 8 mM Na_2HPO_4, and 2 mM KH_2PO_4, pH 7.4) and 100% Fetal Bovine Serum or full serum was used as purchased. All proteins were stored at 4^0C prior use.

2.2.10.3. SPR measurements

Horizon SPRimager (GWC technologies, Madison, WI) was used for in-situ protein adsorption experiments. The grafted pSBMA on gold coated substrates were assembled in flow chamber of the device. Index matching fluid (η= 1.73, Cargille Laboratories, Inc.) was applied to the back of the substrate before mounting it on the prism (60° SF10 glass with η= 1.727) and the reflected beam was detected with a CCD camera (Panasonic Model WV BL200). The images are represented quantitatively by line profiles, which are generated by averaging the pixel values from each column of the CCD camera. The protein solutions were passed through the flow cell at 120 µL/min. A reference image was taken after flowing buffer solution (without protein) through the

flow cell for 10 minutes. Changes in the SPR signal were converted to absolute changes in reflectivity or reflected intensity by the following equation:

Δ%R = 100 * {(SPR sample pixel difference* 0.85) / (s-pol pixel intensity/ (1-f)} (Equation 2.1)

Here 's-pol image intensity' refers to reference image obtained with s-polarized light that is used to convert raw SPR response data to the absolute reflectivity values by normalizing p-polarized light intensity used to elicit the SPR response. Here, f is the density of the filter used. For these measurements, f=75%. Also, a 15% error is accounted for in estimation of change in reflectivity, Δ%R. To determine the surface coverage of the adsorbed protein, the optical film thickness was estimated by,

$$d = \left(\frac{l_d}{2}\right)\left[\frac{\Delta\%R}{s(\eta_a - \eta_s)}\right] \qquad \text{(Equation 2.2)}$$

where s is the slope of a calibration plot of Δ%R versus bulk refractive index determined with DMF solutions, and l_d is decay length of the evanescent field near the gold surface. [242, 244] Finally, the surface coverage of adsorbed protein was estimated from the following equation:

$$\Gamma\ (ng/cm^2) = \left[\frac{d\ (nm)}{Specific\ volume\ of\ protein\ \left(\frac{cm^3}{g}\right)}\right] x100 \qquad \text{(Equation 2.3)}$$

For these calculations, we used a specific volume of 0.77 cm^3/g [216].

In adsorption measurements, the baseline was first established by running buffer or carrier solution for approximately 10 mins. Then the desired protein solution was pumped through the flow cell, until the signal intensity reached a stable plateau, after which carrier buffer washed away unbound protein. The reflectivity difference Δ%R before and after the wash was converted to the surface coverage with Equation 2.3.

2.2.11 Dynamic Light Scattering studies of soluble pSBMA

2.2.11.1 Bulk polymer synthesis using ATRP

pSBMA was synthesized as described previously.[81] Briefly, monomer solution of [2-(methacryloyloxy)ethyl]dimethyl-(3-sulfopropyl)ammonium hydroxide) at 200 mM, ligand 1,1,4,7,10,10-hexamethyltrietylenetetramine (HMTETA) at 0.147 mM and catalyst $CuBr_2$ and CuBr at concentrations of 0.074, 0.711 mM, respectively in 50 v/v% methanol and water were added to reaction vessel while maintaining an inert environment. The polymerization reaction was followed by solvent evaporation, dialysis and further evaporation of excess solvent. The resulting product of pSBMA was a white powder, which was collected in a scintillation via before further use. Molecular weight of pSBMA was estimated by ^{1}H NMR. We prepared 0.5 wt% pSBMA in 20 mM with sodium phosphate buffer (pH 7) with different NaCl concentrations.

2.2.11.2. Dynamic light scattering of pSBMA chains in solution

Dynamic light scattering (DLS) measurements were with a particle analyzer (Model: Anton Paar Litesizer 500) coupled with Kalliope software. A 0.5 wt % pSBMA in 20 mM sodium phosphate buffer (pH 7) containing 0-2 M NaCl was placed in a cuvette, and the scattering intensity was quantified with a 40 mW laser diode (658 nm) and an avalanche photo diode detector at an angle of 175° (back scatter) for samples containing 0 mM or 10 mM NaCl. Scattering was detected at an angle of 90° (side scatter) for all other samples. All measurements were performed at room temperature. The hydrodynamic radii (R_H) were calculated using Stoke-Einstein equation and the polydispersity index (PDI) determined using an advanced cumulant fit of the measured intensity autocorrelation function, described in details elsewhere [81].

2.3 Results

2.3.1 Linear gradients of pSBMA chains grafted from self-assembled thiols on gold

We used linear gradients of pSBMA chains to identify chain grafting conditions that might support protein adsorption. The linear gradients of Br-terminated thiols in an OH-terminated thiol background were characterized by Variable Angle Spectroscopic Ellipsometry (VASE) and by X-ray Photoelectron Spectroscopy (XPS) (Figure 2.1). It is important to note that the OH-terminated alkanethiols were used for two purposes: (1) to maintain a hydrophilic background on gold substrates to prevent primary protein adsorption and (2) to serve as a diluent to control the initiator density. The ratio of Br 3p to S 2P peak intensities versus the position along the gradient confirms the linear variation in the initiator density achieved under the dipping conditions used (Figure 2.1, Panel B). The results are consistent with prior published work. [143]

The polymers synthesized from the initiator gradients were characterized by ellipsometry, and the presence of polymer was verified by the appearance of the N 1s peak, after the polymerization reaction. A representative N 1s spectrum obtained by XPS is shown in Figure 2.7. Ellipsometry measurements showed that the dry pSBMA thickness decreased with decreasing initiator density, as expected (Figure 2.1, Panel A). The molecular weight of the polymer chains is assumed to be constant across the gradient. From the data in Figure 2.1, Panel B, the grafting densities of pSBMA chains (σ) and the distances between grafting sites $s = \sigma^{-1/2}$ were estimated (Table 2.1). The area per initiator was estimated, by using the Br/S ratio and a reported maximum alkanethiol packing density of 2.1 chains/nm^2. [217] Then, the chain density was approximated, by assuming an initiator reaction efficiency of 10%, reported for polystyrene. [210] With the estimated grafting density and measured dry polymer thickness, the molecular weight of grafted polymer was calculated with the following equation: $M_n = (h\rho N_A/ \sigma) \times 10^{-21}$, where M_n is Da or gm/mole, h is the dry brush

thickness, ρ is the dry polymer density of 1.395 gm/cm^3; N_A is Avogadro's number and σ is the chain density (chains/nm^2). [160, 225, 241, 247] These results were then used to estimate the grafted chain configurations, based on the distance between grafting sites, s normalized by the Flory radius, $s/2R_F$. Here, the Flory radius, $R_F = l*N^{3/5}$ where l is the monomer length (≈ 0.3 nm) and N is the degree of polymerization, determined by the ratio of the polymer to monomer molecular weights (i.e. $N=\frac{M_n}{M_m}$). The molecular weight of the monomer, M_m= SBMA is 279.35 gm/mol.

Typically, chains form isolated mushrooms when $s/2R_F >> 1$ and stretched brushes when $s/2R_F << 1$. [196, 219] Weakly overlapping chains are intermediate between mushrooms and brushes. For the purpose of discussion, in this study we designate three polymer 'configurations' as brush $0<s/2R_F<0.3$; weakly overlapping chains $0.3<s/2R_F<1$; and mushrooms $s/2R_F>1$. At the top of the gradient (z=0), chains are at the highest grafting density on the gradient and were determined to be in the brush regime ($s/2R_F \approx 0.2$), at the indicated molecular weight. The grafting density decreased along the dipping direction to reach the lowest chain density (σ ≈ 0.04 chains/nm^2). The final film thickness was similar to the unmodified SAM comprising only OH-terminated alkanethiols. For chains with the indicated molecular weights, the estimated polymer configurations along one prepared gradient, assuming good solvent, are summarized in Table 2.1.

2.3.2 Polymer solubility

The polymer configurations were estimated, by assuming self-avoiding chains in good solvent. However, the poly(sulfobetaine) solubility and swelling are ionic strength dependent [85]. The hydrodynamic radius of pSBMA chains in bulk solution was studied via Dynamic Light Scattering (DLS) (Figure 2.2), and the swelling of end-grafted chains was determined by ellipsometry using a fluid cell. Dynamic light scattering characterized the size of pSBMA aggregates and the hydrodynamic radii of soluble pSBMA chains (120 KDa), at 0.5 wt% in 20 mM sodium phosphate

buffer at pH=7.4, as a function of increasing NaCl concentration (Figure 2.2). At lower NaCl concentrations (0 to 50 mM), inter and intramolecular chain associations (region 1) cause aggregation/precipitation, which is evident by the formation of large aggregates. At the NaCl concentration of ~ 50mM, polar segment-segment interactions are compensated by interactions with ions in the solution, and the polymer aggregates dissociate (region 2). As the NaCl concentration increases from 100 to 500 mM (region 3), the average size of coils continues to increase. The swelling plateaus beyond this region, and the hydrodynamic radii of the coils become independent of the salt concentration (region 4). These results were used to interpret protein adsorption behavior. Previous studies determined that the θ-solvent conditions for polysulfobetaine are at NaCl concentrations between 60 mM and 74 mM. [249, 250], The latter concentrations are intermediate between 50mM NaCl in 20 mM sodium phosphate buffer, at which we measured the lowest hydrodynamic radius of the conditions investigated and 100 mM NaCl. Thus, the lowest R_H reported in this study may be slightly larger than the R_H measured under actual θ-solvent conditions. The swelling ratio of grafted pSBMA chains was estimated from the ratio of the thickness of water-swollen pSBMA chains to that of dry pSBMA films. The thickness of end-grafted pSBMA chains in bulk solvent was measured by ellipsometry in ultrapure water and in 20 mM sodium phosphate buffer at pH=7.0 with 50, 100, or 150 mM NaCl (Table 2.6). At both high ($s/2R_F$~ 0.32, MW ~38 KDa) and low grafting densities ($s/2R_F$~ 0.72, MW ~10 KDa), the swelling ratio increased with increasing NaCl concentration. Notably, the swelling ratio was the highest for mushroom-like chains (dry thickness = 13 $\pm$ 1 nm, swelling ratio = 3.5, $s/2R_F$~ 0.72) compared to brush-like chains (9.0 ± 0.3 nm, swelling ratio = 1.4, $s/2R_F$ ~ 0.32) at the highest NaCl concentration used (150 mM). As expected, at higher grafting density (i.e. $s/2R_F$ ~0.32), the stretched brushes do not swell substantially, compared to the weakly overlapping chains (i.e. $s/2R_F$

~ 0.72) [222]. Moreover, in ultrapure water (18.2 MΩ.cm at 25^0C) the swelling ratio is less than 1.0 for chains at both high and low grafting densities.

2.3.3 Protein adsorption depends on the pSBMA grafting conditions and ionic strength

Phosphoglycerate kinase (PGK)—a small metabolic protein—and positively charged lysozyme were chosen as model proteins to investigate the influence of grafting parameters and salt concentration on protein adsorption on grafted pSBMA chains. Figure 2.3, Panel A and B show the adsorbed amounts of WT PGK and lysozyme, respectively versus the normalized grafting density $s/2R_F$, measured under different solution conditions. Here, we used SPR and ellipsometry to measure, respectively WT PGK and lysozyme adsorption on grafted pSBMA chains. We confirmed that the protein adsorption measured with the two techniques is comparable, within experimental error (Figure 2.8). The polymer configurations range from dense, stretched brushes to dilute mushrooms, under good solvent conditions.

In sodium phosphate buffer containing different NaCl concentrations, rather than a monotonic decrease in protein adsorption with increasing chain density, the adsorbed amounts of both proteins exhibit bell-shaped curves. Specifically, there is little protein adsorption on dense brushes, and both proteins exhibit a maximum adsorption at intermediate chain densities. In 20 mM sodium phosphate buffer (pH=7.4) containing 0 mM NaCl, the maximum adsorption is 440 ± 50 ng/cm^2 and 210 ± 20 ng/cm^2 for WT PGK and lysozyme, respectively. At the lowest grafting density, the adsorbed amounts plateau at values comparable to adsorption on control OH-terminated alkanethiol substrates without polymer (Table 2.2). The qualitative features of the curves are similar, but the maxima are at $s/2R_F \sim 0.7$ and ~ 1.7 for WT PGK and lysozyme, respectively.

In buffered solutions, the $s/2R_F$ values corresponding to the adsorption maxima do not appear to depend on the NaCl concentration. However, increasing NaCl reduces the adsorbed amounts of

both proteins, indicative of the electrostatic nature of the protein-polymer interactions. The ionic strength does have different effects on PGK and lysozyme adsorption. In buffered solution with 100 mM NaCl, there is still detectable PGK adsorption, but lysozyme adsorption is negligible and independent of the grafting conditions, within error.

In pure water, the polymer solubility is low, and the chains are not swollen. Under these conditions, the adsorption profiles are similarly bell-shaped, but the adsorption maxima shift to lower values of $s/2R_F$. The maximum adsorbed amount of WT PGK is 500 ± 50 ng/cm^2 at $s/2R_F \sim 0.39$, and the maximum amount of adsorbed lysozyme is 330 ±30 ng/cm^2 at $s/2R_F \sim 0.94$. For both proteins, the $s/2R_F$ values corresponding to the maxima are given in Table 2.3.

We also used ellipsometry to investigate the adsorption behavior of Bovine Serum Albumin (BSA) in PBS (1X solution containing 137 mM NaCl, 2.7 mM KCl, 8 mM Na_2HPO_4, and 2 mM KH_2PO_4, pH 7.4) and of Fetal Bovine Serum (FBS, full serum). BSA is a prolate ellipsoid with dimensions 2 x 7 nm. [223] In both cases, the adsorption profiles are similarly bell-shaped, with maxima around $s/2R_F \sim$ 0.8 and 0.43 for BSA and FBS, respectively (Figure 2.9). The amount of protein adsorbed from FBS is much larger than that of BSA alone. Although albumin is the most abundant protein in serum, FBS contains many other proteins with different charges and sizes. The latter would account for differences, relative to BSA, in both the position of the maximum and the adsorbed amount. At lower grafting density (i.e. $s/2R_F > 1$), the adsorbed amount for FBS (50$\pm$ 10 ng/cm^2) was similar to adsorption on the OH-terminated SAM.

2.3.4 Dependence of adsorption on protein size

Studies with WT PGK and PGK-FRET in 20 mM sodium phosphate buffer tested the influence of protein size on adsorption. The molecular weights of PGK fused to the two fluorescent proteins mCherry and AcGFP (PGK-FRET) has a molecular weight of ~100 KDa, and WT PGK has a

molecular weight of 45 KDa. We assumed PGK-FRET and PGK to be spherical, for the purpose of rationalizing the experimental findings. In molecular dynamics simulations, the estimated radius of gyration of WT PGK was $2.0 \leq R_g \leq 2.4$ nm. [224] However, the actual shape of PGK-FRET in solution is not known. Assuming spherical geometries, the approximate radii (R_p) of PGK-FRET and of WT PGK are 3.1 and 2.4 nm, respectively. The latter values were calculated by $R_p = (\frac{3V}{4\pi})^{1/3}$, where V ($nm^3$) = 1.212×10^{-3} x MW (Da). [225]. The average distance between grafted chains, s, the corresponding grafting density, σ (chains/nm^2), and the estimated protein radii are given in Table 2.4.

At the higher grafting densities, the PGK-FRET diameter exceeds the grafted chain spacing ($s << 2R_P$; $R_P \approx 3.1$ nm). Under these conditions, the osmotic repulsion would prevent the protein from penetrating the brush and binding to the chains. The adsorbed amount was less than 10 ng/cm^2 at different NaCl concentrations on grafted pSBMA brush (Figure 2.10). At all other grafting conditions where $s \geq 2R_P$, protein can penetrate into the polymer layer.

The adsorbed amounts of WT PGK and PGK-FRET adsorbed on end-grafted pSBMA chains were quantified by SPR, and plots of the adsorbed amounts versus $s/2R_F$ are in Figure 2.4. Both WT PGK and PGK-FRET exhibit bell-shaped curves, with adsorption maxima at $s/2R_F \sim 0.7$. The maximum adsorbed protein is 440 $\pm$ 50 ng/cm^2 and 150 $\pm$20 ng/cm^2 for WT PGK and PGK-FRET, respectively. Above $s/2R_F \sim 0.75$, the adsorbed amounts decrease to the same level as on OH-terminated alkanethiol SAMs: namely, 50 $\pm$ 5 ng/cm^2 for PGK-FRET and 240 $\pm$ 10 ng/cm^2 for WT PGK. The striking difference in the amounts of adsorbed WT PGK and PGK-FRET is likely due to the different sizes and amino acid compositions of the two proteins.

2.4 Discussion

This study confirms that proteins do adsorb to thin pSBMA films. The results reconcile recent findings that pSBMA chains in the bulk bind proteins [81] with reports that ZI polymers like pSBMA form 'ultra-low fouling' surface coatings. [4,50,67,70,201] Here we identified conditions under which proteins can adsorb to weakly attractive ZI polymers, by quantifying protein adsorption on gradients of grafted pSBMA, as a function of the scaled parameter $s/2R_F$ and of the NaCl concentration. Rather than exhibiting a monotonic decrease in adsorption with increasing chain density (decreasing distance between chains), as expected for protein-repelling polymers like poly(ethylene glycol) [134] the adsorption profiles for all proteins examined here are bell-shaped. The latter profile was predicted for particle interactions with weakly attractive, end-grafted chains. [101, 159] Similar behavior was also reported for protein adsorption on poly(N-isopropyl acrylamide) brushes above the lower critical solution temperature where the polymer binds proteins. [79]

The physics underlying the bell-shaped profile is rationalized as follows (Figure 5). At high grafting densities where $s/2R_F \leq 0.3$, the amount of adsorbed protein is less than 10 ng/cm^2 (Figure 2.10), similar to prior reports. [22, 35] Under such conditions, the large osmotic penalty for protein insertion into grafted brushes overwhelms weak protein-polymer attraction. [77, 226] Importantly, prior studies of protein adsorption on ZI thin films used dense, end-grafted polymers [4, 35]. However, at intermediate grafting densities $0.3<s/2R_F<1$, weak protein-segment attraction may overcome the osmotic repulsion, enabling protein insertion into the layer and association with the chains (Figure 2.5). The use of OH-terminated monolayers reduces adsorption to the underlying substrate (primary adsorption); hence, after reaching a maximum, the adsorption decreases with increasing $s/2R_F$, due to the decreasing number of pSBMA chains available for binding. [221] Adsorption finally plateaus at levels measured with control OH-terminated SAMs. Therefore,

competing effects of osmotic/steric repulsion and protein-segment attraction account for the observed bell-shaped adsorption profile.

Importantly, we cannot quantitatively predict either the adsorbed amount or the adsorption maxima based on current models, because we lack quantitative measurements of both protein-segment and segment-segment interaction energies at different ionic strengths. As the DLS results show, in the bulk, interchain attraction at low ionic strength enables the formation of polymer aggregates. The swelling of both soluble and grafted chains also depends on ionic strength. Thus, the size of the grafted chains, the osmotic barrier, and protein-chain attraction vary with the ionic strength. Nevertheless, polymer models serve as qualitative guides for interpreting the results.

The observed adsorption maxima depend on protein size and on the NaCl concentration (ionic strength). The dependence on protein size is expected because as the osmotic penalty is overcome by the protein-polymer attraction force, the adsorbed amount scales with $V_P^{3/4}$, where V_P is the volume of the protein [73]. Proteins adsorb when the protein-polymer attraction exceeds the osmotic repulsion. Assuming equal chain-protein attraction, the $s/2R_F$ value at the adsorption maximum is predicted to vary with the protein size. We observe this dependence, when comparing PGK and lysozyme adsorption (Figure 2.3). The adsorption maximum at lower $s/2R_F$ values for serum versus BSA is attributed to the diverse sizes of serum proteins. This size-dependence does not hold in all cases, as in the comparison of WT PGK and PGK-FRET. In the latter case, the proteins, which differ in size and composition, may not be spherical and may have different pSBMA binding propensities.

Under solution conditions where the chains are dispersed in the bulk and swollen (i.e. buffered NaCl solutions), the adsorption maximum varies detectably with ionic strength. However, in unbuffered water, it shifts to lower values of $s/2R_F$, for both PGK and lysosome. Two factors likely

contribute to this change. In good solvent, the size of isolated, grafted coils scales as $R_F \approx lN^{3/5}$, where l is the monomer size and N is the degree of polymerization. [226] In poor solvent, the size of collapsed coils scales as $R_{globule} \approx lN^{1/3}$ [220, 227]; thus, proteins could diffuse more easily between shrunken coils. Also, greater interchain association in water suggests 'stickier' monomers, which would also have a greater binding propensity for polar solutes such as proteins.

The ionic strength dependence of protein adsorption is attributed to electrostatic screening and to ion competition for polar sites on the polymer backbone. Ion interactions with the polymer contribute to salt dependent pSBMA swelling and would similarly displace proteins as the ions disrupt polymer aggregates. Thus, at NaCl concentrations above ~100mM, protein adsorption is low to negligible at all $s/2R_F$ values.

2.5 Conclusion

Prior attempts to identify design rules for non-fouling zwitterionic polymer coatings focused on the film thickness [27], percentage of methanol in reaction solvent, polymerization time, and ionic strength [228], for example, but not on the physics of protein interactions with polymer thin films. Also, the majority of studies of protein fouling used dense, grafted brushes, which we demonstrate here to be a specific condition that blocks protein insertion into brushes. The bell-shaped adsorption profiles reported here reveal conditions that do support protein adsorption. These results thus reconcile the reported ultra-low fouling properties of pSBMA with findings that proteins bind pSBMA chains in the bulk. These results further identify design parameters that tune the protein resistance of zwitterionic polymer films that are based on the physics of protein interactions with grafted polyzwitterions.

2.6 Figures and tables

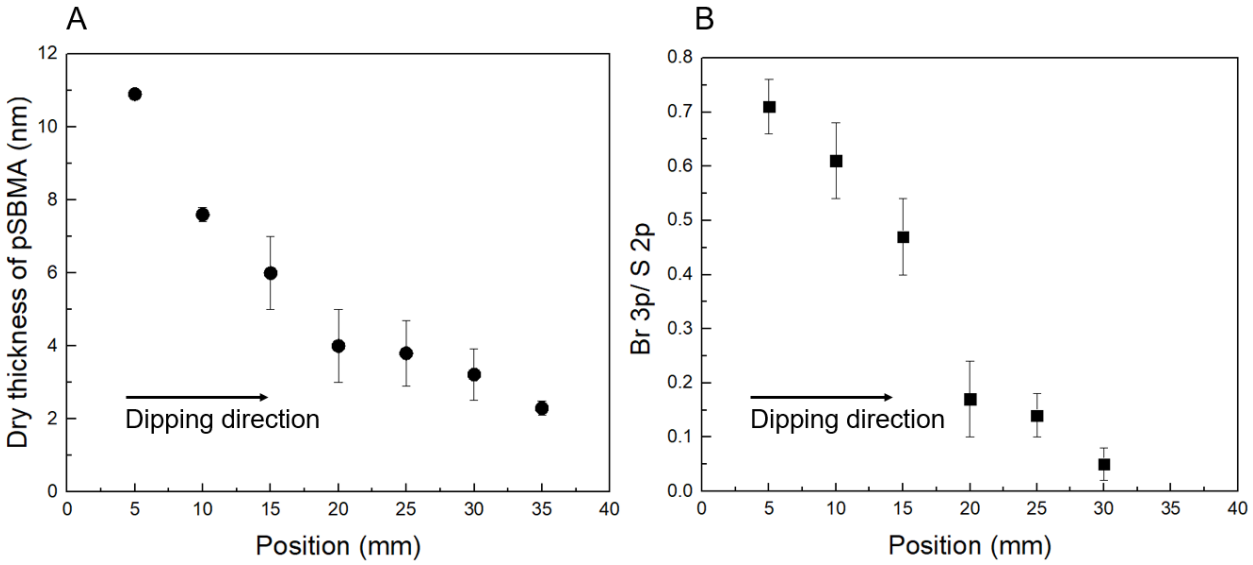

Figure 2.1: Characterization of linear gradients of grafted pSBMA and alkanethiol monolayers on gold coated substrates. (A) Thickness of dry pSBMA film along the dipping direction, as measured by ellipsometry. (B) X-ray Photoelectron Spectroscopy (XPS) measurements of the ratio of Br 3p/ S 2P at different positions along the gradient. In both cases, z=0 corresponds to the top of the gradient, which is immersed in the thiol solution for the longest duration.

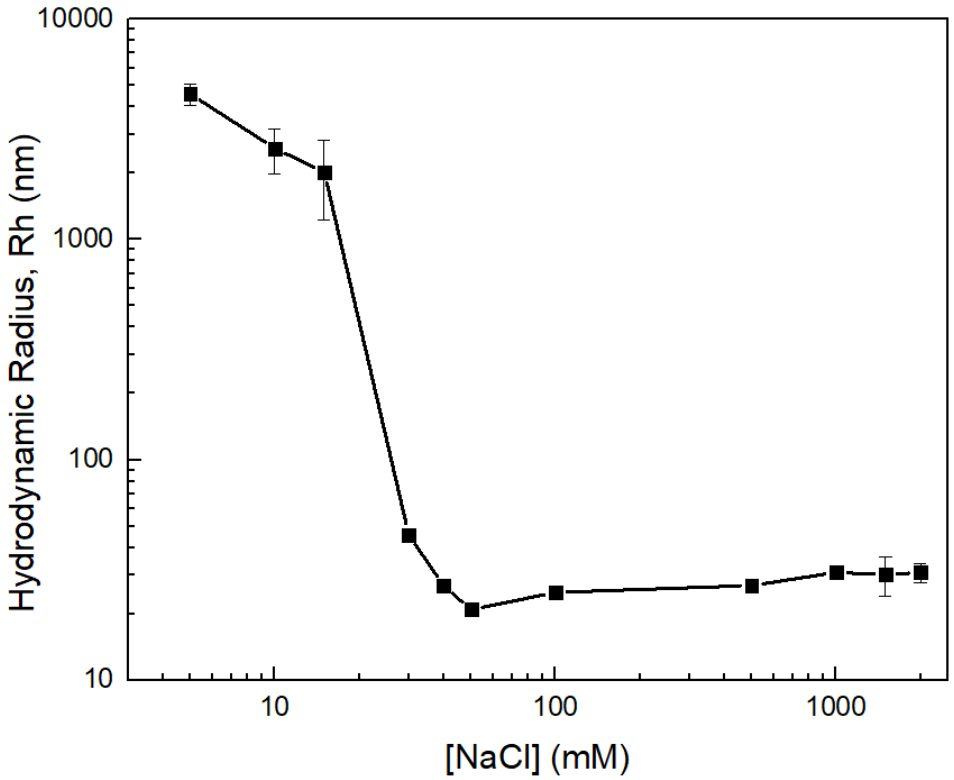

Figure 2.2: Measured hydrodynamic radius of pSBMA chains in buffered solution as a function of the NaCl concentration. The hydrodynamic radius (R_H) of 0.5 wt % pSBMA (~ 120 KDa) was measured by Dynamic Light Scattering (DLS) in 20 mM sodium phosphate buffer at pH=7.4 at different NaCl concentrations.

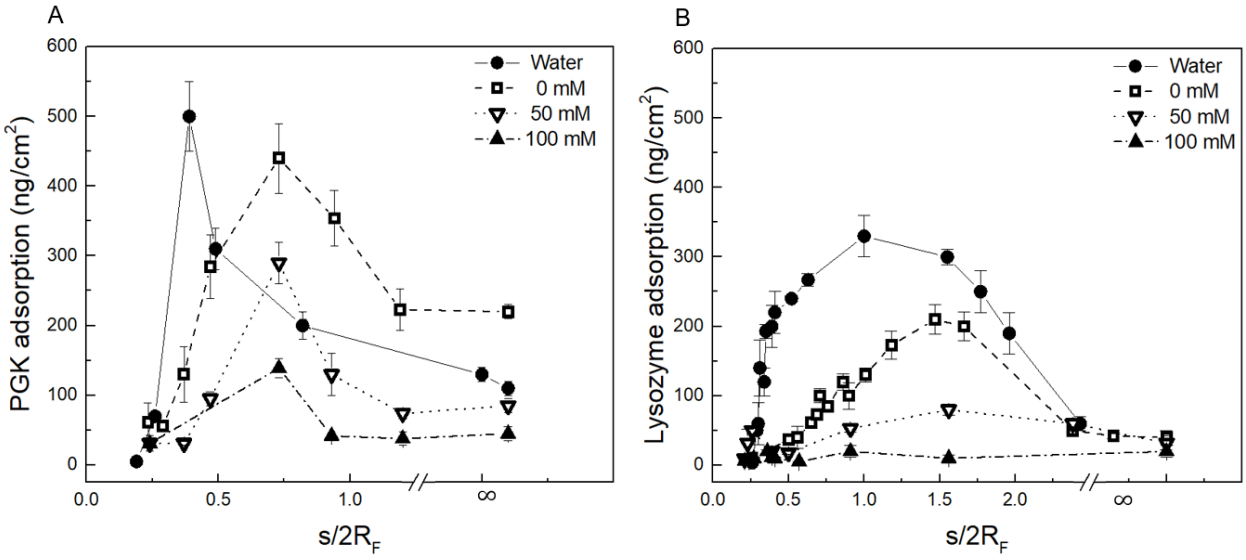

Figure 2.3: Protein adsorption on grafted pSBMA films versus the scaled grafting parameter, $s/2R_F$. (A) Phosphoglycerate kinase (PGK) adsorption on end-grafted pSBMA chains determined by SPR. In measurements, proteins were in unbuffered water (●) at pH 6.4 and in 20mM phosphate buffer at pH 7.4 containing NaCl at 0 mM (□), 50 mM (▽) and 100 mM (▲). Each data point is the mean ± sd of n=3 measurements done with pSBMA grafted from self-assembled monolayers at uniform initiator densities. (B) Lysozyme adsorption on a linear gradient of end-grafted pSBMA chains determined by ellipsometry. Measurements were done in unbuffered, ultrapure water (●) and in 20mM sodium phosphate buffer at pH 7.4 containing [NaCl] at 0 mM (□), 50 mM (▽) and 100 mM (▲). The adsorbed amount at infinite $s/2R_F$ (no grafted polymer) refers to protein adsorption on the OH-terminated alkanethiol monolayer on gold (control). The connected lines are to guide the eye.

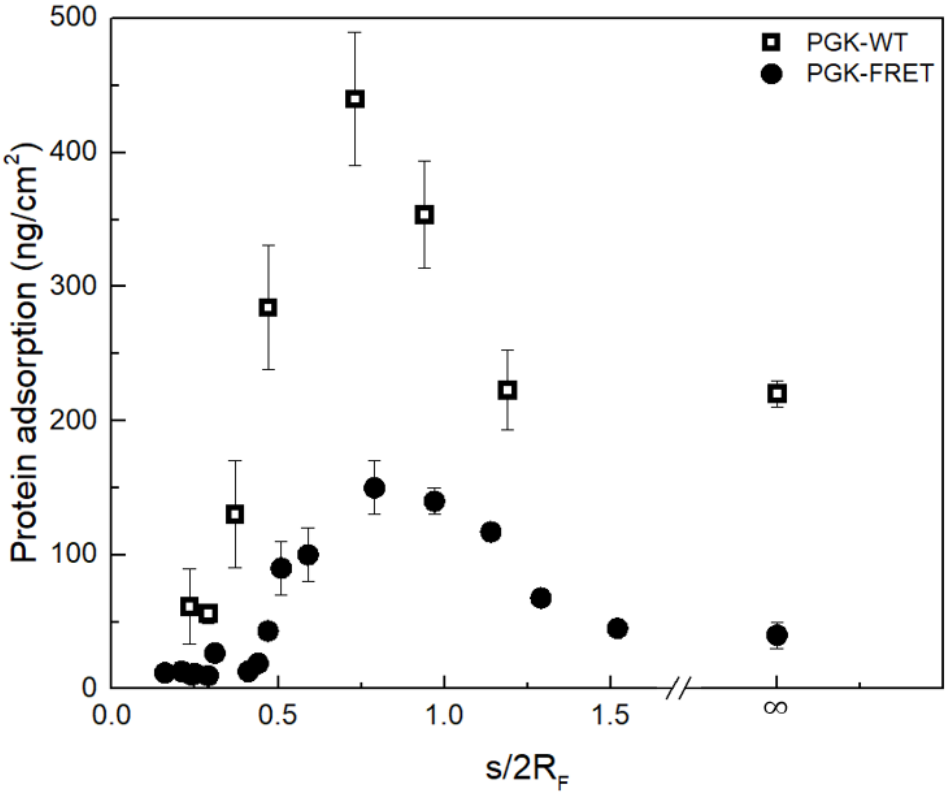

Figure 2.4: Adsorption of PGK proteins on end-grafted pSBMA chains determined by surface plasmon resonance. Data show the protein adsorption (ng/cm^2) versus the normalized pSBMA grafting density $s/2R_F$. Proteins studied include PGK-FRET (●) and WT PGK (□). The protein molecular weights are 100 KDa and 45 KDa, respectively. Proteins (6.50 µM) were in 20 mM Na_2PO_4 buffer at pH 7.4.

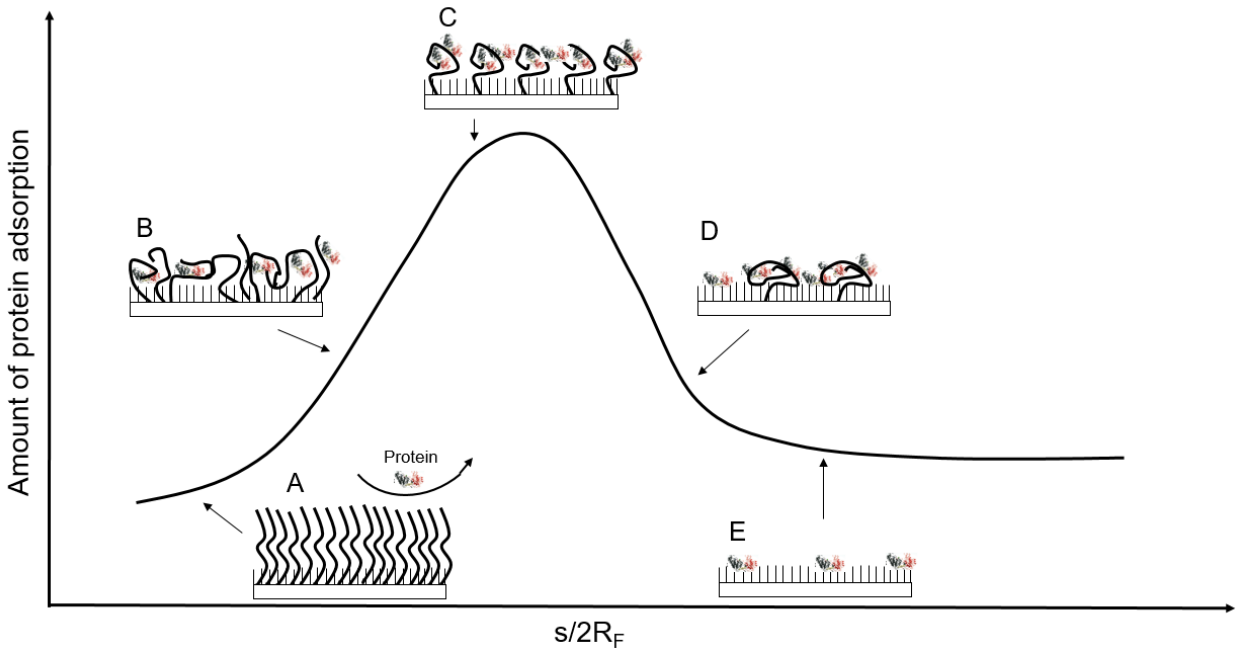

Figure 2.5: Proposed mechanism of protein adsorption on weakly attractive, end-grafted pSBMA chains. (A) At high grafting densities ($s/2R_F$ <<1) protein penetration of into the grafted polymer layer is prevented by the high osmotic repulsion. (B) As the distance between grafting sites decreases ($s/2R_F$ <1), the spacing between the weakly-overlapping chains is such that attractive protein-polymer segment interactions can overcome the osmotic repulsion, enabling protein adsorption. (C) The protein adsorption increases until it reaches a maxima around $s/2R_F$ ~1, beyond which there are too few polymers to support protein adsorption. Here, proteins can adsorb weakly to the underlying OH-terminated alkanethiols (D). At high $s/2R_F$ values (sparse chains), protein adsorption plateaus at the level adsorbed on control substrates (E).

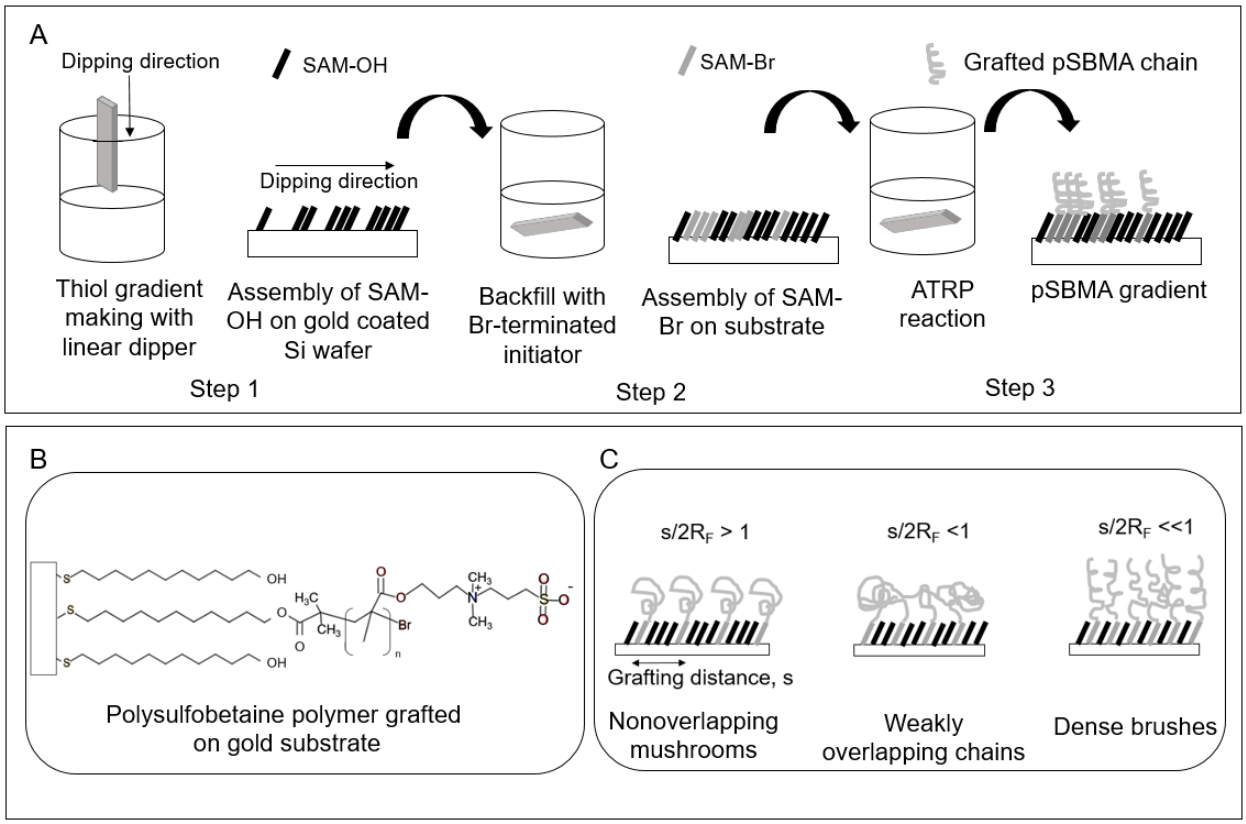

Figure 2.6: Fabrication of linear gradient of grafted pSBMA chains on gold coated substrates using a linear dipper. (A) Three step process of fabricating linear gradient of pSBMA chains on substrates. The ATRP synthesis results in end-grafted pSBMA chains that are 'grown-from' the substrates. The surface density of self-assembled Br-terminated initiator along the length of the substrate changes, creating a linear gradient of grafted pSBMA chains on substrate. (B) The chemical structure of grafted pSBMA chains on gold-coated substrates. (C) The approximate configurations of end-grafted pSBMA chains on substrates in good solvent, either grafted from linear gradient as shown in (A) or from a uniform self-assembled monolayer of Br and OH-terminated thiols.

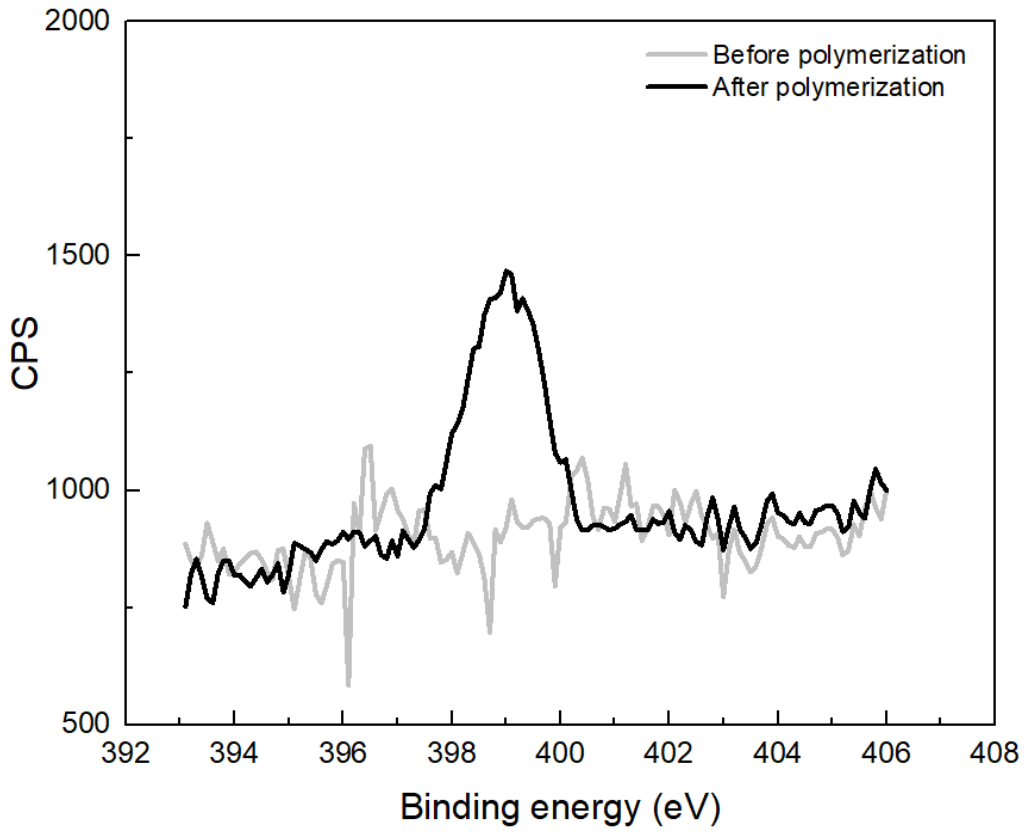

Figure 2.7: N 1s spectrum obtained by X-ray Photoelectron Spectroscopy (XPS) before (light gray line) and after (black line) pSBMA polymerization on alkanethiol monolayers assembled on gold films from ethanolic solutions of 10% Br-terminated and 90% OH-terminated alkanethiols.

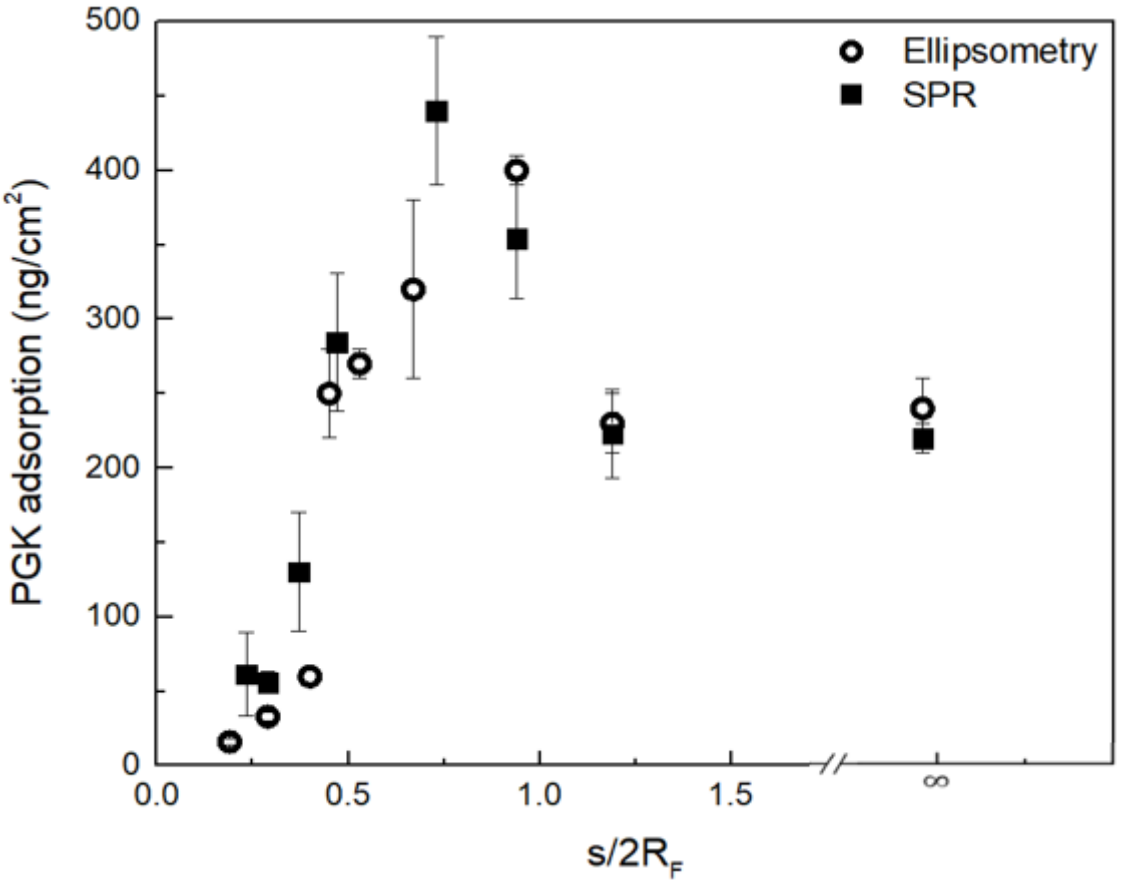

Figure 2.8: Comparison of adsorbed WT PGK determined by SPR and by ellipsometry as a function of $s/2R_F$. Data shown were obtained by ellipsometry (○) or by surface plasmon resonance (SPR) (■). The pSBMA chains were grafted from alkanethiol monolayers on gold coated glass chips (SPR) and on silicon wafers (ellipsometry). PGK adsorption was measured in 20 mM sodium phosphate at pH 7.4 (mean ± sd; n=3).

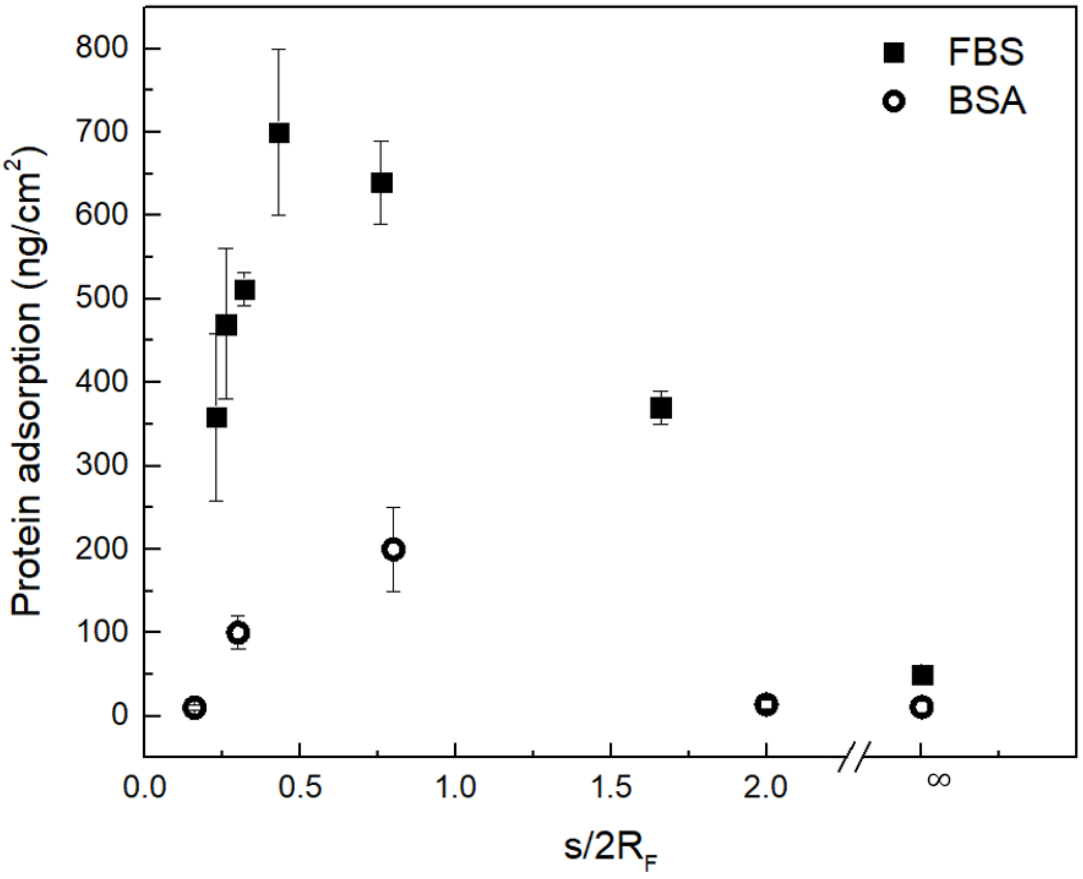

Figure 2.9: Protein adsorption on grafted pSBMA films versus the scaled grafting density, $s/2R_F$ was measured by variable angle spectroscopic ellipsometry. (■) Fetal Bovine Serum (FBS), full serum and (○) Bovine Serum Albumin (BSA) at 30 μM in phosphate buffered saline (137 mM NaCl, 2.7 mM KCl, 8 mM Na_2HPO_4, and 2 mM KH_2PO_4) at pH 7.4 were adsorbed on grafted pSBMA films. Data shown here are mean +/- sd for n=3 independent measurements.

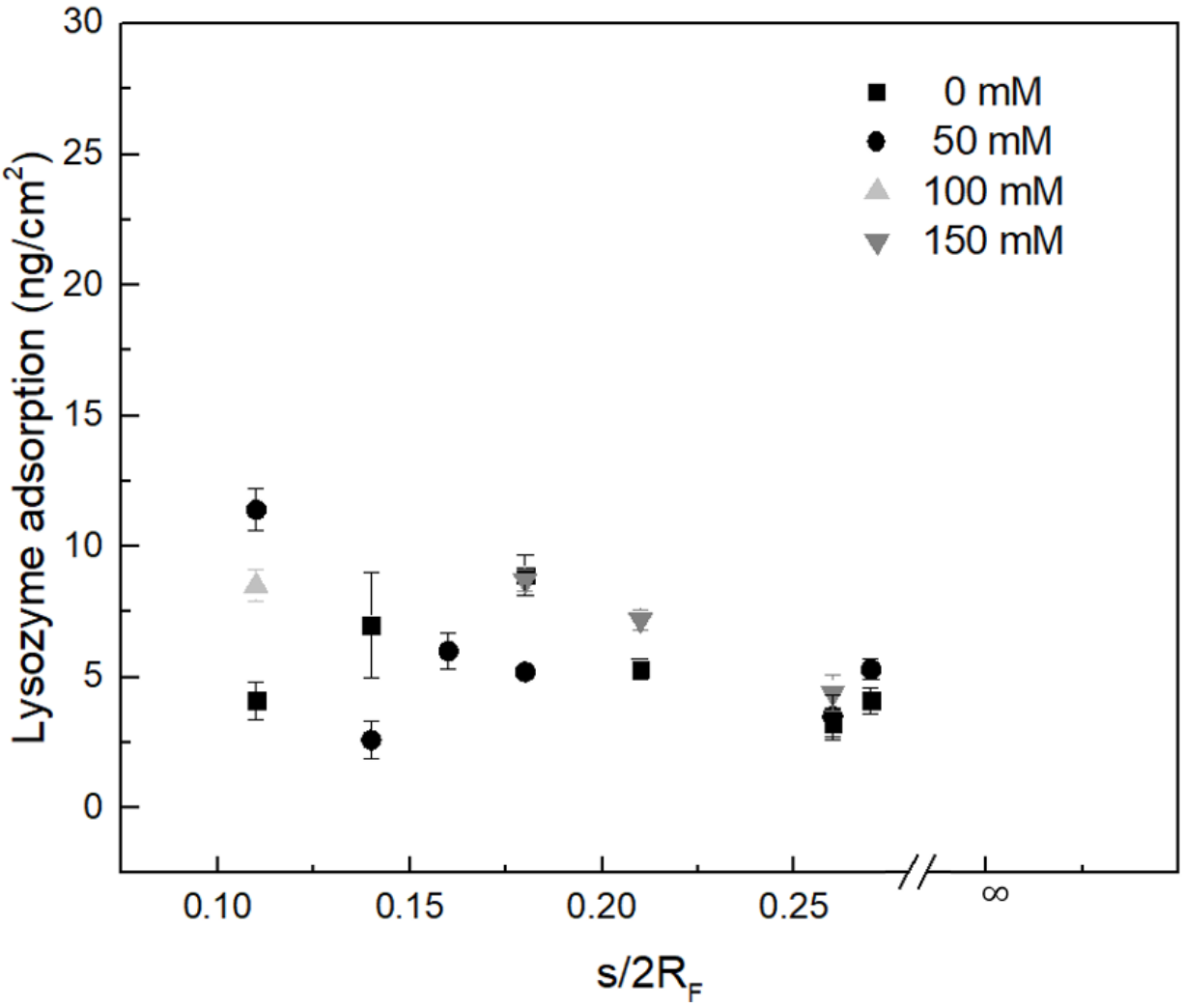

Figure 2.10: Adsorption of Lysozyme on end-grafted pSBMA brushes in 20mM phosphate buffer (pH 7.4) at different NaCl concentrations, measured by SPR. The lysozyme concentration was 140 μM. The NaCl concentrations are indicated in the figure.

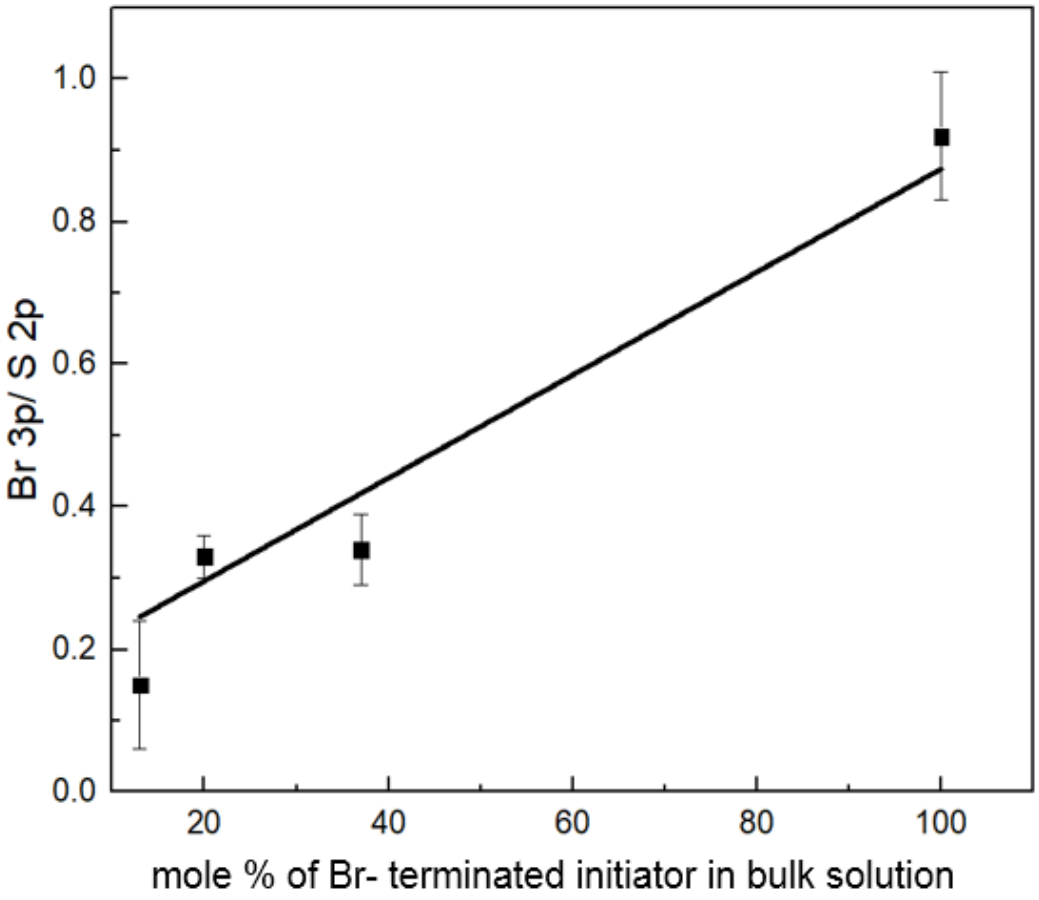

Figure 2.11: Characterization of grafting density on uniformly grafted pSBMA chains on substrates by XPS. Using the linear fit, values for Br 3p/ S 2p ratios were extrapolated for concentrations lower than 13 mol% Br-terminated initiator in thiol solution.

Table 2.1: Summary of Polysulfobetaine or pSBMA chain parameters.

Position from top (cm)	Dry Thickness [i] (nm)	Grafting density, σ (chains/nm^2)	MW (KDa)	s/2R_F	Polymer configuration
1	10.9±0.1	0.21	32.3±0.3	0.22	Brush
2	7.6±0.2	0.18	22.2±0.3	0.29	Brush
3	6±1	0.14	19.0±0.4	0.36	Weakly overlapping
4	4±1	0.05	20±1	0.59	Weakly overlapping
5	3.8±0.7	0.04	20±1	0.64	Weakly overlapping
6	3.2±0.7	0.02	22±4	1	Mushroom
7	2.3±0.2 [ii]	-	-	-	-

[i] Polymer film thickness *including* the thickness of the SAM (2.5±0.3 nm);

[ii] thickness of the SAM layer without polymer growth on the OH-terminated SAM.

Table 2.2: PGK adsorption on OH-terminated SAM (OH-SAM) on gold coated substrates

Protein in carrier buffer at pH= 7.4	Amount adsorbed (ng/cm^2) on OH-SAM at the indicated NaCl concentrations			
	Unbuffered water	0 mM	50 mM	100 mM
PGK-WT (6.50 µM)	110 ± 10	240 ± 10	90 ±10	50 ± 10
Lysozyme (140 µM)	66 ± 3	40 ± 10	32 ± 3	20 ± 10

Table 2.3: Maximum amount of protein adsorbed at different ionic strength and corresponding $s/2R_F$ ratios of end-grafted pSBMA chains

Protein in carrier buffer at pH=7.4	Maximum amount of protein adsorbed (ng/cm^2) at corresponding $s/2R_F$ ratios			
	Unbuffered water	[NaCl] mM in 20 mM sodium phosphate at pH=7.4		
		0 mM	50 mM	100 mM
WT PGK (6.50 µM)	500 ± 50 at $s/2R_F$= 0.39	440 ± 50 At $s/2R_F$= 0.94	290 ± 30 at $s/2R_F$ =0.73	140 ± 10 at $s/2R_F$= 0.73
Lysozyme (140 µM)	330 ± 30 at $s//2R_F$= 1	210 ± 20 at $s/2R_F$= 1.47	80 ± 8 at $s/2R_F$= 1.56	Not detected

Table 2.4: Protein dimensions and estimated distance between grafted pSBMA chains

Grafting density, σ (chains/nm^2)	Distance between grafted chains, s (nm)	Protein size/dimension, R_p (nm)		
		PGK-WT	PGK-FRET	Lysozyme
0.21	2.2	2.4[i]	3.1[ii]	4.5x3.5x 3.5 [iii]
0.16	2.5			
0.08	3.6			
0.07	3.7			
0.04	5.2			
0.03	6.3			
0.02	8.0			

[i] A. Dhar, A. Samiotakis, S. Ebbinghaus, L. Nienhaus, D. Homouz, M. Gruebele , M. S. Cheung, *PNAS* **2010**, *107 (41)*, 17586.

[ii] Estimated by assuming a spherical molecule;

[iii] A. Halperin, G. Fragneto, A. Schollier, M. Sferrazza, *Langmuir* **2007**, *23*, 10603.

Table 2.5: Estimated grafting density of pSBMA chains grown from uniform SAM-Br films

mol% of SAM-Br in thiol solution	Br/S	Estimated grafting density (chains/nm^2)
100	0.92	0.21
37	0.34	0.08
20	0.33	0.07
13	0.15	0.04

Table 2.6: Measured thickness of pSBMA chains in different solvent

$s/2R_F$	Polymer thickness (nm) ; Swelling ratio= $\frac{\text{Wet thickness}}{\text{Dry thickness}}$				
	In air	In water (0 mM NaCl)	In 20 mM phosphate buffer, pH= 7.4		
			50 mM NaCl	100 mM NaCl	150 mM NaCl
0.32	6.3 ± 0.1; 1.0	2.6 ± 0.2 ; 0.41	6.3 ± 0.1; 1.0	7.5 ± 0.5 ; 1.2	9.0 ± 0.3 ; 1.4
0.72	3.73 ± 0.05; 1.0	3.3 ± 0.1; 0.88	3.87 ± 0.03; 1.0	5.4 ± 0.3; 1.4	13 ± 2; 3.5

CHAPTER 3: IONIC STRENGTH DEPENDENT FORCES BETWEEN END-GRAFTED POLY(SULFOBETAINE) FILMS AND MICA

This chapter is adapted in part from journal article: Ahmed, Syeda Tajin; Madinya, Jason J.; Leckband, Deborah E. Ionic Strength Dependent Forces Between End-Grafted Poly(sulfobetaine) Films and Mica. *J Colloid Interface Sci*. 2021, 606 (1), 298-306 (doi:https://doi.org/10.1016/j.jcis.2021.08.004) with permission [copyright 2021 Elsevier].

3.1 Introduction

Polymer covered surfaces generate repulsive osmotic force as the surfaces approach each other and the segments begin to overlap due to unfavorable entropy associated with confining the segments between the two surfaces. As such, the generated steric or osmotic barrier help stabilize or prevent from aggregation of nanoparticles or colloids in aqueous solutions. Such a small amount of addition of polymers to provide steric stabilization of particles has many practical applications. Zwitterionic polymers are an excellent candidate to provide both steric and electrostatic stabilization because in electrolyte solutions the charges on the side chains do not undergo excessive electrostatic screening. At extreme environments, such as API brine (8% NaCl + 2% $CaCl_2$) and elevated temperatures of 90^0 C, polymer coatings containing sulfonate groups such as 2-acrylamido-2- methylpropane sulfonic acid (AMPS)[229, 230] or sulfobetaines have been shown to stabilize iron oxide nanoparticles for 30 days.[29, 110] In presence of divalent Ca^{2+} polyzwitterions also perform very well, [30] which is a difficult problem to solve with polyelectrolytes which bind strongly to cations and are poorly solvated in brine, resulting in loss of steric stabilization of nanoparticles.[231]

The impact of electrolyte concentrations on the solubility and swelling of zwitterionic polymers coatings is not universal by any means. The hydrodynamic radii of soluble phosphorylcholine polymers [112] and swelling behavior of grafted brushes ,[111] reportedly decreased or showed no change with increasing monovalent salt concentrations. Conversely, poly(carboxybetaine) brushes at an air-water interface swelled with increasing salt concentration, similar to poly(sulfobetaines).[113] Although some reports suggested that hydrodynamic radii of poly(sulfobetaines) increases with NaCl concentrations between 10^{-2} M and 1 M,[95] other findings suggested that the chains contract.[96] Given these different results, it is important to establish how the chain density and ionic strength influence the interfacial properties of grafted, zwitterionic polymer films.

Here, Surface Forces Apparatus (SFA) measurements were used to quantify the molecular scale forces between end-grafted poly(sulfobetaine) polymers and mica, as a function of the grafting density and molecular weight, at different monovalent salt concentrations. To quantitatively compare the salt-dependence of the interfacial forces, the force-distance profiles determined with brushes were compared with Millner-Witten-Cates theory.[199] Data obtained with dilute chains were compared with Dolan and Edwards theory.[193] These simple polymer models do not account for segment-segment attraction prevalent in zwitterionic polymers. These polymer models do not account for electrostatic segment-segment attraction prevalent in zwitterionic polymers. However, the dependence of fitted model parameters on the ionic strength provide insights into how salt-dependent, polymer behavior alters the interfacial forces at different polymer surface coverages. These results have direct implications for the use of pSBMA to stabilize colloidal particles or prevent surface fouling, in aqueous electrolyte solutions.

3.2 Materials and methods

3.2.1 Chemicals

Monomer 2-(Methacryloyloxy) ethyl] dimethyl-(3-sulfopropyl) ammonium hydroxide or SBMA (95%, $H_2C=C(CH_3)CO_2CH_2CH_2N(CH_3)_2(CH_2)_3SO_3$, Molecular Weight 279.35) was purchased from Sigma Aldrich (Product # 537284, St Louis, MO). Bis[2-(2'-bromoisobutyryloxy) undecyl]disulfide or the Br- terminated initiator (MW 704.70) was purchased from Sigma-Aldrich (Product # 733350, St Louis, MO). Ligand 1,1,4,7,10,10-Hexamethyltriethylenetetramine or HMTETA (97%, $[(CH_3)_2NCH_2CH_2N(CH_3)CH_2-]_2$, Molecular Weight 230.39) was purchased from Sigma Aldrich (Product # 366404, St Louis, MO). Copper (I) bromide and Copper (II) Bromide were (Product # 254185 and 221775, respectively) purchased from Sigma Aldrich (St Louis, MO). 11-Mercapto-1-undecanol or the OH- terminated thiol (97%, Linear Formula $HS(CH_2)_{11}OH$, Molecular Weight 204.37) was purchased from Sigma-Aldrich (Product # 447528, St Louis, MO). Ultrapure water (resistance 18.2 MΩ.cm at 25^0C) was obtained using Synergy® UV (Millipore Sigma) water purification system. Methanol was purchased from Thermo Fisher Scientific. Sodium phosphate (dibasic, anhydrous, lab grade) was from Ward's Science (Rochester, NY, Product # 470302-660). Sodium nitrate ($NaNO_3$, Molecular Weight 84.99) was purchased from Sigma-Aldrich (Product # 221341, St Louis, MO).

3.2.2 pSBMA synthesis on gold-coated hemi-cylindrical silica discs or silicon wafers

Poly(sulfobetaine) methacrylate (pSBMA) was synthesized from gold coated silica discs or Si wafers (University Wafer Inc., Boston, MA), using Atom Transfer Radical Polymerization (ATRP) as described previously.[232, 48] The Si wafers were used for film thickness measurements, by variable angle ellipsometry.

The silica discs and Si wafers were coated by first evaporating an adhesion-promoting, 2 nm chromium layer, followed by a 55 nm gold film. Metal films were deposited with a thermal evaporator (Kurt J. Lesker Nano36 Thermal Evaporator System; Frederick Seitz Materials Research Laboratory, University of Illinois at Urbana-Champaign) under vacuum (5×10^{-6} Torr) at a deposition rate of 0.1 nm/sec. After the metal deposition, the gold coated discs were cleaned by immersion in a solution of 13% (v/v) ammonium hydroxide and 4 % (v/v) hydrogen peroxide at 70°C for 90 seconds. Then the substrates were thoroughly rinsed with ultrapure water (resistivity at 18MΩ cm at 25 °C; Millipore, Sigma), followed by ethanol (200 Proof, anhydrous, Decon Laboratories, Inc.), and then sonicated first in ethanol for 1 min and then in ultrapure water for 1 min. Finally, the gold coated discs were rinsed copiously with water and dried under a N_2 stream. Self-assembled alkanethiol monolayers (SAMs) on the gold coated substrates were prepared from a 3.4 mM ethanolic stock solution of initiator Bis[2-(2′-bromoisobutyryloxy) undecyl]disulfide (SAM-Br) and a 5.87 mM stock ethanolic solution of 11-Mercapto- 1-undecanol (SAM-OH). Substrates were immersed in the alkanethiol solutions overnight at 4oC. The two different alkanethiol solutions used in these studies contained 100 mol% (3.4 mM) SAM-Br or 20 mol% (0.68 mM) SAM-Br and 80 mol% (5.87 mM) SAM-OH, which is used as a diluent. At these two concentrations of Br-terminated thiol, the synthesized polymers form densely grafted brushes and dilute, non-overlapping mushrooms.

After the substrates were incubated with the alkanethiols overnight at 4ºC, they were transferred to custom-made one-armed reaction vessels sealed with a rubber septum and connected with a Schlenk line, to maintain an inert atmosphere of ultrapure Ar gas during the reaction. In a round bottom flask, monomer [2-(Methacryloyloxy)ethyl]dimethyl-(3-sulfopropyl)ammonium hydroxide was dissolved in 1:1 volumetric mixture of methanol and water at a final concentration

of 0.2 M. The monomer solution was degassed and kept under Ar gas at all time. Next, $CuBr_2$, ligand HMTETA, and CuBr were added at a final concentration of 16.79, 46, and 0.56 mM, respectively. After mixing, the reactant solution was transferred to the reaction vessel using a 10 ml glass syringe. The polymerization reaction proceeded at room temperature under Ar for 15 min. Next, the reaction was terminated by removing substrates from the solution.

The samples were then treated to an extensive cleaning procedure as follows. First, the discs were rinsed copiously with a 50:50 methanol: water mixture. Because the pSBMA chains are insoluble in water, the polymer samples were then rinsed with 20 mM sodium phosphate, Na_2HPO_4 buffer, to remove any physisorbed pSBMA chains or monomers. After rinsing, the discs were immersed in the buffer and sonicated for 20s. A total of two rinse/sonication cycles were performed. The sonication time was adjusted so that it did not damage the gold coating. After the final sonication, the discs were rinsed with buffer and then rinsed copiously with water and dried under a N2 stream. The discs were stored in small Petri dishes under vacuum before use in force measurements.

3.2.3 Polymer Film Thickness Determinations by Ellipsometry

The dry polymer film thicknesses were determined by ellipsometry, using a Variable Angle Spectroscopic Ellipsometer (J.A. Woollam VASE). Gold coated Si wafers were used that underwent the entire pSBMA synthesis procedure under the similar reaction conditions as used to prepare thin polymer films on silica discs used for SFA measurements. After assembling alkanethiol monolayers and then following pSBMA synthesis, the dried samples were scanned in three different regions of the sample at three different angles of incidence (65°, 70°, and 75°) in the visible region (300–900 nm). The bare, gold-coated Si wafer and 100 mol% SAM-OH monolayers on gold coated Si wafers were used as references. The resulting scans were fit to a multilayer model consisting of bulk silicon of default thickness 1 mm, a silicon oxide layer of 2

nm, Cr of 2 nm and Au metal layers, and a Cauchy dispersion layer. The thiol and polymer layers were treated as one Cauchy dispersion layer, by using a refractive index of 1.46 for the organic layer.[218] As a control, substrate incubated in thiol-only solution were used to determine the SAM layer thickness, which was subsequently subtracted from the SAM and polymer layer thickness to estimate the polymer film thickness.

3.2.4 Grafting density estimation from X-Ray Photoelectron Spectroscopy (XPS)

To estimate the chain grafting density, we used the method reported previously.[48] Briefly, the surface density of Br-terminated alkanethiols was determined by X-ray photoelectron spectroscopy (XPS, Kratos AxisULTRA spectrometer, Frederick Seitz Materials Research Laboratory, University of Illinois at Urbana-Champaign). The chemical compositions of S and Br on surface were collected from the S 2p and Br 3p spectra respectively. The initiator density was then determined from the relative Br/S ratios, calculated by the integrated peak areas in the XPS spectra using CasaXPS software (Version 2.3 19PR1.0). The excitation source was the monochromatic Al K α radiation at 1486.6 eV (225 W, 40 eV pass energy). The C 1s hydrocarbon peak at 285.0 eV was used as the reference peak, to measure the binding energy. From the estimated Br/S ratios, the grafting densities σ (chains/nm^2) and corresponding distances between grafting sites, $s= \sigma^{-1/2}$ (nm) were determined were estimated (*see details in Results*).

3.2.5 Sample preparation for surface force apparatus (SFA) measurements

SFA measurements quantified the forces between end-grafted pSBMA films and a bare mica sheet on opposing fused silica disks. The pSBMA chains were grafted from alkanethiol monolayers on gold-coated, hemicylindrical, fused silica disks with a 2cm radius of curvature. The second surface was freshly cleaved, atomically smooth ruby mica (grade 2, S&J Trading Inc., Glen Oaks, NY) that was back silvered with a 40 nm of a reflective silver layer. The silver was deposited by thermal

evaporation, using conditions described for the deposition of gold films. The mica was glued silvered-side down (sym-diphenylcarbazide powder, 98%, ACS reagent, ACROS Organics™, Fisher Scientific) on a second, hemicylindrical silica disc (ESCO Optics, Oak Ridge, NJ). The thus prepared samples were then mounted in the chamber of the SFA. Then the prepared samples were then mounted in the chamber of the SFA. The opposing silver and gold films form a Fabry-Perot interferometer. Prior to use, all glassware was cleaned for at least 2 h in a base bath, consisting of 500 g of potassium hydroxide dissolved in 1 L water and then mixed in ~8 L of isopropanol. After incubation, the glassware was rinsed thoroughly with DI water.

3.2.6 Surface force measurements

A Mark-II surface force apparatus (SFA) was used to measure forces between the end-grafted polymer films and mica as a function of the sample separation distance. Samples were immersed in phosphate buffered solutions (20 mM Na_2HPO4) at pH=7.0 with added 10, 100 or 1000 mM NaNO3. The corresponding ionic strengths of the resulting solutions are, respectively, 54 mM, 144 mM and 1044 mM. In all SFA measurements, $NaNO_3$ was used instead of NaCl because halide ions corrode the reflective silver coating on the mica. The solutions were prepared with ultrapure water, filtered twice through a surfactant free 0.2 μm Durapore membrane (Millipore Sigma), and stored in clean glass flasks at room temperature. Before the measurements, the two silica discs were installed in cross-cylindrical geometry inside the SFA chamber (Figure 3.1). The distance between the surfaces are determined by interferometry, using the fringes of equal chromatic order (FECO). A DC regulated power supply (Newport / Oriel 68735) is used to send a collimated white light (tungsten-halogen lamp, 120 watt) normally through the opposing samples in the SFA chamber. The image of the FECO at contact between two surfaces are observed by focusing the contact between two surfaces by microscope objective lens and directing light by two prisms (45-

45-90^{o}) onto the spectrometer slit. The FECO thus obtained are recorded using an Andor Zyla 5.5 sCMOS camera (Oxford Instruments) with an exposure time of 0.3 seconds. A mercury arc lamp (Oriel Instruments, 50 Hz, 4 Amps, model #5047) was used to calibrate the measured wavelengths of the FECO in the field of view. The assembled pSBMA films on the alkanethiol monolayers, opposing mica and intervening aqueous medium form to a 2-layer, asymmetric interferometer. [119,132] The surface roughness of the evaporated gold film limits the distance resolution to ~1 nm. The measured force, normalized by the geometric average radius of the crossed hemicylinders (F/R) is related to the interaction energy per area between two, equivalent parallel plates, by the Derjaguin approximation. The resolution is F/R ~0.001 mN/m. Force-distance measurements were conducted either with the sample chamber filled with solution or by injecting a liquid droplet between the surfaces. In droplet measurements, a droplet of the pre-filtered solution was introduced between the two opposing disks with a clean, glass syringe (20 µl Microliter Syringe, Hamilton Co., Nevada). To prevent evaporation of the droplet between the two surfaces, a boat containing ~3 ml of ultrapure water was placed inside the chamber. All measurements were performed in a temperature-controlled dark room at 21 ± 0.1^{o}C. The equipment was supported on a vibration-isolation table.

Force-distance measurements were conducted under quasi-equilibrium conditions. For statistics, at least five replicate force-distance curves were measured at each of at least three, different asperity free regions on the samples, to establish consistent results. The reported number of force measurements, N_{meas} varied between 10 to 15 for each polymer grafting density and molecular weight studied here. At least two experimental replicates were done for each polymer grafting density and molecular weight. The figures show results from one experimental replicate (n_{exp}=1) but are representative of all measurements under similar conditions.

3.3 Results

3.3.1 Characterization of pSBMA thin films on gold coated silica

XPS measurements assessed the Br-terminated to OH-terminated thiols in the SAMs and confirmed polymer synthesis. The N 1s spectra (before and after polymer synthesis) and Br 3p and S 2p spectra of SAM-only substrates are shown in Figure 3.4 (panel B and C). The N 1s peak confirmed the presence of pSBMA on the substrates. Peak areas are summarized in Table 3.1. From the Br/S ratios and a maximum thiol packing density of 2.1 alkanethiols/nm^2 [210] on gold, we calculated the initiator density. We then estimated the chain grafting density, σ and distance between grafting sites, s= $\sigma^{-1/2}$ (nm), by assuming an initiator conversion efficiency of 10%.[217] The thus estimated densities of the end-grafted polymer chains were 0.21 ± 0.01 and 0.04 ± 0.02 chains/nm^2, and the corresponding distances between chains, s were 2.2 ± 0.5 and 5.2 ± 0.5 nm, respectively (Table 3.1).

The polymer molecular weight and degree of polymerization were calculated using the chain density and measured thickness of the dried polymer films. The measured thicknesses of the reference 100 mol% Br- or OH-terminated SAMs were 2.5 ± 0.3 nm and 2.3 ± 0.2 nm (n=5), respectively. The average thicknesses of the brush and mushroom polymer films were 13.5 ± 0.4 nm and 3.34 ± 0.05 nm (n=3), respectively. We then calculated the molecular weights of the polymers using the equation, $M_n = (h\rho N_A/\sigma) \times 10^{-21}$,[233] where M_n is molecular weight of polymer (Da or gm/mole), h is the dry brush thickness (nm), ρ is the monomer density of 1.395 gm/cm^3,[218] N_A is Avogadro's number and σ is the chain density (chains/nm^2). The degree of polymerization was estimated from the ratio of the polymer to monomer molecular weights (i.e. N=$\frac{M_n}{M_m}$). Here, the molecular weight of the monomer SBMA is, M_m= 279.35 gm/mol. Next, values of the scaled grafting parameter, s/2R_F were calculated, to estimate the grafted chain configurations. Here, s is

the distance between grafting sites and the Flory radius, $R_F = l \times N^{3/5}$ where l is the monomer length (≈ 0.3 nm) and N is the degree of polymerization.[234] Calculated molecular weights were 43 ± 2 KDa and 11 ± 1 KDa (Table 3.1), and the corresponding Flory radii, were 6.14 ± 0.03 nm and 2.7 ± 0.1 nm, respectively. Results are reported in terms of the scaled parameter, $s/2R_F$ which is 0.18 ± 0.01 and 1.0 ± 0.6 for the brushes ($s/2R_F << 1$) and non-overlapping mushrooms ($s/2R_F \sim 1$), respectively.

3.3.2 Forces between grafted pSBMA chains and mica at different monovalent salt concentrations

The experimental configuration of samples in the Surface Force Apparatus (SFA) is shown in Figure 3.1. The silica discs with opposing pSBMA thin films and back silvered mica sheets are mounted in the apparatus. Forces were measured as a function of separation distance, D, where D=0 is defined as contact between the self-assembled monolayer (SAM) surface and mica, in air (Figure 3.1). Samples were bathed in 20 mM sodium phosphate buffer at pH 7 containing added 10, 100 or 1000 mM $NaNO_3$. The corresponding ionic strengths are 54 mM, 144 mM and 1044 mM. In the majority of experiments, the samples were bathed in solution by placing a droplet of buffer between the opposing disks. This experimental setup is referred to as a 'droplet measurement'. Otherwise, the entire sample chamber of the SFA was filled with buffer.

The compressed thicknesses of the grafted polymer thin films were determined at the end of each experiment, by subjecting the samples to very high loads (F/R > 500 mN/m). The thus determined thicknesses were 11 ± 1 nm for the brush and 2 ± 1 nm for mushrooms (n=3), in good agreement with the dry thicknesses measured by ellipsometry.

3.3.2.1 Forces between pSBMA brushes and mica

The force-distance profiles between bare mica and a brush ($s/2R_F$ =0.18 ± 0.01, MW = 43 ± 2 KDa, σ = 0.21 ± 0.01 chains/nm^2) in buffered solutions containing different $NaNO_3$ concentrations are shown in Figure 3.2. At all ionic strengths, the force-distance profiles are purely repulsive, but the range and the magnitude of the repulsion depended on the ionic strength. Figure 3.2 shows the force, normalized by the geometric average radius of the crossed-cylinders, F/R as a function of the separation distance. In solution with an ionic strength of 54 mM, the onset of the repulsion occurs at ~50 nm and increases monotonically with decreasing separation. At distances less than ~15 nm, the normalized force increases sharply, and the samples flatten due the deformation of the epoxy glue between the mica and silica disk. At an ionic strength of 144 mM, the range of the repulsion is farther out at ~85 nm, and the amplitude of the force at separations less than ~40 nm does not increase significantly, relative to forces measured at the lower ionic strength. At the ionic strength, μ = 1044 mM, the distance at the onset of the repulsive force did not increase significantly, relative to that at μ= 144 mM, but the amplitude of the repulsion increased at all distances.

The force-distance profiles between the brushes and mica at the different salt concentrations were compared quantitatively, by fitting the data to the Milner-Witten-Cates model (MWC) [235] for the interaction between opposing polymer brushes. The MWC theory assumes a parabolic segment concentration profile normal to the surface. The model predicts that the compression energy of the brush will vary as the cube of the compression distance, D. The MWC equation for the distance-dependent free energy per area between end-grafted chains in good solvent is given by:

$$\frac{F(D)}{R} = -4\pi P_0 \left[\frac{2L_0}{D} + \left(\frac{D}{2L_o}\right)^2 - \frac{1}{5}\left(\frac{D}{2L_o}\right)^5 - \frac{9}{5}\right]$$

where, D is the distance between mica and the grafted polymer and L_0 is the equilibrium brush extension. In this model, $L_0 \sim N(\sigma w)^{1/3}$ and $P_0 \sim N(\sigma w)^{2/3}(\sigma^2/12)^{1/3}$, where N is the degree of polymerization and w is an excluded volume parameter. The free energy of the compressed brushes is determined by the osmotic repulsion within the brush and by the elastic restoring energy of the chains. The first term in the above equation is the osmotic contribution, and the second and third terms reflect the chain elasticity. This model describes well the energy between grafted chains with narrow polydispersity. It does not account for segment-segment attraction or osmotic contributions from ions within the brush.

To adapt the above equation for our asymmetric system (grafted brush and bare mica surfaces), $2L_o$ is replaced by L_o, as described previously.[200, 132]

$$\frac{F(D)}{R} = -4\pi P_0 \left[\frac{L_0}{D} + \left(\frac{D}{L_o}\right)^2 - \frac{1}{5}\left(\frac{D}{L_o}\right)^5 - \frac{9}{5}\right] \qquad \text{(Equation 3.1)}$$

In this study, we globally fit all force-distance measurements obtained with a single sample at the same salt concentration. In nonlinear least squares fits of data to Equation 3.1, both P_0 and L_0 were allowed to vary. The fitted values reported in Table 3.2 are the mean ± SEM for at least 10 force measurements the same sample (n_{exp}=1).

With solutions of ionic strength of 54 mM, 144 mM or 1044 mM, the fitted L_o values are 43.9 ± 0.3, 66 ± 1 and 67 ± 1 nm, respectively. At ionic strengths of 144 mM and 1044 mM, the best-fit, equilibrium chain extensions L_0 do not differ significantly ($p>0.05$, N_{meas} = 10 and 15 respectively). However, the magnitude of the repulsion is significantly higher at the higher salt concentration (Figure 3.7). This increase is reflected quantitatively in the fitted prefactors P_o, which are 0.10 ± 0.06 and 0.21 ± 0.05 mN/m, at ionic strengths of, respectively, 144 mM and 1044 mM (Table 3.2).

Although $NaNO_3$ is the dominant salt at the higher ionic strengths, the phosphate ions could have a greater influence on the polymer behavior at μ= 54mM. We used 20 mM sodium phosphate buffer to mimic conditions that we and others used to study protein adsorption on the pSBMA thin films. These conditions are used in many of the biomedical applications of SBMA coatings. The charged groups are in principle fully ionized under the conditions used in this study and over a large range of pH values. However, polysulfobetaine thin films reportedly exhibited a zeta potential of -40mV. [236] They can also hydrolyze when exposed to aqueous media for extended periods. [237] The buffer may mitigate these effects. Controls compared force profiles measured with a grafted pSBMA brush ($s/2R_F$ = 0.1, dry thickness = 22.8 ± 0.4 nm, M_n = 80 ± 1 KDa, R_F ~9 nm) bathed in 10 mM $NaNO_3$ with 20 mM phosphate (pH=7) versus the identical sample bathed in a $NaNO_3$ solution at the equivalent ionic strength of 54 mM. Figure 3.6 shows that the force curves are similar. In addition, parameters obtained from data fits to Equation 3.1 are statistically similar (($p>0.05$, N_{meas} = 10, Table 3.5). The fitted values of the equilibrium chain extension, L_0 are 89 ± 4 nm in $NaNO_3$ and 87 ± 5 nm in 10 mM $NaNO_3$ and 20mM sodium phosphate. The prefactors, P_o were also similar ($p>0.05$, N_{meas} = 10). The ratio of L_0 to the degree of polymerization, N is approximately 0.3, similar to the pSBMA brushes with lower MW (L_0 ~43 nm, N~150). These results confirm that, at these concentrations, the phosphate ions do not alter the polymer behavior.

3.3.2.2 Forces between pSBMA mushrooms and mica

Forces between dilute end-grafted mushrooms ($s/2R_F$ = 1.0 ± 0.6, MW = 11 ± 1 KDa, σ = 0.04 ± 0.02 chains/nm^2) and mica were similarly measured in buffered solutions containing different added $NaNO_3$ concentrations. Figure 3.3 compares forces measured at different ionic strengths, μ = 54 mM, 144 mM and 1044 mM. There are qualitative and quantitative differences between force

curves measured with the identical samples but bathed in different solutions. At μ = 54 mM, the forces exceed ~0.01 mN/m at D < 35 nm, and the normalized force increases exponentially at distances, D < 20 nm (Figure 3.3). At μ = 144 mM, the range of the repulsion increases to ~50 nm, and the force increases exponentially at D < 30 nm. At the highest ionic strength of 1044 mM, the onset of the repulsion increases to ~75 nm and the force increases exponentially at D < 40 nm. Although the ranges of the forces differ, the amplitudes at smaller separations (D < 5nm) are similar, at the different ionic strengths.

The force profiles were compared quantitatively, by fitting the data to the Dolan and Edwards model (D&E),[193] which describes the forces between two surfaces with sparse, end-grafted chains in theta solvent:

$$\frac{F(D)}{R} \approx Ae^{-\frac{D}{R_g}} \qquad \text{(Equation 3.2)}$$

Here, the prefactor, $A \approx \frac{72\pi KT}{\Gamma}$, where Γ is the area per chain, K is the Boltzmann constant, and T is the absolute temperature. For chains in theta solvent, the decay length is the radius of gyration of a random coil, R_g. However, with pSBMA chains, the solvent quality and hydrodynamic radius depends on the salt concentration. We therefore deem the decay constant an "effective R_g", or R_{eff}. The prefactor and R_{eff} under the different solution conditions were estimated from nonlinear least squares fits of the data to Equation 3.2. The best fit parameters are summarized in Table 3.3. The fitted values are mean ± SEM for at least 10 force measurements on the same sample (n_{exp}=1). The fitted decay lengths increase with ionic strength. Values for R_{eff} determined with the same samples in solutions of ionic strengths of 54 mM, 144 mM or 1044 mM are, respectively 7.1 ± 0.2 nm, 11.8 ± 0.5, and 17 ± 1 nm. These values are approximately 2, 4, and 6 times the estimated Flory radius, $R_F \approx 3$ nm. The increase in the effective coil size is similar to the increase in brush height with increasing ionic strength. In contrast to the dense brushes, the prefactor A which scales

the amplitude of the repulsion, did not vary significantly with ionic strength (t-test, $p>0.05$, N_{meas} =10 at 54 mM, 15 at 144 mM, N_{meas} =10 at 1044 mM). However, the distances at which the forces deviate from the exponential curve depend weakly on the salt concentration. Deviations determined from the residuals of the nonlinear least-squares fits occur at ~ 20, 26, and 35 nm at ionic strengths of 54 mM, 144 mM and 1044 mM, respectively. We note that measurements at the highest ionic strength of 1044 mM were done with a droplet between the discs, rather than with the chamber filled with solution. However, both approaches give statistically similar results (Figure 3.5, Table 3.4).

3.4 Discussion

The surface force measurements reveal quantitatively how repulsive forces generated by grafted, zwitterionic poly(sulfobetaine) depend on the chain density and ionic strength. Prior studies documented salt dependent swelling of soluble and grafted poly(sulfobetaines), but these surface force measurements quantified how such swelling can impact the range and magnitude of the surface forces. Moreover, the sensitivity of the SFA measurements enabled quantitative comparisons of the force-distance curves with polymer models. The ionic strength-dependent behavior of grafted pSBMA differs from the salt-independent forces measured with end-grafted poly(ethylene glycol), PEG. [133, 198] In contrast to PEG chains, which do not interact with ions, ions screen segment-segment interactions in pSBMA polymers and increase the osmotic pressure within the polymer films. Both effects will increase chain swelling.

The major results of this study document the ionic strength dependent swelling behavior of grafted pSBMA thin films and the impact of this behavior on the nanoscale interfacial forces. At a single $NaNO_3$ concentration, the features of force-distance profiles measured with dense

poly(sulfobetaine) brushes agree qualitatively with Millner-Witten-Cates (MWC) model. Similarly, the force profiles of dilute mushrooms are described by the Dolan and Edwards model. However, neither model accounts for the salt-dependence of electrostatic segment-segment interactions; therefore, they do not describe the effect of salt on the chain extensions and force profiles. This salt-dependent behavior differs from the salt-insensitive forces measured with other neutral polymers, like PEG.[133, 198] The model comparisons and fitted parameters obtained with grafted pSBMA were thus used to compare the interfacial forces, as a function of the polymer coverage, $s/2R_F$ and ionic strength.

The behavior of pSBMA brushes also differs from polyelectrolyte (PE) brushes. [118, 145] At low salt concentrations, the equilibrium thickness of strong PE brushes ($L_o \cong \alpha^{1/2}$ Na, where α is the fraction of free counterions per chain, N = number of segments of Kuhn length a) is independent of the salt concentration, c_s. At high salt concentration, the chain extension decreases, with a weak power law dependence: $L_o \propto c_s^{-1/3}$. These two scenarios are known as the 'osmotic brush regime' and 'salted brush regime', respectively.[115] At high salt, weak PEs also shrink, according to $L \propto c_s^{-1/3}$. However, at low salt, the brush height is predicted to increase [116, 117] with a power law dependence, $L \propto c_s^{1/3}$. At lower ionic strengths, L_o for the pSBMA brush increased significantly from ~43 nm at μ = 54 mM to ~67 nm at μ = 144 mM. This is qualitatively similar to weak PEs, although we lack sufficient data to establish the power law exponent. The increased chain extension measured at the lower ionic strengths is attributed to screened electrostatic segment-segment interactions and to increased osmotic repulsion in the brush. [85, 194] Although the brush height changed, between μ = 54 and 144 mM, the fitted prefactors were similar. At high ionic strength, the pSBMA brushes behave very differently from weak and strong PEs. Between μ = 144 mM and 1044 mM, L_0 did not increase significantly, in contrast to PE brushes, which shrink.

However, the compression energy increases significantly at μ = 1044 mM. We attribute the latter to increased osmotic repulsion due to excess ions within the brush.

Force profiles measured with dilute pSBMA chains also depended on the salt concentration, but the force profiles changed in different ways. The amplitude of the normalized force at short separations did not change significantly with increasing salt, but the exponential decay length did. In the approximate expression for the Dolan and Edwards model (Equation 3.2), the prefactor depends on the chain coverage ($1/s^2$) but not on the volume of the chains; thus, swelling was not expected to alter the prefactor, as we observed. However, the decay length scales with R_g, in theta solvent. In good solvent the chains swell and increase the range of repulsion.[49, 58] The radii of pSBMA coils in salt solutions can exceed R_F, which scales with the segment length. Ions reportedly increase the excluded volume strength of sulfobetaine segments.[238] These data show that the resultant swelling increased the range of the repulsion: namely, R_{eff} increased from ~$2R_F$ at the lowest salt concentration to ~$6R_F$ at μ = 1044 mM. Thus, salt alters both the range of the repulsion and how the force decays with distance.

The Dolan and Edwards model predicts that the force decays exponentially from D=2Rg to D=8Rg. Here, $R_g \approx$ 3 nm, and the exponential fit describes data from D~$6R_g$ to D~$10R_g$. The deviation of the measured forces from the model at D>$10R_g$ could be due to polydispersity. Neutron Reflectometry studies could shed more light on segment density profiles. Poly(sulfobetaine) swelling in salt solutions was reported for chains in solution and at surfaces [239, 240], but the latter studies did not determine how such swelling behavior alters the interfacial forces. Also, studies of tethered chains focused on dense brushes. AFM measurements documented salt-dependent swelling of dense brushes of polysulfobetaines.[194, 238] Neutron reflectivity showed that

brushes collapse in pure water but swell with increasing NaCl. [105] At low salt, the segment densities were concentrated near the surface. Chains remained somewhat condensed near the theta salt concentration, but the segment density profiles were parabolic in 500 mM NaCl.[105] The MWC model, which assumes a parabolic segment density profile, describes well the force curves measured with pSBMA brushes, at all salt concentrations considered here. The good agreement with the MWC model could be due to our use of salt concentrations near or above the reported theta NaCl concentration of ~74 mM.[241] The force curves and model fits did not indicate collapsed brushes, but the more rapid decrease in force at large separations at lower salt concentration may be due to lower chain solubility.

The crossed-cylinder geometry and Derjaguin approximation make it possible to estimate repulsive potentials of similar pSBMA coatings used to stabilize colloids in concentrated brine or to impede biofouling on polymer coated surfaces.[188, 264, 265] The results confirm assumptions regarding the steric stabilization of ZI-coated nanoparticles under extreme conditions, such as in oil reservoirs.[39, 40] They also reveal possible differences in the steric stabilization efficacy of sparse and dense pSBMA chains in electrolyte solutions. Such findings can also inform other models that predict the dependence of protein adsorption on weakly attractive polymer films, such as pSBMA.[73]

3.5 Conclusion

Here, surface force apparatus measurements quantified the ionic-strength-dependence of the magnitudes and ranges of the molecular surface forces between tethered pSBMA chains and mica, at different polymer densities. Prior studies documented the swelling behavior of dense, pSBMA

brushes or of coils in solution, but they did not determine how the salt-dependent, polymer swelling or polymer surface coverage alter the interfacial forces. These results demonstrate that, at the ionic strengths considered here, end-grafted pSBMA films can be described by models for grafted polymers in good solvent. Parameters determined from data fits to the Milner-Witten-Cates or Dolan and Edwards models for dense and dilute chains, respectively, varied with ionic strength, in ways that reflect the ionic-strength-dependent, excluded volume strength of chain segments and corresponding chain swelling. These force measurements provide new insight into how grafting density and salt cooperate to regulate pSBMA steric barriers. The force measurements and quantitative comparisons with polymer models constitute the major difference from prior studies that focused on swelling behavior in solution or at surfaces. Moreover, results from this study set the stage for future studies of the effects of specific ion interactions, as well as zwitterionic monomer chemistries on the surface forces that impact commercial products and processes based on these materials.

3.6 Figures and tables

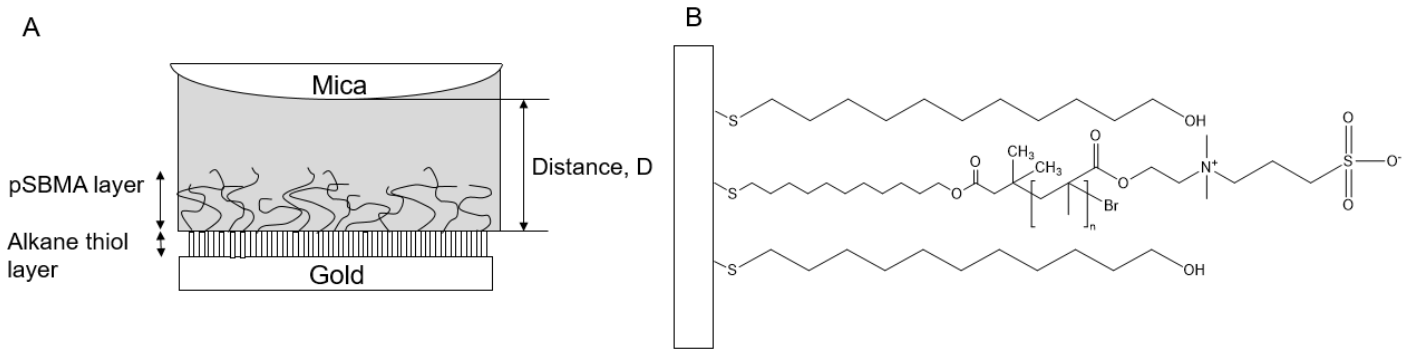

Figure 3.1: Surface Force Apparatus sample configuration. (A) Forces are measured between pSBMA chains grafted from alkanethiol monolayers on gold substrates and mica surfaces in aqueous solutions of 20 mM sodium phosphate (pH=7.0) containing different $NaNO_3$ salt concentrations. (B) Chemical structure of grafted pSBMA chains on gold-coated substrates. The OH-terminated thiols are diluents to control the initiator-terminated thiol densities and resulting polymer grafting densities.

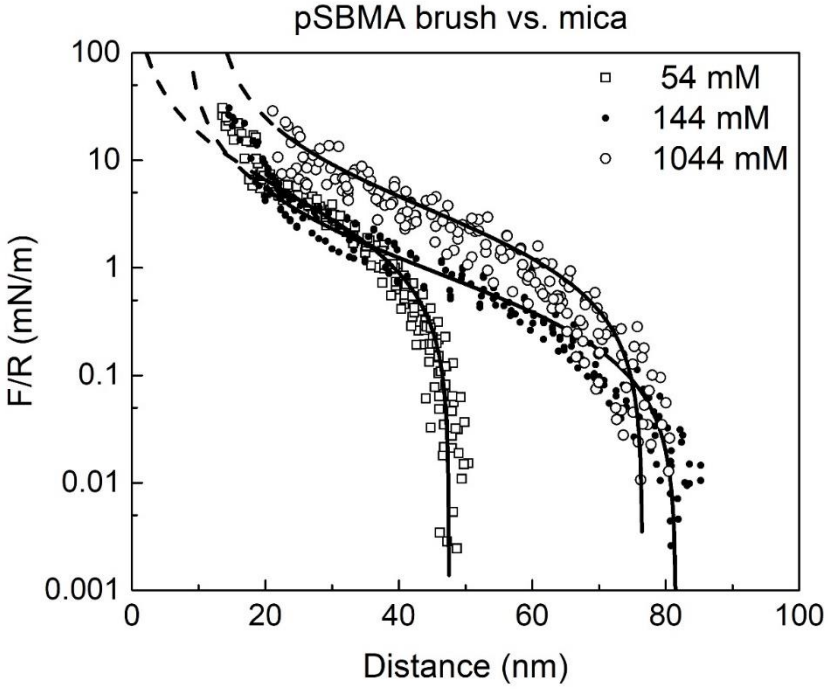

Figure 3.2: Normalized forces F/R between end-grafted pSBMA brushes (s/2RF ~ 0.2) and mica as a function of the separation distance. Measurements were done with samples bathed in aqueous solutions containing 20 mM sodium phosphate at pH=7.0 and 10 mM NaNO3 or ionic strength of 54 mM (number of force measurements, N_{meas}= 15, number of independent replicate, n_{exp}=1, white squares), 100 mM NaNO3 or ionic strength of 144 mM (number of force measurements, N_{meas} = 10, number of independent replicate, n_{exp} =1, black circles), or 1000 mM NaNO3 or ionic strength 1044 mM (number of force measurements, N_{meas} = 15, number of independent replicate, n_{exp} =1, white circles). The solid lines are nonlinear least squares fits of data at distances > 20nm to the Milner-Witten-Cates model (Equation 3.1). Best fit values for the equilibrium thickness, L_o and prefactor, P_o for brushes at the indicated salt concentrations are summarized in Table 3.2. The dashed regions of the curves indicate the regime where the measured forces are not described by theory.

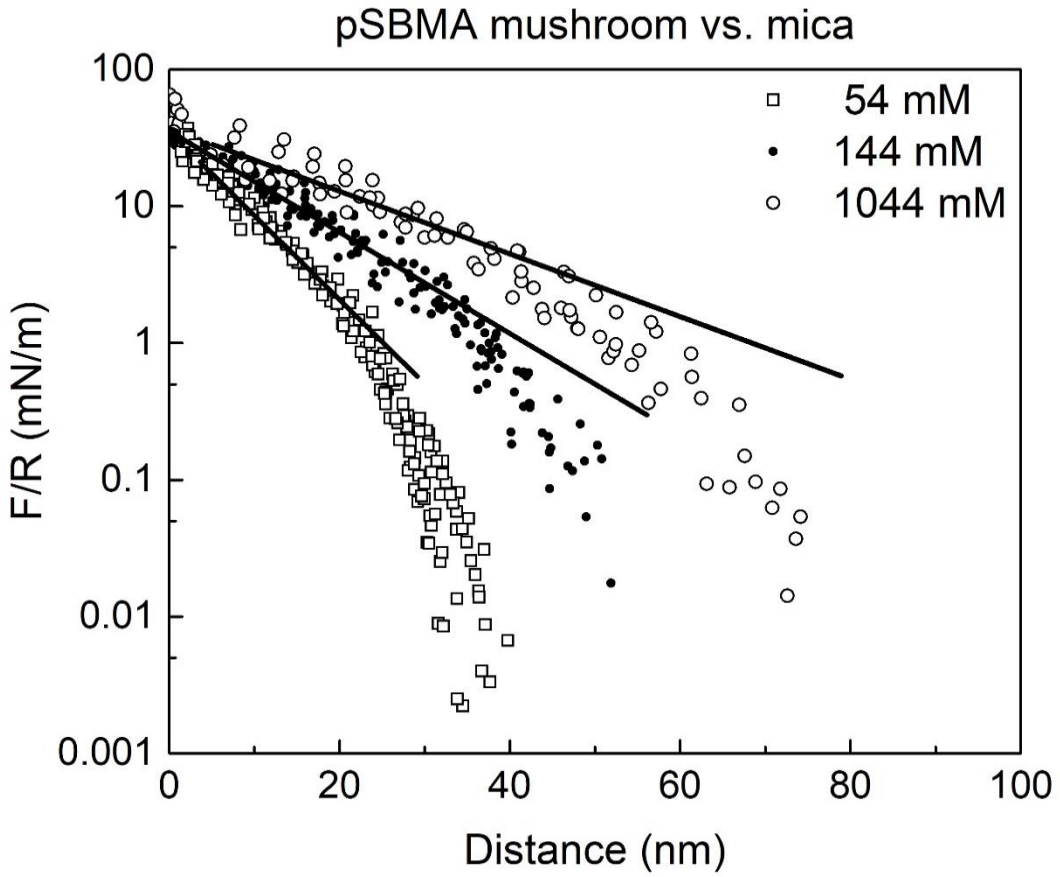

Figure 3.3: Normalized forces F/R between end-grafted pSBMA mushrooms ($s/2R_F \sim 1$) and mica as a function of the separation distance. Measurements were done with samples bathed in aqueous solutions containing 20 mM sodium phosphate at pH=7.0 and 10 mM $NaNO_3$ or ionic strength of 54 mM (number of force measurements, N_{meas} =10, number of independent replicate, n_{exp}=1, white squares), 100 mM $NaNO_3$ or ionic strength of 144 mM (number of force measurements, N_{meas} =15, number of independent replicate, n_{exp}=1, black circles), or 1000 mM $NaNO_3$ or ionic strength 1044 mM (number of force measurements, N_{meas} = 10, number of independent replicate, n_{exp}=1, white circles). The solid lines are non linear least squares fits of the data to the Dolan and Edwards model (Equation 3.2). The best fit values for the decay length, R_{eff} and prefactor, A at different salt concentrations are summarized in Table 3.3.

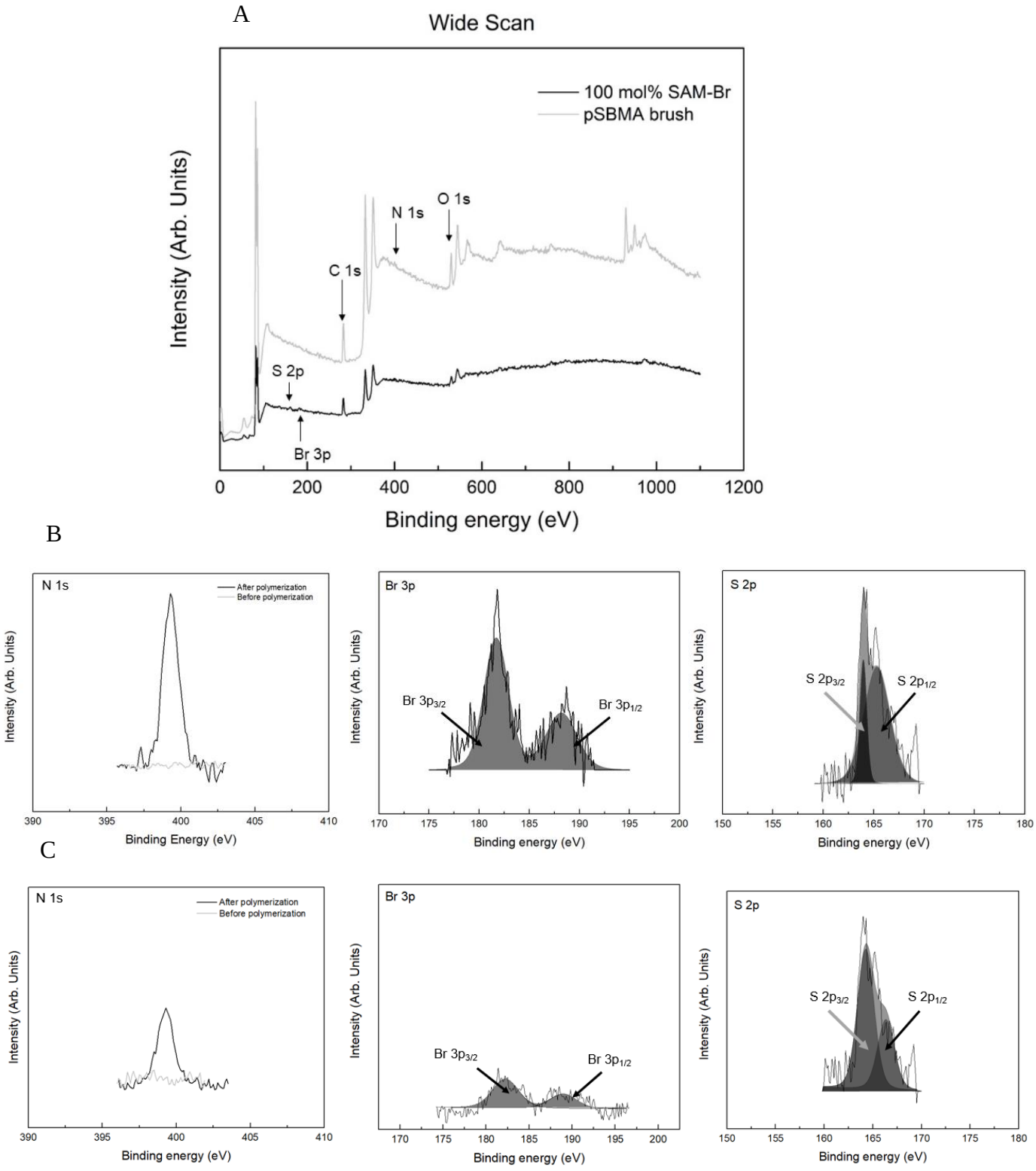

Figure 3.4: The wide scan of surfaces modified with 100 mol% SAM-Br and pSBMA brush after polymerization is obtained from XPS spectra. (A) the N 1s, S 2p and Br 3p peaks form the 100

Figure 3.4: (cont.) mol% and 20 mol% SAM layer is identified and zoomed in panel (B) and (C) respectively. The presence of N1s peak after the reaction indicate the presence of quaternary ammonium in the side chain of polymer. The integrated area under the peak of S 2p and Br 3p were used to determine Br/S ratios, and subsequently the chain grafting densities, as listed in Table 3.1.

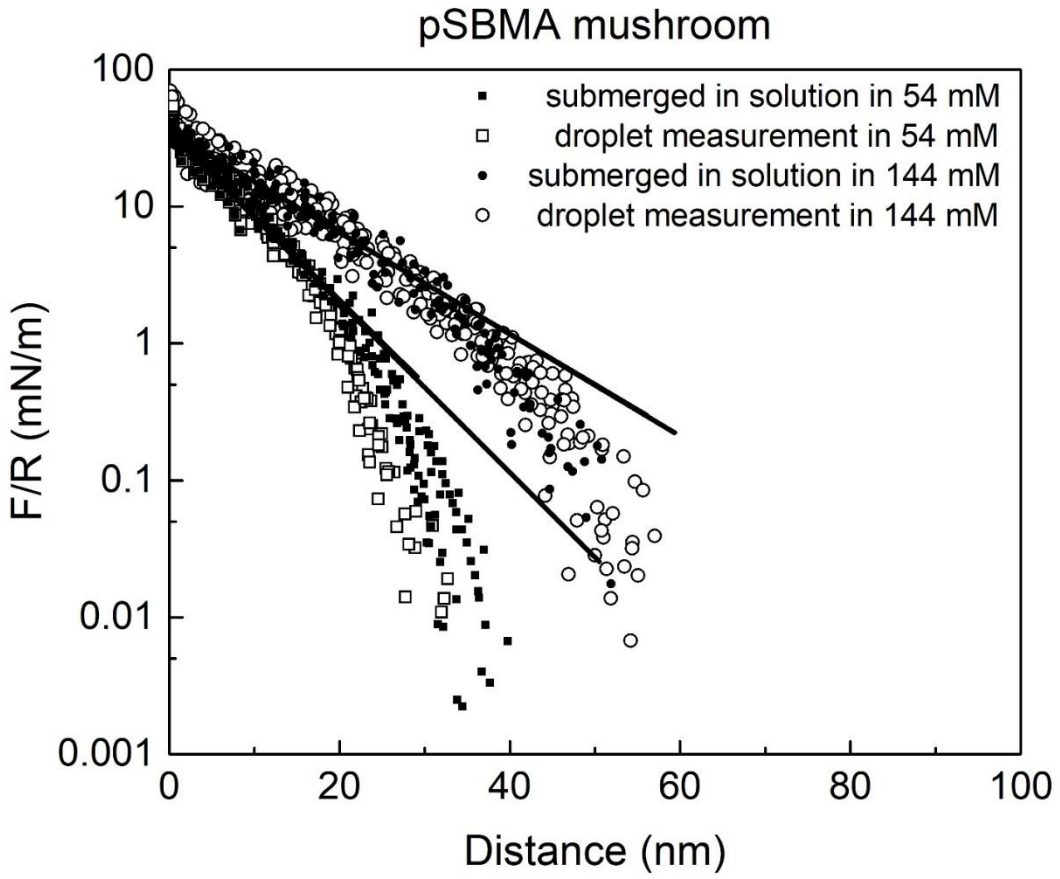

Figure 3.5: Comparison of forces measured with a droplet confined between the disks (open symbols) versus submerged in solution (solid symbols) containing 20 mM sodium phosphate at pH=7.0 and 10 mM $NaNO_3$ (open and solid squares, number of force measurements, N_{meas} = 10, number of independent replicate, n_{exp}=1, ionic strength = 54 mM) or 100 mM $NaNO_3$ (open and solid circles, number of force measurements, N_{meas} =10 for droplet measurements and 15 for submerged condition, number of independent replicate, n_{exp}=1, ionic strength = 144 mM) between dilute, grafted pSBMA chains ($s/2R_F \approx 1.0$) and mica. The solid lines are nonlinear least squares fits of the data to Eq.2. The best fit parameters for R_{eff} and the prefactor, A are given in Table 3.4.

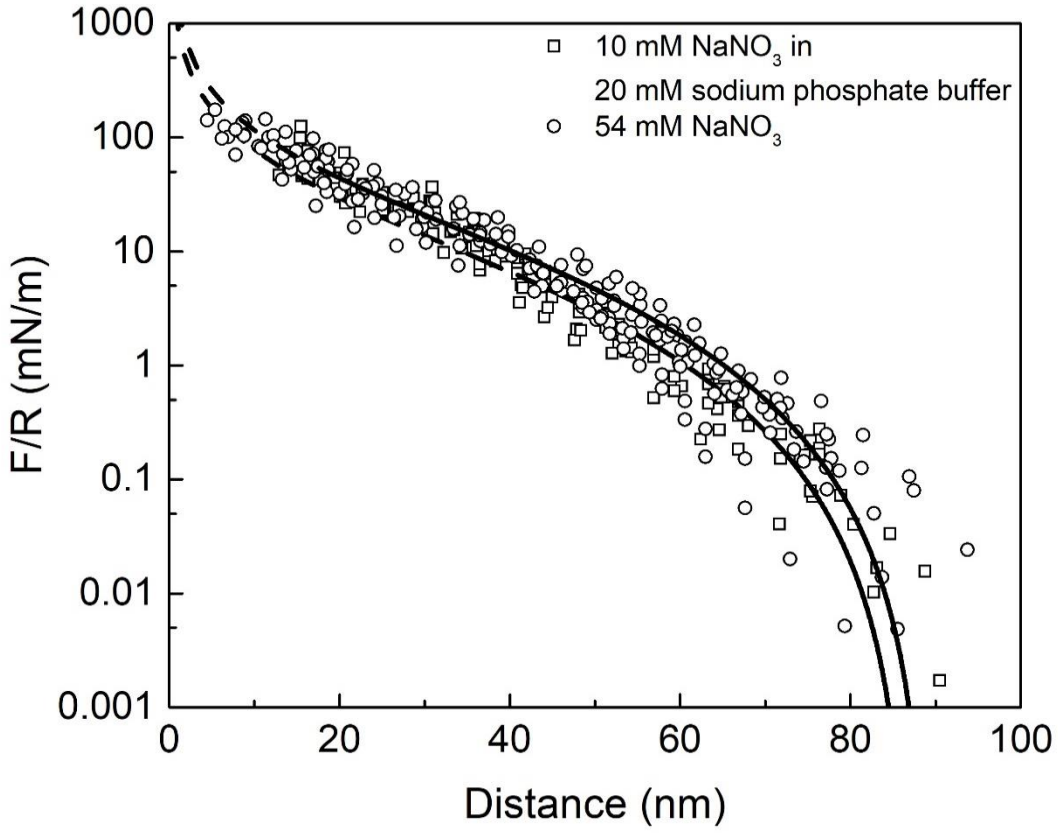

Figure 3.6: Normalized force F/R versus the distances between dilute, grafted pSBMA chains ($s/2R_F \approx 1.0$) and mica in 54 mM $NaNO_3$ (white circles) or 10 mM $NaNO_3$ in 20 mM sodium phosphate buffer at pH 7 (black squares). The total number of force measurements, N_{meas} = 10 on the same surface (number of independent replicate, n_{exp}=1). Measurements were done with a droplet of buffer confined between the disks. The solid lines are nonlinear least squares fits of the data to MWC theory (Equation 3.1). Best fit values for the equilibrium thickness, L_0 and prefactor, P_0 for brushes at the indicated salt concentrations are summarized in Table 3.5.

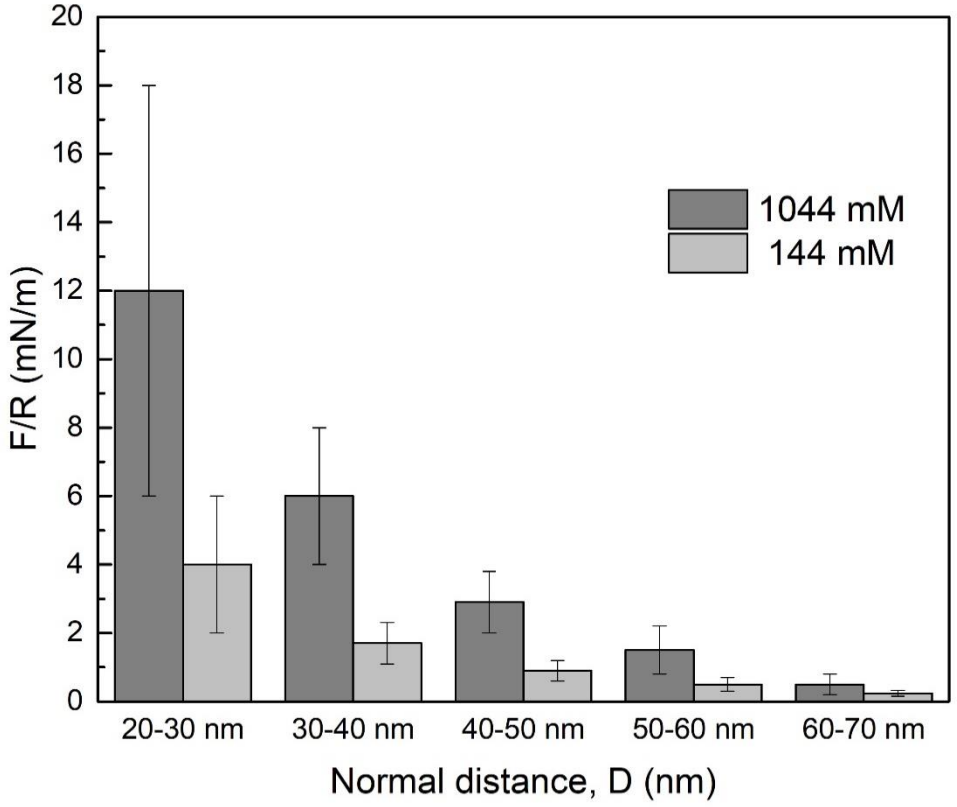

Figure 3.7: Normalized force (F/R) between brushes and mica at the indicated separation distances brushes shown in *Figure 3.2* at a given normal distance between the grafted pSBMA chains and mica at total ionic strength of 144 mM and 1044 mM. The column and bar represent the mean and standard deviation respectively at a given 10 nm distance group. Here, the mean values of the normalized force F/R at the indicated separation distances are all significant determined by t-test ($p<0.05$, number of force measurements, N_{meas} =10 at 144 mM and 15 at 1044 mM).

Table 3.1: Summary of grafted pSBMA chain parameters

Dry polymer thickness* (nm)	Estimated grafting density, σ (chains/nm^2)	Grafting distance, s (nm)**	Molecular weight, M_n (KDa)	$s/2R_F$	Polymer configuration
13.5 ± 0.4	0.21 ± 0.01	2.2± 0.5	43 ± 2	0.18 ± 0.01	Brush
3.34± 0.05	0.04 ± 0.02	5.2± 0.5	11 ± 1	1.0 ± 0.6	Mushroom

*Polymer film thickness including the thickness of the SAM (2.5 ± 0.3 nm)

** s is calculated from $s=1/\sigma^{-1/2}$; tabulated values are mean ± std, n_{exp} =3.

Table 3.2: Parameters obtained by fitting forces between pSBMA brushes and mica to the Milner-Witten-Cates model (Eq. 3.1). The fitted values are mean ± SEM for atleast 10 force measurements on the same sample (n_{exp} =1).

$NaNO_3$ (mM)	Chain extension L_0 (nm)	Prefactor P_0 (mN/m)
10	43.9 ± 0.3	0.13 ± 0.02
100	66 ± 1	0.10 ± 0.06
1000	67 ± 1	0.21 ± 0.05

Table 3.3: Parameters obtained by fitting forces between pSBMA mushrooms and mica to the Dolan and Edwards model (Eq. 3.2). The fitted values are mean ± SEM for atleast 10 force measurements on the same sample (n_{exp} =1).

$NaNO_3$ (mM)	R_{eff} (nm)	Prefactor, A (mN/m)
10	7.1 ± 0.2	37 ± 2
100	11.8 ± 0.5	34.7 ± 0.5
1000	17 ± 1	35.4 ± 0.6

Table 3.4: Comparison of forces measured with a droplet confined between the disks versus submerged in solution between pSBMA mushrooms and mica. Parameters obtained from nonlinear least squares fits of measured force-distance curves to the Dolan and Edwards model (Eq. 3.2). The corresponding normalized force (F/R) vs. distance (D) data are given in Figure 3.5. The fitted values are mean ± SEM for atleast 10 force measurements on the same sample (n_{exp} =1).

Method of measurement	Total ionic strength (mM)	R_{eff} (nm)	Prefactor, A (mN/m)
Droplet measurements	54	7.0 ± 0.2	37 ± 2
	144	11.7 ± 0.3	34.7 ± 0.5
Substrates submerged in solution	54	7.1 ± 0.2	37 ± 2
	144	11.8 ± 0.5	34.7 ± 0.5

Table 3.5: Parameters obtained from nonlinear least squares fits of measured force-distance curves between pSBMA mushrooms and mica to the MWC model (Equation 3.1). Measurements were done with liquid droplets placed between the samples. The fitted values are mean ± SEM for atleast 10 force measurements on the same sample (n_{exp} =1).

Medium	Dry brush thickness, nm	Flory radius, R_F nm	Chain extension L_0 (nm)	Prefactor P_0 (mN/m)
54 mM $NaNO_3$	22.8 ± 0.4	9	89 ± 4	1.3 ± 0.1
10 mM $NaNO_3$ and 20 mM sodium phosphate buffer			87 ± 5	1.0 ± 0.5

CHAPTER 4: FORCES BETWEEN MICA AND END-GRAFTED STATISTICAL COPOLYMERS OF SULFOBETAINE AND OLIGOETHYLENE GLYCOL IN AQUEOUS ELECTROLYTE SOLUTIONS

This chapter is reproduced in part from the accepted journal article for publication: Ahmed, Syeda Tajin and Leckband, Deborah E. Forces Between Mica and End-grafted Statistical Copolymers of Sulfobetaine and Oligoethylene Glycol in Aqueous Electrolyte Solutions in Journal of Colloid and Interface Science in September 2021.

4.1 Introduction

In order to incorporate the beneficial properties of different monomers into a single material, there is increasing interest in developing chemically heterogeneous polymers for a range of applications, such as protein resistance,[245] protein stabilization,[246, 247] controlled drug release,[248] and reduced biofouling.[249] The most widely studied protein resistant and biocompatible materials are non-ionic poly(ethylene glycol) or PEG [250,251] and zwitterionic (ZI) polymers.[252, 253] Studies that compared the antifouling performance of each of the homopolymers reported similar outcomes for both polymer classes,[254] or, in some cases, moderately better performance by ZI polymers. [11, 255] PEG has long been considered the 'gold standard' of biocompatible, nonfouling materials.[251, 13, 14] Yet PEG-coated surfaces exhibit varying degrees of non-specific protein adsorption. [173,174, 258–261] The polymer oxidizes in biological media, [262, 263] and it produces toxic breakdown products.[264] In some instances, PEG reportedly reduced the activity of tethered proteins.[265] Conversely, PEG is used to increase the circulation time of drug carriers and protein therapeutics.[14, 25] PEG-based surface coatings bind unfolded proteins and appear to function as a

chaperone, by preventing aggregation and facilitating refolding.[15, 18, 19] PEG weakly binds proteins, presumably through interactions with nonpolar regions of the protein.[267, 17, 18, 27]

The limitations of PEG motivate the search for alternatives, and zwitterionic (ZI) polymers have shown promising results.[49] ZI polymers contain both positive and negative charged groups on each monomer. [26,101,109] They have been explored as smart, stimuli-responsive coatings [269] and colloid stabilizers,[29,30,270,271] or to prevent biofouling in ultrafiltration membranes [249] and marine coatings. [63] In many examples, they exhibit exceptional protein resistance and biocompatibility as biomedical materials. [272–274] However, studies also report protein adsorption. [27] Kisley et al. showed that zwitterionic poly(sulfobetaine) (pSB) in solution can bind and destabilize proteins.[28] Proteins also adsorb to end-grafted pSB thin films, but the adsorption can be tuned by the polymer coverage and ionic strength.[48] Taking advantage of the weak protein-segment interactions, polyzwitterions were also studied as potential protein stabilizers and chaperones. [39, 40]

Given the advantages and distinct but complementary properties of different homopolymers, such as PEG and pSB, one strategy has been to generate statistical AB copolymers of different monomers. The premise is that the resulting chemically heterogeneous material will reflect the composite properties of both monomers. Changing the chain composition is one strategy used to tune interfacial energies of polymer films.[150] Extensive studies documented the effect of chemical sequence on the efficacy of copolymers as 'chemical compatibilizers' between incompatible polymer blends, or between polymers and surfaces. [150, 157] Statistical copolymers more effectively compatibilize interfaces between incompatible homopolymers than diblock copolymers.[150] Theoretical studies also suggest that statistical copolymers compatibilize immiscible polymer blends, by maximizing energetically favorable contact between the favorable components while optimizing entropy by forming loops. [166]

In some applications, the monomers are mutually compatible, but other applications exploit segment-segment immiscibility and differences in solvent-segment interactions.[159, 158] For example, copolymers of zwitterionic (ZI) poly(sulfobetaine) (pSBMA) and non-ionic poly(N-isopropyl acrylamide) (PNIPAM) exploited the temperature-dependent phase behavior of the two components, at temperatures between the lower critical solution temperature of NIPAM segments (~32°C) and the upper critical solution temperature of the ZI component.[189] A statistical AB copolymer brush consisting of oligoethylene glycol methacrylate (OEGMA) and SBMA was designed to stabilize adsorbed proteins.[192] The authors reasoned that distributed SBMA monomers would interact with polar side chains on the protein to promote the native structure, while ethylene glycol monomers would interact with exposed hydrophobic groups to prevent aggregation and facilitate refolding. Consistent with this premise, the greatest protein stabilization was achieved at intermediate SBMA content. Copolymers of SBMA and OEGMA were also used to engineer non-fouling hydrogels for controlled protein release [275] and for skin regeneration.[276] The interfacial properties of these "chemically heterogeneous" coatings determine their performance in different applications, but how do the surface properties vary with copolymer composition? In the case of SBMA/OEG copolymers, the solubility, swelling and viscosity of poly(sulfobetaine) methacrylate (pSBMA) increase with increasing ionic strength, due to screening of electrostatic segment-segment interactions.[84,85,88,89,104,105,201,277] By contrast, the properties of ethylene oxide homopolymers are independent of the ionic strength.[133, 198] Protein adsorption on PEG coatings is similarly ionic strength independent, except when the underlying surface carries residual charge.[198]

This study used surface force apparatus measurements to determine how the interfacial properties of end-grafted random copolymers of SBMA and OEGMA vary with the mole% of SBMA in the

chains. Measurements quantified the molecular scale forces between end-grafted poly(SMBA-co-OEGMA) chains and mica, at low grafting density (weakly overlapping chains) and at high density (brushes). We also assessed the impact of the copolymer composition on the ionic strength dependence of the interfacial forces. Fits of the force measurements to different polymer models revealed a continuous variation in the interfacial forces, with increasing SBMA content. The ionic strength dependence of the forces similarly increased progressively with the SBMA content. The results suggest that OEGMA and SBMA behave as non interacting monomers that proportionally influence chain swelling and interfacial forces in electrolyte solutions.

4.2 Materials and methods

4.2.1 Chemicals

Monomer 2-(Methacryloyloxy) ethyl] dimethyl-(3- sulfopropyl) ammonium hydroxide (SBMA) (95%, MW 279.35) was purchased from Sigma- Aldrich (Product # 537284, St Louis, MO). Monomer oligoethylene glycol methacrylate (OEGMA, MW 500, containing 900 ppm monomethyl ether hydroquinone, MEHQ as inhibitor) was from Sigma-Aldrich (Product # 409529, St Louis, MO). Bis[2-(2'-bromoisobutyryloxy) undecyl]disulfide or the Br- terminated initiator (MW 704.70) was purchased from Sigma-Aldrich (Product # 733350, St Louis, MO). Ligand 1,1,4,7,10,10-Hexamethyltriethylenetetramine or HMTETA (97%, MW 230.39) was from Sigma-Aldrich (Product # 366404, St Louis, MO). Copper (I) bromide and Copper (II) Bromide (Product # 254185 and 221775, respectively) were purchased from Sigma-Aldrich (St Louis, MO). 11-Mercapto-1-undecanol or the OH- terminated thiol (97%, MW 204.37) was purchased from Sigma-Aldrich (Product # 447528, St Louis, MO). Ultrapure water (resistance 18.2 MΩ cm at 25 °C) was obtained using Synergy UV (Millipore Sigma) water purification system and pure

methanol was purchased from Thermo Fisher Scientific. Sodium phosphate (dibasic, anhydrous) was from Ward's Science (ON, Canada, Product # 470302-660).

4.2.2 Substrate Preparation for polymer Synthesis

Four different sizes of substrates were prepared for this study. The 1"x 1" Si wafer (University Wafer Inc., Product # 452) was used for ellipsometry. A 2 x 0.5 in Si wafer was used for ATR-FTIR. A 0.5 x 0.5 in Si wafer was used for XPS and (4) hemicylindrical silica discs of ~1 cm radius were used in SFA measurements. All substrates were initially rinsed with ethanol and water, and dried under a filtered N_2 stream. Then the substrates were assembled into the sample holder inside a thermal evaporator (Kurt J. Lesker Nano36 Thermal Evaporator System; Seitz Materials Research Laboratory, University of Illinois at Urbana-Champaign). The substrates were coated with an adhesion-promoting layer of 2 nm chromium, followed by a 55 nm film of gold under vacuum (5×10^{-6} Torr). The substrates were further treated with ozone plasma with Harrick Plasma Cleaner prior to formation of self-assembled monolayer (SAM). The treated surfaces were incubated in mixture prepared from stock solution: 3.4 mM ethanolic solution of initiator Bis[2-(2′-bromoisobutyryloxy) undecyl]disulfide (SAM-Br) and 5.87 mM ethanolic solution of 11-Mercapto-1-undecanol (SAM-OH) and the final mixture containing 100 and 20 mol% SAM-Br for synthesis of high and low grafting densities respectively. The substrates were incubated in the alkanethiol solutions for ≈8 h at 4 °C, after which the substrates were rinsed with absolute ethanol, and dried in a filtered N_2 stream.

4.2.3 Synthesis of SBMA-co-OEGMA copolymer

100% OEGMA (0% SBMA), 40% SBMA, and 80% SBMA were synthesized by atom transfer radical polymerization (ATRP). Briefly, the SAM-grafted substrates were sealed inside a custom-made, one-armed reaction vessel with rubber septum and connected to the Schlenk lines for

maintaining an inert environment. The substrates in the individual scintillation vials were degassed with three cycles of vacuum and Ar gas. In a round bottom flask, monomer [2-(Methacryloyloxy)ethyl]dimethyl-(3-sulfopropyl)ammonium hydroxide (SBMA) and monomer oligoethylene glycol methacrylate (OEGMA) were dissolved in 1:1 volumetric mixture of methanol and water to a final concentration of 0.2 M. Before synthesis, the inhibitor MEHQ in OEGMA monomer was removed by chromatography, using a column containing inhibitor-remover beads (Sigma-Aldrich, Product # 311332). Polymer brushes and weakly overlapping chains were synthesized from the initiator monolayer via surface ATRP using a 0:1, 1:1, and 3:1 molar feed ratios of SBMA to OEGMA. The monomer solution was degassed with a glass frit and kept under Ar gas (ultra-high purity grade) during the reaction. Then $CuBr_2$, ligand HMTETA, and CuBr were added to the flask at a final concentration of 16.79, 46, and 0.56 mM in this order. When the reactants are well mixed, the mixture was transferred into the reaction vessel by a glass syringe. The reaction proceeded in room temperature under Ar atmosphere for 1 hr for brush synthesis and for 15 min, for weakly overlapping chain synthesis. After that, the reaction was terminated by removing substrates from the solution and rinsing them with a 1:1 mixture of methanol and water, followed by several washes with 20 mM sodium phosphate buffer. Finally, the substrates were dried under a nitrogen stream and stored under vacuum before use. Prior to use, all glassware was cleaned for at least 2 h in a base bath, which consists of 500 g of potassium hydroxide dissolved in 1 L water and then mixed in ~8 L of isopropanol in a Nalgene container (Thermo Scientific Nalgene™ Heavy-Duty Rectangular Tank with Cover, LLDPE, 32 Gallon, Item #: T9FB2224702).

4.2.4 Attenuated Total Reflectance-Fourier Transfer Infrared Spectroscopy (ATR-FTIR) for determination of % SBMA content in copolymer

We used a Nicolet 6700 FTIR (Thermo Fisher) with 1 cm^{-1} resolution infrared spectra (1000 scans) to determine the composition of the end-grafted polymers. Peaks corresponding to the polymer backbone (C=O stretching, centered at 1730 cm^{-1}), OEGMA (C-O stretching, centered at 1083 cm^{-1}), and SBMA (SO_3^- symmetric stretching, centered at 1041 cm^{-1}) were integrated, and the peak areas are given in Table 4.5. Represented spectra are in Figure 4.9. The peak area of each monomer was divided by the peak area of the backbone C=O stretch. Because the extinction coefficients of the peaks at 1083 cm^{-1} and 1041 cm^{-1} differ, the normalized values corresponding to 100% OEG and 100% SBMA homopolymers were used as references. With these values, the mole percentages of each monomer in the copolymer brushes were calculated to be 0, 40 and 80% SBMA.

4.2.5 Initiator grafting density and % SBMA content determination by X-Ray Photoelectron Spectroscopy

The density of Br-terminated alkanethiols was determined by X-ray photoelectron spectroscopy (XPS, Kratos AxisULTRA spectrometer) from the Br 3p/S 2s ratios. The excitation source was the monochromatic Al K α radiation at 1486.6 eV (225 W, 40 eV pass energy). The samples were loaded on a rectangular metal support, using double-sided adhesive tape, and analyzed at a pressure of 10^{-9} Torr. The C 1 s hydrocarbon peak at 285.0 eV was used as the reference peak to measure the binding energy. Surface chemical compositions were determined from the integrated peak areas of N 1s and S 2p in the XPS spectra, using CasaXPS software (Version 2.3 19PR1.0). By assuming the maximum packing density of 2.1 bromine initiator/nm^2 [210] and a 10% conversion efficiency reported for polystyrene,[217] the grafting density was estimated for substrates that were incubated in 100 and 20 mol% Br-terminated thiol initiator prior synthesis.

4.2.6 Film thickness determinations by Ellipsometry

The thickness of the dried films was measured using a Variable Angle Spectroscopic Ellipsometer (J.A. Woollam VASE). Scans were acquired at three different spots on each sample, at three different angles of incidence (65°, 70°, and 75°). The scanned wavelength range was 300–900 nm. The bare, gold-coated Si wafer and 100 and 20 mol% SAM-Br monolayers on gold-coated Si wafers were used as references. The resulting curves were fit to a multilayer model consisting of bulk silicon of default thickness of 1 mm, 2 nm silicon oxide layer, 2 nm Cr, 2 nm Au metal layer, and a Cauchy dispersion layer. The thiol and polymer layers were fit to quantify the polymer film thickness. For the Cauchy dispersion layer, a refractive index of 1.46 was used for the organic layer. [212]

4.2.7 Surface force measurements

A Mark-II surface force apparatus (SFA) was used to measure forces between the end-grafted polymer films and mica as a function of the sample separation distance. Samples were immersed in phosphate buffer at pH 7 to maintain physiologically relevant pH with added 10, 100 and 1000 mM $NaNO_3$ i.e. a total ionic strength of 54, 144 and 1044 mM respectively. The solutions were prepared with ultrapure water, filtered twice through a surfactant free 0.2 μm Durapore membrane (Millipore Sigma), and stored in clean glass flasks at room temperature.

Before the measurements, the two hemicylindrical silica discs with the mica and polymer sample were installed in a cross-cylindrical geometry inside the SFA chamber. The distance between the surfaces are determined by interferometry, using the fringes of equal chromatic order (FECO). A DC regulated power supply (Newport / Oriel 68735) sends collimated white light (tungsten-halogen lamp, 120 watt) normally through the opposing samples. The image the FECO is acquired by focusing the transmitted light onto a microscope objective lens and directing the light onto the

entrance slit of an Ebert spectrometer. The images are recorded using an Andor Zyla 5.5 sCMOS camera (Oxford Instruments) with an exposure time of 0.3 seconds. A mercury arc lamp (Oriel Instruments, 50 Hz, 4 Amps, model #5047) was used to calibrate the measured wavelengths projected onto the focal plane of spectrometer.

Force-distance measurements were conducted with a liquid droplet injected between the surfaces. A droplet of the filtered solution was introduced between the two opposing disks with a clean, glass syringe (20 µl Microliter Syringe, Hamilton Co., Nevada). To prevent evaporation of the droplet, a boat containing approximately 3 ml of ultrapure water was placed inside the chamber. All measurements were performed in a temperature-controlled dark room at 21^{o}C. The SFA setup was installed on a vibration-isolation table.

Forces were measured between the mica and polymer thin films in buffered solutions in quasi-static mode. The assembled samples comprising the grafted copolymer films on alkanethiol monolayers (1) and mica in aqueous solution (2) corresponded to a 2 layer asymmetrical interferometer. The corresponding equations used to determine separation distances based on the FECO are described elsewhere. [55, 71] The surface roughness of the evaporated gold film limits distance resolution to ~1 nm. In these measurements, D=0 corresponds to contact between the surface of the alkanethiol monolayer and mica. This was established, by measuring the wavelengths of the FECO when the gold coated silica discs with self-assembled thiol monolayers were in contact with the mica surface in air, prior to the polymer synthesis. The measured forces as a function of the separation distance, D are normalized by the geometric average radius of curvature of the crossed hemicylinders, F/R with a resolution is ~0.001 mN/m. For statistics, multiple replicate force-distance curves were measured at each of at least 5 different clean, asperity free regions on the samples, to establish statistical significance.

4.3 Results

4.3.1 Characterization of end-grafted statistical Poly(SBMA-co-PEGMA) copolymers on gold coated silica surfaces

XPS measurements assessed the ratio of Br 3p (initiator) to S 2p (total thiol), determined the initiator density. The Br/S ratio in a 100% initiator terminated self-assembled monolayers (SAM) was 0.92, and in monolayers used to graft dilute polymer chains, the average Br/S ratio was 0.17. The maximum packing density of a 100% Br-terminated SAM is 2.1 chains/nm^2, so the initiator density on the mixed SAMs is 0.4 chains/nm^2. XPS also confirmed polymer grafting from the SAMs. The N 1s peak of XPS spectra confirmed the presence of SBMA in chains on the substrates. The latter peak was absent in PEG homopolymer films (Figure 4.8).

The polymer composition was determined, by ATR-FTIR, using the integrated peak areas for the polymer backbone, OEG, and SO_3^{-1} groups (Table 4.5). Representative spectra are shown in Figure 4.9. The peak area of each monomer was normalized by the peak area for the backbone C=O stretching vibration. Because the extinction coefficients of the peaks at 1083 cm^{-1} and 1041 cm^{-1} differ, the normalized values corresponding to 100% OEG and 100% SBMA homopolymers were used as references. With this information, the mole percentages of each monomer in the copolymer brushes were calculated to be 0, 40 and 80% SBMA (Tables 4.5 and 4.6).

The grafting densities, σ (chains/nm^2) of the copolymers were estimated as follows. Using the maximum packing of initiator-terminated monolayers (2.1 chains/nm^2) [210] and assuming a 10% chain initiation efficiency [217], the estimated grafting densities of the polymers were are 0.21 and 0.04 chains/nm^2 for high and low density polymers. The distance between the grafted chains were determined by using the equation, $s=1/\sigma^{-1/2}$. The corresponding distance between the chains, s is 2.2 nm and 5 nm for brush and weakly overlapping chains, respectively (Tables 4.1 and 4.2).

The thicknesses of the polymer films determined from ellipsometry were 30 ± 4 nm, 23 ± 1 and 24 ± 1 nm for brushes with 0, 40 and 80% SBMA content. The thicknesses of dilute chains were 7.0 ± 0.5, 5.9 ± 0.4 and 6.0 ± 0.7 nm with 0, 40% and 80% SBMA, respectively (n=3). The measured thickness of pure Br or OH-terminated self-assembled monolayers (SAMs) were 2.5 ± 0.3 nm and 2.3 ± 0.2 nm (n=5), respectively.

The molecular weights of the polymers were then calculated using the estimated chain density of 0.21 chains/nm^2 for copolymer brushes and 0.04 chains/nm^2 for high and low density copolymer chains, the weighted density of dry monomer, the measured dry polymer thickness, and the equation, $M_n = (h\rho N_A/ \sigma) \times 10^{-21}$.[233] Here, M_n is the molecular weight of polymer (Da or gm/mole) and h is the dry film thickness (nm). Here, ρ is the dry monomer density. The SBMA monomer density is 1.395 gm/cm^3,[218] and the dry PEGMA monomer density is 1.101 gm/cm^3. The fractional average of the copolymer was used to determine the molecular weight of the copolymers. N_A is Avogadro's number and σ is the chain density (chains/nm^2). The calculated molecular weights were 110 ± 10, 72 ± 4 and 84 ± 4 KDa for brushes with, respectively, 0, 40%, or 80% SBMA (Table 4.1). The molecular weights of weakly overlapping chains were 66 ± 9, 56 ± 4 and 58 ± 7 KDa with, respectively, 0, 40%, or 80% SBMA (Table 4.2). The corresponding polymer volume in good solvent is determined by the Flory radius, $R_F = l \times N^{3/5}$ where l is the monomer length (≈ 0.3 nm) and N is the degree of polymerization.[234] The degree of polymerization, N was determined from the ratio of the polymer to monomer molecular weights (i.e. $N=\frac{M_n}{M_m}$). Here, the molecular weight of SBMA, M_m= SBMA is 279.35 gm/mol and PEGMA is 500 gm/mol. Average monomer molecular weights were used for the copolymers. We report the results in terms of the scaled parameter, $s/2R_F$ which is ~ 0.1 for brushes and ~0.4 for weakly overlapping chains. The thus determined molecular weights are in Table 4.1 and 4.2. Additionally,

static water contact angle of dried, end-grafted polymer films were measured with Rame-Hart goniometer using ultrapure water at 21^{o}C, shown in Figure 4.10. Here, the contact angles measured with both weakly overlapping and densely grafted chains decreased in proportion to the %SBMA content. The large deviation between brushes and weakly overlapping chains is presumably due to the greater exposure of the underlying alkanethiol monolayers with the more dilute polymers.

4.3.2 Forces between grafted chains and mica at different monovalent salt concentrations

The sample configuration in the Surface Force Apparatus (SFA) is shown in Figure 4.1. It consists of end-grafted polymer thin films on alkanethiols and an opposing, back silvered mica sheet. Samples are bathed in 20 mM sodium phosphate buffer, at pH 7. The solutions contained 10, 100 or 1000 mM $NaNO_3$ with a total ionic strength of 54, 144 and 1044 mM respectively. Here the force was measured as a function of separation distance, D, where D=0 is defined as contact between the self-assembled monolayer (SAM) and mica in air. The samples were bathed in solution, by placing a droplet of buffer between the opposing disks. The data shown in Figure 4.2-4.7 are representative force-distance curves measured at atleast 3 clean, asperity-free contacts on the same samples, number of force measurements=10, and one independent experimental replicate.

4.3.2.1 Forces between brushes and mica in electrolyte solutions

The force-distance profiles were measured between bare mica and high density, grafted brushes with different relative amounts of sulfobetaine and ethylene glycol. Measurements in buffered solutions containing different $NaNO_3$ concentrations are shown in Figures 4.2, 4.3 and 4.4. At all ionic strengths, the force-distance profiles are purely repulsive, but the range and the magnitude of the repulsion depended on both the ionic strength and on the % SBMA present in the brush. Figure 4.2 shows the force, normalized by the geometric average radius, F/R as a function of the separation distance between mica and the alkanethiol substrate, for a 100% PEG brush at total

ionic strength of 54, 144 and 1044 mM. For 100% PEG brushes the onset of repulsion occurs at ~50 nm and increases monotonically with decreasing separation.

For 40% poly(SBMA-co-OEGMA) brush, both the distance of the onset of the repulsion and the amplitude of the force increase with the increasing salt concentration (Figure 4.3). At 54 mM ionic strength, the onset of repulsion is at ~70 nm, but the range increases to ~150 nm at higher ionic strengths. The amplitude of the force at separations greater than ~50 nm increases with increasing ionic strength. For example, at D=75 nm, F/R is 0.01, 0.5 and 2 mN/m in in 54, 144 and 1044 mM ionic strength of solutions, respectively.

The forces measured with the 80% poly(SBMA-co-PEGMA) brush show a qualitatively similar trend as described for the 40% brush. The onset of repulsion is measured at approximately 70, 150 and 160 nm, in total ionic strength of 54 mM, 144 and 1044 mM, respectively (Figure 4.4). Moreover, the repulsive forces at separation distance larger than ~50 nm, also increase with increasing ionic strength.

The force-distance profiles between the brushes and mica at the different ionic strengths were compared quantitatively by fitting the data to the Millner-Witten-Cates model (MWC). Here, we performed a global fit of all force-distance measurements obtained with a single sample bathed in the same solution. The Milner-Witten-Cates model (MWC) [235] predicts the interaction energy between end-grafted chains in good solvent as a function of the distance between the grafting surfaces. The distance-dependent free energy between two surfaces with end-grafted chains in good solvent is given by:

$$\frac{F(D)}{R} = -4\pi P_0 \left[\left(\frac{2L_0}{D}\right) + \left(\frac{D}{2L_o}\right)^2 - \frac{1}{5}\left(\frac{D}{2L_o}\right)^5 - \frac{9}{5}\right]$$

where, D is the distance between the grafting substrates, L_0 is the equilibrium brush extension, and P_0 scales the amplitude of the normalized force, F/R. To adapt this equation for our asymmetric

system (grafted brush and bare mica surfaces), $2L_o$ is replaced by L_o, as described previously.[200, 132]

$$\frac{F(D)}{R} = -4\pi P_0 \left[\left(\frac{L_0}{D}\right) + \left(\frac{D}{L_o}\right)^2 - \frac{1}{5}\left(\frac{D}{L_o}\right)^5 - \frac{9}{5}\right] \quad \text{(Equation 4.1)}$$

When fitting the data to Equation 4.1, using non-linear least squares analysis, both P_0 and L_0 were allowed to vary. The best fit parameters are reported in Table 4.3.

The best fit equilibrium chain extension, L_0 did not change significantly with the ionic strength for 100% PEG brushes (paired t test, $p>0.05$, number of force measurements=17 at 54 mM, 21 at 144 mM and 10 at 1044 mM). The best fit values of the prefactor, P_0 were also statistically similar at the different salt concentrations (t test, $p>0.05$, number of force measurements=17 at 54 mM, 21 at 144 mM and 10 at 1044 mM). This behavior is similar to prior reports of force measurements of end-grafted PEG.[133] The results are summarized in Table 4.3.

With 40 and 80% poly(SBMA-co-OEGMA) brushes, the fitted L_o values increased significantly (number of minimum force measurements=10, $p<0.05$), when the ionic strength increased from 54 mM to 1044 mM (Table 4.3). The magnitude of the change depended on the SBMA content in the polymer. With 40% SBMA brushes, the chain extension increased from 78 ± 3 nm to 162 ± 3 nm, when the ionic strength increased from 54 mM to 1044 mM. However, at 80% SBMA, the fitted chain extension increased from 91 ± 8 nm in 54 mM to 200 ± 10 nm in 1044 mM ionic strength of solution. The chain extension was more sensitive to added salt at the lower concentrations (10-100 mM), with the relative change decreasing at salt concentrations between 100 mM and 1 M $NaNO_3$ salt.

The influence of SBMA content and interactions with ions on the polymer extension is apparent when comparing the fitted values of L_0 with the theoretically predicted values, based on the Flory radius[278] and distance between grafting sites: $L_{Th} \sim R_F (R_F/s)^{2/3}$ (Table 4.7). For 100% PEG

brushes, the theoretical chain extension, L_{Th} is approximately 20 nm for R_F ~ 6 nm. The ranges of interaction here is ~50 nm, which is similar to the fitted equilibrium chain extension derived from MWC theory, L_0. This observation is similar to a previously reported study. [198] The deviation from the theoretical extension for the polyethylene polymer is probably due to uncertainty in using 10% chain efficiency for estimating grafting density of chains, that was reported for polystyrenes. The ratio L_0/L_{Th} for the copolymer increases monotonically with increasing SBMA content, at any given ionic strength (Table 4.7). This behavior reveals the increasing influence of the polar monomer interactions with ions. Increasing concentration of ions would presumably increase the osmotic pressure in the brush and increase chain swelling. These observations indicate that the interfacial properties can be tuned by simple variation of the ratios of these two monomers.

Comparisons of the fitted prefactors reveal that the repulsion measured with the copolymers depends on the ionic strength, but the sensitivity to changes in ionic strength depends on the SBMA content. With PEG homopolymer brushes, the prefactor is statistically similar at all ionic strengths ($p>0.05$, number of force measurements=17 at 54 mM, 21 at 144 mM and 10 at 1044 mM). With 40% SBMA copolymer, the prefactors exceed that of the PEG homopolymer brushes and exhibit a moderate dependence on ionic strength. The values were 0.24 ± 0.04 mN/m, 0.20 ± 0.02 mN/m, and 0.31 ± 0.02 mN/m at ionic strengths of, respectively, 54 mM, 144 mM, and 1044 mM (number of force measurements =17 at 54 mM, 14 at 144 mM and 21 at 1044 mM). However, with 80% SBMA brushes, the prefactor depended strongly on the ionic strength, with values of 0.20 ± 0.05 mN/m, 0.5 ± 1 mN/m, and 0.6 ± 0.1 mN/m at the respective ionic strengths of 54 mM, 144 mM, and 1044 mM (number of force measurements =10 at 54 mM, 11 at 144 mM and 10 at 1044 mM). Thus, the ionic strength-dependence of both the range and magnitude of the forces increases in proportion to the SBMA content.

It is important to note that, in all cases, the force curves did not exhibit any behavior indicative of structural changes in the layers that might arise from demixing, for example, at lower ionic strength where the SBMA segments are less soluble. The range and magnitude of the long-ranged repulsive forces increased monotonically with the SBMA content.

4.3.2.2 Forces between weakly overlapping copolymer chains and mica

Forces between dilute end-grafted copolymer chains ($s/2R_F$ ~ 0.4, MW ~ 150 KDa, σ ~0.04 chains/nm^2) and mica were similarly measured in buffered solutions containing different $NaNO_3$ concentrations. Figures 4.5, 4.6 and 4.7 show the semi-log plot of the normalized force (F/R) between dilute, grafted pSBMA chains and mica versus the separation distance, D. Forces were similarly measured in 20 mM phosphate buffered solutions containing 10 mM, 100 mM, or 1 M $NaNO_3$ with a total ionic strength of 54, 144 and 1044 mM respectively.

There are qualitative and quantitative differences between the force curves, which were determined with different copolymers and at different ionic strengths. The forces measured with 100% PEG homopolymers were independent of the salt concentration, within experimental error. The forces exceed ~0.1 mN/m at D <20 nm, and the normalized force increases exponentially (Figure 4.5). At higher ionic strength, the range of the repulsion increases slightly, but the range of the exponential decay is similar ($p>0.05$, number of force measurements=10). The forces between poly(SBMA-co-OEGMA) polymers and mica similarly decay exponentially, but the decay lengths vary with both the SMBA content and the salt concentration. With 40% SBMA copolymers in 54 mM (number of force measurements=14), the onset of repulsion is ~75 nm, but the range increases to ~150 nm in 144 mM (number of force measurements=14) and ~200 nm in 1044 mM (number of force measurements=15) given in Figure 4.6. Similarly for 80% SBMA copolymers in 54 mM, the onset of repulsion is ~150 nm (number of force measurements=12), but the range of repulsion

increases to ~200 nm in 144 mM (number of force measurements=18) and ~250 nm in 1044 mM (number of force measurements=14) ionic strength of medium shown in Figure 4.7.

The force profiles were compared quantitatively, by fitting the data to the Dolan and Edwards model (D&E),[279] which describes the forces between sparse, end-grafted chains in good solvent:

$$\frac{F(D)}{R} \approx Ae^{-\frac{D}{Rg}} \qquad \text{(Equation 4.2)}$$

Here, the prefactor, $A \approx \frac{72\pi KT}{\Gamma}$, where Γ is the area per chain, K is the Boltzmann constant and T is absolute temperature. The model predicts that the force decays exponentially with a length given by the radius of gyration, R_g for simple chains in good solvent. However, with copolymer chains containing zwitterionic SBMA, the solvent quality and chain swelling depend on the ionic strength. We therefore refer to the decay constant as an "effective R_g", or R_{eff}. The prefactor and R_{eff} were estimated from nonlinear least squares fits of the data to Equation 4.2and the best fit parameters are summarized in Table 4.4.

The fitted decay length, R_{eff} of dilute PEG homopolymers is ~10 nm and does not change significantly with the ionic strength. This is approximately 2 times of Flory radius of 6 nm, which was calculated using the estimated polymer molecular weight. The fitted prefactors are also independent of the salt concentration, within experimental error ($p>0.05$, number of force measurements=10).

For the copolymers, the fitted decay lengths, R_{eff} increase with SBMA content. In these measurements, R_{eff} for each copolymer was determined with the identical sample, but the buffer was exchanged to alter the ionic strength. At an ionic strength of 54 mM, the decay lengths of 100% PEG, 40% SBMA, and 80% SBMA polymers were, respectively, 10 ± 3 nm, 16.6 ± 0.5 nm, and 20 ± 1 nm (Table 4.4). However, the decay lengths of the copolymers increased with ionic strength, and the increases were greatest for the 80% SBMA copolymers. With 40% SBMA at

ionic strengths of 54 mM, 144 mM, and 1044 mM, the fitted values are 16.6 ± 0.5 nm, 27.2 ± 0.8 nm, and 27 ± 1 nm. These values are approximately 2.7 and 4.5 times the estimated Flory radius, $R_F \approx 6$ nm. The ratio of R_{eff}/R_F are given in Table 4.8. There was no statistically significant change R_{eff}, between ionic strengths of 144 mM and 1044 mM (Student's t test, $p>0.05$, number of force measurements=15). With 80% SBMA weakly overlapping chains, changes in R_{eff} with ionic strength were much greater. Fitted values were 20 ± 1 nm, 31.9 ± 0.7 nm, and 41 ± 2 nm, at ionic strengths of 54 mM, 144 mM, and 1044 mM, respectively. These values are approximately 2.8, 4.5 and 5.8 times the estimated Flory radius of 7 nm. Interestingly, chains with greater SBMA content continue to expand at $NaNO_3$ concentrations above 100 mM, whereas salt-dependent swelling by copolymers with 40% SBMA content appears to asymptote at lower ionic strengths. The R_{eff}/R_F increases only moderately for 80% SBMA in copolymer at high ionic strength of 1044 mM.

The increase in R_{eff} with increasing ionic strength and SBMA content parallels the increase in brush extension. In contrast to the brushes, the prefactors, which scale the amplitude of the normalized force are relatively insensitive to increases in ionic strength. Additionally, the separation distances beyond which the data deviate from Equation 4.2 are ionic strength dependent. At ionic strengths of 54 mM, 144 mM, and 1044 mM, forces measured with 40% copolymer deviate from the exponential curve at ~ 60, 100, and 200 nm in, respectively (Figure 4.6). With 80% SBMA chains, the deviations are at ~125, 210 and 240 nm, respectively (Figure 4.7).

4.4 Discussion

The major finding of this study is that the interfacial properties of grafted statistical poly(SBMA-co-OEGMA) copolymers change smoothly in proportion to increasing zwitterionic SBMA content. This apparent in both the force measurements and in the static water contact angle measurements. The OEGMA and SBMA segments thus appear to behave as compatible monomers that proportionally contribute to the magnitude and range of repulsive interfacial barriers. The SBMA content of the chains affects the film thickness, and it increases the impact of ionic strength on both the film thickness and repulsive forces.

At high grafting density, MWC theory describes the force profiles measured with both PEG homopolymer and copolymer brushes. pSBMA homopolymers behave similarly.[280] However, the fitted parameters P_0 and L_0 both depend on the ionic strength, and thus reflect the electrostatic SBMA interactions. With poly(sulfobetaine) homopolymer brushes, ionic strength-dependent changes in both fitted parameters were attributed to screened electrostatic segment-segment interactions and to excess ions in the brush.[280].

The influence of SBMA content and ionic strength on the brush extension is apparent when comparing the fitted values of L_0 with the theoretically predicted values, $L_{Th} \sim R_F (R_F/s)^{2/3}$ (Table 4.7) [278]. For all polymers and ionic strengths considered, $L_0/L_{Theor} > 1$. This is expected because water is a good solvent for PEG, and the lowest ionic strength of 54 mM is near the theta salt concentration of 74 mM for pSBMA homopolymers.[241]

The ratio L_0/L_{Th} for the copolymer increases in proportion to the SBMA content, at any given ionic strength (Table 4.7). This behavior reveals the increasing influence of the charged monomer and ion interactions. Increased sensitivity to ionic strength with SBMA content also affects the L_0/L_{Th} values. Ions screen electrostatic segment-segment interactions and promote chain swelling. Hence,

the 80% SBMA copolymers exhibited the greatest ionic strength dependent changes in L_0/L_{Th}. These proportional changes in both the brush thickness and compressibility with SBMA content reveals that the molecular scale interfacial properties can be tuned continuously, by simple variation of SBMA/OEGMA ratios.

The prefactors determined from data fits to the MWC model increased systematically with ionic strength, but the SBMA content altered the magnitudes of the changes. With PEG homopolymers, increasing the ionic strength from 54 mM to 1044 mM had no effect on P_0. However, with copolymers, P_0 increased modestly with 40% SBMA and tripled with 80% SBMA, over the same range of ionic strengths. The behavior is qualitatively similar to poly(sulfobetaine) homopolymer brushes and is attributed to both electrostatic screening of segment interactions and excess ions in the brush.[280] These trends in the fitted parameters indicate that SBMA and OEGMA do not segregate under conditions studied, but contribute proportionally to the interfacial properties. The force measurements also did not exhibit any features indicative of structural changes that might arise from monomer segregation.

With weakly overlapping chains, the force profiles are well described by the Dolan and Edwards theory (Equation 4.2). This model also does not account for electrostatic segment-segment interactions. However, the determined decay constant R_{eff} increased with SBMA content, at any single ionic strength (Table 4.4). At the ionic strength of 1044mM, the ratio R_{eff}/R_F was 1.8, 4.5 and 5.8 for copolymers with 0, 40 and 80% SBMA, respectively (Table 4.8).

As with brushes, the SBMA content sensitizes the ratio R_{eff}/R_F to the ionic strength. With PEG homopolymer, R_{eff}/R_F is ionic strength independent. However, with 40% and 80% SBMA copolymers, R_{eff}/R_F determined at μ = 1044 mM increased by ~67% and ~100%, respectively, relative to measurements at μ = 54 mM. Despite the changes in R_{eff} with ionic strength, the

prefactors did not change significantly, with any of the copolymers. This agrees with the model (Equation 4.2), which predicts that the amplitude of the force depends on the temperature and grafting density.

The deviation of the force curves from the model at large distances is most likely due to chain polydispersity. Interestingly, the range of exponential decay and distances over which the data agrees with the model increases at higher ionic strengths. We postulate that the latter behavior is due to increased chain solubility and swelling.

In prior studies of dilute PEG chains, the decay constant determined from fits to the Dolan and Edwards model was statistically similar to R_F, such that $R_{eff}/R_F \sim 1$. In the latter case, the average grafting density and the polymer molecular weight were known. Here, we attribute the slightly higher value ($R_{eff}/R_F > 1$) to uncertainty in the estimation of the grafting density. This uncertainty would also affect the L_0/L_{Th} values. Although error in the grafting density will affect the absolute values of the fitted parameters, it will not alter the data trends.

4.5 Conclusion

The main findings of this study is that end grafted random copolymers consisting of OEGMA/SBMA which are two chemical structurally different but non-interacting and compatible components behave independently and proportionally affect the swelling behavior at varying ionic strength of the surrounding medium. The osmotic repulsion barrier i.e. interfacial forces of copolymers can be tuned at varying grafting densities, relative amount of zwitterionic content and ionic strength of solutions, which have potential applications as 'chemical compatibilizers'. A popular means of modification of interfacial properties involving grafting polymers on surfaces or using compatibilizers for polymer-polymer interfaces to mediate the interfacial energies.[157] Here,

poly(SBMA-co-OEGMA) having good biocompatibility and non-interacting properties can be used for tuning interfacial energies between two surfaces. The ability to tune the osmotic repulsion barrier also have important implications for use as biomaterials for protein drug delivery, which rely on differential interactions between protein and the SBMA and OEGMA monomers.[281] Here the lateral or vertical phase segregation of random copolymer made of SBMA/OEGMA has not been investigated for poor solvent condition for sulfobetaine monomers which merits further investigation in future.

4.6 Figures and tables

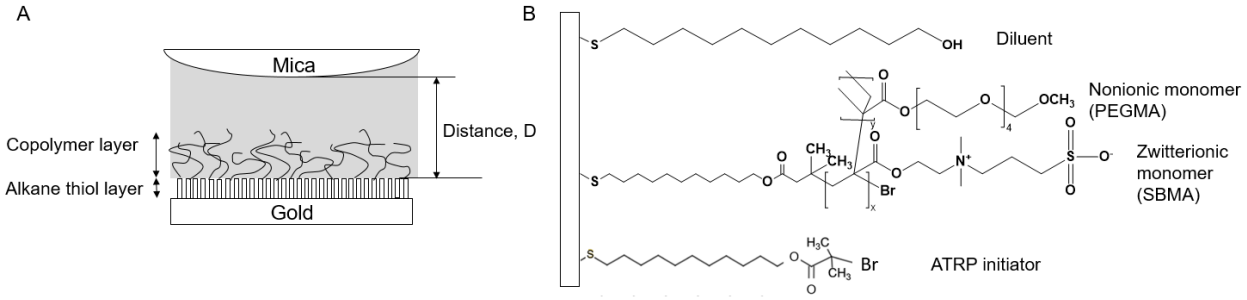

Figure 4.1: Surface Force Apparatus sample configuration. (A) Forces are measured between poly(SBMA-co-PEGMA) chains grafted from alkanethiol monolayers on gold substrates and mica surfaces in aqueous solutions of 20 mM sodium phosphate (pH=7.0) containing different $NaNO_3$ salt concentrations. (B) Chemical structure of grafted copolymer chains on gold-coated substrates. The OH-terminated thiols are diluents to control the initiator-terminated thiol densities and resulting polymer grafting densities. The Br-terminated thiols are the ATRP initiators.

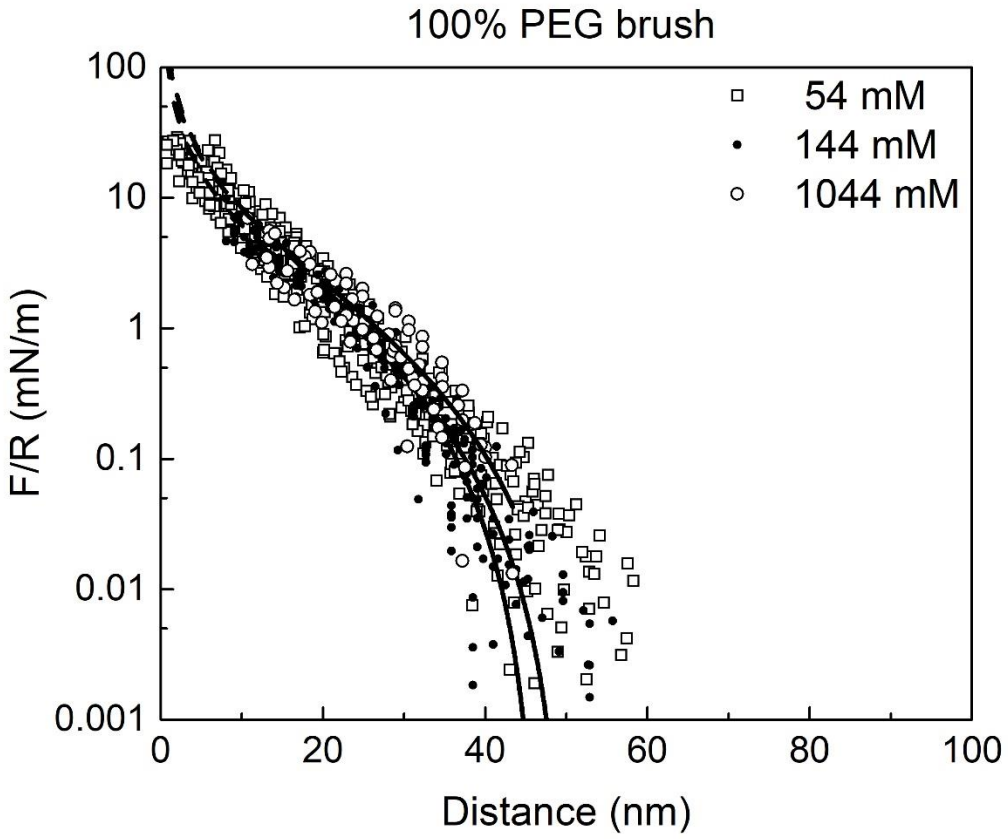

Figure 4.2: Normalized force, F/R (mN/m) between mica and grafted PEG homopolymer brushes ($s/2R_F \approx 0.1$) versus the separation distance. Samples were bathed in aqueous solutions of 20 mM sodium phosphate at pH=7.0 with $NaNO_3$. The solution ionic strengths were 54 mM (white squares, $N_{meas} = 17$, $n_{exp} = 1$), 144 mM (black circles, $N_{meas} = 21$, $n_{exp} = 1$) and 1044 mM (white circles, $N_{meas} = 10$, $n_{exp} = 1$). The solid lines are nonlinear least squares fits of the data to the MWC model (Equation 4.1) with the best-fit parameters summarized in Table 4.3. The dashed lines show the regime where the measured forces are not described by theory.

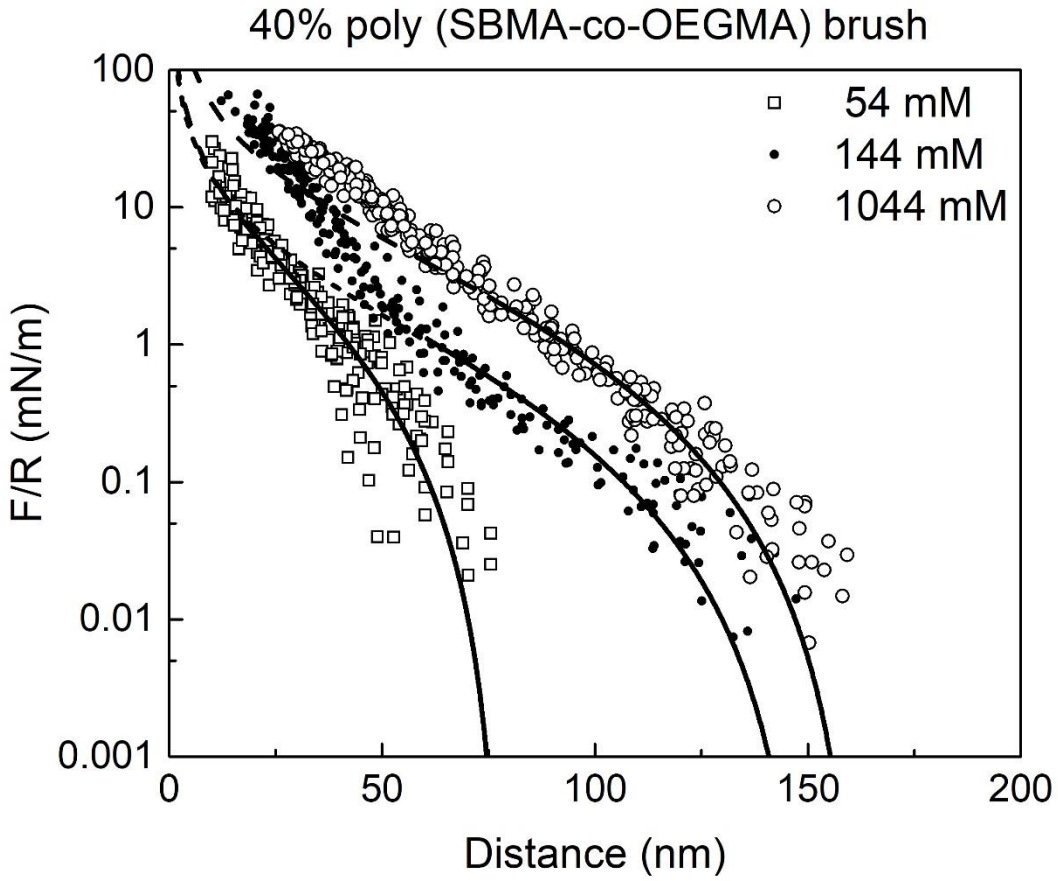

Figure 4.3: Normalized force, F/R (mN/m) between mica and grafted 40% SBMA copolymer brushes ($s/2R_F \approx 0.1$) versus the separation distance. Samples were bathed in aqueous solutions of 20 mM sodium phosphate at pH=7.0 with $NaNO_3$. The solution ionic strengths were 54 mM (white squares, $N_{meas} = 17$, $n_{exp} = 1$), 144 mM (black circle, $N_{meas} = 14$, $n_{exp} = 1$) and 1044 mM (white circles, $N_{meas} = 21$, $n_{exp} = 1$). The solid lines are nonlinear least squares fits of the data to the MWC model (Equation 4.1) with the best-fit parameters summarized in Table 4.3. The dashed lines show the regime where the measured forces are not described by theory.

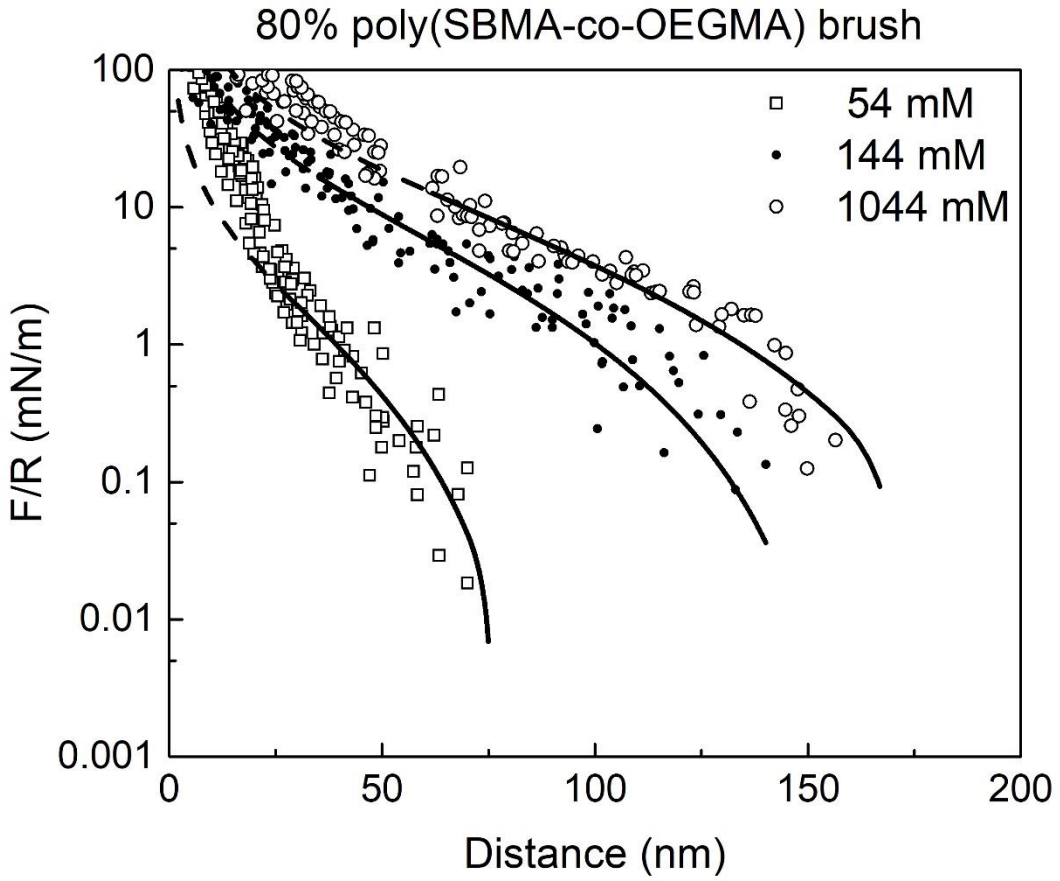

Figure 4.4: Normalized force, F/R (mN/m) between mica and grafted 80% SBMA copolymer brushes ($s/2R_F \approx 0.1$) versus the separation distance. Samples were bathed in aqueous solutions of 20 mM sodium phosphate at pH=7.0 with $NaNO_3$. The solution ionic strengths were 54 mM (white squares, $N_{meas} = 10$, $n_{exp} = 1$), 144 mM (black circle, $N_{meas} = 11$, $n_{exp} = 1$) and 1044 mM (white circles, $N_{meas} = 10$, $n_{exp} = 1$). The solid lines are nonlinear least squares fits of the data to the MWC model (Equation 4.1) with the best-fit parameters summarized in Table 4.3. The dashed lines show the regime where the measured forces are not described by theory.

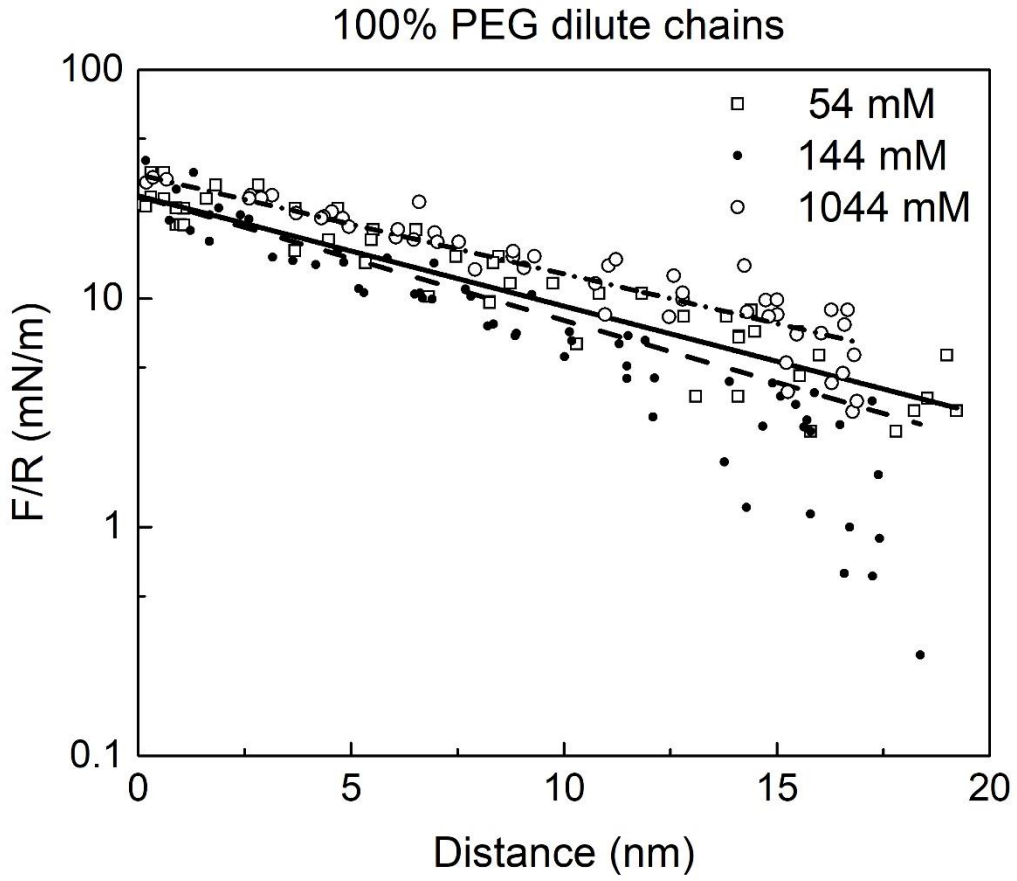

Figure 4.5: Normalized force, F/R (mN/m) between mica and grafted PEG homopolymer dilute chains ($s/2R_F \approx 0.4$) versus the separation distance. Samples were bathed in aqueous solutions of 20 mM sodium phosphate at pH=7.0 with $NaNO_3$. The solution ionic strengths were 54 mM (white square, N_{meas} =10, n_{exp} = 1), 144 mM (black circle, N_{meas} =10, n_{exp} = 1) and 1044 mM (white circles, N_{meas} =10, n_{exp} = 1). The solid lines are the fit of the D&E model (Equation 4.2). From a fit to the data, we estimated the coil size or effective radius of gyration, R_{eff} and prefactor, A for the grafted non-overlapping chains at respective salt concentrations (Table 4.4).

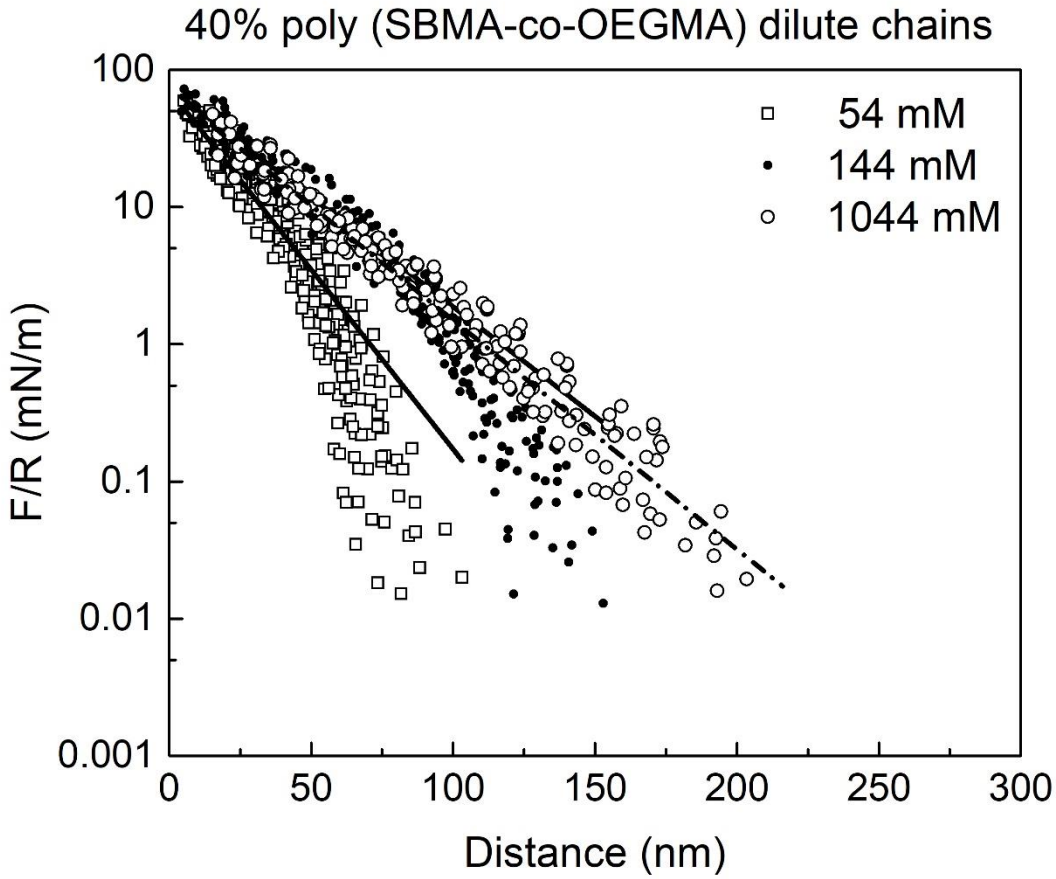

Figure 4.6: Normalized force, F/R (mN/m) between mica and grafted 40% SBMA copolymer dilute chains ($s/2R_F \approx 0.4$) versus the separation distance. Samples were bathed in aqueous solutions of 20 mM sodium phosphate at pH=7.0 with $NaNO_3$. The solution ionic strengths were 54 mM (white square, N_{meas} =14, n_{exp} = 1), 144 mM (black circle, N_{meas} =14, n_{exp} = 1) and 1044 mM (white circles, N_{meas} =15, n_{exp} = 1). The solid lines are nonlinear least squares fits of the data to the Dolan and Edwards model (Equation 4.2). Best fit values for R_{eff} and the prefactor, A are summarized in Table 4.4.

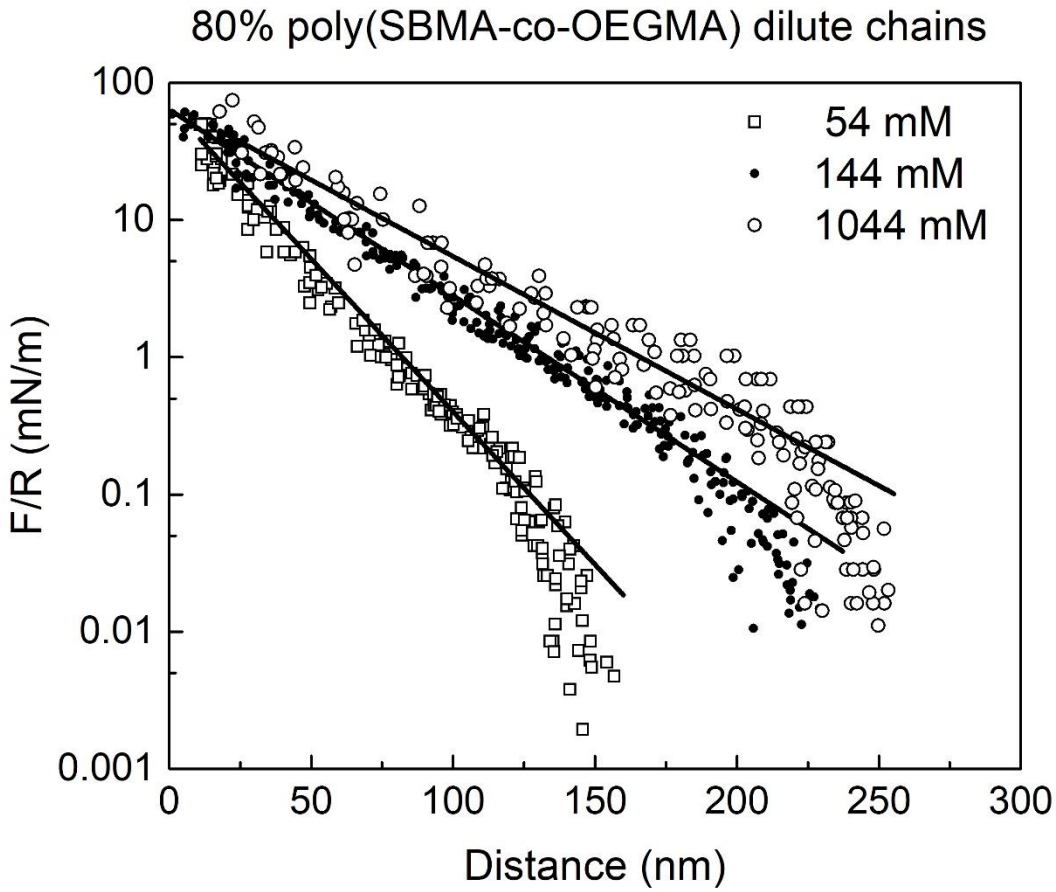

Figure 4.7: Normalized force, F/R (mN/m) between mica and grafted 80% SBMA copolymer dilute chains ($s/2R_F \approx 0.4$) versus the separation distance. Samples were bathed in aqueous solutions of 20 mM sodium phosphate at pH=7.0 with $NaNO_3$. The solution ionic strengths were 54 mM (white square, N_{meas} =12, n_{exp} = 1), 144 mM (black circle, N_{meas} =18, n_{exp} = 1) and 1044 mM (white circles, N_{meas} =14, n_{exp} = 1). The solid lines are nonlinear least squares fits of the data to the Dolan and Edwards model (Equation 4.2). Best fit values for R_{eff} and the prefactor, A are summarized in Table 4.4.

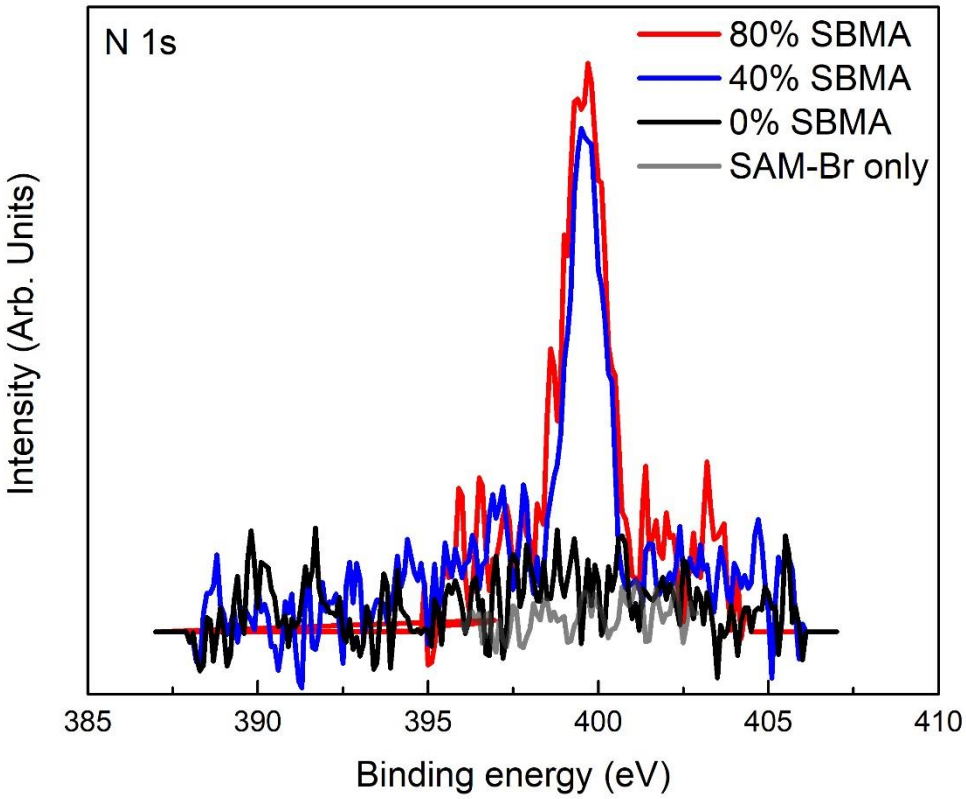

Figure 4.8: N 1s spectra obtained from XPS

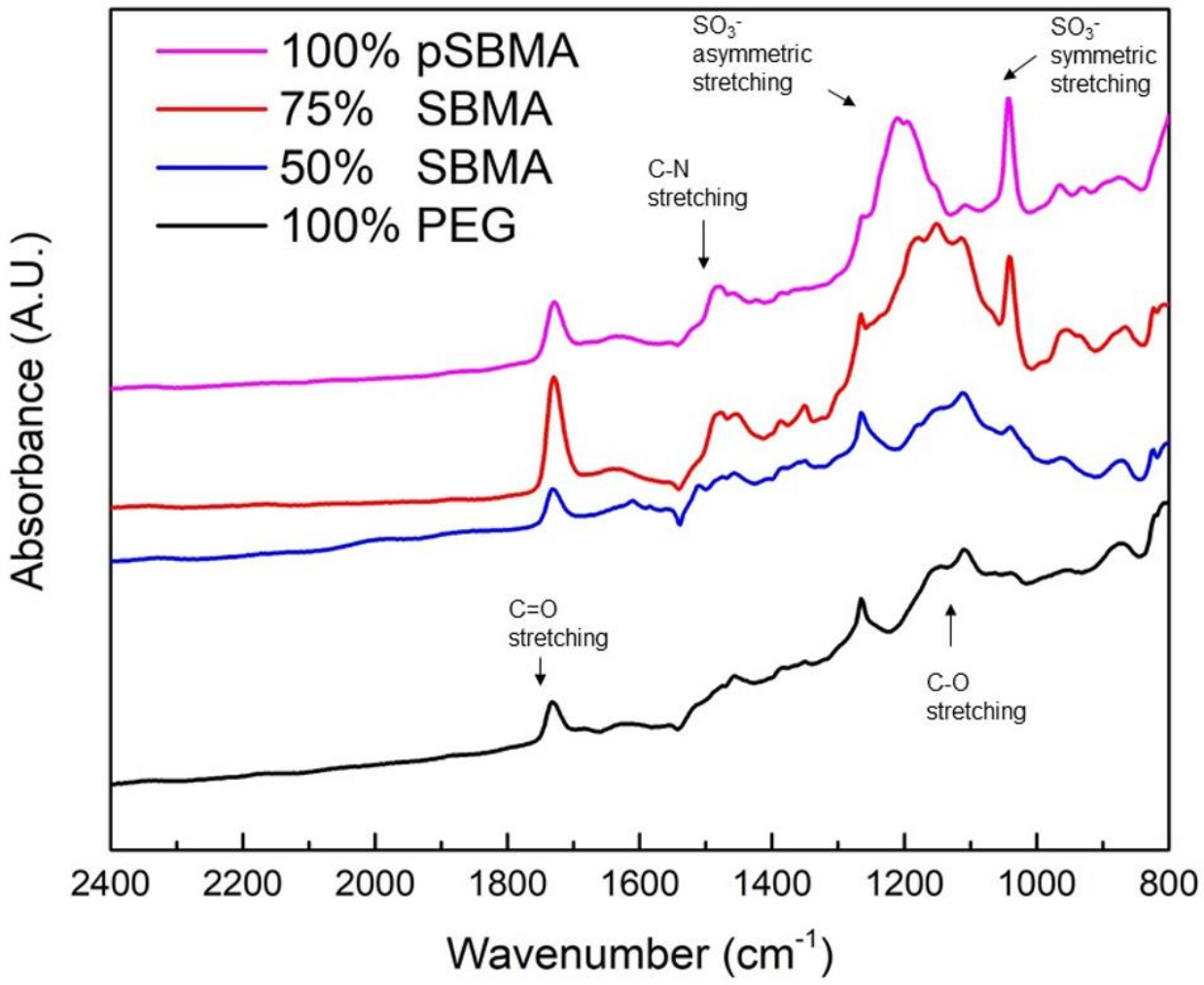

Figure 4.9: The ATR-FTIR spectra of polymers grafted from alkanethiols on a gold coated silicon wafer. The scans were obtained with PEG homopolymer (black line), 40% (blue), 80% (red), and 100% (magenta) SBMA brushes. Stretching transitions used to assess the polymer composition are indicated.

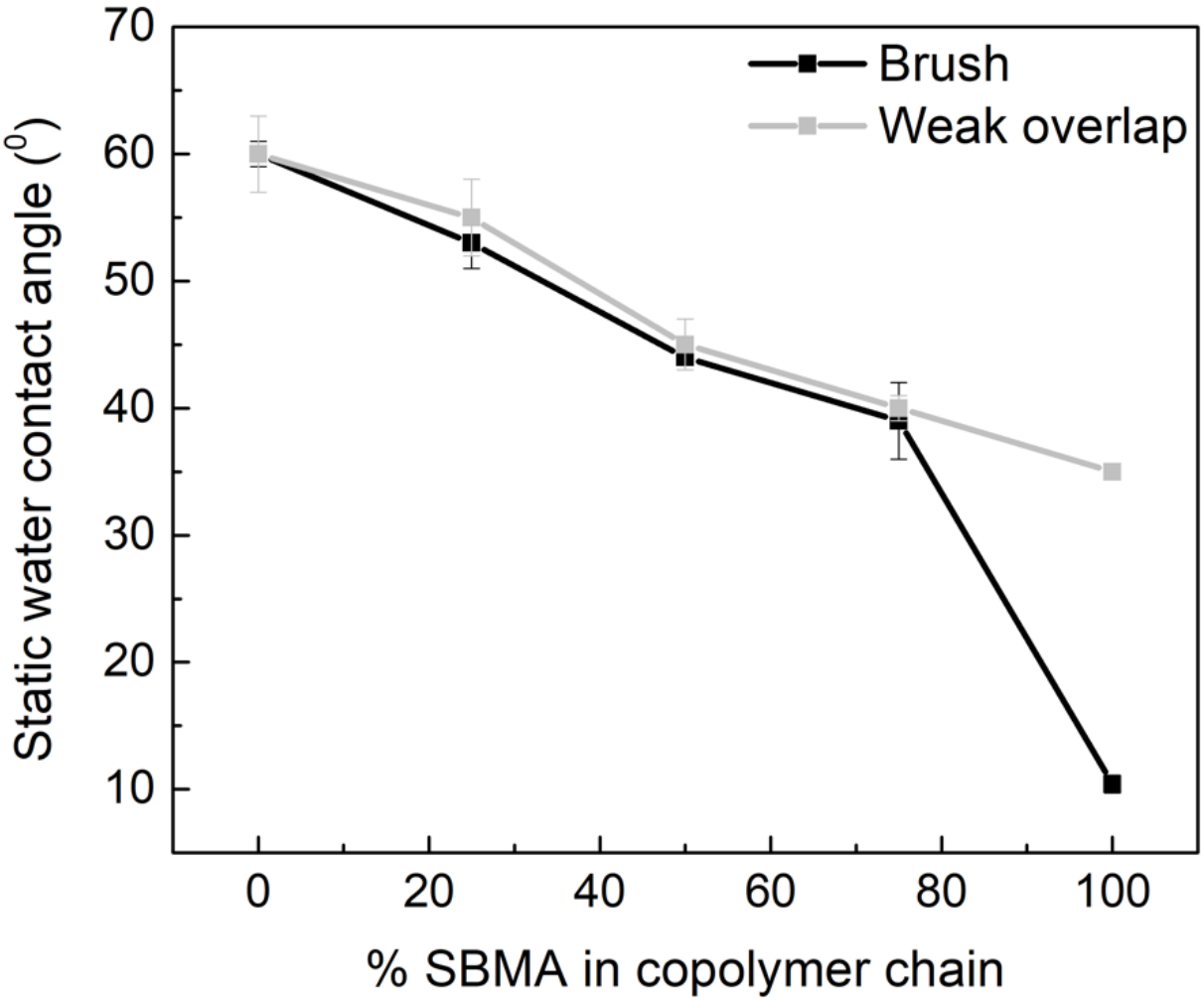

Figure 4.10: Static water contact angle of synthesized poly(SBMA-co-PEGMA) brush and weakly overlapping chains via Rame-Hart goniometer using ultrapure water (resistance 18.2 MΩ.cm at 21°C). The values reported are the average of three measurements taken at three different locations of the surface.

Table 4.1: Brush poly (SBMA-co-OEGMA) chain parameters

Zwitterionic content in chains (%)	Dry polymer thickness* (nm)	Estimated grafting density, σ chains/nm^2	Grafting distance, s (nm)**	Weighted molecular weight, M_n (KDa)	Degree of polymerization, N	R_F (nm)	$s/2R_F$
0	30 ± 4	0.21	2.2	110 ± 10	220 ± 20	7.6 ± 0.8	0.1
40	23 ± 1	0.21	2.2	72 ± 4	174 ± 9	6.6 ± 0.3	0.2
80	24 ± 1	0.21	2.2	84 ± 4	260 ± 10	8.4 ± 0.4	0.1

*Polymer film thickness including the thickness of the SAM (2.5 ± 0.3 nm); ** s is calculated from $s=1/\sigma^{-1/2}$; the tabulated values are mean ± standard deviation for n=3.

Table 4.2: Weakly overlapping poly (SBMA-co-OEGMA) chain parameters

Zwitterionic content in chains (%)	Dry polymer thickness (nm)	Estimated grafting density, σ chains/nm^2	Grafting distance, s (nm)**	Weighted molecular weight, M_n (KDa)	Degree of polymeri-zation, N	R_F (nm)	$s/2R_F$
0	7.0 ± 0.5	0.04	5	66 ± 9	130 ± 20	5.6 ± 0.8	0.4
40	5.9 ± 0.4	0.04	5	56 ± 4	137 ± 9	5.7 ± 0.4	0.4
80	6.0 ± 0.7	0.04	5	58 ± 7	180 ± 20	6.7 ± 0.8	0.4

*Polymer film thickness including the thickness of the SAM (2.5 ± 0.3 nm); ** s is calculated from $s=1/\sigma^{-1/2}$; the tabulated values are mean ± standard deviation for n=3.

Table 4.3: Fitted parameters of poly (SBMA-co-OEGMA) brush to MWC theory

Zwitterionic content in chains (%)	Chain extension, L_0 (nm) in ionic strength			Prefactor, P_o (mN/m)		
	54 mM	144 mM	1044 mM	54 mM	144 mM	1044 mM
0	50 ± 2	47 ± 2	53 ± 3	0.15 ± 0.02	0.22 ± 0.04	0.18 ± 0.04
40	78 ± 3	150 ± 7	162 ± 3	0.24 ± 0.04	0.20 ± 0.02	0.31 ± 0.02
80	91 ± 8	160 ± 5	200 ± 10	0.20 ± 0.05	0.46 ± 0.1	0.6 ± 0.1

Table 4.4: Fitted parameters of poly (SBMA-co-OEGMA) dilute chains to D & L theory

Zwitterionic content in chains (%)	Decay length, R_{eff} (nm) in ionic strength			Prefactor, A (mN/m)		
	54 mM	144 mM	1044 M	54 mM	144 mM	1044 mM
0	10 ± 3	9 ± 3	11 ± 1	28 ± 1	28 ± 1	32 ± 4
40	16.6 ± 0.5	27.2 ± 0.8	27 ± 1	71 ± 2	74 ± 2	70 ± 3
80	20 ± 1	31.9 ± 0.7	41 ± 2	68 ± 1	64 ± 6	71 ± 1

Table 4.5: Quantitative analysis of ATR-FTIR spectra of poly(SBMA-co-OEGMA) brushes

Zwitterionic content in feed (%)	Peak area (C=O stretching)	Peak area (C-O stretching)	Peak area (SO_3^- symmetric stretching)	Normalized by backbone peak (C=O stretching)		Brush composition (%)	
				C-O stretching	SO_3^- symmetric stretching)	OEGMA	SBMA (from symmetric peak)
0	0.074	0.186	0	2.494	0	100	0
25	0.070	0.140	0.016	2.0	0.23	80	17
50	0.072	0.108	0.041	1.496	0.570	60	42
75	0.074	0.037	0.075	0.500	1.01	20	80
100	0.100	0	0.135	0	1.350	0	100

Table 4.6: Quantitative analysis of ATR-FTIR spectra of poly(SBMA-co-OEGMA) dilute chains

Zwitterionic content in feed (%)	Peak area (C=O stretching)	Peak area (C-O stretching)	Peak area (SO_3^- symmetric stretching)	Normalized by backbone peak (C=O stretching)		Copolymer composition (%)	
				C-O stretching	SO_3^- symmetric stretching)	OEGMA	SBMA (from symmetric peak)
0	0.035	0.039	0	1.114	0	100	0
50	0.038	0.025	0.030	0.658	0.789	60	36
75	0.039	0.010	0.069	0.256	1.769	23	80
100	0.038	0	0.084	0	2.211	0	100

*the standard error of means are calculated by propagation of error

Table 4.7: Comparison of fitted values of L_0 to the theoretical brush extension, L_{Th}

Zwitterionic content in copolymer chains (%)	Theoretical chain extension, L_{th} (nm)	L_0/L_{th} at Ionic strength		
		54 mM	144 mM	1044 mM
0	19.0 ± 0.1	2.50 ± 0.04	2.40 ± 0.04	2.70 ± 0.06
40	16.1 ± 0.07	3.90 ± 0.04	7.50 ± 0.05	8.10 ± 0.02
80	19.0 ± 0.1	4.60 ± 0.09	8.03 ± 0.03	10.00 ± 0.05

L_0 was estimated from data fits to Eq. 4.1.

The theoretical chain extension is $L_{Th} \sim R_F (R_F/s)^{2/3}$

* Standard error of the mean calculated by propagation of error

Table 4.8: Comparison of R_{eff} to the Flory radius, R_F

Zwitterionic content in copolymer chains (%)	Flory radius, R_F (nm)	R_{eff}/R_F at Ionic strength		
		54 mM	144 mM	1044 mM
0	5.6 ± 0.8	1.6 ± 0.3	1.5 ± 0.4	1.8 ± 0.2
40	5.7 ± 0.4	2.70 ± 0.08	4.50 ± 0.08	4.50 ± 0.08
80	6.7 ± 0.8	2.8 ± 0.1	4.5 ± 0.1	5.8± 0.1

*the standard error of means are calculated by propagation of error

CHAPTER 5: ADHESION FREQUENCY MEASUREMENTS OF CADHERIN MEDIATED CELL BINDING KINETICS

This work is undertaken in collaboration with Prof. Volker Spindler, Department of Biomedicine at University of Basel and Prof. Sabine Stahl, Center of Organismal Studies at Heidelberg University. The chapter is reproduced in part from the published journal article: Ellen C. Qin, Syeda Tajin Ahmed, Poonam Sehgal, Vinh H. Vu, Hyunjoon Kong, and Deborah E. Leckband, Comparative effects of N-cadherin protein and peptide fragments on mesenchymal stem cell mechanotransduction and paracrine function. *Biomaterials* 2020, 239:119846 (doi: 10.1016/j.biomaterials.2020.119846) with permission [copyright 2020 Elsevier]. I also would like to acknowledge Dr. Nitesh Shashikanth for initial training and assistance on Micropipette Aspiration Assays with the skin blistering disease project.

5.1 Introduction

Cadherins are single-pass transmembrane glycoproteins that belong to a superfamily of adherens junction protein. They are one of the well-known cell adhesion molecules that form adhesive binding interfaces between cells. The binding specificity of cadherins plays an important role in maintaining cell-cell contacts and tissue barrier integrity.[282–286] Depending on the activation pathway of intracellular signal transduction in cells, cadherins are also involved in axonal growth, synaptic plasticity and cell migration.[287] Morphological changes during tissue development are accompanied by changes in expression levels of different types of cadherins.[288] Depending on tissue specific expression patterns, cadherins can promote epithelial, endothelial or neuronal cell adhesion. The tissue-specific expression of cadherins during embryogenesis is also highly

regulated. Therefore, understanding how the intercellular contacts are maintained and regulated gives us insight to the fundamental mechanism of tissue development as well as impairment of function during disease.

5.1.1 Cadherin structure and functions

The type I "classical" cadherins are first subtype of the cadherin family identified, and studied in details. These type of cadherins are expressed in almost all vertebrate tissues, form primarily homophilic cell–cell interactions, are often concentrated in the adherens junction (AJ), and appear to modulate adhesion through dynamic interactions with the actin cytoskeleton. They share a common structure consisting of a cytoplasmic domain, a transmembrane domain and five extracellular domains (EC1-5, where EC1 being the outermost, N-terminal domain) which contains the adhesive interface. Each extracellular domain is comprised of ~110 amino acids, and three Ca^{2+} ions bind at each junction between the consecutive EC domains, and are thought to help in rigidifying the structure and in maintaining function.[289] The single pass transmembrane segment is an alpha helix consisting of 34 amino acids. The intrinsically disordered cytoplasmic domain binds to cytosolic proteins called catenins that are involved in actin coupling and signaling. The first two extracellular domains EC1-2 contain the adhesive domain, and are involved in trans-dimerization between cadherins from apposing cell surfaces. The N-terminus of EC1 domain comprises of 10 amino acid sequence, including 'DWVI' sequence that is highly conserved throughout all type I cadherins.[290,291]

The first extracellular domain (EC1) of cadherins forms the adhesive binding domain, and it is a sequence within EC1 consisting of His-Ala-Val (HAV) is evolutionarily conserved across species consisting of His-Ala-Val (HAV) motif. The adhesive interface is formed by the trans-dimer or the strand-swapped dimer is formed, and occurs when a side chain from Trp2 (W2) residue is

inserted into a complementary hydrophobic pocket on EC1 of the apposing protein.[292] Examples of classical cadherins are: N-cadherin or neuronal cadherin, which is usually expressed on neural cells.[12, 13] endothelial, and invasive cancer cells; E-cadherin or epithelial cadherin, which is predominantly expressed by epithelial cells; P-cadherin (origin: placenta) which is expressed in extra-embryonic ectoderm and visceral endoderm.[295]

5.1.2 Differences between N and E-cadherin binding pocket

High-resolution crystal structures of the N-cadherin extracellular region and mutagenesis studies showed that EC1 is critical for cell-cell adhesion, and both the W2 residue and HAV motif are critical for cadherin mediated adhesion.[296]

Although highly conserved across species, the binding pocket sequence of N-cadherin is different from that of E-cadherin. The extracellular domain (EC-1) of N-cadherin has the sequences 'HAVDI' and 'INPISGQ' that are identified as two important binding motifs.[297] The crystal structure of the N-cadherin adhesive dimer interface revealed that the INPI sequence in one monomer is in close contact with the VDI sequence in the second monomer, and thus forms the binding pocket. Both 'INPI' and 'VDI' sequences were identified as key residues at the N-cadherin dimer interface.[298] While HAV is involved in the adhesive domain formation, the amino acid sequence next to it is also important. Makagiansar et al. (2001)[299] showed, using trans epithelial electrical resistance measurements that binding between E-cadherins can be modulated by changing the amino sequence followed by the HAV sequence. In this study, the modulation of intercellular junctions of MDCK (Madin-Darby Canine Kidney) cells were evaluated by measuring the ability to lower the transepithelial electrical resistance (TEER) of cell monolayer cultured on Transwell™ membranes. For example, Ac-SHAVAS-NH_2 and Ac-SHAVSA-NH_2 were more effective than Ac-

SHAVSS-NH_2 at mimicking the binding pocket sequence of E-cadherin. Therefore, although the HAV sequence is a primary binding motif for all of the classical cadherins, the selectivity is postulated to be determined by the flanking amino acids, which differ among the classical cadherins.

5.1.3 Importance of the first two extracellular domains of classical cadherins in forming adhesive binding pocket

Over the years there have been several reports on the discovery of a second cadherin interface other than that involving the trans-dimerization, which was later known as the X-dimer. The crystal structure of N-cadherin with an unprocessed N-terminal methionine revealed an inactive form of EC1-2 which was the first evidence on an X-dimer structure.[300] Later, a W2A mutant of E-cadherin as well as the EC1-2 fragment of a non-classical, truncated T-cadherin, the similar X-dimer was crystallized in previous work. [301] Structural studies done with Surface Plasmon Resonance (SPR) and Analytical Ultracentrifuge (AUC) by Harrison et al. [302] showed that X-dimers are formed when strand swapping is prevented by mutations in E-cadherin (K14E mutant) and that X-dimer increases activation barrier in the dimerization pathway but it doesn't affect the dissociation constant, K_D. Single-bond rupture measurements with AFM were performed based on lifetimes of single cadherin bonds between EC1-2 fragments subjected to constant applied force by Rakshit et al. [303] This study identified the X-dimer as a catch bond, *i.e.* it ruptures more slowly (as its lifetime increases) at increasing force and therefore the bonds appear to be more stable at higher forces. On the other hand, the strand dimer is a slip bond *i.e.* it ruptures more quickly at increasing force and therefore, the bonds appear to be less stable and thus its dissociation rate increases. From these studies, it was postulated that the X-dimer could be an important

intermediate in the strand-dimerization pathway that lowers the activation energy and accelerates the formation of more stable (lower-K_d) strand dimers.[304, 305]

5.1.4 E cadherin adhesion in O-mannosylation deficient POMT deficient HEK 293 T cells

Defects in protein *O*-mannosylation lead to severe congenital muscular dystrophies collectively known as α-dystroglycanopathy. A hallmark of these diseases is the loss of the *O*-mannose-bound matriglycan on α-dystroglycan, which reduces cell adhesion to the extracellular matrix. Mutations in protein *O*-mannose β1,2-N-acetylglucosaminyltransferase 1 (POMGNT1), which is crucial for the elongation of *O*-mannosyl glycans, have mainly been associated with muscle–eye–brain (MEB) disease. In addition to defects in cell–extracellular matrix adhesion, aberrant cell–cell adhesion has occasionally been observed in response to defects in POMGNT1. However, specific molecular consequences of POMGNT1 deficiency on cell–cell adhesion are largely unknown. We used POMGNT1 and POMT2 (one of the major subfamilities of protein O-mannosyltransferases) knockout HEK293T cells and to gain deeper insight into the molecular changes in POMGNT1 and POMT2 deficiency. Since there are more than 20 potential O-glycosylation sites in E-cadherin distributed throughout the E-cadherin polypeptide,[306] it was not feasible to mutate all sites, apart from the possible effects on protein folding. Recently, the role of O-mannosylation in E-cadherin had been tested using mice in which two critical genes encoding for isoforms of O-mannosyl transferases POMGNT1 and POMT2 were knocked out. Individual cells in these knockout mice were incapable of transferring sugars to potential Ser/Thr sites on proteins. The loss of O-glycans E-cadherin was confirmed in mice knockouts, with antibodies specific for O-mannosylated sites on E-cadherin.[307]

Posttranslational modification is one mechanism that regulates the function of adhesion proteins, like cadherins. Apart from direct phosphorylation of the cytoplasmic domain, glycosylation is the

most common posttranslational modification in cadherins.[308] Both N-glycosylation and O-glycosylation are prevalent in classical cadherins, with N-linked Glycosylation making up to ~20% of the molecular weight of cadherin itself. [307–310]

It is well established that N-glycosylation is essential not only for E-cadherin expression, folding and trafficking, but also for the stability of the adherens junctions.[308] Studies demonstrated that N-glycosylation affects the molecular composition and organization of cadherin junctions.[311,312] In breast tumors, the ectodomains of E-cadherin exhibit highly branched N-glycans on extracellular domains EC4 and EC5. Hyperglycosylation at the latter sites destabilized epithelial junctions and increased tumor progression.[313] Conversely, hypo-glycosylation, achieved by treatment with a known glycosyl transferase inhibitor tunicamycin.[314,315] or by mutating an N-glycosylation site in EC4 enhanced intercellular junction assembly, cytoskeletal remodeling at junctions, and transepithelial resistance. [310]

More recent studies investigated the role of O- glycosylation, with particular emphasis on the first O-mannosylation step. In mouse embryos, depleting E-cadherin of O-mannosylation affected embryonic development in mice and growth was arrested beyond the morula stage.[307,316] Treating MDCK cells expressing E-cadherin treated with an O-mannosylation specific antibody Tα1-mann reduced cell-cell aggregation.[307] The broad impact of N- and O-linked E-cadherin glycosylation on cell-cell adhesion and cadherin functions are not well understood. Structural studies cannot investigate the impact of glycosylation on cadherin interactions, because of the difficulty of obtaining crystal structures of glycosylated proteins. Adhesion frequency measurements, described in section 5.1 are ideally suited to address this question. Prior adhesion frequency measurements of N-cadherin and its N-glycosylation mutants tested the hypothesis that N-glycosylation regulates cadherin binding function.[317] The latter study demonstrated that N-

glycosylation does not affect the trans-binding affinity, but instead alters the two-stage binding kinetics.[318] Together with prior cross-linking results, the latter results support a mechanism in which initial, EC1-dependent trans binding is followed by additional cadherin interactions that enhance binding. The presence of N-glycans localized at three sites in the EC2-EC3 domains of N-cadherin slowed the second kinetic step, reduced wound healing rates, and increased the population of cadherin dimers on cell membranes. [319]

Here, micropipette aspiration (MPA) measurements were conducted to quantify the affinities between hypo-O-mannosylated E-cadherin expressed on HEK 293T cells and wild type, glycosylated E-cadherin ectodomains (EC1-5) bound to opposing red blood cells (RBCs). We quantify changes in binding kinetics in POMT2 and PomGnT1 deficient cells relative to wild type E-cadherins expressed on HEK cells. The goal was to quantify the impairment of binding functions of E-cadherins in PomT deficient mouse embryos, having O-mannosylated sites either mutated or deleted.

5.1.5 Binding of Autoantibodies in Skin Blistering Disease with desmosomal cadherin

The objective of this project was to elucidate mechanisms by which auto-antibodies disrupt distinct cell-cell adhesion structures in disease. We focused on desmosomes, which are specialized adhesive structures at cell-cell junctions. Desmosomes are most abundant in tissues exposed to high degrees of mechanical stress such as the epidermis, and are crucial for tissue integrity and function.[320,321] In this regard, the regulation of desmosomal cohesion is surprisingly poorly understood. Desmosomal function is severely compromised in pemphigus, a group of blistering skin diseases, which are caused by autoantibodies targeting desmogleins (Dsgs), Dsg3 and/or Dsg1—cadherin-type adhesion molecules in the desmosomes. Autoantibody binding disrupts cell-cell adhesion, and causes painful blistering and erosions of mucous membranes and the epidermis

with accompanying infections due to lost barrier integrity. This results in cleft formation in the epidermis and the oral mucosa. Macroscopically, the patients present with painful blisters and erosions that disrupt the barrier function and are prone to massive infections.[322] The mechanisms by which the autoantibodies disrupt cell cohesion are only partially understood, as underscored by the fact that the disease can only be treated by strong, non-specific immunosuppression. Specifically, it is largely unknown how the autoantibodies interfere with desmogleins binding, and it is also unclear how altered desmoglein binding relates to changes in intracellular signaling, which is required to induce the full loss of cell-cell adhesion. The common assumption that auto-antibodies sterically block desmoglein (Dsg) binding does not account for the role of signaling in skin blistering.

Here, we studied Dsg3 binding affinity with full length E-cadherin with and without the autoantibody AK23. Building on the findings of this study, future work will explore postulate that autoantibodies allosterically regulate both Dsg3 affinity and intracellular signaling. This work advances a recent study that showed activating anti-E-cadherin antibodies allosterically regulate binding and signaling by a related protein, E-cadherin.[323]

Here, we measured Dsg3 mediated cell-cell binding kinetics and Dsg3 adhesion to cell surfaces was carried out in the absence and presence of auto-antibodies. In future studies, we predict that kinetic signatures will distinguish between allosteric regulation and simple steric interference.

5.1.6 Significance of 2D binding kinetics studies

The adhesion processes sensitively depend on the binding rate constants for the membrane-bound receptor and ligand proteins that mediate adhesion. The ligand-receptor interactions of cadherins on two apposing cell surface are very specific which is better modeled by reaction kinetics. [324]

There are many methods available for measuring binding kinetics, for example, 3D binding constants when at least one of the receptor-ligand pairs are in solution conducted in a flow chamber [325] as well as, 2D binding kinetics when the receptor-ligand molecules are bound to two apposed surfaces as in the case of cell-cell or cell-substrate adhesion by micropipette aspiration assay (Figure 5.1 and 5.2).[326] In micropipette aspiration assay, a test cell is aspirated in one of the micropipettes and usually a red blood cell (RBC or Erythrocyte) is aspirated in another. These cells are then made to come in contact by a programmable piezo-electric controller for a definite period of time (0.5 s to 20s) and retracted to observe any adhesion that might have occurred. The test outcome is scored as 1 if any adhesion is observed and 0 if not. Thus, the adhesion probability, rather than adhesion strength is measured from the running frequency of binding events for receptor-ligand pairs (150 tests per contact duration). The kinetic rates i.e. forward and reverse reaction constants and the equilibrium binding constants i.e. affinities are extracted from the measured adhesion probability versus contact duration data of the aspirated molecules in question. RBCs are preferable because it provides a smooth cell surface when swollen completely, without any excess cell surface protrusion allowing

The model that we have adapted for evaluating the binding interaction is McQuarrie's [327] probabilistic formulation of kinetics in small systems and the analytical solution of the master equations have been solved by Chesla et al.[326]. It describes the dependence of adhesion probability on the contact duration as follows,

$$P_a = 1 - \exp\{-A_C m_r m_l K_A^0 [1 - \exp(-k_r^0 t)]\} \qquad \text{Equation 5.1}$$

Where A_c is the contact area (μm^2), m_R and m_L are cadherin densities on the two cells (number/μm^2), k_a is the two-dimensional affinity (μm^2), and k_{off} is the dissociation rate (seconds).

Thus micropipette aspiration assay has been used to investigate the binding kinetics of cell-cell adhesion molecules quantitatively.

5.2 Materials and methods

5.2.1 Cell lines and culture conditions

HEK293T cells were maintained in high-glucose Dulbecco's modified Eagle's medium (DMEM) (Thermo Fisher Scientific) supplemented with 10% fetal bovine serum (FBS) (Thermo Fisher Scientific), 1% nonessential amino acids (Thermo Fisher Scientific), and 1% Pen/Strep (Thermo Fisher Scientific) (referred to as complete media) at 37º C in a humidified incubator with 5% of CO_2. Generation of TALEN-mediated POMGNT1 and POMT2 knockout cells, plasmids and transfection of HEK293T cells and generation of stable cell lines were performed by Prof. Sabine Strahl's research group at Centre for Organismal Studies (COS), Glycobiology, Heidelberg University, Heidelberg, Germany.[328] The details of the plasmid map was previously published elsewhere. [329] In this study, the knockout cell lines are going to be referred as ΔPOMGnT1 E-cadherin and Δ POMT2 E-cadherin HEK293T cells respectively. HaCat keratinocytes were also maintained and cultured in similar condition as that of HEK293T cells. Clonally derived mouse bone marrow stromal mesenchymal stem cells (MSCs, D1 cells; ATCC, CRL-12424) were maintained at sub-confluence in standard MSC growth medium containing DMEM Dulbecco's Modification of Eagle's (DMEM) medium with 4.5 g/L glucose, L gluatmine, and sodium pyruvate (Corning, Catalog #: 10-013-CV) supplemented with 10 v/v% FBS and 1 v/v% P/S.

5.2.2 Quantification of cadherin densities on cell surfaces by flow cytometry

The densities of immobilized or expressed cadherin densities on cell surfaces was quantified by flow cytometry, as previously described. [326,330] The fluorescence intensity of labeled cells and of

the standardized calibration beads for Alexa 647 (Bangs Laboratories, Inc., IN) were quantified using an LSR II flow cytometer (BD Biosciences, San Jose, CA). The fluorescence intensities were converted to total bound cadherin densities on the cells using the calibration curves according to the manufacturer's instructions.[331]

5.2.2.1 Determination of E-cadherin densities on HEK293T cells and E-cadherin Fc densities on RBCs

To determine the surface density of E-cadherin on HEK 293T cells, the cells were first labeled with primary, rat anti-E-cadherin monoclonal antibody which binds the fifth extracellular repeat domain (EC5) of murine and human E-cadherin.[332, 290] (DECMA-1, Sigma-Aldrich, St Louis, MO) at 1:300, followed by washing with 1X PBS (twice) and then incubation with secondary polyclonal antibody goat anti-rat IgG-Alexa 647 (Abcam, 2 mg/ml) at 1:400. Readers are advised to use monoclonal secondary antibodies because the use of polyclonal antibodies introduce some errors in surface density determination by flow cytometry. Next, approximately 10^5 cells were used for labeling and incubation with both primary and secondary antibodies. Incubations were done in a cold room at 40°C for ~45 mins. The labeling was performed in Dulbecco's Phosphate Buffer Saline (DPBS) with 0.9 mM calcium. For quantifying E-cadherin Fc full length surface densities on RBCs, first the cells were incubated in Anti-hu Fc IgG expressed in goat (Sigma-Aldrich, Batch # 115M475V, IgG concentration: 2.1 mg/ml, storage -20^{0}C) in 4^{0}C for 45 minutes, followed by incubation with secondary antibody donkey anti-goat Alexa 647 IgG (Santa Cruz-362285) for 45 minutes.

5.2.2.2 Determination of Dsg3-cadherin surface densities on HaCat cells and Dsg3 Fc surface densities on RBC

The HaCat cells were incubated with primary Dsg3 binding antibody AK23 (expressed in mouse) for 45 minutes in 4^0C, followed by incubation with secondary antibody goat anti-mouse Alexa 647 (Thermofisher) for 45 minutes. For RBC labeling, they were first incubated with Dsg 3 Fc full length, followed by incubation with AK23 primary antibody and finally incubation with goat anti-mouse Alexa 647 secondary antibody.

5.2.2.3 Determination of N-cadherin surface densities on D1 cells and N-cadherin Fc surface densities on RBC

D1 cells or MSCs were labeled with primary antibody (1:200); rabbit polyclonal N-cadherin antibody (Protein Tech, 48 ug/150 ul), followed by the secondary Cy5™ labeled, goat anti-rabbit antibody (Invitrogen, 2 mg/ml) at a dilution of 1:400. The cells were washed with twice with 1X Phosphate Buffered Saline (PBS) before and after the incubation with the secondary antibody in order to remove the unbound, excess antibodies. RBCs displaying full length N-cad EC1-5 were labeled for 45 min with a rabbit, anti- N-cadherin polyclonal antibody that specifically binds to the EC1-2 domain (1:600 in cPBS with 2% BSA, ProteinTech, Catalog #: 13769-1-AP). After, the cells were incubated with secondary Cy5™ goat anti-rabbit antibody (1:400 in PBS with 0.9 mM calcium; Invitrogen, Catalog #: A-21245) for 45 min.

5.2.3 Isolation and modification of red blood cells

Whole blood was collected from healthy donors at Community Blood Services of Illinois (CBSI) and red blood cells were isolated and purified from whole blood by a protocol reviewed and approved by the Institutional Review Board (IRB; protocol # 08669).

Briefly, the capture proteins such as E or N cadherins are covalently coupled to glycoproteins on the RBCs surface that were chemically activated by $CrCl_3$ treatment.[333,334] Approximately 10 million RBCs were washed five times with 0.9 (w/v)% NaCl and resuspended in 0.9 (w/v) % NaCl solution. The primary antibody (either anti-mouse Fc IgG or the streptavidin-Alexa 647 conjugate) was added to RBC solution typically at 10 µg/ml. [326] Then, serial dilutions of $CrCl_3$ were prepared from 0.1 (v/v) % $CrCl_3$ solution in 0.02 mM sodium acetate and 0.9 (w/v) % NaCl in separate microcentrifuge tubes. The $CrCl_3$ solution was added to the RBC containing salt solution to allow for the coupling reaction (reaction time is 5 minutes). The cells were washed twice with phosphate buffer saline (PBS) containing 5 mM EDTA and 1 w/v% bovine serum albumin (BSA) and finally resuspended and stored in erythrocyte storage buffer called EAS 45 buffer, formulated by Zarnitsyna and Zhu.[335] In this reaction, the resulting density of antibodies immobilized to the cell surface was controlled by titrating the $CrCl_3$ solution. The surface density of the anti-mouse Fc IgG was determined by flow cytometry using the secondary antibody goat anti-mouse IgG-Alexa 647 (Invitrogen). The labeling was performed in Dulbecco's Phosphate Buffer Saline (DPBS) with 0.9 mM calcium with an incubation period of 45 minutes at 4^0C. The molecules of equivalent soluble fluorochrome (MESF) values (approximately the number of antibodies) determined from flow cytometry, were converted into surface density of cadherins on RBCs (cadherins/area), assuming two cadherins bind to one IgG antibody. The estimated surface area of RBCs is ~168 μm^2.

5.2.4 Micropipette aspiration assay (MPA) to study 2D binding kinetics

In order to quantify the interactions between N-cadherin fragments and N-cadherin expressed on MSCs, the binding kinetics and binding constants were determined using the micropipette adhesion frequency assay. The binding kinetics between cells displaying full-length N-cadherin

and its fragments were quantified with micropipette adhesion frequency measurements, as described previously. [330] In micropipette measurements, a test cell is aspirated in one of the micropipettes and a red blood cell (RBC or Erythrocyte) is held in the opposing micropipette. These cells are then brought into contact with a programmable piezo-electric controller for a definite period (0.5 s to 40s) and then separated (Figure 5.1 and Figure 5.2). The test outcome is scored 1 if adhesion is observed and 0 if not. Thus, the adhesion probability, and not the adhesion strength, is determined from the running frequency of binding events for receptor-ligand pairs (150 measurements per contact duration). The dissociation rate and steady state binding constants are extracted from model fits to the measured adhesion probability versus contact duration. The model adapted for evaluating the binding interaction is based on McQuarrie's probabilistic formulation of kinetics in small systems.[327] For a simple second order binding reaction, the analytical solution of the master equations derived by Chesla et al.[326] describes the time-dependence of the adhesion probability as:

$$P_a = 1 - \exp\{-A_c m_r m_l K_a [1-\exp(-k_{off} t)]\} \qquad \text{Equation 5.5}$$

where A_c is the contact area (μm^2), m_r and m_l are cadherin densities on the two cells (number/μm^2), K_a is the two-dimensional affinity (μm^2), and k_{off} is the dissociation rate (seconds).

The binding occurs between endogenous N-cadherin expressed on MSCs, or E-cadherin expressed on HEK 293T cells (for glycosylation mutation studies) or Dsg3 expressed on HaCat cells (for Pemphigus vulgaris disease study) and the N or E-cadherin fragments immobilized on the RBCs or autoantibodies AK23 blocking Dsg3 Fc immobilized on RBCs respectively. The binding kinetics between different E-cadherin or Dsg3 Fcs can also be probed with two RBCs with the immobilized cadherin constructs on the surface. The cells were kept in a hypotonic L-15 medium (Leibovitz's L-15 Medium, (Invitrogen, Carlsbad, CA) containing 2.0 mM $CaCl_2$ diluted 1:1 with

deionized water to maintain a rounded form. Cells were observed with a 100x oil immersion objective on a Zeiss Axiovert 200 microscope, interfaced with CCD camera (Pike, Allied Vision Technologies). The contact area was controlled at ~ 7.2 μm^2. For each cell-cell contact time, three different cell pairs were subjected to 50 cell-cell touches (N_T= 50), in order to determine the binding probability, which is the ratio of the number of adhesion events and total cell-contacts (i.e. P= n_b/N_T). The binding probability reflects the number of stable bonds formed. Reported probabilities are the average values and standard deviation. The details of the micropipette aspiration assay set up is given in *Appendix F*.

5.2.5 Statistical analysis: Model fits to the EC1-mediated binding step

The initial increase in the kinetic profile obtained from binding probability vs. contact time is due to trans-dimerization and is described by a kinetic model (Equation 5.5) but the more complex kinetic behavior requires the full ectodomain for all classical cadherins that have been studied.[55, 56] Thus, the first, fast rising to low probability stage p1 is fitted to the model involving only EC1-2 (fit shown by the dotted line in all figures) and the slow rising phase to a higher probability stage, p2 is not fitted, which involves all EC1-5 domains. This two stage kinetics is typical of the binding kinetics exhibited by classical cadherins like E and N-cadherins.

The measured contact time dependent adhesion probability data was fitted to Equation 5.5 by using Levenberg Marquadt algorithm for performing nonlinear, least squares regression in OrginLab program (Northampton. MA). For each contact time, the adhesion probability was measured with three different cell pairs. The best, unbiased estimated parameter is determined by weighted non-linear least squares fit of the data to Equation 5.5, with the weighting factor for each time point being the inverse of the variance at that time point.

A non-linear lack-of-fit test [338] identified the time points associated with the first, EC1 strand swapping step. The test compares the model's residuals to the inherent variability in the data, normalized to an F-distribution, as described by Langer et al. [317]

$$F = \frac{\Sigma_{i=1}^{n}\{n_i(\bar{y}_i - \hat{y}_i)\text{^}2|(n-2)\}}{\Sigma_{i=1}^{n}\Sigma_{j=1}^{n_i}\{(y_{ij} - \bar{y}_i)\text{^}2|(N-n)\}}$$ Equation 5.6

For this test statistic, n is the number of distinct time points observed, n_i is the number of observations at each time point, means the average value of observations at time point i, refers to the model prediction at time point i, refers to each individual measurement, and N is the total number of observations. A Student's t-test was performed in order to determine the statistical significance of differences between 2D affinities measured, for given mean, standard error of mean (SEM) and number of observations (N).

5.3 Results

5.3.1 E-Cadherin on POMGnT1 deficient HEK 293T cells vs. E-Cad Fc on RBC

Micropipette measurements quantified the two-dimensional protein-protein binding affinities between E-cadherin fragments on modified Red Blood Cells (RBCs) and E-cadherin expressed on HEK293T cells. Figure 5.3 shows the time dependence of the binding probability measured between HEK293Ts expressing WT E-cadherin and red blood cells displaying with E-cadherin EC1-5. Figure 5.3 and 5.4 show the time dependent binding probability measured between red blood cells modified with E-cadherin EC1-5 and ΔPOMGnT1 E-cadherin and Δ POMT2 E-cadherin expressing HEK 293T cells respectively. The initial rise to a limiting plateau is representative of the trans-dimerization kinetics, and this step in the binding kinetics is well

described by Equation 5.5. The dissociation rate and 2D trans-binding affinity were estimated from the data fits to Equation 5.5.

The two-dimensional affinity between WT E-cadherin expressed on HEK293T cells (33 E-cadherin/μm^2) and red blood cells modified with E-cadherin EC1-5 (28 cadherin/μm^2) was 1.35 ± 0.07 x10^{-4} μm^2. For HEK293Ts expressing ΔPOMGnT1 E-cadherin (33 cadherin/μm^2) against RBCs modified with E-cadherin EC1-5 (28 cadherin/μm^2), the binding affinity was an order of magnitude lower, that is 7.33 ± 0.03 x10^{-5} μm^2 (Figure 5.4). Similarly, HEK293Ts expressing Δ POMT2 E-cadherin (33 cadherin/μm^2) against RBCs modified with full length E-cadherin (28 cadherin/μm^2), the binding affinity was 5.45 ± 0.03 x10^{-5} μm^2 (Figure 5.5). These results show that there is no significant difference in the binding affinities measured between the POMGnT1 and POMT2 deleted mutant expressing HEK293T cells and the full length E-cadherin Fcs. But the binding affinity is an order of magnitude less than the case of WT E-cadherins, where the O-mannosyl glycans still remain.

The loss of O-mannosylated glycans on E-cadherin expressed on either POMGnT1 or POMT2 deficient HEK293T cells resulted in significantly lower affinities by ~ 2 and 2.5 fold respectively compared to E-cadherin expressed on wild type HEK 293T cells. This supports the suggestion by Lommel et al. [339] that hypo O-mannosylation impairs the binding function of E cadherins.

In the bead aggregation studies performed by Strahl et al. (personal communication), it has been shown that when beads are decorated with the WT protein, large aggregates are formed in a calcium-dependent manner, whereas, the mutant E-cadherin extracellular domains mediated bead adhesion to a much smaller extent although aggregate formation was not fully abolished. Interestingly, the dissociation rate (k_{off}) was not affected by loss of O-mannosylation, within experimental error, suggesting that hypo-O-mannosylation decreases the 2D association rate.

Mutations in POMT1 and POMT2 genes were shown to affect the O-linked mannose that is present on EC4 of E-cad. [339] A previous crystal structure analysis of E-cad had identified at least nine additional O-linked monosaccharide modifications of EC2–4 whose exact identity remained unknown.[340] Therefore, the binding kinetics data indirectly indicates that there must be an O-mannosylated sites at the binding adhesive interface made of EC1 and EC2, the deletion of which results in a lower binding affinity.

Future studies will test whether deglycosylating the first two EC domains (EC1-2-His_6) by expressing the fragment in bacteria, or in POMGnT1 or POMT2 deficient HEK293T cells affects the E-cadherin binding affinities. We focus on the EC1-2 fragment which is postulated to be the minimal adhesive fragment of E-cadherin. These studies will identify the key O-mannosylation sites that impact the protein binding function. In future studies, we want to see the effect of hypo-O-mannosylation in N-cadherin as well with the following arrangements-

1. N-cadherin WT (HEK 293T) vs. N-cadherin WT (RBC)
2. POMGnT1 deficient N-cadherin (HEK 293T) vs. N-cadherin WT (RBC)
3. POMT2 deficient N-cadherin (HEK 293T) vs. N-cadherin WT (RBC)

5.3.2 Binding affinity measurement of Dsg3 with or without autoantibody AK23 by micropipette aspiration assay

The binding kinetics between Dsg3 ectodomains on red cells and Dsg3 on HaCaT keratinocytes exhibited a monotonic rise to a steady state plateau at probability, P1 ~0.6 (Figure 5.7). Controls used unmodified red cells. Fits of the rate equation 5.5 (above) to the binding probability time course determined the homophilic Dsg3 binding affinity and dissociation rate (solid line). First the binding affinity of RBCs modified with Dsg3 Fc (64 cadherins/μm^2) were measured (Figure

5.6) and it was compared with that of RBCs modified with Dsg3 Fc blocked with AK23 (the autoimmune antibody, cadherin density of 56 cadherins/μm^2). The binding affinity or 2D equilibrium binding constant of Dsg3 Fc EC 1-5 without antibody is 4.1 (± 0.6) $x10^{-5}$ μm^2 and off rate, k_{off} = 0.6 ± 0.1 s^{-1}, which is not significantly different from Dsg3 Fc antibody blocked with AK23 antibody (K_a = 3.20 (± 0.07) $x10^{-5}$ μm^2, k_{off} = 1.0 ± 0.1 s^{-1}). The fitted parameters of Equation 5.5 is given in Table 5.4.

Next, the binding affinity of Dsg3s was measured on HaCat cells (54 cadherins/μm^2) that endogenously express Dsg3s with RBCs modified with Dsg 3 Fc with or without the antibody AK23 (Figure B.6). The binding affinity of HaCat cells expressing Dsg3 with Dsg3 Fc on RBC is two times higher (K_a = 6.0 (± 0.3) $x10^{-5}$ μm^2) than that blocked with AK23 antibody against Dsg3 Fc on RBC (K_a = 3.0 (± 0.2) $x10^{-5}$ μm^2). Moreover, the rise to the plateau of the curve, which is given by the off rate constant of binding, k_{off} is low when Dsg3 is blocked with antibody (1.0 ± 0.1 s^{-1}) than the case when it is not (k_{off} = 2.0 ± 0.1 s^{-1}). The fitted parameters are given in Table 5.5. These results show that Dsg 3 full length fragment of ectodomains 1-5 may not mimic the case when Dsg3 is expressed on cell surface, with its transmembrane and endoplasmic domains in addition to ectodomains. There is a decrease in binding affinity when Dsg3 is blocked by autoimmune antibody AK23.

5.4 Conclusion

Comparison of results obtained with Dsg3-Fc versus Dsg3 in the cell context reveals cellular influences on Dsg3 binding. In addition to quantifying Dsg3 binding parameters, we will similarly compare the results with models for competitive inhibition and negative allosteric inhibition by quantifying the affinity as a function of antibody concentration. Here we showed that the binding

kinetics and fitted binding constants measured between Dsg3 ectodomains on two opposing RBCs were statistically similar to values determined with HaCaT cells. The latter result ruled out any contribution from heterophilic Dsg3 binding to other possible interactors on HaCaT cells. Treatment of HaCaT cells with pemphigus antibody AK23 lowered the amplitude of the steady-state plateau (Figure 5.7 and Table 5.5), and corresponding affinity. Initial analyses suggest that AK23 increased the off-rate without altering the on-rate. The latter might argue against steric interference: merely blocking the active site would reduce the association rate, but not necessarily the off-rate. However, further measurements are needed to verify this.

For the glycosylation MPA experiments, we showed that the loss of O-mannosylated glycans on E-cadherin expressed on either POMGnT1 or POMT2 deficient HEK293T cells resulted in significantly lower affinities by 1.9 and 2.5 fold respectively compared to wild type E-cadherin expressed on wild type HEK 293T cells. This supports the suggestion by Lommel et al. [339] that hypo O-mannosylation impairs the binding function of E cadherins.

5.5 Figures and tables

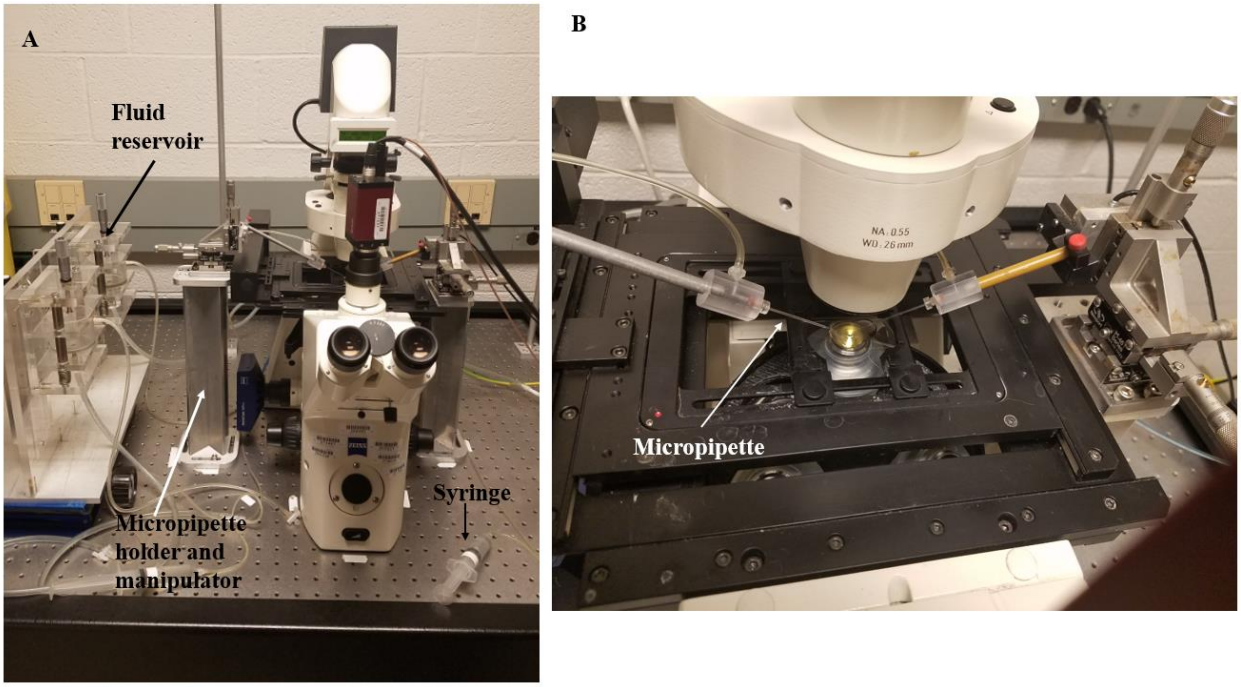

Figure 5.1: (A) Micropipette Aspiration Assay setup and (B) a zoomed in view of two micropipettes focused on the microscope stage.

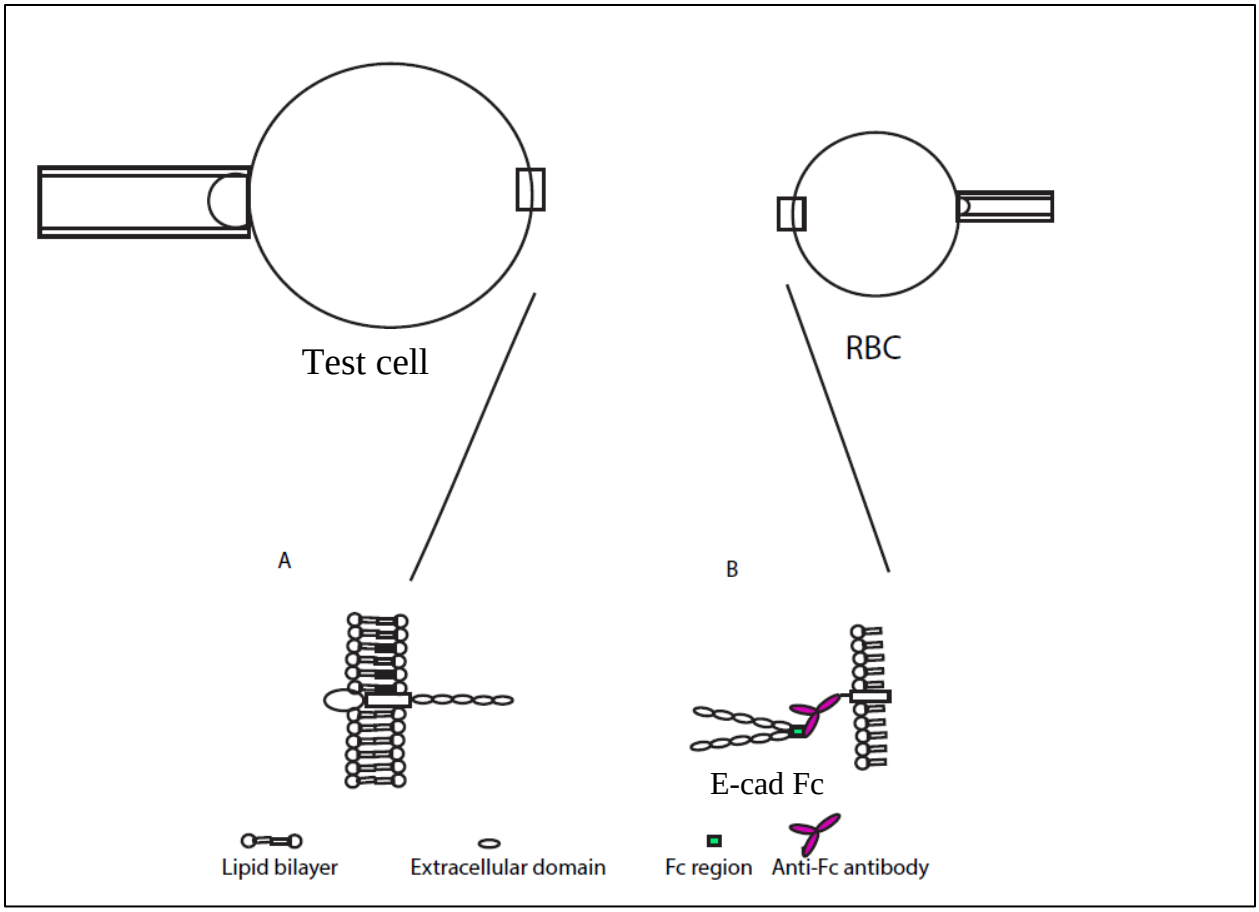

Figure 5.2: Schematic of the micropipette setup. A test cell expressing membrane bound wild type E-cadherin is aspirated using a micropipette of diameter ~ 7.2 μm^2. (a) On the other micropipette of diameter ~1.5 μm^2 a red blood cell (RBC) modified with full length E-cadherin constructs is aspirated. For affinity measurement experiments, E-cadherin EC1-5 Fc is covalently attached with anti-Fc antibody on the RBC membrane.

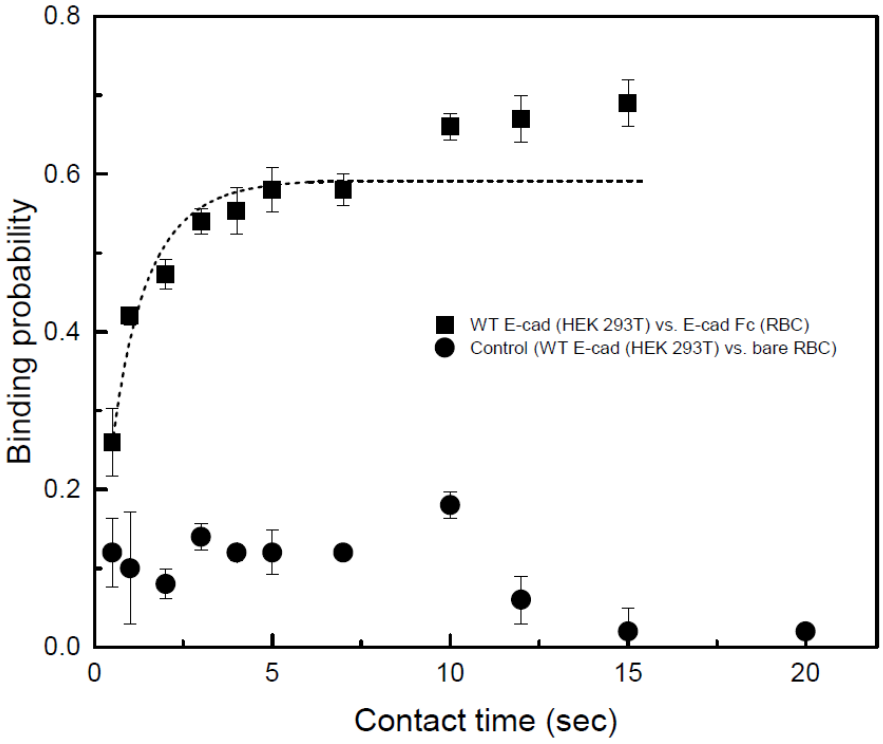

Figure 5.3: Binding affinity measurement of WT E-Cadherin on HEK 293T vs. E-Cad-Fc on RBC.

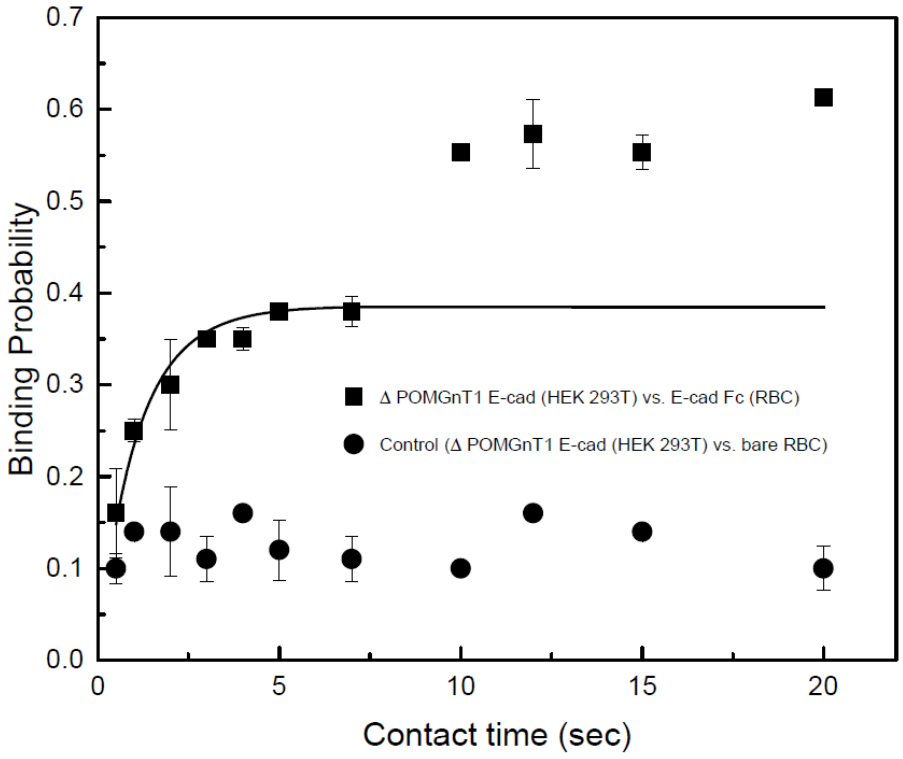

Figure 5.4: Binding affinity measurement of E-Cadherin on POMGnT1 deficient HEK 293T cells vs. E-Cad-Fc on RBC.

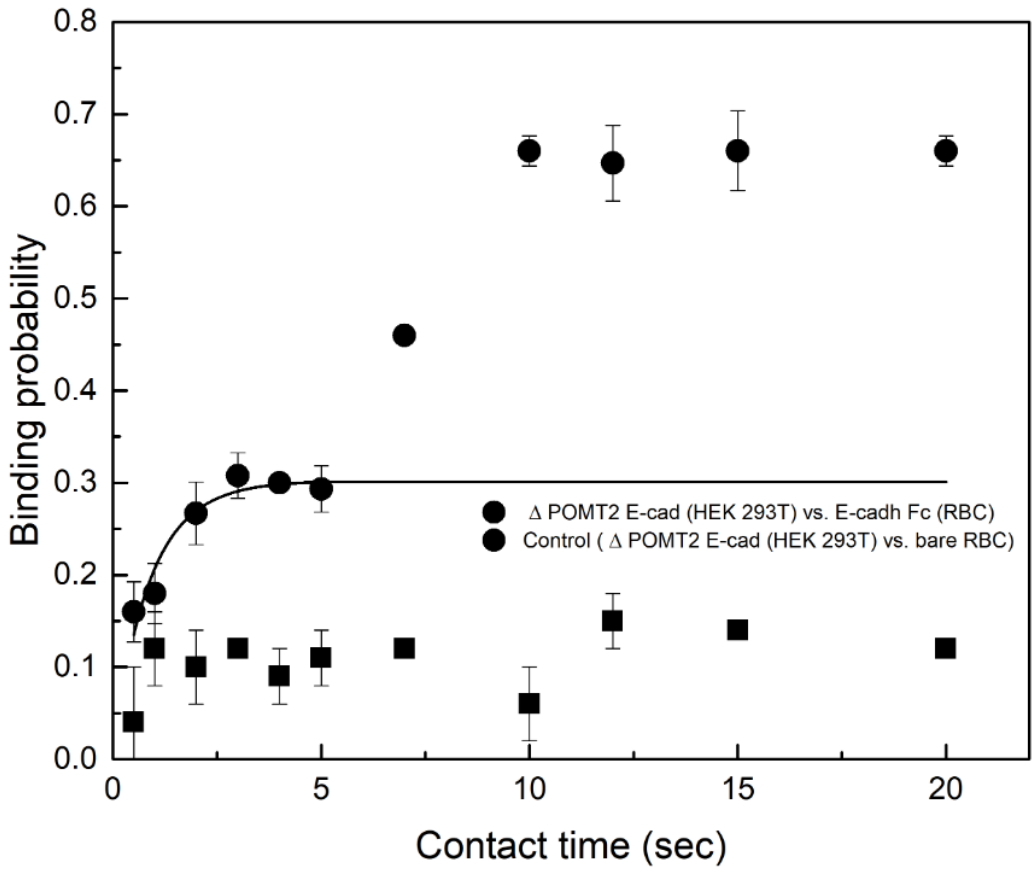

Figure 5.5: Binding affinity measurement of E-Cadherin on POMT2 deficient HEK 293T cells vs. E-Cad-Fc on RBC.

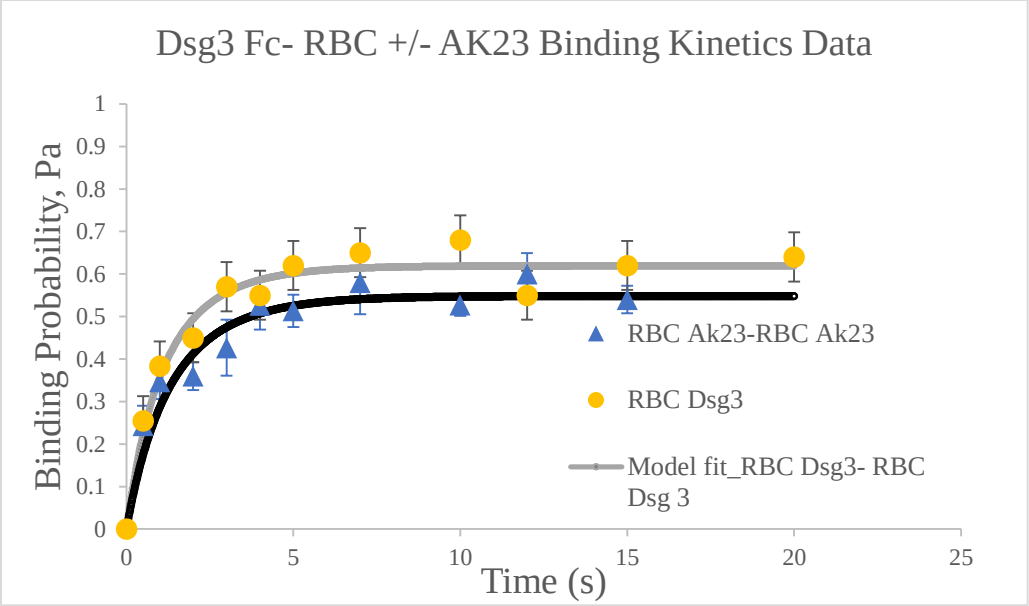

Figure 5.6: Binding affinity measurement of red blood cells modified with Dsg3; without antibody AK23 (data in yellow circles, fit to model in gray solid line) and with antibody (blue triangle, black solid line).

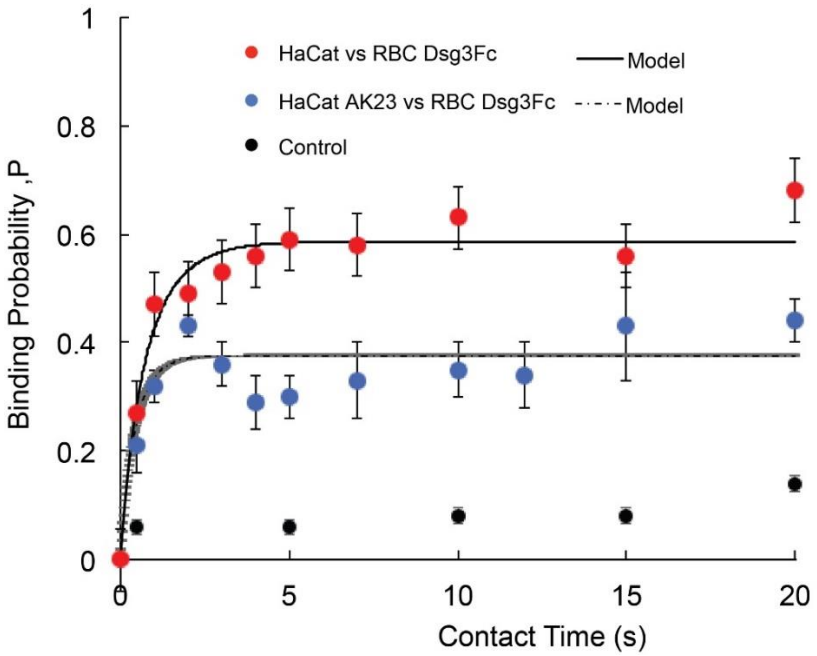

Figure 5.7: Binding affinity measurement of HaCat cells modified with Dsg3 against red blood cells modified with Dsg 3 Fc; without antibody AK23 (data in red circles, fit to model in solid line) and with antibody (blue circles, dash-dotline). The control is HaCat cells with naked RBCs (black circles)

Table 5.1: Fitted parameters of model in Equation 5.5. The estimates are mean values ± SEM.

Model Parameters	**Estimates**	**Units**
K_a	1.35 (± 0.07)x10^{-4}	μm^2
k_{off}	0.8 ± 0.1	s^{-1}
m_r	33	cadh/μm^2
m_l	28	cadh/ μm^2
A_c	7.2	μm^2

Table 5.2: Fitted parameters of model in Equation 5.5. The estimates are mean values ± SEM.

Model parameters	**Estimates**	**Units**
K_a	7.33 (± 0.03) x10^{-5}	μm^2
k_{off}	0.8± 0.1	s^{-1}
m_r	33	cadh/μm^2
m_l	28	cadh/ μm^2
A_c	7.2	μm^2

Table 5.3: Fitted parameters of model in Equation 5.5. The estimates are mean values ± SEM.

Model parameters	**Estimates**	**Units**
K_a	5.45 (± 0.03) $x10^{-5}$	μm^2
K_{off}	1.1 ± 0.2	s^{-1}
m_r	33	cadh/μm^2
m_l	28	cadh/ μm^2
A_C	7.2	μm^2

Table 5.4: Micropipette Aspiration Assay data for Dsg-3 Fc RBC-RBC. The estimates are mean values ± SEM.

Experiment	Parameters	Value	Units
RBC AK23-Dsg3-RBC AK23-Dsg3			
	m_R	56	cadherins/um^2
	m_L	56	cadherins/um^2
Known	A_C	7.2	um^2
	K_a (2D)	3.2 (± 0.07) $x10^{-5}$	um^2
Calculated	koff	1.0 (+/- 0.1)	sec^{-1}
RBC Dsg3-RBC Dsg3			
	m_R	64	cadherins/um^2
	m_L	64	cadherins/um^2
Known	A_C	7.2	um^2
	K_a (2D)	4.1 (± 0.6)$x10^{-5}$	um^2
Calculated	koff	0.6 (+/- 0.1)	sec^{-1}

Table 5.5: Micropipette Aspiration kinetics data for HaCat Dsg3 +/- AK23 Binding Kinetics

Parameters	Symbol	Value	Unit
HaCat –Dsg3 Fc RBC			
Known:	mR	54	cadherins/um^2
	mL	38	cadherins/um^2
	Ac	7.2	um^2
Calculated:			
	K_a (2D)	6.0 (± 0.3)X10^{-5}	um^2
	koff	1.0 ±0.2	sec^{-1}
HaCat AK23 –Dsg3 Fc RBC			
Known:	mR	54	cadherins/um^2
	mL	38	cadherins/um^2
	Ac	7.2	um^2
Calculated:			
	K_a (2D)	3.0(± 0.2)X10^{-5}	um^2
	koff	2.0 ± 0.1	sec^{-1}

CHAPTER 6: CONCLUSIONS AND FUTURE DIRECTIONS

6.1 Conclusions

6.1.1 Investigating interactions with polyzwitterions and proteins at the nanoscale

Here, we demonstrated that protein adsorption on end-grafted, zwitterionic poly(sulfobetaine) (pSBMA) thin films depends on the grafting density, molecular weight, and ionic strength. Zwitterionic polymers exhibit ultralow nonspecific fouling (protein adsorption) and excellent biocompatibility. This picture contrasts with a recent report that soluble pSBMA chains bind proteins and alter the protein folding stability. To address this apparent contradiction, the dependence of protein adsorption on the chain grafting parameters was investigated: namely, the grafting density, molecular weight, and ionic strength. Studies compared the adsorption of phosphoglycerate kinase and positively charged lysozyme versus the scaled grafting parameter $s/2R_F$, where s is the distance between grafting sites and R_F is the Flory radius. Plots of the adsorbed protein amount versus $s/2R_F$ exhibit a bell-shaped curve, with a maximum near $s/2R_F \approx 1$ and an amplitude that decreases with ionic strength. This behavior is qualitatively consistent with theoretical models for colloid interactions with weakly attractive, grafted chains. The results confirm that proteins do adsorb to pSBMA thin films, and they suggest an underlying mechanism. Comparisons with polymer models further identify design rules for pSBMA films that effectively repel protein.

6.1.2 Effect of ionic strength and grafting density on gorces between grafted poly(sulfobetaine) films and mica

The molecular surface properties of grafted zwitterionic polymers are central to their ultra-low fouling properties and effectiveness as steric stabilizers. Here we reported Surface Force Apparatus

measurements of the interfacial forces of end-grafted poly(sulfobetaine) methacrylate as a function of chain grafting density, molecular weight, and ionic strength. Forces were quantified between end-grafted chains and mica, at low and high grafting densities. The ionic strength of solution was varied from 54 mM to 1044 mM. At high grafting densities, the equilibrium chain extension increased ~1.6 fold, as total ionic strength increased from 54 mM to 1044 mM. Although the ranges of repulsive forces did not change significantly between 144 mM and 1044 mM, the brushes were less compressible at the highest ionic strength of 1044 mM. At low grafting density, the repulsive force increased exponentially with decreasing separation distance. The exponential decay constant depended on the ionic strength, and increased to nearly six times the Flory radius, in 1044 mM. These results demonstrate that grafted poly(sulfobetaine) exhibits characteristic swelling behavior, distinct from that of both neutral, water soluble poly(ethylene glycol) and polyelectrolytes. The findings reveal how polymer coverage and salt concentration tune the range and magnitude of the repulsive barrier generated by grafted poly(sulfobetaine) thin films.

6.1.3 Tuning interfacial energies by changing composition of random statistical polymer with zwitterionic content

This study investigated the interfacial forces associated with end-grafted, statistical (AB) co-polymers of sulfobetaine and oligoethylene glycol (poly(SBMA-co-OEGMA)). Surface force apparatus measurements of copolymers containing 0, 40, or 80 mole% sulfobetaine methacrylate (SBMA) compared the interfacial forces of end-grafted thin films at low density (weakly-overlapping chains) and at high density (brushes). At high density, the range of repulsive forces did not change significantly with increasing SBMA content, but at low chain density, both the range and the amplitude of repulsion increased with the percentage of SBMA in the chains. The ionic strength dependence of the chain extension and repulsive forces increased similarly with

SBMA content, reflecting the increasing influence of charged monomers and their interactions with ions in solution. The proportional change in surface forces with SBMA content suggests that ethyene glycol and sulfobetaine behave as non interacting, miscible monomers that contribute independently to the polymer extension and chain interactions with ions. The results suggest that the interfacial properties of the copolymer thin films can be readily tuned by simple variation of the copolymer content.

6.1.4 Binding frequency measurement of cell adhesion molecules

In this study we showed that the binding kinetics and fitted binding constants measured between Dsg3 ectodomains on two opposing RBCs were statistically similar to values determined with HaCaT cells. The latter result ruled out any contribution from heterophilic Dsg3 binding to other possible interactors on HaCaT cells. Treatment of HaCaT cells with pemphigus antibody AK23 lowered the amplitude of the steady-state plateau, and corresponding binding affinity. Initial analyses suggest that AK23 increased the off-rate without altering the on-rate. The latter might argue against steric interference: merely blocking the active site would reduce the association rate, but not necessarily the off-rate. Future experiments will be carried out to test this hypothesis. Comparison of results obtained with Dsg3-Fc versus Dsg3 in the cell context also reveals cellular influences on Dsg3 binding. In addition to quantifying Dsg3 binding parameters, future work will similarly compare the results with models for competitive inhibition and negative allosteric inhibition by quantifying the affinity as a function of antibody concentration.

For the glycosylation MPA experiments, we showed that the loss of O-mannosylated glycans on E-cadherin expressed on either POMGnT1 or POMT2 deficient HEK293T cells resulted in significantly lower affinities (by 1.9 and 2.5 fold respectively) compared to wild type E-cadherin

expressed on wild type HEK 293T cells. This supports the suggestion by Lommel et al. [339] that hypo O-mannosylation impairs the binding function of E cadherins.

6.2 Future directions

In this thesis we have seen that grafted zwitterionic polymers have the potential to be used for modifying underlying surfaces to facilitate or prevent protein adsorption, tune surface forces or osmotic repulsion barriers depending on the ionic strength of the medium, grafting densities, molecular weight of polymer and/or copolymer. The construction of random copolymers using two chemical structurally different, but compatible homopolymers of OEGMA and pSBMA have been shown to have potential for tuning surface energies of grafted surfaces at different ionic strengths, at varying copolymer compositions. In this chapter I will discuss extending our knowledge of grafted brush made of polyzwitterions, and/or copolymers with zwitterions for the study of protein folding at interfaces.

6.2.1 Proteins at interfaces

A universal challenge for all technologies that exploit the unique functions of bio-macromolecules as device components is to preserve their unique functions in artificial environments. The variety of both potential and realized applications is vast and includes biosensors, functionalized biomaterials, immobilized enzymes, drug carrier targeting, small molecule detection, and many more. However, upon adsorption on surfaces due to high surface energy, the immobilized proteins tend to lose activity caused by accelerated unfolding [341] (relative to soluble protein, for example) and form protein corona (non-specific protein adsorption) resulting in decreasing sensitivity of the device or loss of performance, reduced shelf lives etc. The inactivation of high value proteins also substantially increases material costs. This is a long-standing problem, and thus, the challenge

remains to establish robust design criteria that preserve protein stability and function, based on fundamental knowledge of material interactions that degrade or enhance macromolecular stability. Proteins are only marginally stable, with ΔG_f typically 5-8 kcal/mole. [342] Interfacial properties such as local dielectric constants, surface charge densities, hydrogen bonding surface groups, and local pH could perturb folding energies and protein structures. However, our limited understanding of physical chemical links between surface chemistry, interfacial force fields and protein folding energies is a major obstacle to identifying materials design guidelines that preserve biochemical function in non biological contexts.

From our previous chapters we have seen that polyzwitterions are great candidate for tuning protein adsorption on grafted substrates, and they provide means of tuning surface energies that control protein-material interactions. In future work, this knowledge can be extended to identify the causal relationship between surface chemistries and protein folding stability.

The hypothesis is that highly solvated surface groups like sulfobetaines, caroxybetaines as well as polymers generate repulsive steric barriers that repel proteins, but also have low interfacial energies in water and therefore, such surface chemistries should favor the folded state of proteins. Previous study with proteins at interfaces with grafted copolymers at varying zwitterionic content, it was postulated that the segregation of hydrophilic groups on the zwitterionic monomer near the hydrophilic region of the protein surface and the segregation of amphiphilic OEGMA near the hydrophobic patches on the protein result into increasing folding stability. [192] However, this hasn't been experimentally proven , especially for cases when proteins form attractive protein-segment interactions upon penetration into the brush (ternary adsorption) which is more likely to take place at an intermediate grafting densities of the said copolymers. Such interactions with proteins will prove its efficacy as biomaterials to be used for protein carrying drugs.

The folding stability of proteins immobilized on zwitterionic polymers have not been previously determined, despite many studies showed that these low fouling coatings are assumed to also be protein compatible, regardless of their different compositions.[228,343–345] Using fluorimeter in bulk polymer solution, Kisley et al. showed that soluble polysulfobetaine chains directly interact with structurally different proteins, causing a decrease in melting temperature, which is an indication of protein instability. [195] For a preliminary test of our hypothesis, copolymers of OEGMA and SBMA monomers will be synthesized in bulk solution, and the tryptophan fluorescence of different proteins will be monitored to collect information about the melting temperatures (section 6.2). We expect that at intermediate %SBMA content the % of folded population will increase, which will be indicated by an increase in melting temperature of the proteins. The protein-material interactions can be quantified at sub nm-resolution with Surface Force Apparatus (section 6.3). And finally the protein folding dynamics at the interface of grafted brushes will be studied in temperature jump study using a Fast Relaxation Imaging technique (section 6.4).

For conditions where proteins do adsorb on the grafted zwitterionic polymer brush/mushroom like chains, such as- intermediate grafting densities at low ionic strength, it will be interesting to investigate upon adsorption, do proteins retain their functionalities i.e. remain folded? In addition to polyzwitterionic homopolymers, copolymers with varying zwitterionic composition can also be tested to identify surface chemistries that stabilize or destabilize proteins.

The details of the experimental setup and characterization of the copolymers are discussed in the following sections.

6.2.2 Protein folding in copolymer solutions

Influence of protein folding in presence of copolymers consisting of zwitterionic monomers can be studied by temperature melts of a protein in solution in a fluorimeter. The procedure and sample preparation of this study is described in details below for archival purpose only. The experimental results were inconclusive and therefore the studies need to be repeated in the future. A few recommendations to improve the technique are added at the end of this subsection. The fluorimeter readings were carried out by Roger Chang, Ph.D candidate in Chemical and Biomolecular Engineering. The synthesis of the copolymer, the characterization by Dynamic Light Scattering was performed by myself.

6.2.2.1 Materials and methods

Chemicals: Monomer 2-(Methacryloyloxy) ethyl] dimethyl-(3- sulfopropyl) ammonium hydroxide or SBMA (95%, MW 279.35) was purchased from Sigma- Aldrich (Product # 537284, St Louis, MO). Monomer poly(ethylene glycol) methacrylate or PEGMA (MW 500, containing 900 ppm monomethyl ether hydroquinone, MEHQ as inhibitor) was purchased from Sigma-Aldrich (Product # 409529, St Louis, MO). Initiator 1- (phthalimidomethyl) 2-bromoisobutyrate (MW 326.14) was purchased from Sigma-Aldrich (Product # 777277, St Louis, MO). Ligand 1,1,4,7,10,10-Hexamethyltriethylenetetramine or HMTETA (97%, MW 230.39) was purchased from Sigma-Aldrich (Product # 366404, St Louis, MO). Copper (I) bromide and Copper (II) Bromide were (Product # 254185 and 221775, respectively) purchased from Sigma-Aldrich (St Louis, MO). Ultrapure water (resistance 18.2 MΩ cm at 25 °C) was obtained using Synergy UV (Millipore Sigma) water purification system and pure methanol was purchased from Thermo Fisher Scientific. Sodium phosphate (dibasic, anhydrous) was from Ward's Science (ON, Canada, Product # 470302-660).

Synthesis of poly(SBMA-co-PEGMA): Bulk copolymer with pSBMA and PEGMA was synthesized by atom transfer radical polymerization based on the method reported by Sundaram et al. In a round bottom flask, monomer [2-(Methacryloyloxy)ethyl]dimethyl-(3-sulfopropyl)ammonium hydroxide (SBMA) and monomer poly(ethylene glycol) methacrylate (PEGMA) was dissolved in 0:1, 1:3, 1:1, 3:1 and 1:0 molar feed ratio in 1:1 volumetric mixture of methanol and water to a final concentration of 0.2 M. Before synthesis the inhibitor MEHQ in PEGMA monomer was removed by running the mixture solution in a column containing inhibitor remover beads, available commercially (Sigma-Aldrich, Product # 311332). The monomer solution was first degassed with a glass frit and kept under Ar gas (ultra-high purity grade) at all time throughout the reaction. Then $CuBr_2$, ligand HMTETA, CuBr and initiator were added to the flask to a final concentration of 0.147, 0.074, 0.711 and 5 mM in this order. The polymerization reaction proceeded at room temperature with stirring under Ar atmosphere for 24 h. After synthesis, the reaction was stopped by exposure to air and excess solvent was removed by a rotary evaporator. The polymer precipitate was dissolved in 1.5 M $NaNO_3$. Heat was briefly applied by heat gun to assist in removal of the polymer from the sides of the flask. The salt solution was then exchanged with pure Millipore water by placing the polymer solution in a dialysis tubing with a molecular weight cutoff of 3500 Da (ThermoFisher, SnakeSkin), exchanging every 8-12 hours for three times. The final polymer was recovered by removing excess water by rotary evaporation and then dried under high vacuum (0.01−0.05 Torr). The final product was stored in dry scintillation vials before use.

Hydrodynamic Radius and Polydispersity measurement by Dynamic light scattering (DLS): DLS measurements were performed using an Anton Paar Litesizer 500 running Kalliope software. A 40 mW single frequency laser diode was used at 658 nm with an avalanche photo diode detector. The

scattered light was detected at an angle of 175° (back scatter) for samples containing 0 mM or 10 mM NaCl and at an angle of 90° (side scatter) for all other samples. The temperature was allowed to stabilize to 22 °C for 1 min before measurements. The particle hydrodynamic radius (R_h) and polydispersity index (PDI) were calculated using an advanced cumulant fit of the measured intensity autocorrelation function. Reported values are an average of three separate measurements and the bars represent the standard deviation from the mean (details of DLS measurements are given in *Appendix A*).

Fluorimeter Measurements and Analysis of Protein: The protocol was established by Dr. Lydia Kisley in the published journal article: Kisley L, Serrano KA, Davis CM, et al. Soluble Zwitterionic Poly(sulfobetaine) Destabilizes Proteins. Biomacromolecules. 2018;19(9):3894-3901. doi:10.1021/acs.biomac.8b01120]

Copolymer solutions were prepared at 0.05 to 5% (w/w) polymer and 0 to 1 M $NaNO_3$ concentrations in 20 mM sodium phosphate buffer, pH 7. To ensure disruption of the inter- and intramolecular interactions of the sulfobetaine monomers upon initial preparation, the copolymers solutions were placed in a 70 °C water bath for ∼5 min and sonicated. The final solutions were cooled to room temperature and filtered through a 0.45 μm filter (Millipore).

PGK-FRET in HEPES buffer was diluted to 1−7 μM in the respective polymer solutions. The thermal denaturation of the proteins was measured with a Jasco spectrofluorimeter FP-8300 in a 1 cm path length quartz cuvette. Mineral oil was placed on top of the protein solutions to prevent evaporation. The temperature was increased in 2 °C steps at a heating rate of 120 °C hr−1 with a 180 s equilibration time before each spectral measurement from 20^0C to 62^0C, allowing 2 minutes of equilibrating after each temperature increase. The donor and emission wavelengths used are 507 nm (mEGFP emission wavelength) and 610 nm (mCherry emission wavelength) and the ratio of

intensities is used to calculate D/A. From the resulting fluorescence thermal unfolding data of λ_{max} versus temperature, T, the thermal denaturation midpoint, Tm, and thermal folding cooperativity parameter, δg_1, were obtained from fitting to Equations 6.4 to 6.7 [346] in OriginPro 2015:

$$\langle\lambda\rangle = (m_F T+b_F) f_F+(m_U T+b_U)f_U \qquad \text{Eq. 6.4}$$

where the fraction of folded, f_F, and unfolded, f_U, protein is given by-

$$f_F=\exp[-\Delta G/RT]/(1+\exp[-\Delta G/RT]) \qquad \text{Eq. 6.5}$$

$$f_U=1-f_F \qquad \text{Eq. 6.6}$$

and the dependence of free energy, ΔG, on temperature over a narrow temperature range is represented by the linear expansion: $\Delta G \approx \delta g_1(T-Tm)$.[347] Eq. 6.7

Here, the T_m is the temperature at which f_F and f_U are equal and is located at the inflection point of the sigmoidal curve. The 'cooperativity index,' δg_1, is a measure of the slope of the transition from folded to unfolded states and indicates how likely unfolding of one region of the protein causes disruption and unfolding of other regions. Linear baselines with slopes, *m*, and offsets, *b*, above and below T_m (*i.e.*, folded, *F*, and unfolded, *U*) are also obtained. The calculated T_m from the fit to the curve of peak wavelength of emission, λ vs. temperature gives 40^0C.

6.2.2.2 Preliminary results:

DLS measurements. DLS measurements confirmed that the copolymer chains follows the expected anti-polyelectrolyte effect. At low salt concentrations below 50 mM, sulfobetaine monomers in the copolymer aggregate, having μm-sized R_h due to strong inter- and intramolecular interactions between the zwitterionic components. At salt concentrations above 50 mM the intermolecular interactions are disrupted, which is more prominent with increasing %ZI content. The R_h is approximately 30 nm and 60 nm beyond $NaNO_3$ concentration of 50 mM for 25 and 50% SBMA content in the copolymers (Figure 6.1) with a polydispersity less than 30% which shows that the

polymers are moderately polydisperse. With 100% pSBMA homopolymers the hydrodynamic radius, R_h is 30 ± 3 nm in more than 1 M NaCl.[8, 17] Previously Kisley et al. measured the hydrodynamic radius of PEG 600 KDa (Acros Organics 178612500) solution of 5% (w/w) in 20 mM sodium phosphate buffer, pH 7, and 1.5 M NaCl to be 5.36 ± 0.05 nm at PDI =10.3 ± 0.6.

Fluorimeter measurements. The melt curve of PGK-FRET proteins deviate significantly from their signature D/A curve (shown in Figure 6.2.A) possibly due to impurities, and/or insoluble polymer aggregates (Figure 6.2B-D). The opacity of the solution may have contributed to its low signal and incorrect curvature of D/A when calculated. This will be reviewed during the bulk synthesis step. At this time, results are inconclusive of the bulk polymer effect on protein folding stability. Future experiments will be carried out with less polydisperse copolymer samples, void of impurities during the purification process.

6.2.3 Measurement of protein-material interactions

Sensitive force probe measurements with Surface Force Apparatus (SFA) will quantify nanoscale, interfacial forces associated with surface chemistries and their impact on protein-material attraction/repulsion. The SFA arrangement is shown in Figure 6.4. The SFA can be employed for polyzwitterions such as- polysulfobetaine, polycarboxybetaine, polyphosphorylcholine or mixed brushes by ATRP growth from method which allow grafting of chains with Br-terminated initiators on substrates (for example- thiol conjugated gold substrate). On the other surface, a back silvered mica can be used to deposit lipid bilayer by Langmuir-Blodgett technique. His-tagged PGK will be immobilized to the lipid bilayer by EDC/NHS chemistry to Ni-NTA. [348]

By employing SFA, the objective is to quantify molecular forces between proteins and surface chemistries (Figure 6.4 and 6.5), and test current hypotheses regarding relationships between assumed protein repulsion (or attraction) by these materials and their biological activity. Force

measurements give the range and magnitude of protein-material forces that support nonspecific adsorption or alter immobilized protein stability/function and these measurements will complement the bulk protein fluorescence measurements, discussed in section 6.2.

6.2.4 Fast Relaxation Imaging (FReI) technique for studying protein folding dynamics

A novel approach to study interactions of protein on brush modified surfaces, in situ at the single molecular level is developed by Gruebele.[349] The technique is called Fast Relaxation Imaging or FReI, which enables studying the folding/unfolding dynamics of single proteins combining imaging capability of fluorescence resonance energy transfer (FRET) reporters with localized temperature jumps on surfaces. Following a brief (~15ps) temperature jump of every 5°C to induce partial unfolding of proteins, a spatial map of protein folding dynamics in an observation volume can be recorded at micron resolution. This is a powerful technique which give information at the interfaces between proteins and brushes that we are most interested in. Conventional techniques like fluorescence measurement in bulk solution of proteins and polymers do not capture the surface level information. In previous studies, they demonstrated that a model protein, Phsophoglycerate kinase (PGK) that is immobilized on gold nanorods is more stable than PGK in solution.[350] Here using this technique, we will study protein folding dynamics for intermediate grafting densities where proteins are allowed to penetrate into the brush and form attractive protein-segment interactions for grafted polyzwitterions or mixed charge polymers (Figure 6.5).

6.2.5 Immobilization of proteins for FReI measurements

PGK can be immobilized in the following ways-

(1) on Ni-NTA-functionalized OEG-terminated SAM (Fig. 6.5A),

(2) on supported lipid bilayers (Fig. 6.4),

(3) non-specifically adsorb PGK proteins to pSB , to pCB or Mixed chain (MC) polymer or various statistical copolymers, including poly(OEGMA-co-SBMA) chains at non-overlapping chains or intermediate chain grafting densities $0<s/2R_F<1$,

(4) site selectively immobilized to NTA-functionalized peptide monolayers (Fig. 6.5B); The N-terminal amines of peptide monolayers will be functionalized with AB-NTA. Peptides with C-terminal Cys and protected lysines will be assembled on gold by gold-thiol chemistry. After glutaraldehyde activation of the N-terminal amines and cross-linking to AB-NTA, the lysines will be deprotected, and PGK-His_6 will be immobilized.

(5) to PCB and MC polymers (Fig. 6.5C); His-tagged PGK will be immobilized to polycarboxybetaine or mixed charged polymers, by lightly activating carboxyl side chains with EDC/NHS, followed by AB-NTA coupling.[11, 12] We would then bind His-tagged PGK to the NTAfunctionalized polymers.

These studies will open new avenues for interrogating surface chemical influences on proteins in situ, and inform a range of applications incorporating immobilized proteins.

6.2.6 Significance

The future studies will test a fundamental hypothesis that interfacial force fields and consequent protein-material interactions determine the stability of immobilized proteins. By exploiting unique complement of molecular level force measurements and bio-macromolecular folding studies—at the level of individual protein motions—we will be able to identify causal links between surface chemistries and the interfacial forces that preserve or shut down protein functions. The outcomes of these studies will enable new molecular level design rules that preserve or enhance the functions of high value, immobilized biomacromolecules.

6.3 Figures

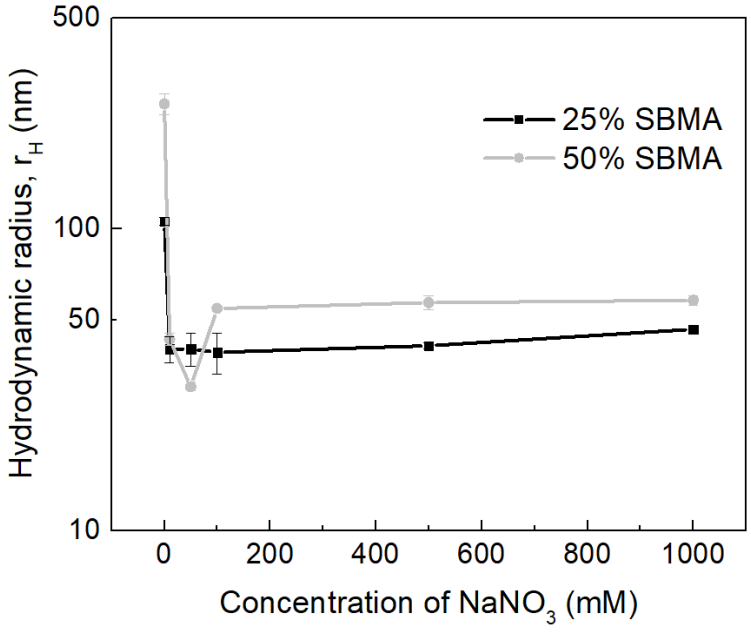

Figure 6.1: Hydrodynamic radius measurement of poly(SBMA-co-OEGMA) chains in 20 mM sodium phosphate buffered solution as a function of the $NaNO_3$ concentration by Dynamic Light Scattering (DLS).

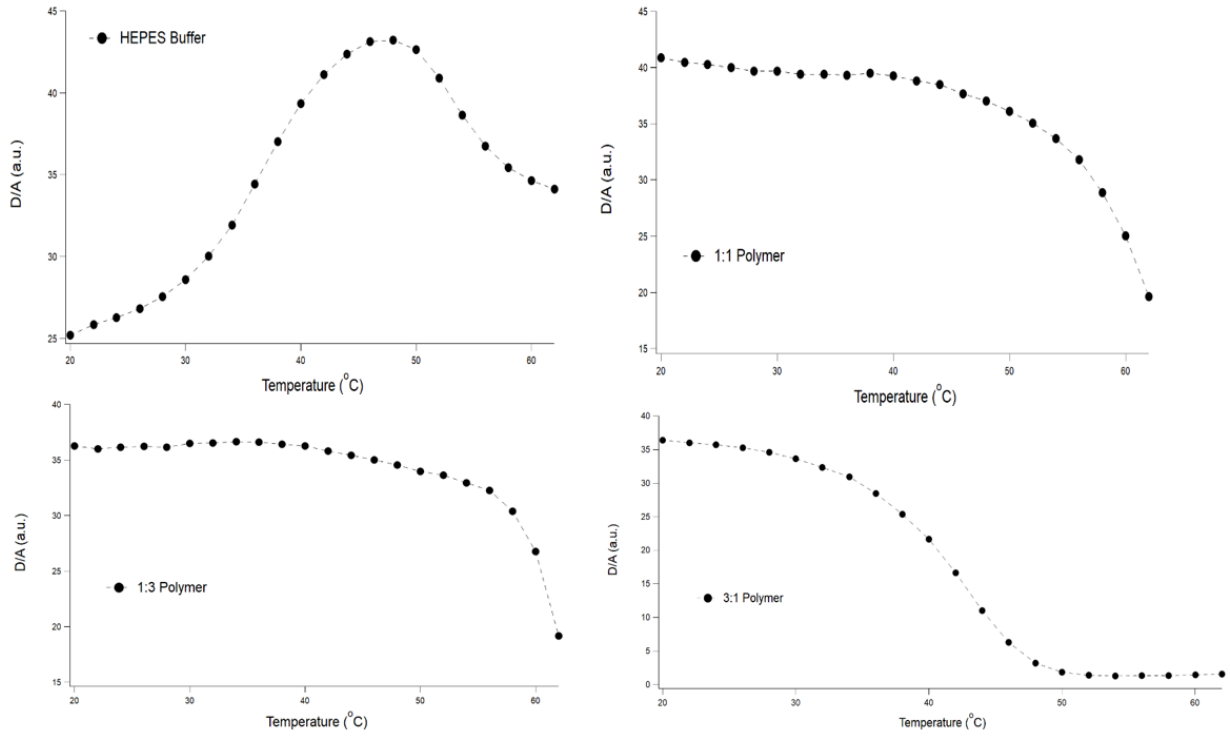

Figure 6.2: Fluorimeter measurements of bulk protein solutions from 20 to 62^0C temperature at 2^0C increment in presence of 1:1, 1:3 and 3:1 SBMA: OEGMA copolymer in 0.5 wt% in HEPES buffer solution with added 100 mM $NaNO_3$ salt. (A) The typical melt curve of PGK-FRET protein is shown here. It starts off at a low D/A ratio and then proceeds to increase in D/A as the temperature increases and then protein unfolds, resulting in decrease D/A. (B)-(D) show a different melt curves of the protein, possibly due to the opaqueness of the samples tested here.

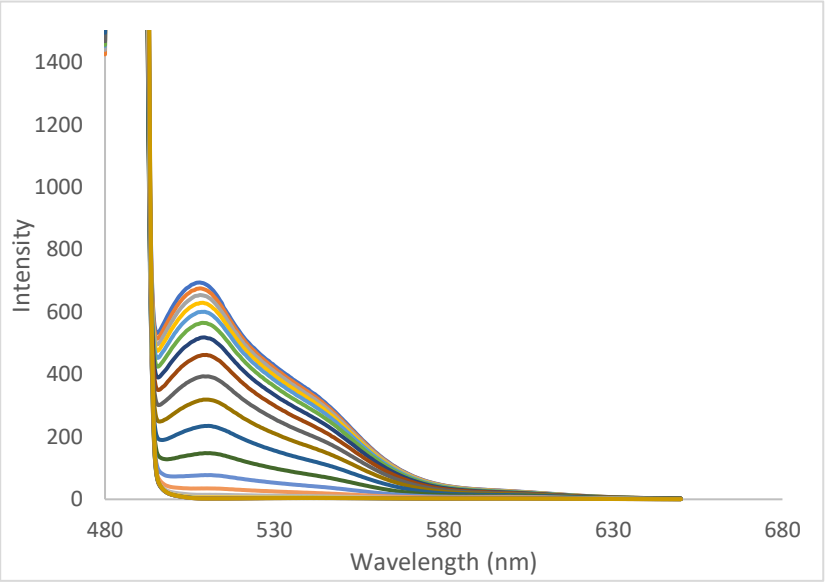

Figure 6.3: A typical wavelength scan of PGK-FRET protein in HEPES across all temperatures with each wavelength decreasing in intensity as temperature increases. The scan was taken from 480 nm to 650 nm with each temperature.

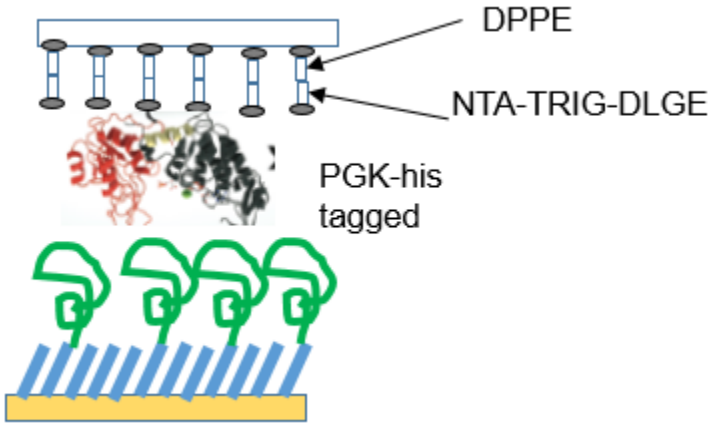

Figure 6.4: Surface Force Apparatus arrangement for measuring interactions between his-tagged protein immobilized on lipid bilayer (NTA-functionalized lipid and DPPE) on mica and grafted polyzwitterions on gold coated substrates.

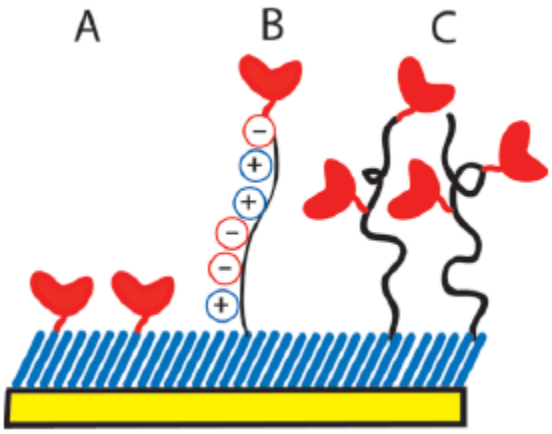

Figure 6.5: Protein immobilization for FReI Studies. (A) His-tagged PGK will be immobilized to terminal NTA terminal groups on mixed COOH/OEG-SAMs, to (B) end functionalized peptides, and (C) to functionalized MC and PCB brushes.

REFERENCES

1. Ratner BD. Reducing capsular thickness and enhancing angiogenesis around implant drug release systems. *J Control Release*. 2002;78:211-218.
2. Anderson, J.M., Rodriguez A, Chang DT. Foreign body reaction to biomaterials. *Semin Immunol*. 2008;20:86-100.
3. Tsai WB, Grunkemeier JM, Horbett TA. Human plasma fibrinogen adsorption and platelet adhesion to polystyrene. *Biomed Mater Res*. 1999;44(2):130-139.
4. Jiang S, Cao Z. Ultralow-fouling, functionalizable, and hydrolyzable zwitterionic materials and their derivatives for biological applications. *Adv Mater*. 2010;22(9):920-932.
5. Callow JA, Callow ME. Trends in the Development of Environmentally Friendly Fouling-resistant Marine Coatings. *Nat Commun*. 2011;2(244):10.
6. Dobretsov S, Abed RMM, Teplitski M. Mini-review: Inhibition of Biofouling by Marine Microorganisms. *Biofouling*. 2013;29(4):423-441.
7. Nie F-Q, Xu Z-K, Huang X-J, Ye P, Wu J. Acrylonitrile-based copolymer membranes containing reactive groups: surface modification by the immobilization of poly(ethylene glycol) for improving antifouling property and biocompatibility. *Langmuir*. 2003;19:9889–9895.
8. Wang YQ, Wang T, Su YL, Peng FB, Wu H, Jiang ZY. Protein adsorption resistance and permeation property of polyethersulfone and soybean phosphatidylcholine blend ultrafiltration membranes. *J Memb Sci*. 2006;270(1-2):108-114.
9. Sakai-Kato K, Kato M, Ishihara, Kazuhiko, Toyo'oka T. An enzyme-immobilization method for integration of biofunctions on a microchip using a water-soluble amphiphilic phospholipid polymer having a reacting group. *Lab Chip*. 2004;4:4-6.

10. Prime K, Whitesides G. Self-Assembled Organic Monolayers: Model Systems for Studying Adsorption of Proteins at Surfaces. *Science (80-).* 1991;252(5009):1164-1167.

11. Zhang L, Cao Z, Bai T, et al. Zwitterionic hydrogels implanted in mice resist the foreign-body reaction. *Nat Biotechnol*. 2013;31(6):553-556. doi:10.1038/nbt.2580

12. Young G, Bowers R, Hall B, Port M. Clinical Comparison of Omafilcon A with Four Control Materials. *CLAO J*. 1997;23(4):249−258.

13. Mizuna Kimura MT, Ishihara K. Biocompatibility and drug release behavior of spontaneously formed phospholipid polymer hydrogels. *J Biomed Mater Res Part A*. 2006;79(4):963-973.

14. Sun JT, Yu ZQ, Hong CY, Pan CY. Biocompatible zwitterionic sulfobetaine copolymer-coated mesoporous silica nanoparticles for temperature-responsive drug release. *Macromol Rapid Commun*. 2012;33(9):811-818.

15. Lynn, A.D., Kyriakides, T.R. & Bryant SJ. Characterization of the in vitro macrophage response and in vivo host response to poly(ethylene glycol)-based hydrogels. *J Biomed Mater Res A*. 2010;93:941-953.

16. Campioni EG, Nobrega JN, Sefton MV. HEMA/MMMA microcapsule implants in hemiparkinsonian rat brain: biocompatibility assessment using [3H]PK11195 as a marker for gliosis. *Biomaterials*. 1998;19(7-9):829-837.

17. Gerhardt W. Oxidation of Polyethyleneoxides and Polyethyleneoxide Ethers-the Formation of Acetaldehyde During the Oxidation of Diethylene Glycol with Oxigen. *Zeitschrift für Chemie*. 1985;25(4):143.

18. Hamburger R, Azaz E DM. Autoxidation of polyoxyethylenic non-ionic surfactants and of polyethylene glycols. *Pharm Acta Helv*. 1975;50(1-2):10-17.

19. Laschewsky A. Structures and synthesis of zwitterionic polymers. *Polymers (Basel)*. 2014;6(5):1544-1601.

20. Zhang Z, Chen S, Chang Y, Jiang S. Surface grafted sulfobetaine polymers via atom transfer radical polymerization as superlow fouling coatings. *J Phys Chem B*. 2006;110(22):10799-10804.

21. Matyjaszewski K, Tsarevsky N V. Nanostructured functional materials prepared by atom transfer radical polymerization. *Nat Chem*. 2009;1(4):276-288.

22. Ladd J, Zhang Z, Chen S, Hower JC, Jiang S. Zwitterionic Polymers Exhibiting High Resistance to Nonspecific Protein Adsorption from Human Serum and Plasma. *Biomacromolecules*. 2008;9(5):1357–1361.

23. Huang CJ, Brault ND, Li Y, Yu Q, Jiang S. Controlled hierarchical architecture in surface-initiated zwitterionic polymer brushes with structurally regulated functionalities. *Adv Mater*. 2012;24(14):1834-1837.

24. Koc J, Schönemann E, Amuthalingam A, et al. Low-Fouling Thin Hydrogel Coatings Made of Photo-Cross-Linked Polyzwitterions. *Langmuir*. 2019;35:1552-1562.

25. Fang K, Wang R, Zhang H, et al. Mechano-Responsive, Tough, and Antibacterial Zwitterionic Hydrogels with Controllable Drug Release for Wound Healing Applications. *ACS Appl Mater Interfaces*. 2020;12(47):52307-52318.

26. Laschewsky A, Rosenhahn A. Molecular Design of Zwitterionic Polymer Interfaces: Searching for the Difference. *Langmuir*. 2019;35(5):1056-1071.

27. Cheng N, Brown AA, Azzaroni O, Huck WTS. Thickness-dependent properties of polyzwitterionic brushes. *Macromolecules*. 2008;41(17):6317-6321.

28. Kisley L, Serrano KA, Davis CM, et al. Soluble Zwitterionic Poly(sulfobetaine)

Destabilizes Proteins. *Biomacromolecules*. 2018;19(9):3894-3901.

29. Foster EL, Xue Z, Roach CM, Larsen ES, Bielawski CW, Johnston KP. Iron oxide nanoparticles grafted with sulfonated and zwitterionic polymers: High stability and low adsorption in extreme aqueous environments. *ACS Macro Lett*. 2014;3(9):867-871.
30. Worthen AJ, Tran V, Cornell KA, Truskett TM, Johnston KP. Steric stabilization of nanoparticles with grafted low molecular weight ligands in highly concentrated brines including divalent ions. *Soft Matter*. 2016;12(7):2025-2039.
31. Zwaal RFA, Schroit AJ. Pathophysiologic implications of membrane phospholipid asymmetry in blood cells. *Blood*. 1997;89:1121-1132.
32. Miyoshi K, Saito K, Shiraishi T, Sugo T. Introduction of taurine into polymer brush grafted onto porous hollow-fiber membrane. *J Membr Sci*. 2005;264:97-103.
33. Nyyssola A. Pathways of glycine betaine synthesis in two extremely halophilic bacteria Actinopolyspora Halophila and Ectothiorhodospira Halochloris. *PhD thesis, Helsinki Univ Technol Finl*. 2001.
34. Andrade JD, Hlady V. Protein Adsorption and Materials Adv., Biocompatibility - a Tutorial Review and Suggested Hypotheses. *Polym Sci*. 1986;79:1-63.
35. Yang W, Chen SF, Cheng G, et al. Film Thickness Dependence of Protein Adsorption from Blood Serum and Plasma onto Poly(sulfobetaine)-Grafted Surfaces. *Langmuir*. 2008;24:9211-9214.
36. Zhang Z, Vaisocherová H, Cheng G, Yang W, Xue H, Jiang S. Nonfouling behavior of polycarboxybetaine-grafted surfaces: Structural and environmental effects. *Biomacromolecules*. 2008;9(10):2686-2692.
37. Vaisocherova´ H, Yang W, Zhang Z, et al. Ultralow Fouling and Functionalizable Surface

Chemistry Based on a Zwitterionic Polymer Enabling Sensitive and Specific Protein Detection in Undiluted Blood Plasma. *Anal Chem*. 2008;80:7894.

38. Nakabayashi N, Williams DF. Preparation of non-thrombogenic materials using 2-methacryloyloxyethyl phosphorylcholine. *Biomaterials*. 2003;24:2431.

39. Zhang X, Lin W, Chen S, Xu H, Gu H. Development of a stable dual functional coating with low non-specific protein adsorption and high sensitivity for new superparamagnetic nanospheres. *Langmuir*. 2011;27(22):13669-13674. doi:10.1021/la202566d

40. Li Y, Giesbers M, Gerth M, Zuilhof H. Generic top-functionalization of patterned antifouling zwitterionic polymers on indium tin oxide. *Langmuir*. 2012;28(34):12509-12517.

41. Nguyen AT, Baggerman J, Paulusse JMJ, van Rijn CJM, Zuilhof H. Stable Protein-Repellent Zwitterionic Polymer Brushes Grafted from Silicon Nitride. *Langmuir*. 2011;27(6):2587-2594.

42. Li G, Cheng G, Xue H, Chen S, Zhang F, Jiang S. Ultra low fouling zwitterionic polymers with a biomimetic adhesive group. *Biomaterials*. 2008;29(35):4592-4597.

43. Zou P, Hartleb W, Lienkamp K. It Takes Walls and Knights Antimicrobial, to Defend a Castle - Synthesis of Surface Coatings from and Antibiofouling Polymers. *J Mater Chem*. 2012;22(37):19579-19589.

44. W. Feng, Zhu S, Ishihara K, Brash JL. Adsorption of Fibrinogen and Lysozyme on Silicon Grafted with Poly(2-methacryloyloxyethyl Phosphorylcholine) via Surface-Initiated Atom Transfer Radical Polymerization. *Langmuir*. 2005;21(13):5980–5987.

45. H. Ma, Hyun J, Stiller P, Chilkoti A. "Non-Fouling" Oligo(ethylene glycol)- Functionalized Polymer Brushes Synthesized by Surface-Initiated Atom Transfer Radical Polymerization.

Adv Mater. 2004;16(4):338-341.

46. Chen S, Yu F, Yu Q, He Y, Jiang S. Strong resistance of a thin crystalline layer of balanced charged groups to protein adsorption. *Langmuir*. 2006;22(19):8186-8191.
47. Zhang Z, Chen S, Jiang S. Dual-functional biomimetic materials: Nonfouling poly(carboxybetaine) with active functional groups for protein immobilization. *Biomacromolecules*. 2006;7(12):3311-3315.
48. Ahmed ST, Leckband DE. Protein Adsorption on Grafted Zwitterionic Polymers Depends on Chain Density and Molecular Weight. *Adv Funct Mater*. 2020;2000757:1-10.
49. Z. Zhang, Chao T, Chen SF, Jiang SY. Superlow Fouling Sulfobetaine and Carboxybetaine Polymers on Glass Slides. *Langmuir*. 2006;22(24):10072–10077.
50. Schlenoff JB. Zwitteration: Coating surfaces with zwitterionic functionality to reduce nonspecific adsorption. *Langmuir*. 2014;30(32):9625-9636.
51. Zhang Z, Zhang M, Chen S, Horbett TA, Ratner BD, Jiang S. Blood compatibility of surfaces with superlow protein adsorption. *Biomaterials*. 2008;29(32):4285-4291.
52. Yang W, Xue H, Li W, And JZ, Jiang S. Pursuing "zero" protein adsorption of poly(carboxybetaine) from undiluted blood serum and plasma. *Langmuir*. 2009;25(19):11911-11916.
53. Cheng G, Zhang Z, Chen S, Bryers JD, Jiang S. Inhibition of bacterial adhesion and biofilm formation on zwitterionic surfaces. *Biomaterials*. 2007;28(29):4192-4199.
54. Li G, Xue H, Cheng G, Chen S, Zhang F, Jiang S. Ultralow fouling zwitterionic polymers grafted from surfaces covered with an initiator via an adhesive mussel mimetic linkage. *J Phys Chem B*. 2008;112(48):15269-15274.
55. Zhang Z, Chao T, Liu L, Cheng G, Ratner BD, Jiang S. Zwitterionic Hydrogels: an in Vivo

Implantation Study. *J Biomater Sci Polym Ed*. 2009;20(13):1845-1859.

56. Erfani A, Seaberg J, Aichele CP, Ramsey JD. Interactions between Biomolecules and Zwitterionic Moieties: A Review. *Biomacromolecules*. 2020;21(7):2557-2573.

57. Wangkanont K, Forest KT, Kiessling LL. The non-detergent sulfobetaine-201 acts as a pharmacological chaperone to promote folding and crystallization of the type II TGF-β receptor extracellular domain. *Protein Expr Purif*. 2015;115:19-25.

58. Ivanova I, Tsachevab I, Stoyanovab V, et al. Chaperone-Like Effect of Polyzwitterions on the Interaction of C1q with IgG. *Z Naturforsch*. 2009;64(c):149-154.

59. Liu S, Jiang S. Zwitterionic polymer-protein conjugates reduce polymer-specific antibody response. *Nano Today*. 2016;11(3):285-291.

60. Liu S, Jiang S. Chemical conjugation of zwitterionic polymers protects immunogenic enzyme and preserves bioactivity without polymer-specific antibody response. *Nano Today*. 2016;11(3):285-291.

61. Lalani R, Liu L. Electrospun zwitterionic poly(sulfobetaine methacrylate) for nonadherent, superabsorbent, and antimicrobial wound dressing applications. *Biomacromolecules*. 2012;13(6):1853-1863.

62. Liu Q, Patel AA, Liu L. Superhydrophilic and underwater superoleophobic poly(sulfobetaine methacrylate)-grafted glass fiber filters for oil-water separation. *ACS Appl Mater Interfaces*. 2014;6(12):8996-9003.

63. Zhang Z, Finlay JA, Wang L, et al. Polysulfobetaine-grafted surfaces as environmentally benign ultralow fouling marine coatings. *Langmuir*. 2009;25(23):13516-13521.

64. Yang W, Zhang L, Wang S, White AD, Jiang S. Functionalizable and ultra stable nanoparticles coated with zwitterionic poly(carboxybetaine) in undiluted blood serum.

Biomaterials. 2009;30(29):5617-5621.

65. Estephan ZG, Jaber JA, Schlenoff JB. Zwitterion-stabilized silica nanoparticles: Toward nonstick nano. *Langmuir*. 2010;26(22):16884-16889.

66. Chen Y, Wang Y, Wang H, et al. Zwitterionic supramolecular prodrug nanoparticles based on host-guest interactions for intracellular drug delivery. *Polymer (Guildf)*. 2016;97:449-455.

67. Yang W, Bai T, Carr LR, et al. The effect of lightly crosslinked poly(carboxybetaine) hydrogel coating on the performance of sensors in whole blood. *Biomaterials*. 2012;33(32):7945-7951.

68. Kostina NY, Rodriguez-Emmenegger C, Houska M, Brynda E, Michálek J. Non-fouling hydrogels of 2-hydroxyethyl methacrylate and zwitterionic carboxybetaine (meth)acrylamides. *Biomacromolecules*. 2012;13(12):4164-4170.

69. Koc J, Schönemann E, Amuthalingam A, et al. Low-Fouling Thin Hydrogel Coatings Made of Photo-Cross-Linked Polyzwitterions. *Langmuir*. 2019;35(5):1552-1562.

70. Zhang L, Cao Z, Bai T, et al. Zwitterionic hydrogels implanted in mice resist the foreign-body reaction. *Nat Biotechnol*. 2013;31(6):553.

71. Huang P, Liu J, Wang W, et al. Zwitterionic nanoparticles constructed from bioreducible RAFT–ROP double head agent for shell shedding triggered intracellular drug delivery. *Acta Biomater*. 2016;40:263-272.

72. Halperin A, Kröger M, Zhulina EB. Colloid-brush interactions: The effect of solvent quality. *Macromolecules*. 2011;44(9):3622-3638.

73. Halperin A, Kröger M. Ternary protein adsorption onto brushes: Strong versus weak. *Langmuir*. 2009;25(19):11621-11634.

74. Szleifer I. Protein adsorption on surfaces with grafted polymers: A theoretical approach. *Biophys J*. 1997;72(2 I):595-612.

75. McPherson T, Kidane A, Szleifer I, Park K. Prevention of protein adsorption by tethered poly(ethylene oxide) layers: Experiments and single-chain mean-field analysis. *Langmuir*. 1998;14(1):176-186.

76. Halperin A, Fragneto G, Schollier A, Sferrazza M. Primary versus ternary adsorption of proteins onto PEG brushes. *Langmuir*. 2007;23(21):10603-10617.

77. Halperin A. Polymer brushes that resist adsorption of model proteins: Design parameters. *Langmuir*. 1999;15(7):2525-2533.

78. Satulovsky J, Carignano MA, Szleifer I. Kinetic and thermodynamic control of protein adsorption. *Proc Natl Acad Sci U S A*. 2000;97(16):9037-9041.

79. Xue C, Choi BC, Choi S, Braun P V., Leckband DE. Protein adsorption modes determine reversible cell attachment on poly(N-isopropyl acrylamide) brushes. *Adv Funct Mater*. 2012;22(11):2394-2401.

80. Halperin A, Kröger M. Collapse of thermoresponsive brushes and the tuning of protein adsorption. *Macromolecules*. 2011;44(17):6986-7005.

81. Kisley L, Serrano KA, Davis CM, et al. Soluble Zwitterionic Poly(sulfobetaine) Destabilizes Proteins. *Biomacromolecules*. 2018;19(9):3894-3901.

82. Wang W, Van Niekerk EA, Zhang YY, et al. Strong Repulsive Forces between Protein and Oligo (Ethylene Glycol) Self-Assembled Monolayers: A Molecular Simulation Study. *Langmuir*. 2019;35(5):158-166.

83. Monroy Soto VM, Galin JC. Poly(sulphopropylbetaines): 2. Dilute solution properties. *Polymer*. 1984;25:254-262.

84. Shao Q, Mi L, Han X, et al. Differences in cationic and anionic charge densities dictate zwitterionic associations and stimuli responses. *J Phys Chem B*. 2014;118(24):6956-6962.

85. Delgado JD, Schlenoff JB. Static and Dynamic Solution Behavior of a Polyzwitterion Using a Hofmeister Salt Series. *Macromolecules*. 2017;50(11):4454-4464.

86. De Grooth J, Ogieglo W, De Vos WM, Gironès M, Nijmeijer K, Benes NE. Swelling dynamics of zwitterionic copolymers: The effects of concentration and type of anion and cation. *Eur Polym J*. 2014;55(1):57-65.

87. Zhang Z, Moxey M, Alswieleh A, et al. Effect of Salt on Phosphorylcholine-based Zwitterionic Polymer Brushes. *Langmuir*. 2016;32(20):5048-5057.

88. Hildebrand V, Laschewsky A, Wischerhoff E. Modulating the solubility of zwitterionic poly((3-methacrylamidopropyl)ammonioalkane sulfonate)s in water and aqueous salt solutions via the spacer group separating the cationic and the anionic moieties. *Polym Chem*. 2016;7(3):731-740.

89. Schulz DN, Peiffer DG, Agarwal PK, et al. Phase behaviour and solution properties of sulphobetaine polymers. *Polymer*. 1986;27(11):1734-1742.

90. Huglin M, Radwan M. Properties of poly[N-2-(methacryloyloxy)ethyl-N,N-dimethyl-N-3-sulfopropylammonium betaine] in dilute solution. *Macromol Chem Phys*. 1991;192(10):2433-2445.

91. Köberle P, Lawhewsky A, Lornax TD. Interactions of a zwitterionic polysoap and its cationic analog with inorganic salts. 1991;433:427-433.

92. Köberle P, Laschewsky A. Hydrophobically Modified Zwitterionic Polymers: Synthesis, Bulk Properties, and Miscibility with Inorganic Salts. *Macromolecules*. 1994;27(8):2165-2173.

93. Hildebrand V, Laschewsky A, Päch M, Müller-Buschbaum P, Papadakis CM. Effect of the zwitterion structure on the thermo-responsive behaviour of poly(sulfobetaine methacrylates). *Polym Chem*. 2017;8(1):310-322.

94. Hildebrand V, Laschewsky A, Zehm D. On the hydrophilicity of polyzwitterion poly (N,N-dimethyl-N-(3-(methacrylamido)propyl)ammoniopropane sulfonate) in water, deuterated water, and aqueous salt solutions. *J Biomater Sci, Polym*. 2014;25:1602–1618.

95. Wang, F.; Yang, J.; Zhao J. Understanding Anti-Polyelectrolyte Level., Behavior of a Well-Defined Polyzwitterion at the Single-Chain. *Polym Int*. 2015;64:999-1005.

96. Lowe, A. B.; Billingham, N. C.; Armes SP. Synthesis and Their, Properties of Low-Polydispersity Poly(Sulfopropylbetaine)s and Block Copolymers. *Macromolecules*. 1999;32:2141-2148.

97. Ning J., Kubota K., Li G., Haraguchi K. Characteristics of zwitterionic sulfobetaine acrylamide polymer and the hydrogels prepared by free-radical polymerization and effects of physical and chemical crosslinks on the UCST. *React Funct Polym*. 2013;73(7):969-978.

98. Li W, Huang L, Ying X, et al. Antitumor drug delivery modulated by a polymeric micelle with an upper critical solution temperature. *Angew Chemie - Int Ed*. 2015;54(10):3126-3131.

99. Higaki Y, Inutsuka Y, Sakamaki T, et al. Effect of Charged Group Spacer Length on Hydration State in Zwitterionic Poly(sulfobetaine) Brushes. *Langmuir*. 2017;33(34):8404-8412.

100. Chen L, Honma Y, Mizutani T, Liaw DJ, Gong JP, Osada Y. Effects of polyelectrolyte complexation on the UCST of zwitterionic polymer. *Polymer*. 2000;41(1):141-147.

101. Lowe AB, McCormick CL. Synthesis and solution properties of zwitterionic polymers.

Chem Rev. 2002;102(11):4177-4189.

102. Leng C, Hung HC, Sun S, et al. Probing the Surface Hydration of Nonfouling Zwitterionic and PEG Materials in Contact with Proteins. *ACS Appl Mater Interfaces*. 2015;7(30):16881-16888.

103. Zheng J, Li L, Tsao H-K, Sheng Y-J, Chen S, Jiang S. Strong Repulsive Forces between Protein and Oligo (Ethylene Glycol) Self-Assembled Monolayers: A Molecular Simulation Study. *Biophys J*. 2005;89:158-166.

104. Xue W, Huglin MB, Liao B. Observations on the swelling characteristics of the zwitterionic hydrogel of poly(1-3-sulfopropyl)-2-vinyl-pyridinium-betaine hydrogel. *Eur Polym J*. 2006;42(11):3015-3023.

105. Kobayashi M, Mitamura K, Terada M, Yamada NL, Takahara A. Characterization of swollen states of polyelectrolyte brushes in salt solution by neutron reflectivity. *J Phys Conf Ser*. 2011;272(1).

106. Kobayashi M, Terayama Y, Yamaguchi H, et al. Wettability and antifouling behavior on the surfaces of superhydrophilic polymer brushes. *Langmuir*. 2012;28(18):7212-7222.

107. Georgiev GS, Kamenska EB, Vassileva ED, et al. Self-assembly, antipolyelectrolyte effect, nonbiofouling properties of polyzwitterions. *Biomacromolecules*. 2006;7(4):1329-1334.

108. Wörz A, Berchtold B, Moosmann K, Prucker O, Rühe J. Protein-resistant polymer surfaces. *J Mater Chem*. 2012;22(37):19547-19561.

109. Blackman LD, Gunatillake PA, Cass P, Locock KES. An introduction to zwitterionic polymer behavior and applications in solution and at surfaces. *Chem Soc Rev*. 2019;48(3):757-770.

110. Ranka M, Brown P, Hatton TA. Responsive Stabilization of Nanoparticles for Extreme

Salinity and High-Temperature Reservoir Applications. *ACS Appl Mater Interfaces*. 2015;7(35):19651-19658.

111. Zhang, Z.; Moxey, M.; Alswieleh, A.; Morse, A. J.; Lewis, A. L.; Geoghegan, M.; Leggett GJ. Effect of Salt on Phosphorylcholine-Based Zwitterionic Polymer Brushes. *Langmuir*. 2016;32:5048–5057.

112. Matsuda Y, Kobayashi M, Annaka M, Ishihara K, Takahara A. Dimension of poly(2-methacryloyloxyethyl phosphorylcholine) in aqueous solutions with various ionic strength. *Chem Lett*. 2006;35(11):1310-1311.

113. Matsuoka H, Yamakawa Y, Ghosh A, Saruwatari Y. Nanostructure and salt effect of zwitterionic carboxybetaine brush at the air/water interface. *Langmuir*. 2015;31(17):4827-4836.

114. Murugaboopathy S, Matsuoka H. Salt-dependent surface activity and micellization behaviour of zwitterionic amphiphilic diblock copolymers having carboxybetaine. *Colloid Polym Sci*. 2015;293(5):1317-1328.

115. Pincus P. Colloid Stabilization with Grafted Polyelectrolytes. *Macromolecules*. 1991;24(10):2912-2919.

116. Fleer GJ. Polyelectrolyte Brushes and Polyelectrolyte Adsorption Layers. *Berichte der Bunsengesellschaft/Physical Chem Chem Phys*. 1996;100(6):936-942.

117. Lyatskaya Y V., Leermakers FAM, Fleer GJ, Zhulina EB, Birshtein TM. Analytical Self-Consistent-Field Model of Weak Polyacid Brushes. *Macromolecules*. 1995;28(10):3562-3569.

118. Balastre M, Li F, Schorr P, Yang J, Mays JW, Tirrell M V. A study of polyelectrolyte brushes formed from adsorption of amphiphilic diblock copolymers using the surface forces

apparatus. *Macromolecules*. 2002;35(25):9480-9486.

119. Israelachvili JN. Thin film studies using multiple-beam interferometry. *J Colloid Interface Sci*. 1973;44(2):259-272.

120. Israelachvili, J. N., McGuiggan PM. Adhesion and Short-Range Forces between Surfaces. Part I: New Apparatus for Surface Force Measurements. *J Mater Res*. 1990;5:2223-2231.

121. Tang Y, Lu JR, Lewis AL, Vick TA, Stratford PW. Swelling of zwitterionic polymer films characterized by spectroscopic ellipsometry. *Macromolecules*. 2001;34(25):8768-8776.

122. McGuiggan PM, Israelachvili JN. Adhesion and Short-Range Forces Between Surfaces. Part II: Effects of Surface Lattice Mismatch. *J Mater Res*. 1990;5(10):2232-2243.

123. Christenson HK, Horn RG. Direct measurement of the force between solid-surfaces in a polar liquid. *Chem Phys Lett*. 1983;98(1):45-48.

124. Claesson PM, Kjellander R, Stenius P, Christenson HK. Direct measurement of temperature-dependent interactions between non-ionic surfactant layers. *J Chem Soc Faraday Trans 1 Phys Chem Condens Phases*. 1986;82(9):2735-2746.

125. Christenson, H. K., Claesson PM. Direct measurements of the force between hydrophobic surfaces in water. *Adv Colloid Interface Sci*. 2001;91(3):391-436.

126. Christenson HK, Horn RG. Solvation forces measured in non-aqueous liquids. *Chem Scr*. 1985;25(1):37-41.

127. Israelachvili JN, Adams GE. Measurement of forces between two mica surfaces in aqueous electrolyte solutions in the range 0-100 nm. *J Chem Soc Faraday Trans 1 Phys Chem Condens Phases*. 1978;74:975-1001.

128. Israelachvili J, Wennerström H. Role of hydration and water structure in biological and colloidal interactions. *Nature*. 1996;379(6562):219-225.

129. Clarkson MT. Multiple-beam interferometry with thin metal films and unsymmetrical systems. *J Phys D Appl Phys*. 1989;22(4):475-482.

130. Horn RG, Smith DT. Analytic solution for the three-layer multiple beam interferometer. *Appl Opt*. 1991;30(1):59.

131. Grabbe A, Horn RG. Double-layer and hydration forces measured between silica sheets subjected to various surface treatments. *J Colloid Interface Sci*. 1993;157(2):375-383.

132. Sheth SR, Efremova N, Leckband DE. Interactions of poly(ethylene oxide) brushes with chemically selective surfaces. *J Phys Chem B*. 2000;104(32):7652-7662.

133. Kuhl TL, Leckband DE, Lasic DD, Israelachvili JN. Modulation of interaction forces between bilayers exposing short-chained ethylene oxide headgroups. *Biophys J*. 1994;66(5):1479-1488.

134. Efremova N V., Huang Y, Peppas NA, Leckband DE. Direct measurement of interactions between tethered poly(ethylene glycol) chains and adsorbed mucin layers. *Langmuir*. 2002;18(3):836-845.

135. Leckband D, Israelachvili J. *Intermolecular Forces in Biology*. Vol 34. Cambridge University Press; 2001.

136. Patel SS, Tirrell M. Measurement of forces between surfaces in polymer fluids. *Annu Rev Phys Chem*. 1989;40:597-635.

137. Claesson PM, Ederth, T., Bergeron V, Rutland MW. Techniques for measuring surface Forces. *Adv Colloid Interface Sci*. 1996;67:119-183.

138. Eom N, Parsons DF, Craig VSJ. Roughness in Surface Force Measurements: Extension of DLVO Theory to Describe the Forces between Hafnia Surfaces. *J Phys Chem B*. 2017;121(26):6442-6453.

139. Kumacheva E. Interfacial friction measurement in surface force apparatus. *Prog Surf Sci*. 1998;58(2):75-120.

140. Tolansky S. *Multiple Beam Interferometry of Surfaces and Films*.; 1949.

141. Tolansky S (1955). *An Introduction to Interferometry. London: Longmans, Green & Co.*; 1955.

142. Farina R, Laugel N, Pincus P, Tirrell M. Brushes of strong polyelectrolytes in mixed mono- and tri-valent ionic media at fixed total ionic strengths. *Soft Matter*. 2013;9(44):10458-10472.

143. Choi S, Choi BC, Xue C, Leckband D. Protein adsorption mechanisms determine the efficiency of thermally controlled cell adhesion on poly(N -isopropyl acrylamide) brushes. *Biomacromolecules*. 2013;14(1):92-100.

144. Plunkett KN, Zhu X, Moore JS, Leckband DE. PNIPAM chain collapse depends on the molecular weight and grafting density. *Langmuir*. 2006;22(9):4259-4266.

145. Zhu X, DeGraaf J, Winnik FM, Leckband D. Tuning the Interfacial Properties of Grafted Chains with a pH Switch. *Langmuir*. 2004;20(4):1459-1465.

146. Kobayashi M, Terayama Y, Kikuchi M, Takahara A. Chain dimensions and surface characterization of superhydrophilic polymer brushes with zwitterion side groups. *Soft Matter*. 2013;9(21):5138-5148.

147. Heinz WF, Hoh JH. Spatially resolved force spectroscopy of biological surfaces using the atomic force microscope. *Trends Biotechnol*. 1999;17(4):143-150.

148. Chen M, Briscoe WH, Armes SP, Cohen H, Klein J. Polyzwitterionic brushes: Extreme lubrication by design. *Eur Polym J*. 2011;47(4):511-523.

149. Lefebvre MD, Olvera De La Cruz M, Shull KR. Phase segregation in gradient copolymer

melts. *Macromolecules*. 2004;37(3):1118-1123.

150. Lefebvre MD, Dettmer CM, McSwain RL, et al. Effect of sequence distribution on copolymer interfacial activity. *Macromolecules*. 2005;38(25):10494-10502.

151. Pierre-Gilles de Gennes. *Flexible Polymers in Nanopores*. Vol 138.; 1999.

152. Surve M, Pryamitsyn V, Ganesan V. Depletion and pair interactions of proteins in polymer solutions. *J Chem Phys*. 2005;122(15).

153. Surve M, Pryamitsyn V, Ganesan V. Dispersion and percolation transitions of nanorods in polymer solutions. *Macromolecules*. 2007;40(2):344-354.

154. Meli L, Arceo A, Green PF. Control of the entropic interactions and phase behavior of athermal nanoparticle/homopolymer thin film mixtures. *Soft Matter*. 2009;5(3):533-537.

155. Huang E, Pruzinsky S, Russell TP, Mays J, Hawker CJ. Neutrality conditions for block copolymer systems on random copolymer brush surfaces. *Macromolecules*. 1999;32(16):5299-5303.

156. Strickland LA, Hall CK, Genzer J. Design of copolymers with tunable randomness using discontinuous molecular dynamics simulation. *Macromolecules*. 2009;42(22):9063-9071.

157. Trombly DM, Pryamitsyn V, Ganesan V. Interfacial properties of statistical copolymer brushes in contact with homopolymer melts. *J Chem Phys*. 2011;134(15).

158. Mansky P, Liu Y, Huang E, Russell TP, Hawker C. Controlling polymer-surface interactions with random copolymer brushes. *Science (80-)*. 1997;275(5305):1458-1460.

159. Huang E, Russell TP, Harrison C, et al. Using surface active random copolymers to control the domain orientation in diblock copolymer thin films. *Macromolecules*. 1998;31(22):7641-7650.

160. Gersappe D, Balazs AC. Random copolymers as effective compatibilizing agents. *Phys Rev*

E. 1995;52(5):5061-5064.

161. Milner ST, Fredrickson GH. Reconsidering Random Copolymers at Interfaces. *Macromolecules*. 1995;28(23):7953-7956.

162. Balazs AC, Sanchez IC, Epstein IR, Karasz FE, MacKnight WJ. Effect of Sequence Distribution on the Miscibility of Polymer/Copolymer Blends. *Macromolecules*. 1985;18(11):2188-2191.

163. Balazs AC, Demeuse MT. Miscibility in Ternary Mixtures Containing a Copolymer and Two Homopolymers: Effect of Sequence Distribution. *Macromolecules*. 1989;22(11):4260-4267.

164. Dadmun M. Effect of copolymer architecture on the interfacial structure and miscibility of a ternary polymer blend containing a copolymer and two homopolymers. *Macromolecules*. 1996;29(11):3868-3874.

165. Kamath SY, Dadmun MD. The effect of chain architecture on the dynamics of copolymers in a homopolymer matrix: Lattice Monte Carlo simulations using the bond-fluctuation model. *Macromol Theory Simulations*. 2005;14(8):519-527.

166. Yeung C, Balaza AC, Jasnow D. Adsorption of Copolymer Chains at Liquid-Liquid Interfaces: Effect of Sequence Distribution. *Macromolecules*. 1992;25(4):1357-1360.

167. Garel T, Huse DA, Leibler S, Orland H. Localization transition of random chains at interfaces. *Epl*. 1989;8(1):9-13.

168. Gersappe D, Fasolka M, Israels R, Balazs AC. Modeling the Behavior of Random Copolymer Brushes. *Macromolecules*. 1995;28(13):4753-4755. doi:10.1021/ma00117a061

169. Marko JF, Witten TA. Correlations in Grafted Polymer Layers. *Macromolecules*. 1992;25(1):296-307.

170. Brown G, Chakrabarti A, Marko JF. Microphase Separation of a Dense Two-Component Grafted-Polymer Layer. *EPL*. 1994;25:239.

171. Lai PY. Binary mixture of grafted polymer chains: A Monte Carlo simulation. *J Chem Phys*. 1994;100(4):3351-3357.

172. Pickett GT. Linear gradient copolymer melt brushes. *J Chem Phys*. 2003;118(8):3898-3903.

173. Cleland, L J, Hedgepeth C, Wang DIC. Polyethylene Glycol Enhanced Refolding of Bovine Carbonic Anhydrase B. *J Biol Chem*. 1992;267(19):13327-13334.

174. Cleland, J., Builder, S., Swartz J et al. Polyethylene Glycol Enhanced Protein Refolding. *Nat Biotechnol*. 1992;10:1013-1019.

175. Holmberg K, Tiberg F, Malmsten M, Brink C. Grafting with hydrophilic polymer chains to prepare protein-resistant surfaces. *Colloids Surfaces A Physicochem Eng Asp*. 1997;123-124:297-306.

176. Keefe AJ, Jiang S. Poly(zwitterionic)protein conjugates offer increased stability without sacrificing binding affinity or bioactivity. *Nat Chem*. 2012;4(1):59-63.

177. Rodríguez-Martínez JA, Solá RJ, Castillo B, et al. Stabilization of α-chymotrypsin upon PEGylation correlates with reduced structural dynamics. *Biotechnol Bioeng*. 2008;101(6):1142-1149.

178. Shao Q, Jiang S. Influence of charged groups on the properties of zwitterionic moieties: A molecular simulation study. *J Phys Chem B*. 2014;118(27):7630-7637.

179. Harder P, Grunze M, Dahint R, Whitesides GM, Laibinis PE. Molecular conformation in oligo(ethylene glycol)-terminated self-assembled monolayers on gold and silver surfaces determines their ability to resist protein adsorption. *J Phys Chem B*. 1998;102(2):426-436.

180. Zheng J, Li L, Chen S, Jiang S. Molecular simulation study of water interactions with oligo

(ethylene glycol)-terminated alkanethiol self-assembled monolayers. *Langmuir*. 2004;20(20):8931-8938.

181. Szleifer I. Polymers and proteins : interactions at interfaces lgal Szleifer. *Curr Opin Solid State Mater Sci*. 1997;2(3):337-344.

182. Chen S, Zheng J, Li L, Jiang S. Strong resistance of phosphorylcholine self-assembled monolayers to protein adsorption: Insights into nonfouling properties of zwitterionic materials. *J Am Chem Soc*. 2005;127(41):14473-14478.

183. He Y, Hower J, Chen S, Bernards MT, Chang Y, Jiang S. Molecular simulation studies of protein interactions with phosphorylcholine self-assembled monolayers. *8th World Biomater Congr 2008*. 2008;1(17):495.

184. Chen S, Li L, Zhao C, Zheng J. Surface hydration: Principles and applications toward low-fouling/nonfouling biomaterials. *Polymer (Guildf)*. 2010;51(23):5283-5293.

185. Galvin CJ, Dimitriou MD, Satija SK, Genzer J. Swelling of polyelectrolyte and polyzwitterion brushes by humid vapors. *J Am Chem Soc*. 2014;136(36):12737-12745.

186. Shao Q, He Y, White AD, Jiang S. Different effects of zwitterion and ethylene glycol on proteins. *J Chem Phys*. 2012;136(22).

187. Shao Q, Jiang S. Molecular understanding and design of zwitterionic materials. *Adv Mater*. 2015;27(1):15-26.

188. Leng C, Hung HC, Sun S, et al. Probing the Surface Hydration of Nonfouling Zwitterionic and PEG Materials in Contact with Proteins. *ACS Appl Mater Interfaces*. 2015;7(30):16881-16888.

189. Chang Y, Chen WY, Yandi W, et al. Dual-thermoresponsive phase behavior of blood compatible zwitterionic copolymers containing nonionic poly(N-isopropyl acrylamide).

Biomacromolecules. 2009;10(8):2092-2100.

190. Chang Y, Shih YJ, Lai CJ, Kung HH, Jiang S. Blood-inert surfaces via ion-pair anchoring of zwitterionic copolymer brushes in human whole blood. *Adv Funct Mater*. 2013;23(9):1100-1110.

191. Song W, Zhu J, Liu L, Liu G. Modulation of the Binding Affinity of Polyzwitterion-Conjugated Protein by Ion-Specific Effects in Crowded Environments. *J Phys Chem B*. 2017;121(30):7366-7372.

192. Faulón Marruecos D, Saleh LS, Kim HH, Bryant SJ, Schwartz DK, Kaar JL. Stabilization of Fibronectin by Random Copolymer Brushes Inhibits Macrophage Activation. *ACS Appl Bio Mater*. 2019;2(11):4698–4702.

193. Dolan AK., Edwards SF. Theory of the stabilization of colloids by adsorbed polymer. *Proc R Soc London A Math Phys Sci*. 1974;337(1611):509-516.

194. Terayama Y, Kikuchi M, Kobayashi M, Hino M, Takahara A. Influence of salt concentration on swelling states of poly(sulfobetaine) brush at aqueous solution interface. *J Phys Conf Ser*. 2009;184.

195. Kisley L, Serrano KA, Davis CM, et al. Soluble Zwitterionic Poly(sulfobetaine) Destabilizes Proteins. *Biomacromolecules*. 2018;19(9):3894-3901.

196. Alexander S. Adsorption of Chain Molecules With a Polar Head. a Scaling Description. *J Phys*. 1977;38(8):983-987.

197. de Gennes PG. Polymers at an interface; a simplified view. *Adv Colloid Interface Sci*. 1987;27(3-4):189-209.

198. Efremova N V., Bondurant B, O'Brien DF, Leckband DE. Measurements of interbilayer forces and protein adsorption on uncharged lipid bilayers displaying poly(ethylene glycol)

chains. *Biochemistry*. 2000;39(12):3441-3451.

199. Witten ST, Milner TA, Cates ME. Theory of the Grafted Polymer Brush. *Macromolecules*. 1988;21(8):2610-2619.

200. Natarajan A, Xie J, Wang S, Masliyah J, Zeng H, Xu Z. Understanding molecular interactions of asphaltenes in organic solvents using a surface force apparatus. *J Phys Chem C*. 2011;115(32):16043-16051.

201. Schönemann E, Laschewsky A, Wischerhoff E, Koc J, Rosenhahn A. Surface modification by polyzwitterions of the sulfabetaine-type, and their resistance to biofouling. *Polymers (Basel)*. 2019;11(6).

202. Limpoco FT, Bailey RC. Real-time monitoring of surface-initiated atom transfer radical polymerization using silicon photonic microring resonators: Implications for combinatorial screening of polymer brush growth conditions. *J Am Chem Soc*. 2011;133(38):14864-14867.

203. Yuan YY, Mao CQ, Du XJ, Du JZ, Wang F, Wang J. Surface charge switchable nanoparticles based on zwitterionic polymer for enhanced drug delivery to tumor. *Adv Mater*. 2012;24(40):5476-5480.

204. Wielema TA, Engberts JBFN. Zwitterionic polymers-I. Synthesis of a novel series of poly(vinylsulphobetaines). Effect of structure of polymer on solubility in water. *Eur Polym J*. 1987;23(12):947-950.

205. Kathmann EE, White LA, McCormick CL. Water soluble polymers: 69. pH and electrolyte responsive copolymers of acrylamide and the zwitterionic monomer 4-(2-acrylamido-2-methylpropyldimethylammonio) butanoate: Synthesis and solution behaviour. *Polymer (Guildf)*. 1997;38(4):871-878.

206. Lau KHA, Sileika TS, Park SH, et al. Molecular Design of Antifouling Polymer Brushes Using Sequence-Specific Peptoids. *Adv Mater Interfaces*. 2015;2:1400225.

207. Schönemann E, J. Koc, Aldred N, et al. Synthesis of Novel Sulfobetaine Polymers with Differing Dipole Orientations in Their Side Chains, and Their Effects on the Antifouling Properties. *Macromol Rapid Commun*. 2020;41:1900447.

208. Szleifer I. Protein adsorption on surfaces with grafted polymers: A theoretical approach. *Biophys J*. 1997;72(2 I):595-612.

209. Morgenthaler S, Lee S, Zürcher S, Spencer ND. A simple, reproducible approach to the preparation of surface-chemical gradients. *Langmuir*. 2003;19(25):10459-10462.

210. Sunday D, Curras-Medina S, Green DL. Impact of initiator spacer length on grafting polystyrene from silica nanoparticles. *Macromolecules*. 2010;43(11):4871-4878.

211. Greszta D, Mardare D, Matyjaszewski K. "Living" Radical Polymerization. 1. Possibilities and Limitations. *Macromolecules*. 1994;27:638-644.

212. Xue C, Yonet-Tanyeri N, Brouette N, Sferrazza M, Braun P V., Leckband DE. Protein adsorption on poly(N -isopropylacrylamide) brushes: Dependence on grafting density and chain collapse. *Langmuir*. 2011;27(14):8810-8818.

213. Jung LS, Campbell CT, Chinowsky TM, Mar MN, Yee SS. Quantitative interpretation of the response of surface plasmon resonance sensors to adsorbed films. *Langmuir*. 1998;14(19):5636-5648.

214. Shumaker-Parry JS, Campbell CT. Quantitative Methods for Spatially Resolved Adsorption/Desorption Measurements in Real Time by Surface Plasmon Resonance Microscopy. *Anal Chem*. 2004;76(4):907-917.

215. Jordan CE, Frutos AG, Thiel AJ, Corn RM. Surface plasmon resonance imaging

measurements of DNA hybridization adsorption and streptavidin/DNA multilayer formation at chemically modified gold surfaces. *Anal Chem*. 1997;69(24):4939-4947.

216. Lundblad RL, Macdonald FM. *Handbook of Biochemistry and Molecular Biology*. Cleveland, OH: CRC Press; 1973.

217. Sindorf DW, Maciel GE. Cross-polarization/magic-angle-spinning silicon-29 nuclear magnetic resonance study of silica gel using trimethylsilane bonding as a probe of surface geometry and reactivity. *J Phys Chem*. 1982;86(26):5208-5219.

218. Mary P, Bendejacq DD, Labeau MP, Dupuis P. Reconciling low- and high-salt solution behavior of sulfobetaine polyzwitterions. *J Phys Chem B*. 2007;111(27):7767-7777.

219. de Gennes PG. Conformations of Polymers Attached to an Interface. *Macromolecules*. 1980;13(5):1069-1075.

220. Kato T, A. Takahashi. Excluded Volume Effects of Sulphobetaine Polymers. *Ber Bunsenges Phys Chem*. 1996;100:100784.

221. Kikuchi M, Terayama Y, Ishikawa T, et al. Chain dimension of polyampholytes in solution and immobilized brush states. *Polym J*. 2012;44(1):121-130.

222. Halperin A. Collapse of Grafted Chains in Poor Solvents. *J Phys Paris*. 1988;49(3):547-550.

223. Squire PG, Moser P, O'Konski CT. The Hydrodynamic Properties of Bovine Serum Albumin Monomer and Dimer. *Biochemistry*. 1968;7(12):4261-4272.

224. Dhar A, Samiotakis A, Ebbinghaus S, et al. Structure, function, and folding of phosphoglycerate kinase are strongly perturbed by macromolecular crowding. *Proc Natl Acad Sci U S A*. 2010;107(41):17586-17591.

225. Erickson HP. Size and shape of protein molecules at the nanometer level determined by

sedimentation, gel filtration, and electron microscopy. *Biol Proced Online*. 2009;11(1):32-51.

226. Jeon SI, Lee JH, Andrade JD, De Gennes PG. Protein-surface interactions in the presence of polyethylene oxide. I. Simplified theory. *J Colloid Interface Sci*. 1991;142(1):149-158.

227. Rubinstein M, Colby RH. Polymer Physics. 2003.

228. Huang CJ, Li Y, Krause JB, Brault ND, Jiang S. Internal architecture of zwitterionic polymer brushes regulates nonfouling properties. *Macromol Rapid Commun*. 2012;33(11):1003-1007.

229. Bagaria HG, Yoon KY, Neilson BM, et al. Stabilization of Iron Oxide Nanoparticles in High Sodium and Calcium Brine at High Temperatures with Adsorbed Sulfonated Copolymers. *Langmuir*. 2013;29:3195-3206.

230. Nap RJ, Park SH, Szleifer I. On the stability of nanoparticles coated with polyelectrolytes in high salinity solutions. *J Polym Sci Part B Polym Phys*. 2014;52(24):1689-1699.

231. Napper DH. *Polymeric Stabilization of Colloidal Dispersions*. Academic Press, New York; 1983.

232. Siegwart DJ, Oh JK, Matyjaszewski K. ATRP in the design of functional materials for biomedical applications. *Prog Polym Sci*. 2012;37(1):18-37.

233. Kang C, Crockett RM, Spencer ND. Molecular-weight determination of polymer brushes generated by SI-ATRP on flat surfaces. *Macromolecules*. 2014;47(1):269-275.

234. Israelachvili JN. *Intermolecular and Surface Forces*. Vol 53. 3rd ed. Academic Press Limited, London; 2011.

235. Milner ST, Witten TA, Cates ME. Theory of the Grafted Polymer Brush. *Macromolecules*. 1988;21(8):2610-2619.

236. Guo S, Jańczewski D, Zhu X, Quintana R, He T, Neoh KG. Surface charge control for zwitterionic polymer brushes: Tailoring surface properties to antifouling applications. *J Colloid Interface Sci*. 2015;452:43-53.

237. Schönemann E, Laschewsky A, Rosenhahn A. Exploring the long-term hydrolytic behavior of zwitterionic polymethacrylates and polymethacrylamides. *Polymers (Basel)*. 2018;10(6).

238. Terayama Y, Arita H, Ishikawa T, et al. Chain dimensions in free and immobilized brush states of polysulfobetaine in aqueous solution at various salt concentrations. *J Phys Conf Ser*. 2011;272(1).

239. Lowe AB, Billingham NC, Armes SP. Synthesis and properties of low-polydispersity poly(sulfopropylbetaine)s and their block copolymers. *Macromolecules*. 1999;32(7):2141-2148.

240. Wang T, Wang X, Long Y, Liu G, Zhang G. Ion-specific conformational behavior of polyzwitterionic brushes: Exploiting it for protein adsorption/desorption control. *Langmuir*. 2013;29(22):6588-6596.

241. Kikuchi M., Terayama Y., Ishikawa T., et al. Salt Dependence of the Chain Stiffness and Excluded-Volume Strength for the Polymethacrylate-Type Sulfopropylbetaine in Aqueous NaCl Solutions. *Macromolecules*. 2015;48:7194-7204.

242. Blackman LD, Gunatillake PA, Cass P, Locock KES. An introduction to zwitterionic polymer behavior and applications in solution and at surfaces. *Chem Soc Rev*. 2019;48(3):757-770.

243. Worthen AJ, Tran V, Cornell KA, Truskett TM, Johnston KP. Steric stabilization of nanoparticles with grafted low molecular weight ligands in highly concentrated brines including divalent ions. *Soft Matter*. 2016;12(7):2025-2039.

244. Vasantha VA, Hua NQ, Rusli W, Hadia NJ, Stubbs LP. Unique Oil-in-Brine Pickering Emulsion Using Responsive Antipolyelectrolyte Functionalized Latex: A Versatile Emulsion Stabilizer. *ACS Appl Mater Interfaces*. 2020;12(20):23443-23452.

245. Pollack KA, Imbesi PM, Raymond JE, Wooley KL. Hyperbranched Fluoropolymer-Polydimethylsiloxane-Poly(ethylene glycol) Cross-Linked Terpolymer Networks Designed for Marine and Biomedical Applications: Heterogeneous Nontoxic Antibiofouling Surfaces. *ACS Appl Mater Interfaces*. 2014;6(21):19265-19274.

246. Panganiban B, Qiao B, Jiang T, et al. Random heteropolymers preserve protein function in foreign environments. *Science.* 2018;359(6381):1239-1243.

247. Faulón Marruecos D, Saleh LS, Kim HH, Bryant SJ, Schwartz DK, Kaar JL. Stabilization of Fibronectin by Random Copolymer Brushes Inhibits Macrophage Activation. *ACS Appl Bio Mater*. 2019; 2:4698−4702.

248. Liu Z, Huang Y, Zhang X, et al. Fabrication of Cyclic Brush Copolymers with Heterogeneous Amphiphilic Polymer Brushes for Controlled Drug Release. *Macromolecules*. 2018;51(19):7672-7679.

249. Sun Q, Su Y, Ma X, Wang Y, Jiang Z. Improved antifouling property of zwitterionic ultrafiltration membrane composed of acrylonitrile and sulfobetaine copolymer. *J Memb Sci*. 2006;285(1-2):299-305.

250. Leckband DE, Sheth SR, Halperin A. Grafted poly(ethylene oxide) brushes as nonfouling surface coatings. *J Biomater Sci Polym Ed*. 1999;10(10):1125-1147.

251. Zalipsky S, Harris JM. Introduction to Chemistry and Biological Applications of Poly(ethylene glycol). In: *Poly(Ethylene Glycol)*. Vol 680. ACS Symposium Series. American Chemical Society; 1997:1.

252. Jiang S, Cao Z. Ultralow-fouling, functionalizable, and hydrolyzable zwitterionic materials and their derivatives for biological applications. *Adv Mater*. 2010;22(9):920-932.

253. Ueda T, Oshida H, Kurita K, Ishihara K, Nakabayashi N. Preparation of 2-methacryloyloxyethyl phosphorylcholine copolymers with alkyl methacrylates and their blood compatibility. *Polym J*. 1992;24(11):1259-1269.

254. Robinson KJ, Coffey JW, Muller DA, et al. Comparison between polyethylene glycol and zwitterionic polymers as antifouling coatings on wearable devices for selective antigen capture from biological tissue. *Biointerphases*. 2015;10:04A305.

255. Welsher K, McManus SA, Hsia CH, Yin S, Yang H. Discovery of protein-and DNA-imperceptible nanoparticle hard coating using gel-based reaction tuning. *J Am Chem Soc*. 2015;137:580–583.

256. Harris JM. *Poly(Ethylene Glycol) Chemistry: Biotechnical and Biomedical Applications.* New York: Plenum Press; 1992.

257. Harris JM, Chess RB. Effect of pegylation on pharmaceuticals. *Nat Rev Drug Discov*. 2003;2:214-221.

258. Faulón Marruecos D, Kastantin M, Schwartz DK, Kaar JL. Dense Poly(ethylene glycol) Brushes Reduce Adsorption and Stabilize the Unfolded Conformation of Fibronectin. *Biomacromolecules*. 2016;17(3):1017-1025.

259. Topchieva, I. N., Sorokina, E. M., Efremova, N. V. and Ksenofontov AL. Noncovalent complexes between poly(ethylene glycol) and proteins. *Biochem*. 1998;63:1312-1318.

260. Sheth SR, Leckband D. Measurements of attractive forces between proteins and end-grafted poly(ethylene glycol) chains. *Proc Natl Acad Sci U S A*. 1997;94(16):8399-8404.

261. Abbott NL, Blankschtein D, Hatton TA. Protein Partitioning in Two-Phase Aqueous

Polymer Systems. 2. On the Free Energy of Mixing Globular Colloids and Flexible Polymers. *Macromolecules*. 1992;25(15):3917-3931.

262. Herold DA, Keil K, Bruns DE. Oxidation of Polyethylene Glycols by Alcohol Dehydrogenase. *Biochem Pharmacol*. 1989;38:73-76.

263. Chapman RG, Ostuni E, Liang MN, et al. Polymeric thin films that resist the adsorption of proteins and the adhesion of bacteria. *Langmuir*. 2001;17(4):1225-1233.

264. Shen MC, L. Martinson, Wagner MS, Castner DG, Ratner BD, T. A. Horbett J. PEO-like plasma polymerized tetraglyme surface interactions with leukocytes and proteins: in vitro and in vivo studies. *Jour Biomater Sci-Polym Ed*. 2002;13(4):367-390.

265. Walsh S, Shah A, Mond J. Improved pharmacokinetics and reduced antibody reactivity of lysostaphin conjugated to polyethylene glycol. *Antimicrob Agents Chemother*. 2003;47(2):554-558.

266. Papahadjopoulos D, Allen TM, Gabizon A, et al. Sterically stabilized liposomes: improvements in pharmacokinetics and antitumor therapeutic efficacy. *Proc Natl Acad Sci*. 1991;88(24):11460 - 11464.

267. Chao, S.-H.; Matthews, S. S.; Paxman, R.; Aksimentiev, A.; Gruebele, M.; Price JL. Two Structural Scenarios for Protein Stabilization by PEG. *J Phys Chem B*. 2014;118:8388-8395.

268. Abbott NL, Blankschtein D, Alan Hatton T. Protein Partitioning in Two-Phase Aqueous Polymer Systems. 1. Novel Physical Pictures and a Scaling-Thermodynamic Formulation. *Macromolecules*. 1991;24(15):4334-4348.

269. Ranneh A-H, Takemoto H, Sakuma S, et al. An Ethylenediamine-based Switch to Render the Polyzwitterion Cationic at Tumorous pH for Effective Tumor Accumulation of Coated

Nanomaterials. *Angew Chemie*. 2018;130(18):5151-5155.

270. Durand-Gasselin C, Koerin R, Rieger J, Lequeux N, Sanson N. Colloidal stability of zwitterionic polymer-grafted gold nanoparticles in water. *J Colloid Interface Sci*. 2014;434:188-194.

271. Suzuki H, Murou M, Kitano H, Ohno K, Saruwatari Y. Silica particles coated with zwitterionic polymer brush: Formation of colloidal crystals and anti-biofouling properties in aqueous medium. *Colloids Surfaces B Biointerfaces*. 2011;84(1):111-116.

272. Venault A, Chang Y. Designs of Zwitterionic Interfaces and Membranes. *Langmuir*. 2019;35(5):1714-1726.

273. Baggerman J, Smulders MMJ, Zuilhof H. Romantic Surfaces: A Systematic Overview of Stable, Biospecific, and Antifouling Zwitterionic Surfaces. *Langmuir*. 2019;35(5):1072-1084.

274. He M, Gao K, Zhou L, et al. Zwitterionic materials for antifouling membrane surface construction. *Acta Biomater*. 2016;40(92):142-152.

275. Wu J, Xiao Z, He C, et al. Protein diffusion characteristics in the hydrogels of poly(ethylene glycol) and zwitterionic poly(sulfobetaine methacrylate) (pSBMA). *Acta Biomater*. 2016;40:172-181.

276. Wu J, Xiao Z, Chen A, et al. Sulfated zwitterionic poly(sulfobetaine methacrylate) hydrogels promote complete skin regeneration. *Acta Biomater*. 2018;71:293-305.

277. Kobayashi, M.; Terayama, Y.; Yamaguchi, H.; Terada, M.; Murakami, D.; Ishihara, K.; Takahara A. Wettability and Antifouling Behavior on the Surfaces of Superhydrophilic Polymer Brushes. *Langmuir*. 2012;28(18):7212−7222.

278. Israelachvili JN. *Intermolecular and Surface Forces*. Third. Academic Press Limited,

London; 1992.

279. Physics T. Theory of the stabilization of colloids by adsorbed polymer. *Proc R Soc London A Math Phys Sci*. 1974;337(1611):509-516.

280. Ahmed ST, Madinya JJ, Leckband DE. Ionic Strength Dependent Forces Between End-Grafted Poly(sulfobetaine) Films and Mica. *J Colloid Interface Sci*. 2021; 606 (1):298-306.

281. Wu J, Zhao C, Hu R, et al. Probing the weak interaction of proteins with neutral and zwitterionic antifouling polymers. *Acta Biomater*. 2014;10(2):751-760.

282. Takeichi M. Cadherin cell adhesion receptors as a morphogenetic regulator. *Science*. 1991;251:1451-1455.

283. Takeichi M. Morphogenetic roles of classic cadherins. *Curr Opin Cell Biol*. 1995;7:619–627.

284. Nagafuchi A., Shirayoshi Y., Okazaki K., Yasuda K. TM. Transformation of cell adhesion properties by exogenously introduced E-cadherin cDNA. *Nature*. 1987:341-343.

285. Niessen CM, Leckband DE, Yap AS. Tissue organization by cadherin adhesion molecules: dynamic molecular and cellular mechanisms of morphogenetic regulation. *Physiol Rev*. 2011;91:691-731.

286. Gumbiner BM. Regulation of cadherin-mediated adhesion in morphogenesis. *Nat Rev Mol Cell Biol*. 2005;6:622-634.

287. Williams G, E-J. W, P. D. Dimeric Versions of Two Short N-cadherin Binding Motifs (HAVDI and INPISG) Function as N-cadherin Agonists. *Jour Biol Chem*. 2002;277(6):4361–4367.

288. Gumbiner BM. Cell adhesion: the molecular basis of tissue architecture and morphogenesis. *Cell*. 1996;84:345-357.

289. Shapiro L, Weis W. Structure and Biochemistry of Cadherins and Catenins. *Cold Spring Harb Perspect Biol*. 2009;1:1-22.

290. Ozawa M, R. K. Correct proteolytic cleavage is required for the cell adhesive function of uvomorulin. *J Cell Biol*. 1990;111:1645-1650.

291. Handschuh G, B L, P H, H H, KF. B. Single amino acid substitutions in conserved extracellular domains of E-cadherin differ in their functional consequences. *J Mol Biol*. 2001;314:445-454.

292. Vendome, J., Posy S, Jin X, et al. Molecular design principles underlying beta-strand swapping in the adhesive dimerization of cadherins. *Nat Struct Mol Biol*. 2011;18:693-700.

293. Peluso, J. J., Pappalardo A, Trolice MP. N-cadherin-mediated cell contact inhibits granulosa cell apoptosis in a progesterone-independent manner. *Endocrinology*. 1996;137:1196-1203.

294. Gumbiner BM. Regulation of Cadherin Adhesive Activity. *J Cell Biol*. 2000;148:399-404.

295. Vieira A.F. PJ. P-cadherin and the journey to cancer metastasis. *Mol Cancer*. 2015;4:178.

296. Leckband, D., Prakasam A. Mechanism and dynamics of cadherin adhesion. *Annu Rev Biomed Eng*. 2006;8:259-287.

297. Skaper, S.D., Facci L, Williams G, Williams E-J, Walsh FS, Doherty P. A dimeric version of the short N-cadherin binding motif HAVDI promotes neuronal cell survival by activating an N-cadherin/ fibroblast growth factor receptor signaling cascade. *Mol Cell Neurosci*. 2004;26:17-23.

298. Williams, E.-J., G. W, Gour BJ, O.W. B, Doherty P. A Novel Family of Cyclic Peptide Antagonists Suggests That N-cadherin Specificity Is Determined by Amino Acids That Flank the HAV Motif. *J Biol Chem*. 2000;256(6):4007–4012.

299. Makagiansar, I.T., Avery M, Hu Y, Audus KL, Siahaan TJ. Improving the Selectivity of

HAV-Peptides in Modulating E-Cadherin-E-Cadherin Interactions in the Intercellular Junction of MDCK Cell Monolayers. *Pharm Res*. 2001;18(4):446-453.

300. Nagar, B., Overduin M, Ikura M, Rini JM. Structural basis of calcium-induced E-cadherin rigidification and dimerization. *Nat.* 1996;380:360–64.

301. Ciatto, C., Bahna F, Zampieri, N., VanSteenhouse, H.C., Katsamba PS, et al. T-cadherin structures reveal a novel adhesive binding mechanism. *Nat Struct Mol Biol*. 2010;17:339-347.

302. Harrison, O.J., Bahna F, Katsamba PS, et al. Two-step adhesive binding by classical cadherins. *Nat Struct Mol Biol*. 2010;17:348-357.

303. Rakshit S, Zhang Y, Manibog K, Shafraz O, Sivasankar S. Ideal, catch, and slip bonds in cadherin adhesion. *PNAS*. 2012;109(46):18815-18820.

304. Leckband DE, de Rooij J. Cadherin adhesion and mechanotransduction. *Annu Rev Cell Dev Biol*. 2014;30:291-315.

305. Hong S, Troyanovsky RB, Troyanovsky SM. Binding to F-actin guides cadherin cluster assembly, stability, and movement. *J Cell Biol*. 2013;201:131-143.

306. Vester-Christensen MB, Halim A, Joshi HJ, et al. Mining the O-mannose glycoproteome reveals cadherins as major O-mannosylated glycoproteins. *PNAS*. 2013;110:21018-21023.

307. Lommel M, Winterhalter PR, Willer T, et al. Protein O-mannosylation is crucial for E-cadherin-mediated cell adhesion. *PNAS*. 2013;110:21024-21029.

308. Pinho SS, Seruca R, Gartner F, et al. Modulation of E-cadherin function and dysfunction by N-glycosylation. *Cell Mol life Sci*. 2011;68:1011-1020.

309. Geyer H, Geyer R, Odenthal-Schnittler M, Schnittler HJ. Characterization of human vascular endothelial cadherin glycans. *Glycobiology*. 1999;9:915-925.

310. Liwosz A, Lei T, Kukuruzinska MA. N-glycosylation affects the molecular organization and stability of E-cadherin junctions. *J Biol Chem*. 2006;281:23138-23149.

311. Zhou F, J S, L F, et al. Unglycosylation at Asn-633 made extracellular domain of E-cadherin folded incorrectly and arrested in endoplasmic reticulum, then sequentially degraded by ERAD. *Glycoconj J*. 2008;25:727-740.

312. Jamal BT, M N-L, Z G, B A, J W, MA K. N-glycosylation status of E-cadherin controls cytoskeletal dynamics through the organization of distinct beta-catenin- and gamma-catenin-containing AJs. *Cell Health Cytoskelet*. 2009;1:67-80.

313. Bassaganas S, S C, AM D, et al. Pancreatic cancer cell glycosylation regulates cell adhesion and invasion through the modulation of alpha2beta1 integrin and E-cadherin function. *PLoS One*. 2014;9:e98595.

314. Kitada T, E M, K N, et al. The addition of bisecting N-acetylglucosamine residues to E-cadherin down-regulates the tyrosine phosphorylation of beta-catenin. *J Biol Chem*. 2001;276:475-480.

315. de Freitas Junior JC, R SB, WF de S, WM de A, ES A, JA. M-D. Inhibition of N-linked glycosylation by tunicamycin induces E-cadherin-mediated cell-cell adhesion and inhibits cell proliferation in undifferentiated human colon cancer cells. *Cancer Chemother Pharmacol*. 2011;68:227-238.

316. Winterhalter PR, Lommel M, Ruppert T, Strahl S. O-glycosylation of the non-canonical T-cadherin from rabbit skeletal muscle by single mannose residues. *FEBS Lett*. 2013;587:3715-3721.

317. Langer MD, Guo H, Shashikanth N, Pierce JM, Leckband DE. N-glycosylation alters cadherin-mediated intercellular binding kinetics. *J Cell Sci*. 2012;125:2478-2485.

318. Langer MD, Guo H, Shashikanth N, Pierce JM, Leckband DE. N-glycosylation alters cadherin-mediated intercellular binding kinetics. *J Cell Sci*. 2012;125:2478-2485.

319. Guo HB, H J, M R, M. P. Regulation of homotypic cell-cell adhesion by branched N-glycosylation of N-cadherin extracellular EC2 and EC3 domains. *J Biol Chem*. 2009;284:34986-34997.

320. Spindler V, Waschke J. Pemphigus-A disease of desmosome dysfunction caused by multiple mechanism. *Front Immunol*. 2018;9:1-8.

321. Spindler V, Eming R, Schmidt E, et al. Mechanisms Causing Loss of Keratinocyte Cohesion in Pemphigus. *J Invest Dermatol*. 2018;138(1):32-37.

322. Stanley JR, Amagai M. Pemphigus, Bullous Impetigo, and the Staphylococcal Scalded-Skin Syndrome. *N Engl J Med*. 2006;355(17):1800-1810.

323. Shashikanth N, YI P, S P, et al. Allosteric Regulation of E-Cadherin Adhesion. *J Biol Chem*. 2015;290:21749-21761.

324. Bell GI. Models for the specific adhesion of cells to cells. *Science* 1978;200:618-627.

325. Décavé, E., Garrivier D, Bréchet Y, Fourcade B, Brucker F. Shear Flow-Induced Detachment Kinetics of Dictyostelium discoideum Cells from Solid Substrate. *Biophys Jour*. 2002;82(5):2383-2395.

326. Chesla SE, Selvaraj P, Zhu C. Measuring two-dimensional receptor-ligand binding kinetics by micropipette. *Biophys J*. 1998;75:1553-1572.

327. Cozens-Roberts, C, Lauffenburger, D.A., Quinn JA. Receptor- mediated cell attachment and detachment kinetics. I. Probabilistic model and analysis. *Biophys J*. 1990;58:841-856.

328. Noor SI, Hoffmann M, Rinis N, et al. Glycosyltransferase POMGNT1 deficiency strengthens N-cadherin-mediated cell–cell adhesion. *J Biol Chem*. 2021;296:100433.

329. Smorodinsky-Atias, K., Goshen-Lago, T., Goldberg-Carp, A., Melamed D, Shir A, Mooshayef, N., Beenstock, J., Karamansha, Y., Darlyuk-Saadon, I., Livnah, O., Ahn NG, Admon A, and Engelberg D. Intrinsically active variants of Erk oncogenically transform cells and disclose unexpected autophosphorylation capability that is independent of TEY phosphorylation. *Mol Biol Cell*. 2016;27:1026–1039.

330. Chien, Y.H., Jiang N, Li F, Zhang F, Zhu C, Leckband D. Two stage cadherin kinetics require multiple extracellular domains but not the cytoplasmic region. *J Biol Chem*. 2008;283:1848-1856.

331. Zhang F, Marcus WD, Goyal NH, Selvaraj P, Springer TA, Zhu C. Two-dimensional kinetics regulation of alphaLbeta2-ICAM-1 interaction by conformational changes of the alphaL-inserted domain. *J Biol Chem*. 2005;280:42207-42218.

332. Vestweber D, Kemler R. Identification of a putative cell adhesion domain of uvomorulin. *EMBO J*. 1985;4:3393-3398.

333. Gold ER, Fudenberg HH. Chromic chloride: a coupling reagent for passive hemagglutination reactions. *J Immunol*. 1967;99:859-866.

334. Kofler R, Wick G. Some methodologic aspects of the chromium chloride method for coupling antigen to erythrocytes. *J Immunol Methods*. 1977;16:201-209.

335. Zarnitsyna VI, Zhu C. Adhesion Frequency Assay for In Situ Kinetics Analysis of Cross-Junctional Molecular Interactions at the Cell-Cell Interface. *J Vis Exp*. 2011;57:3519.

336. Barry, A., Tabdili H, Muhamed I, et al. α-Catenin cytomechanics: role in cadherindependent adhesion and mechanotransduction. *J Cell Sci*. 2014;15:1779-1791.

337. Tabdili H, Langer M, Shi Q, Poh Y-C, Wang N, Leckband D. Cadherin-dependent mechanotransduction depends on ligand identity but not affinity. *J Cell Sci*. 2012:4362-

4371.

338. Neill JW. Testing for lack of fit in nonlinear regression. *Ann Stat*. 1988;16:733-740.

339. Lommel M, Winterhalter PR, Willer T, et al. Protein O-mannosylation is crucial for E-cadherin-mediated cell adhesion. *Proc Natl Acad Sci U S A*. 2013;110(52):21024-21029.

340. Harrison OJ, Bahna F, Katsamba PS, et al. Two-step adhesive binding by classical cadherins. *Nat Struct Mol Biol*. 2010;17(3):348-357.

341. Dominguez-Medina S, Kisley L, Tauzin LJ, et al. Adsorption and Unfolding of a Single Protein Triggers Nanoparticle Aggregation. *ACS Nano*. 2016;10(2):2103-2112.

342. Creighton T. *Proteins: Structures and Molecular Properties*. Second. WH Freeman and Company; 1984.

343. Brault ND, Sundaram HS, Huang CJ, Li, Y., Yu Q, Jiang S. Two-layer architecture using atom transfer radical polymerization for enhanced sensing and detection in complex media. *Biomacromolecules*. 2012;13:4049-4056.

344. Huang CJ, Li Y, Jiang S. Zwitterionic polymer-based platform with two-layer Loading., architecture for ultra low fouling and high protein. *Anal Chem*. 2012;84:3440-3445.

345. Kastantin M, Schwartz DK. Identifying multiple populations from single-molecule lifetime distributions. *Chemphyschem*. 2013;14:374-380.

346. Dhar A, Girdhar K, Singh D, Gelman, H.; Ebbinghaus S., Gruebele M. Protein Stability and Folding Kinetics in the Nucleus and Endoplasmic Reticulum of Eucaryotic Cells. *Biophys Journals*. 2011;101(2):421-430.

347. Ebbinghaus S, Gruebele M. Protein folding landscapes in the living cell. *J Phys Chem Lett*. 2011;2(4):314-319.

348. Rowinska-Zyrek M, Witkowska D, Potocki S, Remelli M, Kozlowski H. His-rich sequences

- Is plagiarism from nature a good idea? *New J Chem*. 2013;37(1):58-70.

349. Ebbinghaus, S., Dhar, A., McDonald, J. D. and Gruebele M. Protein folding stability and dynamics imaged in a living cell. *Nat Methods*. 2010;7:319-323.

350. Boulos SP, Prigozhin MB, Liu Y, et al. The Gold Nanorod-Biology Interface: From Proteins to Cells to Tissue. *Curr Phys Chem*. 2013;3(2):128-135.

351. Carr LR, Xue H, Jiang S. Functionalizable and nonfouling zwitterionic carboxybetaine hydrogels with a carboxybetaine dimethacrylate crosslinker. *Biomaterials*. 2011;32(4):961-968.

APPENDIX A: ANALYTIC TECHNIQUES USED

A.1. Dynamic Light Scattering (DLS)

The hydrodynamic radius (R_h) and polydispersity index (PDI) were calculated using Litesizer Anton Paar 500^{TM} particle analyzer. In this method, particle size is measured by the collecting light scattered by the sample. Any particle suspended in solution is constant undergoing motion, the speed of which depends on its size. The smaller the particle is, the faster it moves. In dynamic light scatter, light at 658 nm is scattered by sample and the scattering is collected many times. Comparison of these records with many others over time, reveals how much the particles have moved in the time between each record. The scattered light is detected by an Avalanche Photo diode detector at 90^0 for side scatter and at 175^0 for back scatter.

The raw scattering fluctuations over time are autocorrelated vs. a lag time, τ to produce the autocorrelation function, $G_2(\tau)$. This function can be expressed as a polynomial function of the lag time as shown below-

$$[(G_2(\tau)-B)/B]=ln\beta-2\bar{\Gamma}\tau+K_2\,\tau^2 \qquad [A.1]$$

where $\bar{\Gamma}$ is the decay rate, K_2 is the second cumulant, which is equivalent to the second moment about the mean, or the variance, and β is an empirical factor dependent on the experimental geometry. From $\bar{\Gamma}$, the diffusion coefficient, D, can be calculated by-

$$D=\bar{\Gamma}/q^2 \qquad [A.2]$$

where q is the magnitude of the scattering wave vector given by-

$$q=\frac{4\pi n}{\lambda}\left(\frac{\theta}{2}\right) \qquad [A.3]$$

with n being the refractive index of the solvent, λ is the laser wavelength, and θ is the scattering angle. The R_h is then calculated using the Stokes-Einstein equation-

$$R_h = k_B T / 6\pi\eta D \qquad [A.4]$$

where k_B is the Boltzmann constant, T is the measurement temperature, and η is the dynamic viscosity. The PDI is calculated from-

$$PDI = \frac{\sqrt{K}}{\bar{\Gamma}} \qquad [A.5]$$

PDI values are < 0.3 are generally desired, indicating that the sample is moderately polydisperse.[1]

A.2 Variable Angle Spectroscopic Ellipsometry

Ellipsometry measures change in polarization of light. In this section, the general work flow to determining optical thickness of layers and corresponding refractive indices is described. The section is adapted from the user manual of WVASE32®.

Briefly, optical experiments never directly measure the sample parameters of interest (thicknesses, optical constants, etc.); rather they measure some quantity that is a function of the parameters of interest. It is then necessary to solve the inverse problem of modeling the measured data to estimate the values of the sample parameters that yield data predicted from the model which best match the measured data. This procedure may be divided into the following four steps, as illustrated in Figure A.1 below.

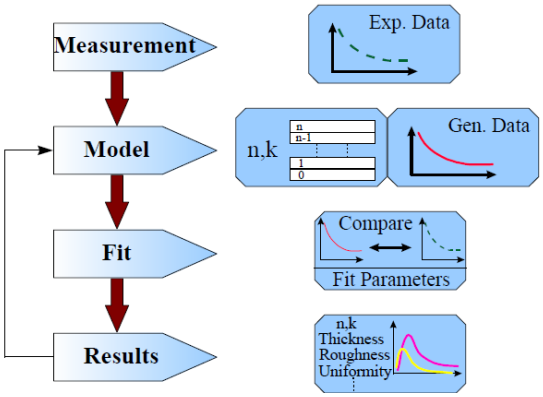

Figure A.1: Flowchart of the procedure for an ellipsometric experiment (Taken from WVASE[32] user manual)

The procedure to calculate the polarization change is discussed below-

The pseudo-Fresnel p- and s-polarized reflection coefficients are related to the amplitude ratio, Ψ and phase difference, Δ as the following equation-

$$\tilde{\rho} = \tan\Psi e^{i\Delta} \equiv \frac{\tilde{R}_p}{\tilde{R}_s} \quad [A.6]$$

Briefly, the expected Ψ and Δ for a single film sample at a given wavelength, λ and angle of incidence, Φ may be calculated with the following procedure:

1. Calculate the phase thickness of the film (β) from-

$$\beta = 2\pi\tilde{n}_1 \frac{d}{\lambda}\cos\tilde{\phi}_1 = 2\pi\frac{d}{\lambda}\sqrt{\tilde{n}_1^2 - n_0^2\sin^2\phi_0} \quad [A.7]$$

Where, d is the film thickness.

2. Calculate the p-plane reflection coefficient for a beam incident on the film from the ambient (with subscript '0' denoting the ambient and '1' denoting the film) as shown below-

$$\tilde{r}_p = \frac{\tilde{n}_1 \cos\phi_0 - \tilde{n}_0 \cos\tilde{\phi}_1}{\tilde{n}_1 \cos\phi_0 + \tilde{n}_0 \cos\tilde{\phi}_1}$$

$$\tilde{r}_s = \frac{\tilde{n}_0 \cos\phi_0 - \tilde{n}_1 \cos\tilde{\phi}_1}{\tilde{n}_0 \cos\phi_0 + \tilde{n}_1 \cos\tilde{\phi}_1} \quad \text{[A.8]}$$

3. Calculate the p-plane reflection coefficient for a beam incident on *the substrate* from the film (from A.8 with subscript '0' denoting the film and '1' denoting the substrate).

4. Calculate the p-polarized pseudo-reflection coefficient for the sample using the interfacial reflection coefficients calculated in steps 2 and 3.

$$\tilde{R}_p \equiv \frac{\tilde{E}^r_{total}}{\tilde{E}^{incident}}$$

,

$$= \frac{\tilde{r}_{01} + \tilde{r}_{12} e^{-i2\beta}}{1 + \tilde{r}_{01}\tilde{r}_{12} e^{-i2\beta}} \quad \text{[A.9]}$$

5. Repeat steps 2 - 4 for the s-polarized case, and obtaining the s-polarized pseudoreflection coefficient for the sample.

6. Evaluate ψ and Δ from the p- and s-polarized pseudo-reflection coefficients via equation A.6.

7. Having obtained optical measurements, we must now construct a model from which we can accurately predict what we should measure from a sample of known properties. This model should contain some known parameters, such as the wavelength of the incident light, the incident beam polarization state, and the angle of incidence. The model should also contain some unknown physical parameters, such as layer thicknesses and optical constants.

7. Multilayer model construction and solving: Assume that we are studying a sample from which we have measured ellipsometric data as a function of wavelength and angle of incidence. We also

have an optical model for our sample, consisting of any number of layers on a substrate and parameterized by the optical constants of the various materials and the thicknesses of the films on the sample. We now wish to vary some parameters in this model such that ellipsometric data calculated from the model matches our experimental data as closely as possible. A flowchart of this general procedure is given below-

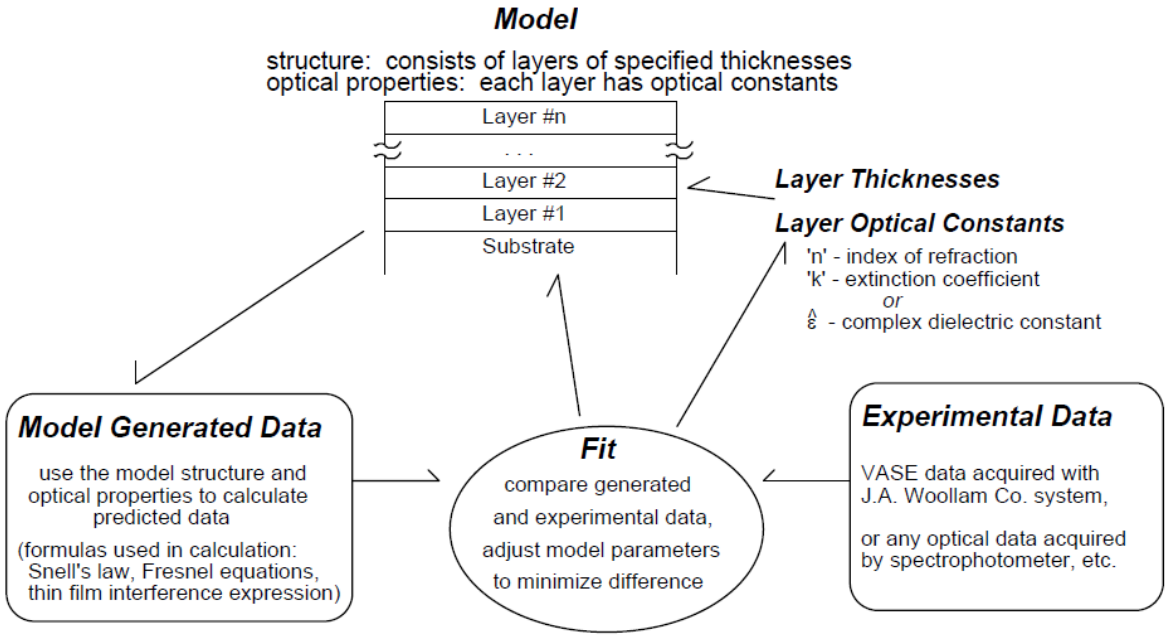

Figure A.2: The flow chart of constructing and fitting multilayer model for deriving layer thicknesses and optical constant of unknown dispersion layer.

First we must define some quantity (called a maximum likelihood estimator) which represents the quality of the match between the data calculated from the model and the experimental data. The maximum likelihood estimator must be positive and should go to zero (or at least an absolute minimum) when the calculated data matches the experimental data exactly. According to the user manual the *WVASE32*™ uses the following maximum likelihood estimator, the mean-squared error (MSE):

$$MSE = \sqrt{\frac{1}{2N-M}\sum_{i=1}^{N}\left[\left(\frac{\psi_i^{\mathrm{mod}}-\psi_i^{\mathrm{exp}}}{\sigma_{\psi,i}^{\mathrm{exp}}}\right)^2+\left(\frac{\Delta_i^{\mathrm{mod}}-\Delta_i^{\mathrm{exp}}}{\sigma_{\Delta,i}^{\mathrm{exp}}}\right)^2\right]} = \sqrt{\frac{1}{2N-M}\,\chi^2} \qquad [A.10]$$

where N is the number of (Ψ,Δ) pairs, M is the number of variable parameters in the model, and σ are the standard deviations on the experimental data points. Another common maximum likelihood estimator, the chi-square ($\chi 2$) is defined in equation A.10 for comparison.

The MSE represents a sum of the squares of the differences between the measured and calculated data, with each difference weighted by the standard deviation of that measured data point. For a very noisy measurement, the corresponding standard deviation will be large and that measurement will not be strongly weighted in the fit.

We have now reduced the fitting problem to finding a set of values for the variable model parameters which yields a single unique absolute minimum of the MSE. This is a minimization problem in that we are trying to find the minimum value of the MSE. For the results to be meaningful, this minimum should occur at a small value of the MSE (usually less than 10), and should be fairly sharp as a function of the variable parameters.

8. Minimization of error: The discussion of minimization methods in the following sections requires the definition of some terms before proceeding.

First, we will henceforth denote all of the measured data points as y_i, where each y_i is either a measured Ψ or Δ value. The corresponding Ψ or Δ value calculated from the model is denoted $y(x_i; a)$, with x_i representing all known model parameters (such as angle of incidence, wavelength, known thicknesses, known optical constants, etc.) and the vector *a* consisting of all variable model parameters. Thus, each element of *a* is a variable parameter such as a layer thickness or optical constant, and the individual elements will be denoted a_j, where j ranges from 1 to M, the total number of variable parameters. Finally, σ_I will denote the standard deviation of the i^{th} data point.

The gradient method was used to minimize the MSE (not discussed here).

A.3 X-ray Photoelectron Spectroscopy (XPS)

In this section, the XPS spectra of Br-terminated thiol wide scan spectra, after grafting of copolymer brush spectra and the subsequent calculated Br 3p/ S 2p ratios are given. These data were not included in the chapter 4.

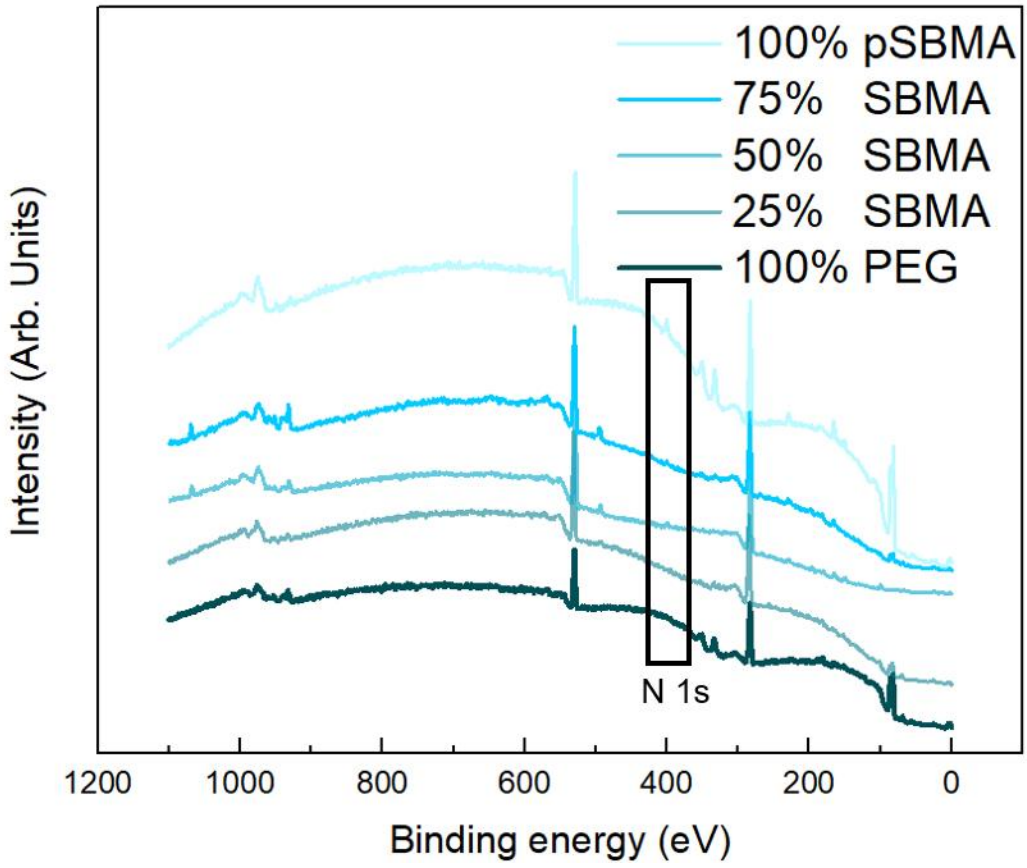

Figure A.3: The wide scan XPS spectra of grafted 0, 25, 50, 75 and 100 % SBMA copolymer brush content (in feed). The N 1s peak is identified and it is zoomed in figure A.4.

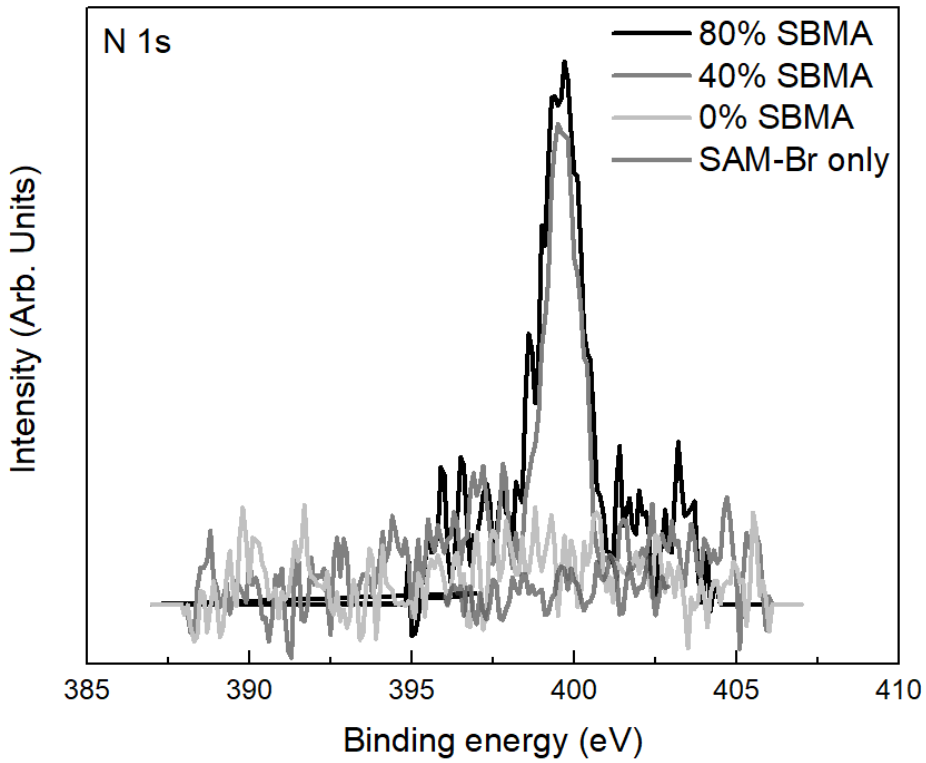

Figure A.4: The N1s spectra of 0, 40 and 80% SBMA in copolymer brush and Br-terminated thiol grafted surfaces. The relative amount of N1s /S2p spectra give the %SBMA content in the copolymer brush, given in Table 4.6.

A.4: Atomic Force Microscopy (AFM)

AFM scans were collected by Asylum Research Cypher Scanning Probe Microscope in tapping mode, in dry conditions in room temperature and scan rate 1 Hz. AFM scans in water were obtained by MFP-3D model and bioheater accessories.

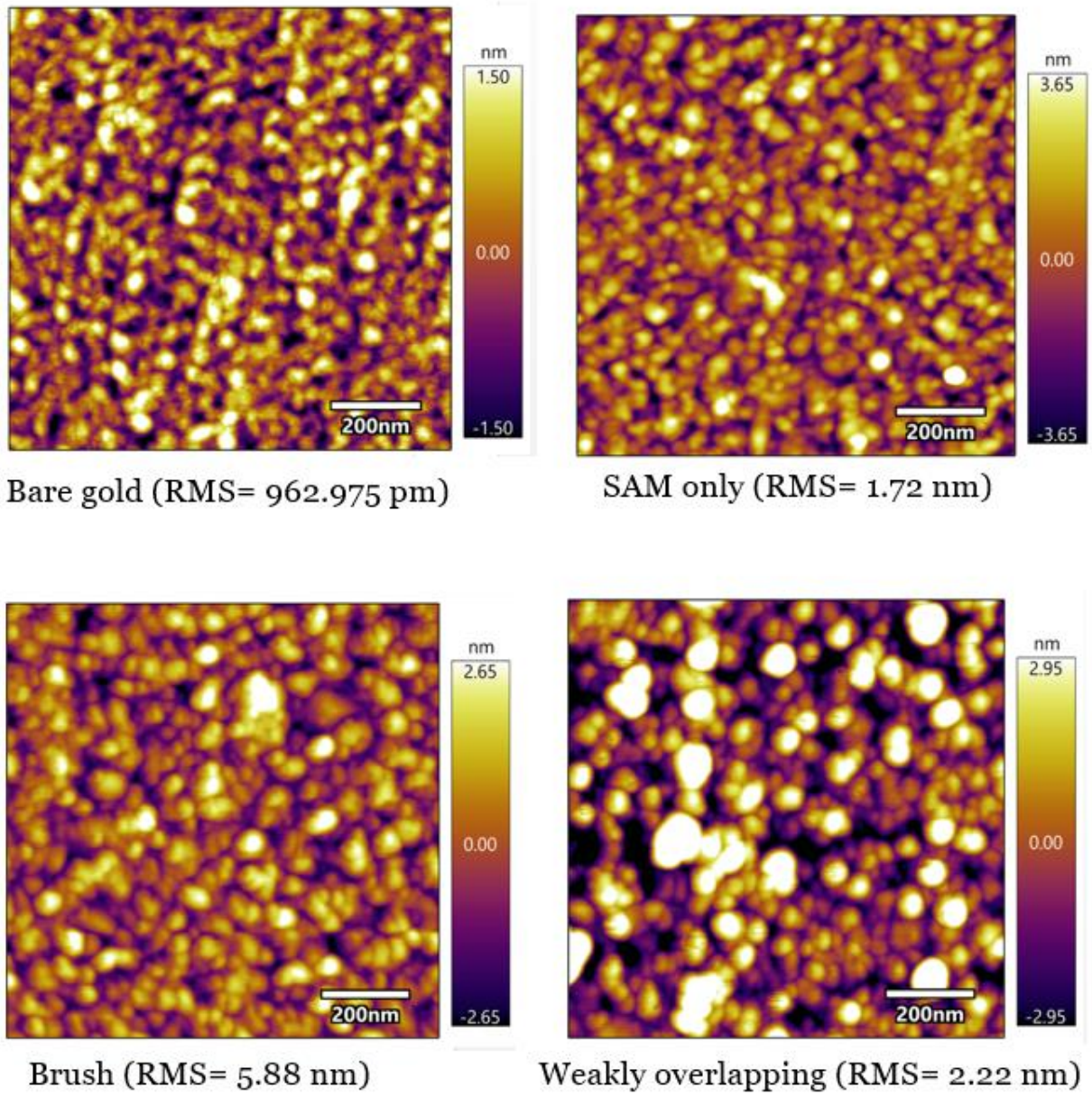

Figure A.5: AFM scan mode: tapping, in air. Samples are grafted polysulfobetaine (bottom row) and gold coated Si wafer (top left) and Br-terminated thiol initiator (top right).

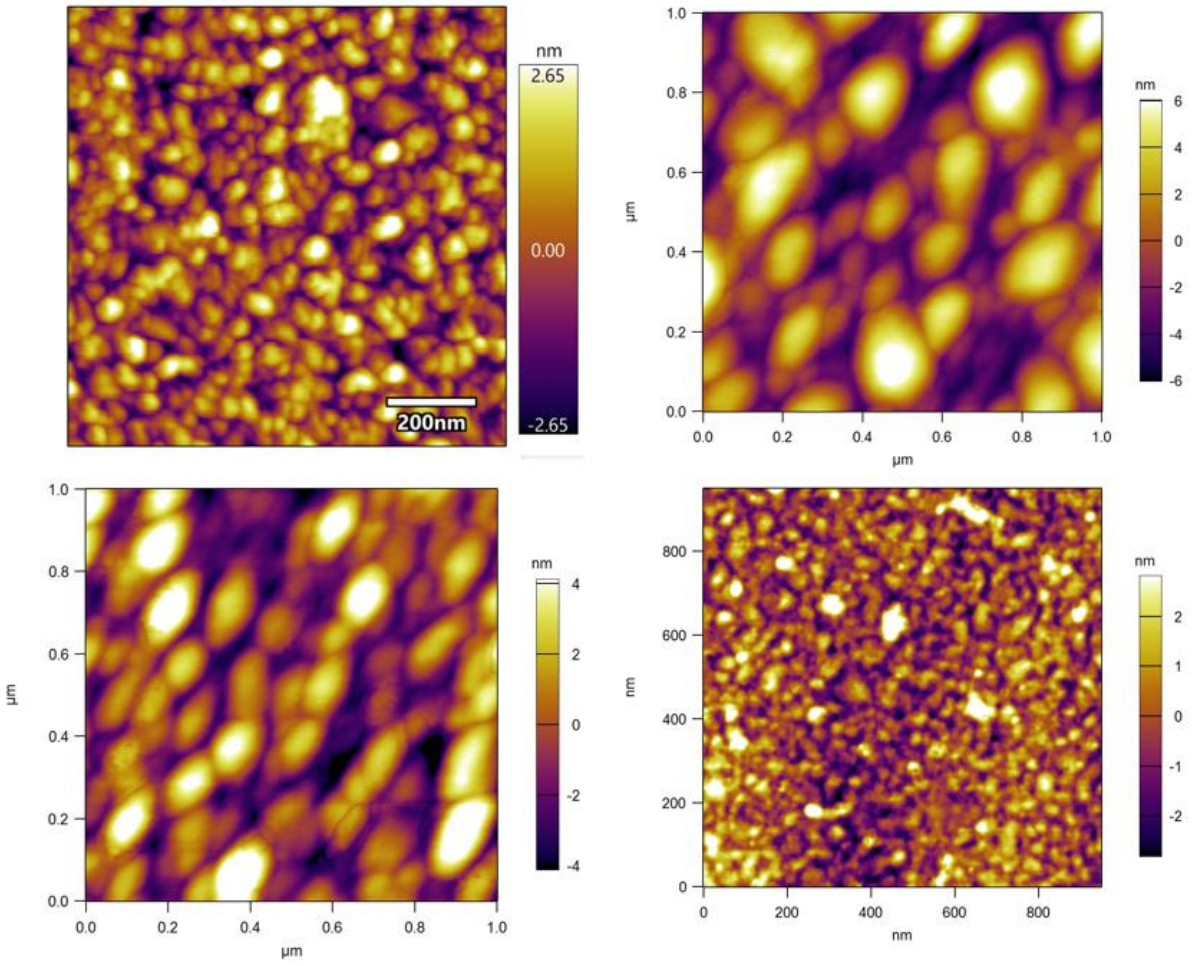

Figure A.6: AFM scan mode: tapping, in air. (Clockwise from top left) Samples are grafted polysulfobetaine on 100, 80, 50 and 20% Br-terminated self-assembled monolayer on gold coated Si wafer.

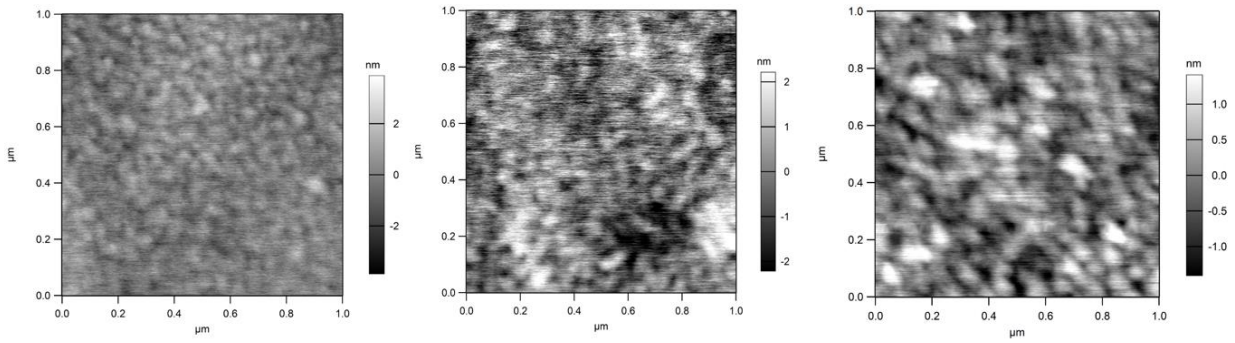

Figure A.7: AFM scan mode: tapping, in pure water in room temperature. (From left to right) Samples are grafted polysulfobetaine chains on 100. 80 and 20 % Br-terminated self-assembled monolayer on gold coated Si wafer.

Reference:

1. Ferreira, J. *et al.* Optimizing the Generation of Narrow Polydispersity “arm-First” Star Polymers Made Using RAFT Polymerization. *Polym. Chem.* **2**, 1671 (2011).

APPENDIX B: IMAGE ANALYSIS OF INTERFERENCE FRINGES

The Matlab code used to process interference fringes was written by Kai A. Schwenzfeier (Institute for Applied Physics, Vienna University of Technology, Wiedner Hauptstrasse 8-10, A-1040 Vienna, Austria, contact email: kai.schwenzfeier@tuwien.ac.at)

The image processing steps are given below-

1. Make stack images of one complete force run at one contact. Open the folder where the images of one force run are saved via ImageJ.

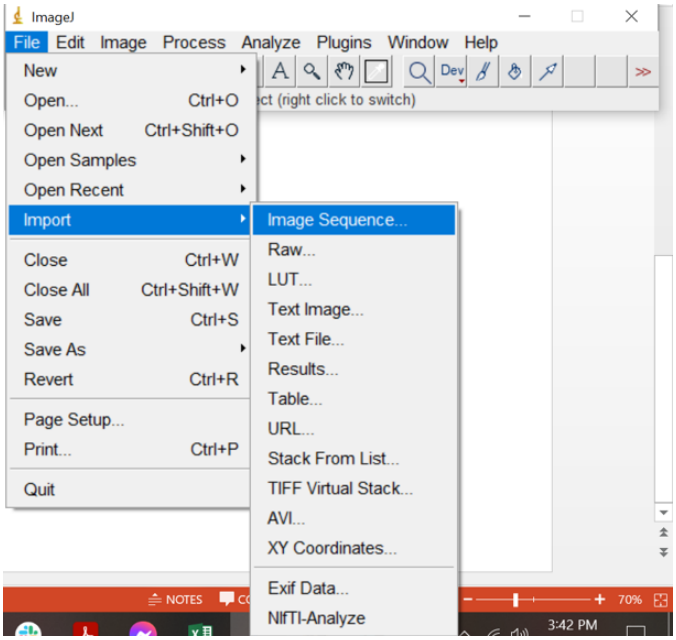

Open ImageJ>Import>Image Sequence>go to the folder where the force run images are saved, usually saved as FR1,FR2 etc. and select the first image only. It will open the following window>click OK

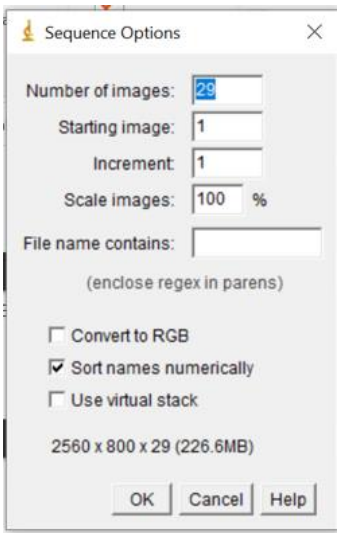

Clicking OK will open the stacked images in ImageJ which can be saved. In this example the image file was saved as ‘in4’.

Open Matlab and save the SFA folder with the required matlab codes for doing data analysis. In the following example the SFA folder is saved in C>Users>Tajin (my name)>Documents>Matlab>SFA

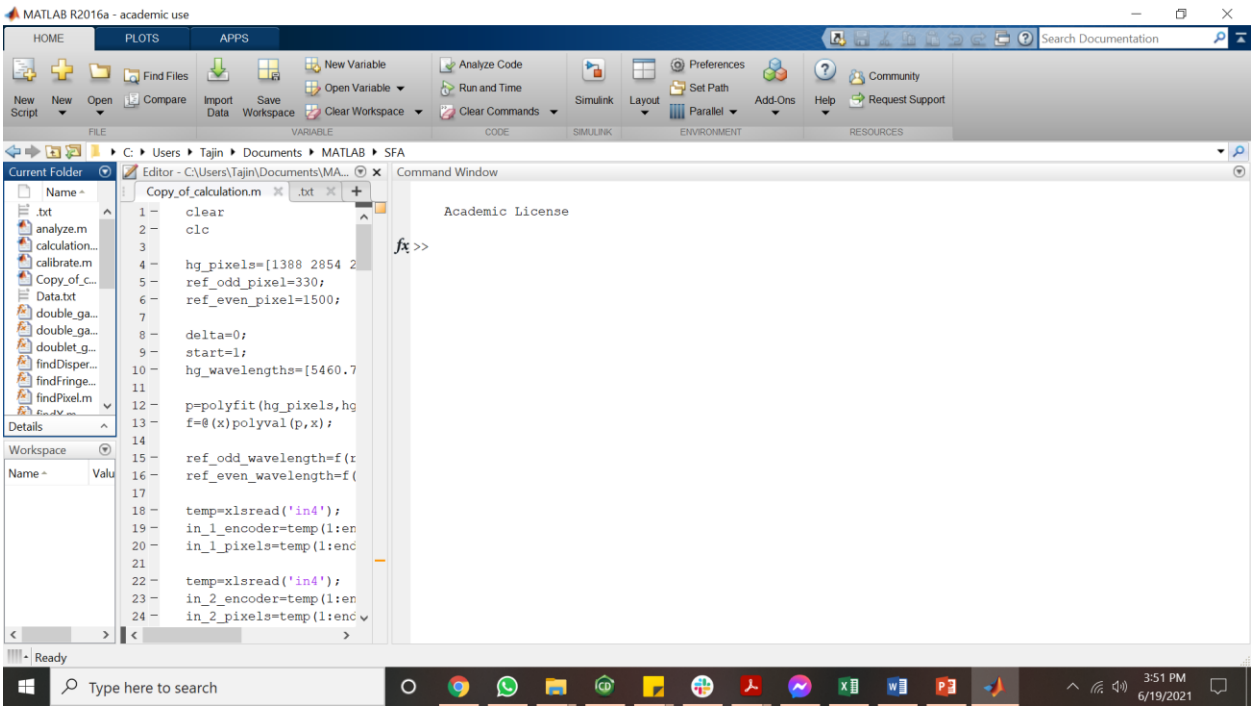

Click and open the SFA folder into the matlab and load the stacked image file called ‘in4’. This is simply done by copying and pasting the file into the current folder window.

Next, type the following commands as showed-

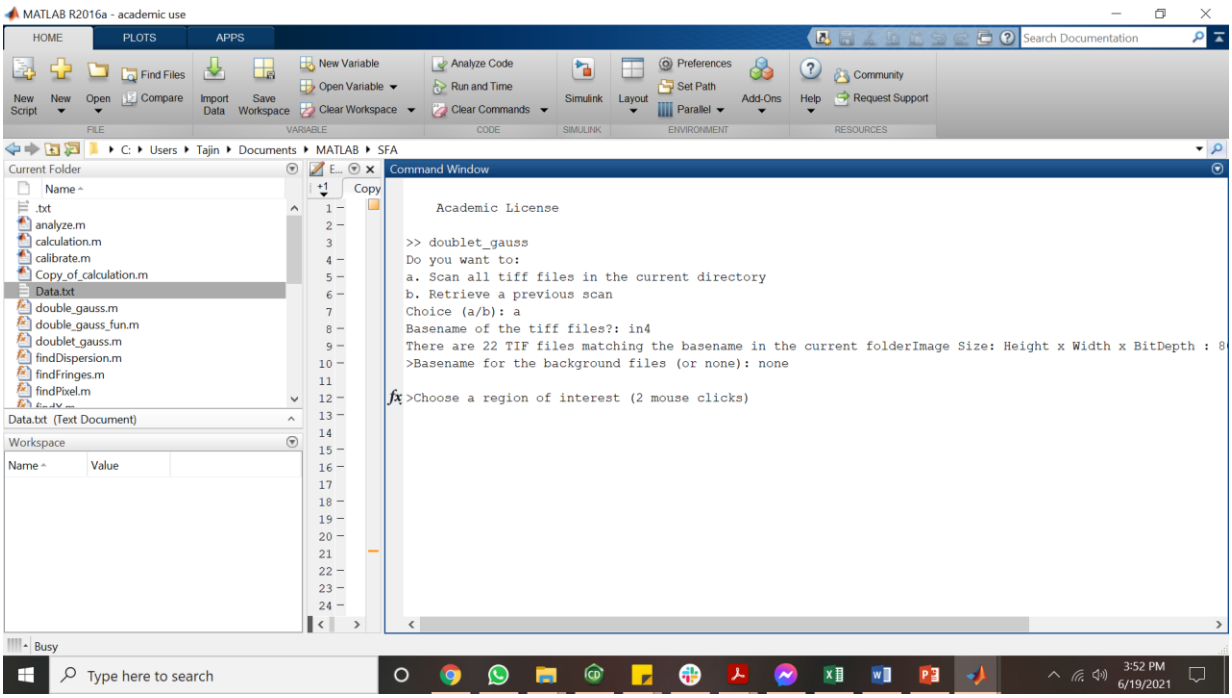

If you want to open an already loaded file, then in Choice command pick ‘b’ instead of ‘a’ and that will prompt the Matlab program to open folder containing the files that are already loaded. After selection the following image opens. This is the first image of the stack. We want to choose the Peak area of the fringe and follow it for all the image stack.

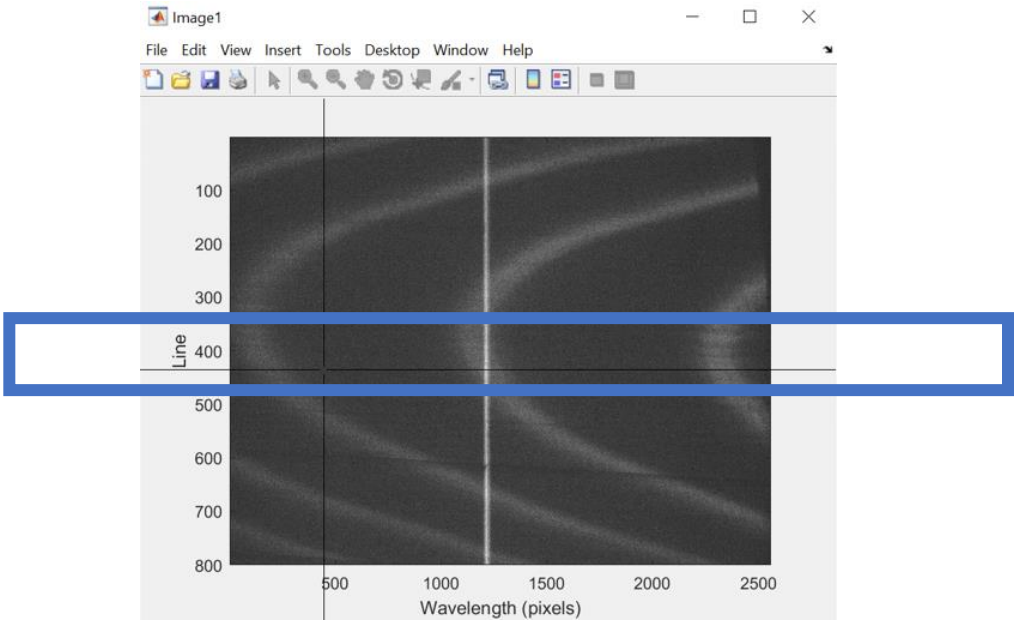

The blue square is chosen and we are following the right most fringe. To choose the area as shown above, click on right side ~400 mark (but not on the axis) and then click again on right ~450 mark. The result is the following-

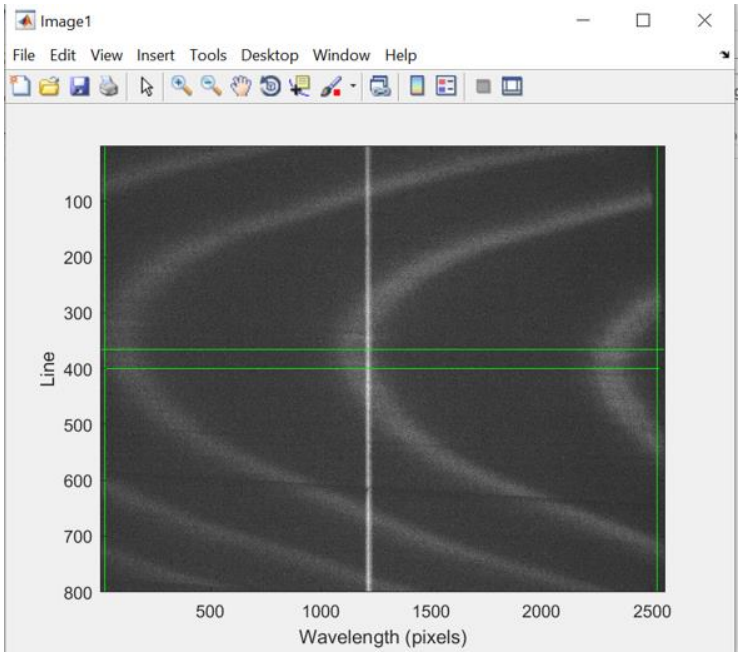

This will prompt the following window to open which shows the image stacks for only the chosen area.

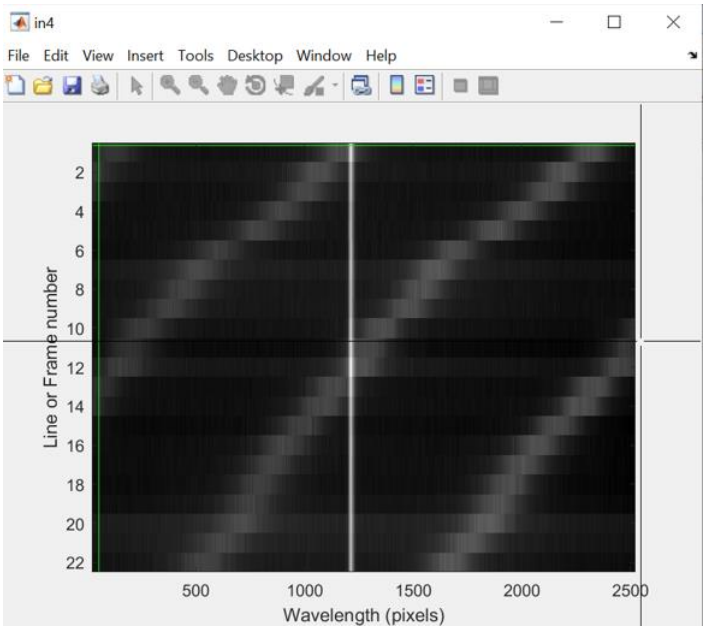

Here the image had 22 stacks, and we will first analyze the first 1-10 frame. To do so, click on the top-left corner (where the green lines meet, for example) to select the first frame and then click on right-approximately on line/frame number=10. The selected first 10 frames are shown below-

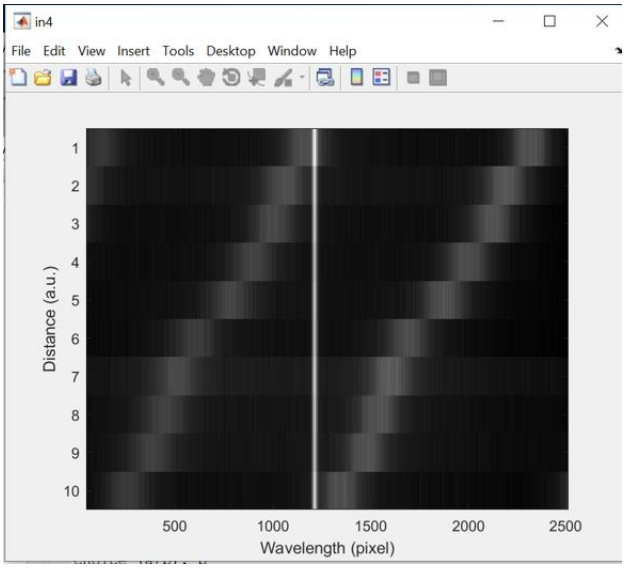

Then click on the first frame you want to analyze. It is always on the first frame number as shown below-

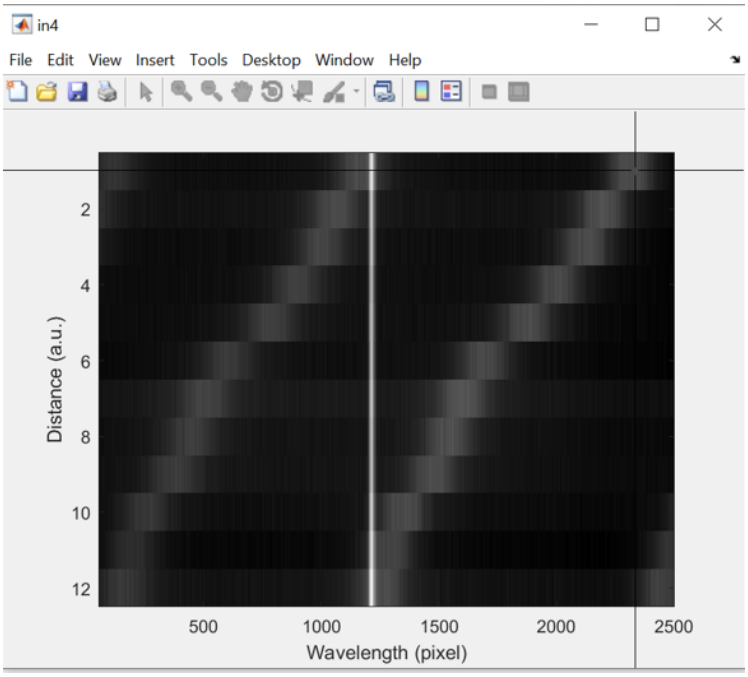

Then the following prompt is shown in the command window-

>Choose a region of interest (2 mouse clicks)

>Choose a line (1 mouse click)

Set initial fit-parameter: Choose 2 peaks to be followed (2 mouse clicks), the initial FWHM (2 clicks) and a third peak (if not needed change fitting function!)

This requires a total of 5 clicks on the images, shown below-

The 3rd and 4th click are arbitrary. The first two clicks are usually on the two adjacent peak we are following. The 5th click is always on the reference Hg line peak (see next page).

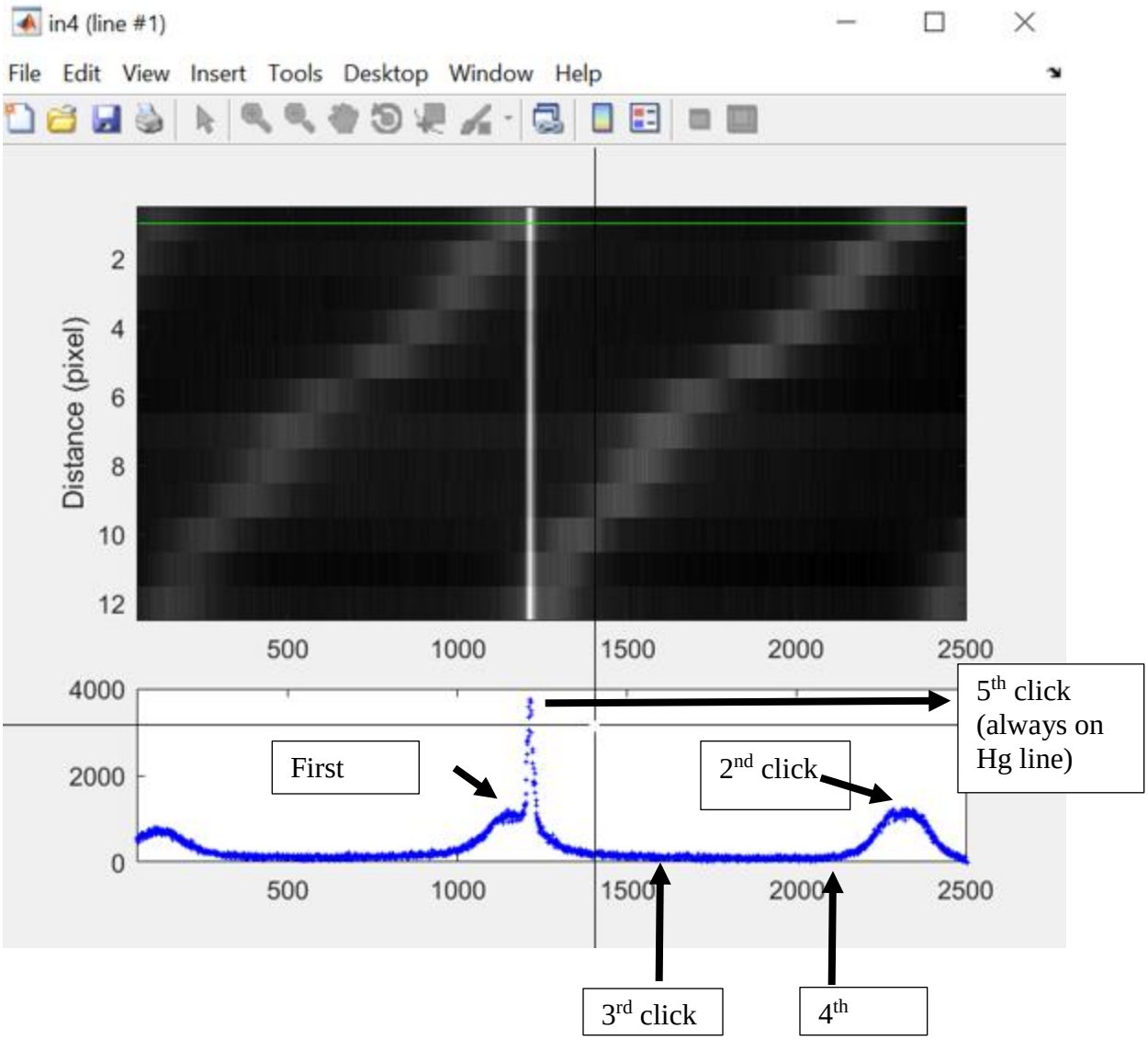

After selection, the Matlab program performs Gaussian fit to the peaks and show the peak pixel values in the following window.

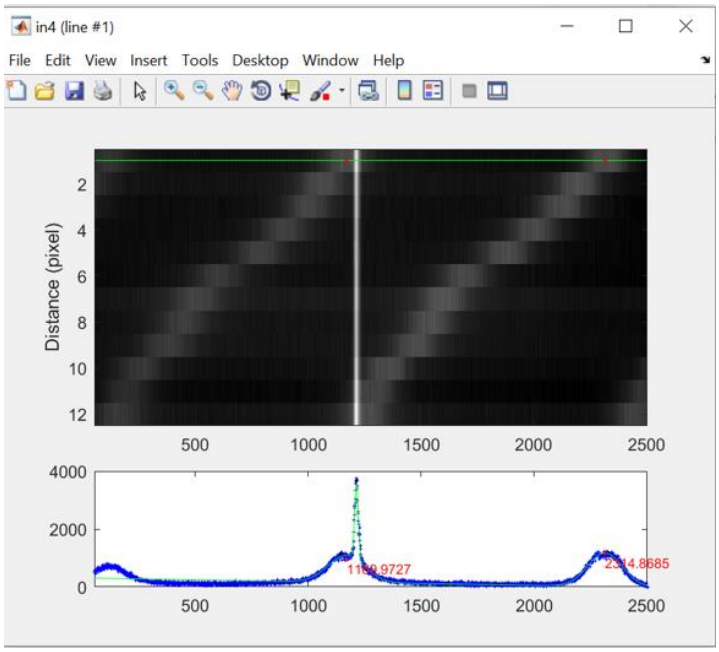

If satisfactory go to the command window, and choose ‘y’ for continue with detection. That will start the process of fitting the peaks of the subsequent 10 frames with the initial values provided.

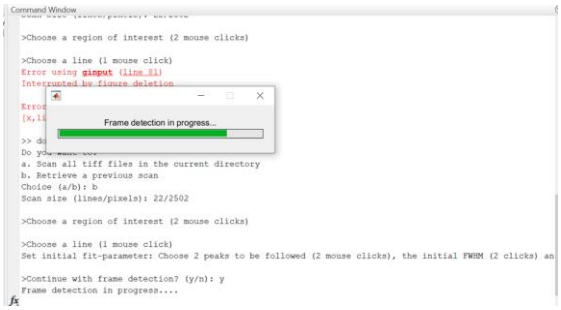

Once the frame detection is complete the fitted peak of the fringes are shown in the following window-

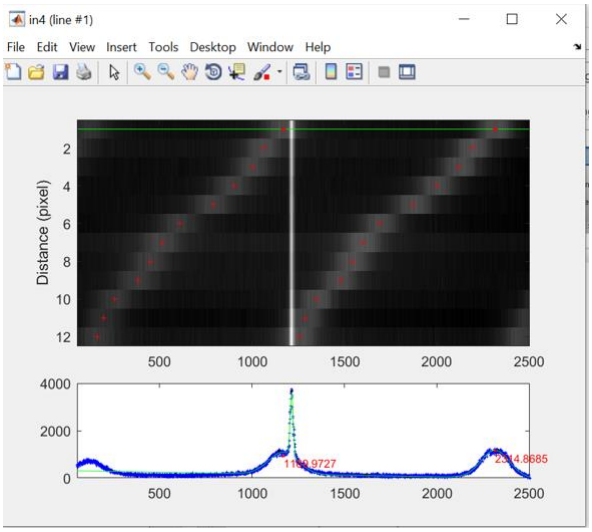

Here, we are following the right most peak and the program did a good job in finding the spot with the maximum intensity, i.e. the peak of the fringes.

Go to the command window and type ‘n’ for ‘do you want to discard any point?’ That will show the peak pixel values with the corresponding frame numbers, and also save these values in an excel file called ‘in4_1_11.xls’.

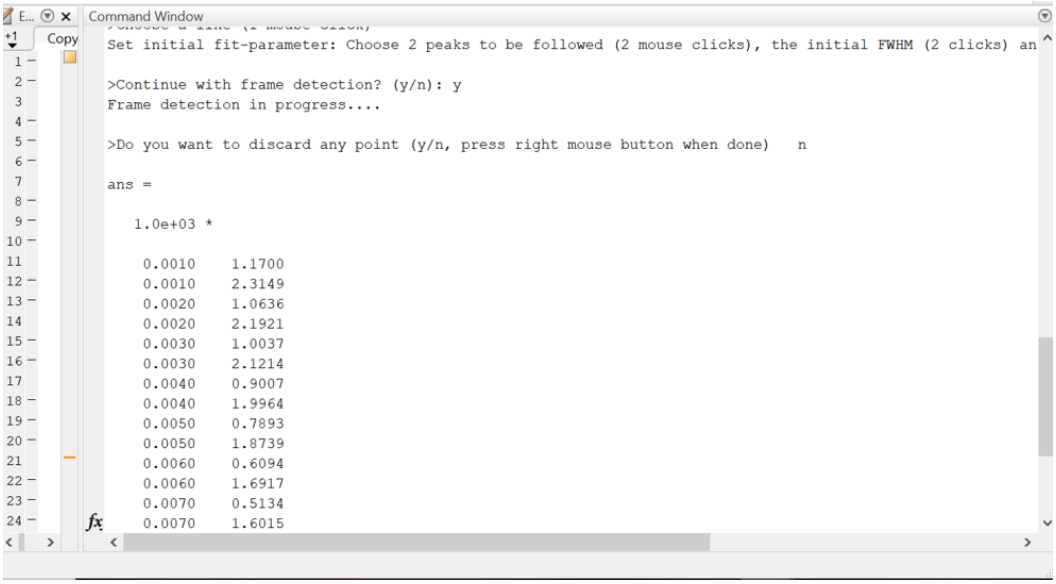

To proceed with the rest of the frames, choose ‘b’ when asked to load image file stack.

```
>> doublet_gauss
Do you want to:
a. Scan all tiff files in the current directory
b. Retrieve a previous scan
Choice (a/b): b
Scan size (lines/pixels): 22/2502
```

This will open the image stack and in the same way choose frame number 10 to the rest of the files. And follow the same procedure as above.

Finally all the excel files can be copied and pasted in a folder and put them all together by Frame number (1,2,3,…) and Pixel values. In another excel file, put the encoder positions, and the corresponding pixel values in one file.

This is saved as ‘in4.xls’ and we will analyze this data file next. First copy paste the ‘in4.xls’ file to the Current Folder window as shown below-

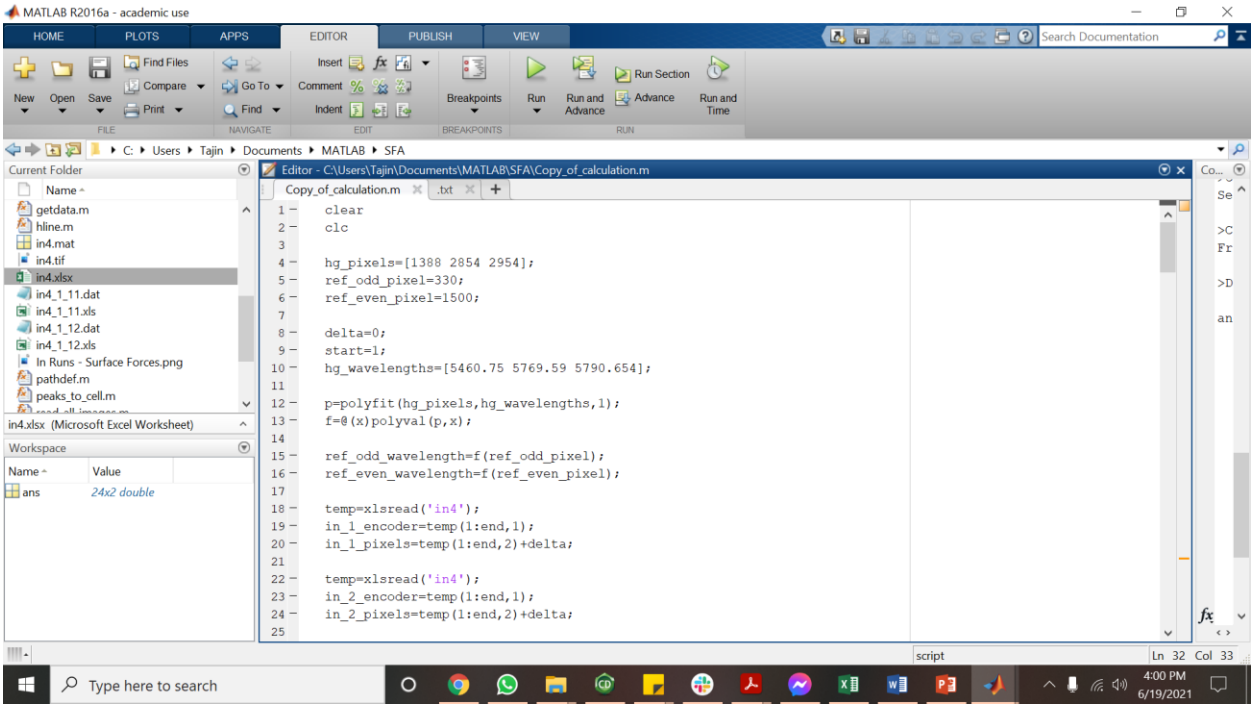

Next open the ‘calculation’ or ‘copy of calculation’ matlab file for doing the analysis. The details of the ‘calculation’ file is added with %comment within the code for clarification.

APPENDIX C: THEORY OF MULTIPLE BEAM INTERFEROMETRY

Multiple Beam Interferometry or MBI technique is used to measure the absolute distance between two surfaces and to obtain information about the contacted region in the Surface Force Apparatus (SFA). [1,2] For a typical SFA experiment a pair of transparent surfaces (e.g. freshly cleaved mica) is used as the surface substrate, which are coated on the back with a highly reflective layer (e.g. silver) for providing a good interfering pattern between the reflecting surfaces. Instead of silvered mica, gold coating of 50 nm thickness can also be used as a reflected surface. In this thesis the SFA work was performed using a back silvered mica and gold coated silica discs. Gold was used for the ease of surface functionalization (with thiol) and polymerization process. However, RMS surface roughness of gold is ~1 nm (Figure A.5, Panel A) and therefore light passing through the interferometer happens at different angle and the obtained fringes are not as sharp as those obtained with mica-mica systems (compare Figure 1.8 and Figure 1.9). After the mica surfaces are prepared and glued onto the silica glass disk, they are mounted in a cross-cylindrical configuration, which simulates a sphere-on-flat geometry. When white light is directed normal to the surfaces the light is reflected back and forth between the silver layers and the transmitted light near the closest contact point between the surfaces creates Newton's rings, as can be seen through a microscope objective. The transmitted light corresponds to a particular set of discrete wavelengths that is made visible by a spectrometer and are the so-called fringes of equal chromatic order (FECO). In this appendix we will only consider this setup with (1) three-layer (e.g. mica-medium-mica) interferometry, which is the most commonly used setup for SFA experiments (section C.1) and (2) two layer asymmetrical system (e.g. medium-mica), which was used in this thesis work (section C.2).

C.1 FECO Fringes of a Symmetrical Three-layer Interferometer

This section is adapted in part from the journal article: Israelachvili, J.N., Thin film studies using multiple-beam interferometry, *Journal of Colloid and Interface Science* 1973, 44 (2), 259-272 with permission [copyright 1973 Elsevier].

When the surfaces are in contact with no medium between them, the interference fringes depend on the mica thickness. Assuming that the mica thickness, T, is the same for both surfaces, T can be determined by the wavelength of the nth order fringe, λ_n^0, by the relation $T = n\,\lambda_n^0/4\mu_{mica}$, where μ_{mica} is the refractive index of mica at λ_n^0. The fringe order, n, is determined by

$$n = \frac{\lambda_{n-1}^0}{\lambda_{n-1}^0 - \lambda_n^0} \quad \text{(Equation C.1)}$$

where λ^0_{n-1} is the next fringe at higher wavelength. It can be shown that when the surfaces are separated by a distance D, the amount that the n^{th} fringe shifts by depends on the refractive index of the medium in the gap between the surfaces, and the original contact positions (because these are related to n and the interferometer thickness).[2, 3]

$$\tan(2\pi\mu D/\lambda_n^D) = \frac{2\bar{\mu}\sin[\pi(1-\lambda_n^0/\lambda_n^D)/(1-\lambda_n^0/\lambda_{n-1}^0)]}{(1+\bar{\mu}^2)\cos[\pi(1-\lambda_n^0/\lambda_n^D)/(1-\lambda_n^0/\lambda_{n-1}^0)] \pm (\bar{\mu}^2-1)} \quad \text{(Equation C.2)}$$

The + sign is taken when n is odd and − is taken when n is even. At the separation distance D, the nth fringe changes wavelength from λ_n^0 to λ_n^D. The effective refractive index is denoted as- $\mu' = \mu_{mica}/\mu$ where μ_{mica} is the refractive index of mica at λ_n^D and μ is the refractive index of the medium between the two surfaces at λ_n^D .

If the positions of three consecutive fringes are known, then an iterative process can be used to determine the thickness and refractive index of the film between the surfaces.

When the surfaces are separated by a distance which results in a fringe shift equal to $\lambda_{n-1}^0 - \lambda_n^0$, then the film thickness is calculated by $D = \lambda_{n-1}^0/2\,\mu$.

When the distance between the surfaces is small (D below ~30 nm), we can use Taylor series expansions to find approximate expressions for the trigonometric functions in Equation C.2:

$$D = \begin{cases} nF_n(\lambda_n^D - \lambda_n^0)/2\mu_{\text{mica}}, & \text{for odd } n, \\ nF_n(\lambda_n^D - \lambda_n^0)\mu_{\text{mica}}/2\mu^2, & \text{for even } n, \end{cases} \qquad \text{(Equation C.3)}$$

where F_n is a correction factor which takes into account the refractive index dispersion and phase change of the reflection at the silvered interfaces. For light with wavelength λ ~500 nm, the correction factor is $F_n \approx 1.024 + 1/n$.

Note that the film thickness determined from the even order fringes depends on μ, the refractive index of the medium between the mica surfaces, but that the film thickness determined from the odd order fringes does not. Therefore, if we know the wavelength shift of two consecutive fringes we can determine an approximate value for the refractive index of the medium:

$$\mu = \mu_{\text{mica}} \sqrt{\frac{(n-1)F_{n-1}}{nF_n} \cdot \frac{\lambda_{n-1}^D - \lambda_{n-1}^0}{\lambda_n^D - \lambda_n^0}}, \qquad \text{for } n \text{ odd.}$$

Equation C.3 can also be used to explain why odd fringes look different than even fringes for small D as shown in Figure 1.5. Equation C.3 is used for measuring the ΔD_{meas} in Equation 1.4.

C.2 FECO Fringes of a Two-layer Interferometer

The method of the last two sections may also be applied to non-symmetrical layers, and as an example we shall derive the formula for FECO fringes of a two-layer interferometer (see Fig. C.1).

$$\tan(2k\mu_3 D)=\frac{(1-r^2)\sin(2k\mu_1 Y)}{2r-(1+r^2)\cos(2k\mu_1 Y)} \qquad \text{(Equation C.4)}$$

For D=0 the nth order fringe at λ^0 is given by $2k\mu_1 Y=2n\pi$ or $\mu_1 Y=n\lambda^0/2$; and for T finite, the fringe shifts by $\Delta\lambda_n$ to a new wavelength λ given by,

$$\tan(2k\mu_3 D)=\frac{(1-r^2)\sin(2n\pi\Delta\lambda_n/\lambda)}{2r-(1+r^2)\cos(2n\pi\Delta\lambda_n/\lambda)} \qquad \text{(Equation C.5)}$$

where $\Delta\lambda_n$ is $\lambda-\lambda^0$. Equation C.5 is the same for both odd and even orders (unlike the symmetric systems) and therefore we cannot simultaneously measure both D and μ_3 to be separately determined.

For small separation, $D = n\Delta\lambda_n\mu_1/2\mu_3^2$ (Equation C.6)

This equation is used to calculate ΔD_{meas} in Equation 1.4 for our experiments.

References:

1. Tolansky, S. *Multiple beam interferometry of surfaces and films*. *London: Oxford University Press.* (1949).
2. Israelachvili, J. N. Thin film studies using multiple-beam interferometry. *J. Colloid Interface Sci.* **44**, 259–272 (1973).
3. Horn, R. G. & Smith, D. T. Analytic solution for the three-layer multiple beam interferometer. *Appl. Opt.* **30**, 59 (1991).

APPENDIX D: MICA PREPARATION FOR INTERFEROMETRY

This section is adapted in part from the journal article: Israelachvili, J.N., Thin film studies using multiple-beam interferometry, *Journal of Colloid and Interface Science* 1973, 44 (2), 259-272 with permission [copyright 1973 Elsevier].

Ruby mica was used for interferometry work in this thesis because of the following reasons- (1) it is easily cleavable, (2) upon cleaving the exposed surface is molecularly smooth and step free for a relatively large area of approximately 10 cm^2. The entire process for cleaving mica and preparation for interferometry work is adapted from previous work. [1, 2]

In a laminar flow cabinet, a thin sheet of ruby mica is first cleaved from a thick mica plate. Cleavage is initiated by inserting the tip of a sharp needle into the edge of the plate and carefully peeling away a thin sheet. This can be done by sharp nails too, if comfortable. The freshly cleaved sheet is again and again cleaved until the mica piece is thin enough. To determine whether it is thin enough, the pieces should be held by a tweezer (prior using the tweezer must be rinsed with ethanol) to examine in the light of an ordinary fluorescent lamp. If the sheet is sufficiently thin interference colors (blue to purple) are seen reflected by the surface. These colors change abruptly at cleavage steps, but remain uniform over regions of constant thickness. With some practice it is possible to recognize regions that are 1-3 μm thick and free of cleavage steps. If a large enough step-free region is found, small rectangular sheets may be cut out of it with a hot platinum wire heated above the melting point of mica by passing a current through it. The rectangular sheets should be cut in such a way so that when two such sheets are later brought into contact they will face each other in their original crystallographic orientation. This is desirable because mica is

birefringent; the two indices of refraction differ by 0.00493 so that the optical thickness of a sheet $\mu_1 Y$ is different for the two polarization directions. As each rectangular sheet is cut free from the main sheet it is held at one edge with tweezers and immediately placed on a large thick sheet of freshly cleaved mica (the backing sheet). The edges of the cleaved mica pieces are damaged or burnt and therefore, they do not adhere to the backing sheet but the rest of the pieces do. This is favorable because we need to pick up the mica pieces again with tweezers after silvering it. Several rectangular sheets may be prepared at the same time and placed on the backing sheet. In this way the surfaces of the rectangular sheets in contact with the backing sheet are protected from contamination so long as they remain there. After silvering using a thermal evaporator (50 nm Ag deposition at 10^{-7} torr at a rate of 0.1nm/s), the back silvered mica is brought back to the laminar flow cabinet. First the cylindrical silica discs on which the back silvered mica will be deposited, are warmed up using an electrically heated hot-plate and placing some sym-diphenylcarbazide powder glue on top of the glass. As soon as the powder melts a mica sheet is stripped off the backing sheet with tweezers and placed on top of the glue, silvered side down. The glue immediately spreads out evenly underneath the mica pulling it into close contact with the glass. The glass plate is removed from the hot-plate and allowed to cool. Now the mica surface is ready to be used for interferometry. Thin and asperity free silvered mica thus produced, provides sharp newton's rings or FECO fringes when projected onto the spectrometer and also provide 2 or 3 fringes in the view area. Therefore, it is easier for the experimenter to follow a particular fringe (most of the time an odd fringe) real time with precision.

References:

1. Israelachvili, J. N. Thin film studies using multiple-beam interferometry. *J. Colloid Interface Sci.* **44**, 259–272 (1973).

2. Israelachvili, J. N., Alcantar, N. A., Maeda, N., Mates, T. E. & Ruths, M. Preparing contamination-free mica substrates for surface characterization, force measurements, and imaging. *Langmuir* **20**, 3616–3622 (2004).

APPENDIX E: SURFACE PLASMON RESONANCE PROTOCOL

The instrument is called Horizon SPRimager by GWC Technologies (Madison, USA). It requires a floor space of 25” x 18” (63cm x 45cm) and uses standard electrical power. For optimum performance, the instrument should be kept somewhere where it is-

1. Vibration-free
2. Away from direct sunlight
3. Clear of any sources of hot or cold air or other temperature disturbances
4. Clear of areas where the instrument may be exposed to water or other liquid spills
5. At least 4” (10cm) clear of obstruction at the rear of the instrument for ventilation and accessibility

The training videos are uploaded in the Leckband official box folder (see video: **SPR holder setup**). Photo courtesy: John Mcguire, Roger Chan and Syeda Tajin Ahmed.

The steps to set up the flow channel on the SPR instrument are given below-

1. Place the single/dual flow gasket in the flow cell.

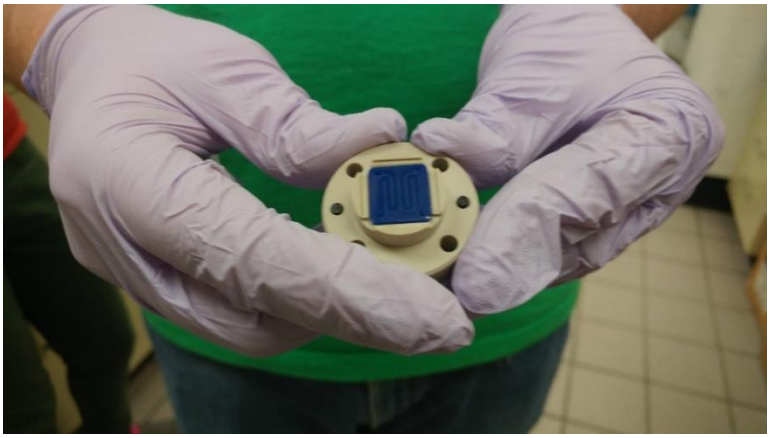

Figure E.1: The dual flow channel (blue) mounted on the SPR holder

2. Place the chip and black mount onto the gasket. Wipe the prism with a drop of ethanol and lens paper (see video: **Cleaning the prism**). Before mounting the prism on to the holder, put a drop of index correction fluid/oil (refractive index=1.705-1.800 $\pm$ 0.0005, ND=1.720, Cargille Laboratory, product ID # 1815Y) on the corner and touch one side of the prism first, then slowly put down the rest of the plane onto the gold side of the chip. This allows even spreading of the oil in between the prism and the chip. Finally, screw in the prism into the holder (see figure below). Tighten the screws lightly and avoid bending the chip.

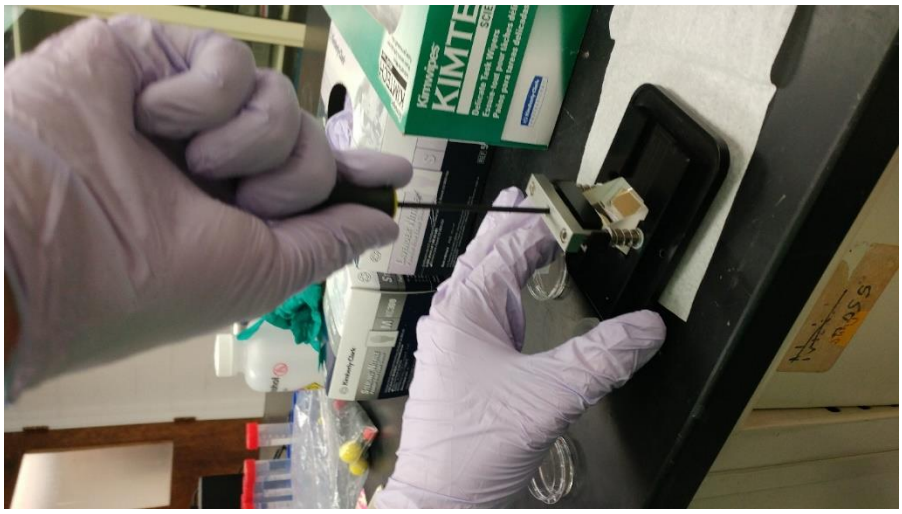

Figure E.2: Tightening screws on top of the SPR chip holder

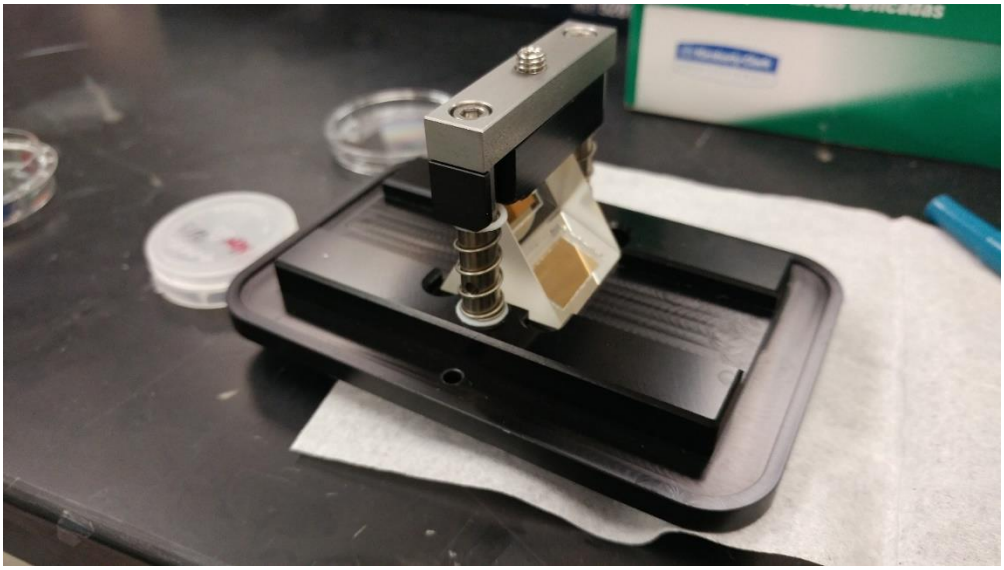

Figure E.3: Assembly of prism and the gold coated SPR chip

3. Put the little screw in tubes into the flow cell. Be careful to note which inlet corresponds to which outlet. In the picture below, the inlets are the short tubes. Look back at the first picture in this document. The flow cell has 6 holes, 2 of them not in corners. The flow cell path crosses the line between these 2 holes. The inlet and outlet are adjacent. Test the flow cell before putting it in the SPR. If it leaks the casing must be opened and the inner prism removed to be cleaned.

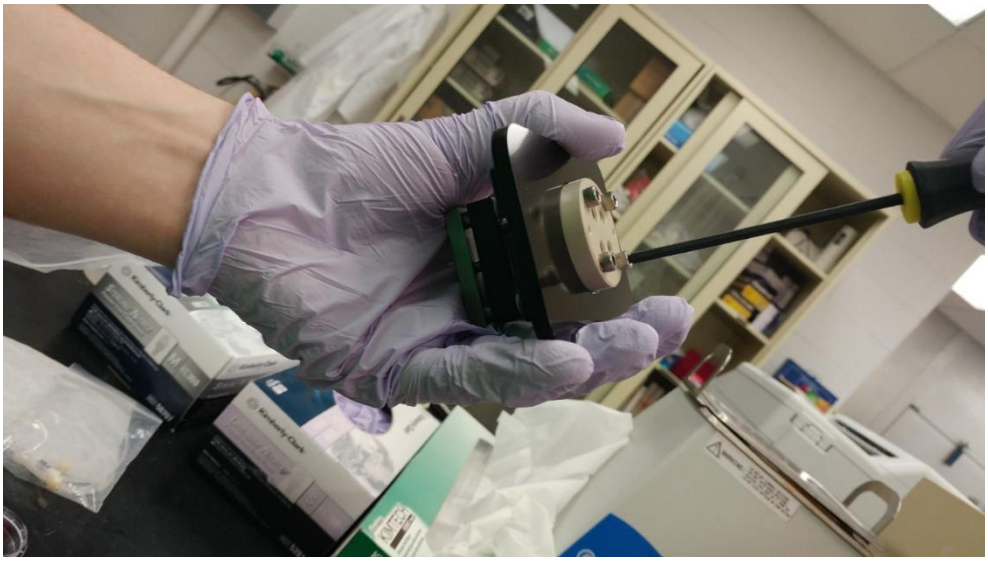

Figure E.4: Setting up the chip holder onto the SPR assembly

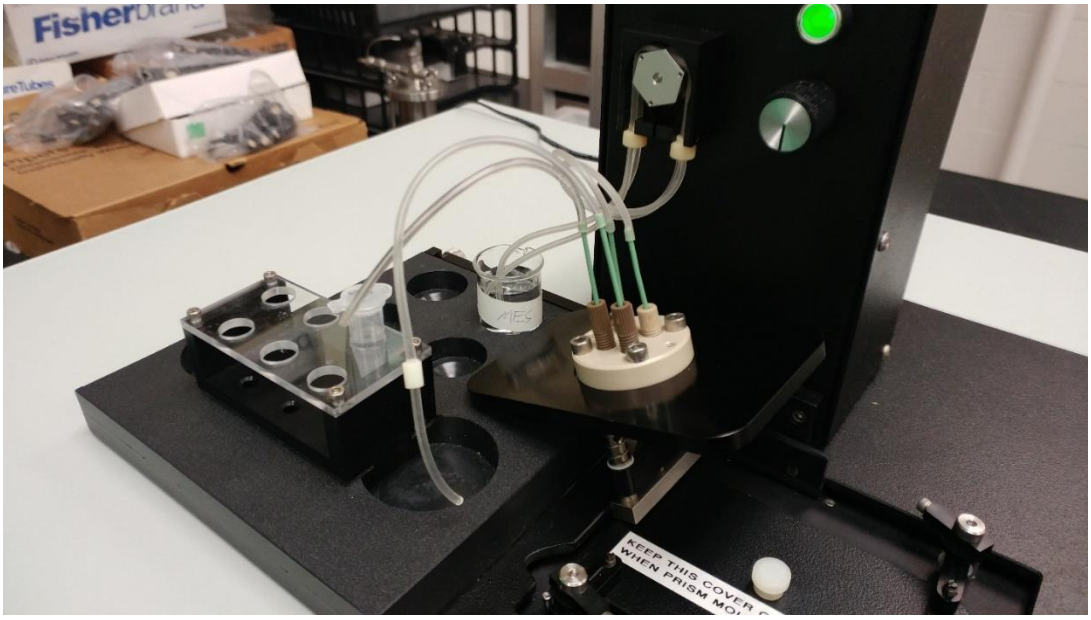

Figure E.5: The inlets and outlets of the dual channel flow

4. Open the program V++. Sometimes the program is finicky and you have to install the modules. This takes about 20 seconds. Open V++, then click on GWC module and then press ‘compile’ once the GWC module opens in a new window.

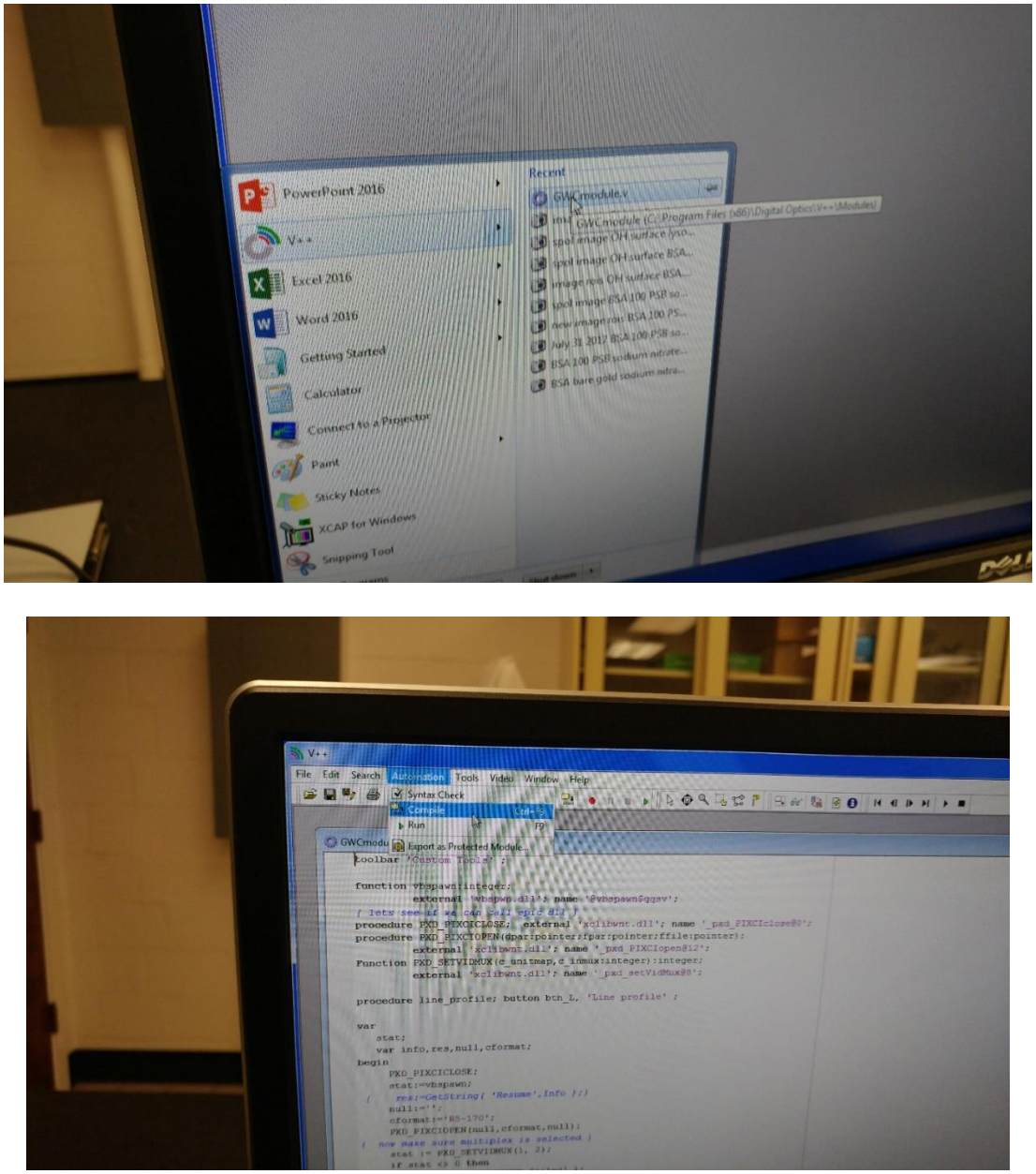

Figure E.6: Opening GWC module on V++ software.

5. Put the flow cell in and tighten the clamps. Optimize the angle of the incident light. Toggle the angle dial until the minimum is found. Note the minimum value, MV. The signal should be rotated clockwise until it is (248-MV)/3+MV. This typically comes out to about 80 pixels.

Figure E.7: The location of the ND filter and the knob that controls the incident angle of light

6. Click on the 'L' button on the program. It will show an image of the channel real time. Draw a line over the channel and adjust the incident angle approximately to 80^{o}

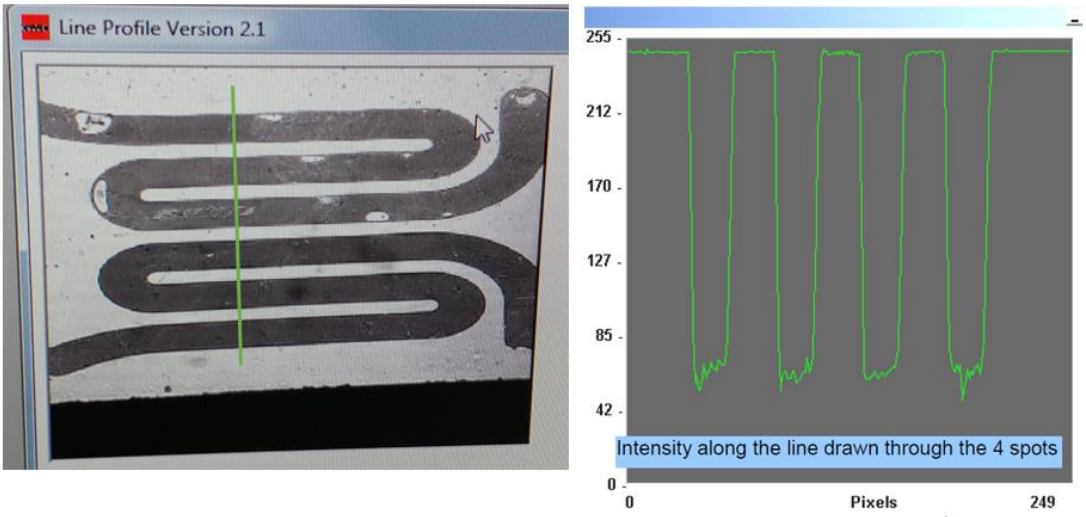

Figure E.8: Select line profile to optimize the incident angle

7. After fixing the incident angle, close the window. Apply the filter by pulling the knob out and set the mode to s-polarization. S-polarized light does not exhibit the surface plasmon

resonance effect. Take an s-pol image and save it. You will need this for data processing. An example s-pol image is given below-

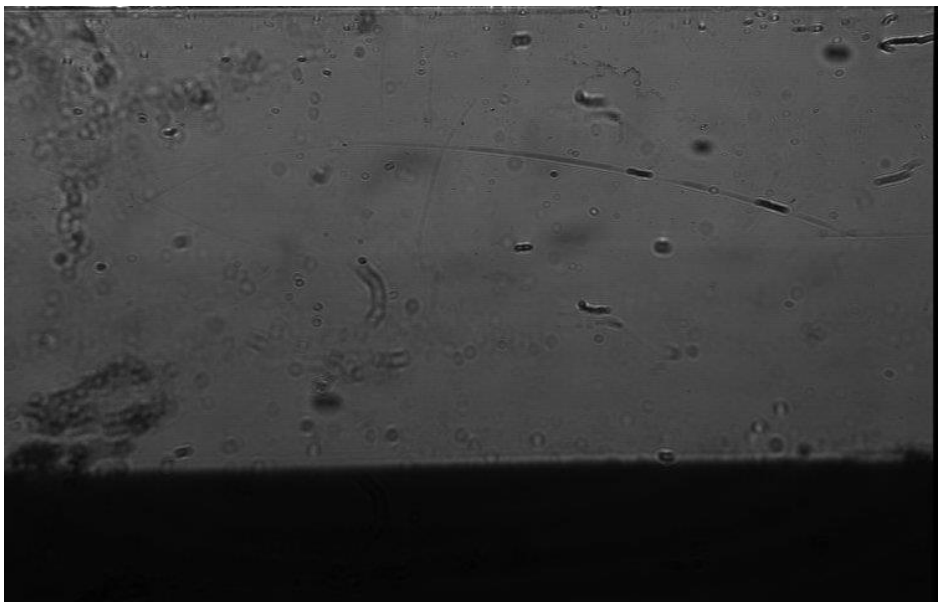

Figure E.9: Typical s-pol image of gold chip

8. Put the filter back off and set it back to p-pol (push the knob in). Take an image and set ROIs. Use a time trial difference image and save your images in real time. You can go back and change ROI's after the experiment. Use the default settings for all other queries (watch video: **Setting up the program for run**).
9. The pump has a dial to control volumetric flowrate and a power switch. Don't turn the pump off using the switch if it is moving. Air bubbles are consistently a big problem in SPR measurements. Pinch the tube downstream of the pump and hold it for a bit to build up pressure. This can sometimes remove the air bubbles. The entire flow cell will, however, have weird oscillations from flow effects. It is often more effective to pick new Region of Interests (ROIs) when the experiment is done. In the dual flow cell, air bubbles tend to aggregate at the edge of the flow cell, likely because of surface tension (see video: **Connect the pump**).

10. Convert SPR signal to Δ%R

Details on what is Δ%R and how it is calculated using the s-pol image and the SPR signal in PIU is described on page 28 of the user manual (see pdf file: **Horizon SPRimager user manual v2**). Time series data can easily be converted to Δ%R by cutting and pasting the spol values for each ROI in the appropriate space in sheet 2 of the "Template DeltaR II" Excel spreadsheet template (SPR template.xls) as follows:

a. In V++ open the spol image saved in your Experiment folder and the Mask image you used to collect your Time Series data.

b. Click on the Average macro button. V++ will prompt you to select two images. Select the Mask image first and the spol image second. V++ will now generate a text window containing the SPOL reflectivity values for each ROI in the order it was created on the Mask image.

c. Copy the data on the text window and paste it on the appropriate space provided on column A on "sheet 2" of the TimeSeriesGold.xls spreadsheet with your raw data collected during the experiment.

d. In the "%R" spreadsheet all the raw data will be re-plotted as Δ%R vs. time for each ROI.

   For adjustment of data to Δ%R, the following formula is pre-populated in the spreadsheet:

   Δ%R = 100 * ((SPR sample pixel difference * 0.85) / (s-pol pixel intensity / (1-d));

   Here, 'd' is the density of the filter used. For example, if you used the recommended filter that transmits only 25% of the light, d = 0.75.Using the 25% transmission filter supplied with the instrument, the above formula is then simplified to

Absolute Δ%R = 100 * ((SPR sample pixel difference * 0.85) / (s-pol pixel intensity *4)

11. To determine the surface coverage of adsorbed protein or molecules, the optical film thickness can be estimated by, d = ($\frac{l_d}{2}$) [$\frac{\Delta\%R}{s(\eta_a-\eta_s)}$], where s is the slope of a calibration plot of Δ%R vs. bulk refractive index of the measured solution (e.g. protein solution at different concentration) and l_d is decay length of the evanescent field near the gold surface, typically with a value of 37±13 % of the wavelength of light. Finally, the surface coverage of adsorbed protein was estimated from the following equation: Γ (ng/cm^2) = [$\frac{d\ (nm)}{Specific\ volume\ of\ protein\ (\frac{cm^3}{g})}$] x100. A typical value of specific volume value of proteins is 0.77 cm^3/g.

In adsorption measurements, the baseline is first established by running buffer or carrier solution for ≈10 min. Then the desired protein solution is pumped through the flow cell, until the signal intensity reached a stable plateau, after which carrier buffer washed away unbound protein. The reflectivity difference Δ%R before and after the wash was converted to the surface coverage with the above mentioned equation.

The SPR imager specification for our system is given below-

	SPR-IMG-802-240
Electrical Supply	220V or 230/240V 50-60Hz
Power consumption	70W
Ambient operating temperature	15 - 35°C
Sample operating temperature	Ambient – 60°C
Sensitivity, SPRchip™ samples	8pg mm^{-2}
Fluid flow rate min-max speed	30-600 µl/min (.031" ID tubing) 15-300 µl/min (.020" ID tubing)
Standard flow cell volume	17µL
Operating wavelength	800nm
Incident light angle range	49-60°
Benchtop footprint	25" x 18" (63cm x 45cm)
Net weight	57lb / 25 kg
CCD camera	1/2" format, 768x494 pixels

APPENDIX F: MICROPIPETTE ASPIRATION ASSAY SETUP

F.1 The micropipette aspiration setup

The micropipette system used in this study is a house designed and built system by Dr. Cheng Zhu's lab. The system consists of optical microscopy with camera, micromanipulation and pressure regulation subsystems.

The optical microscope is a Zeiss inverted microscope (Axiovert 200M, NA: 0.55, WD: 26mm; Oberkocan, Germany) with a 100x oil immersion, 1.25 N.A. objective and integrated with a HAL 100 Halogen Illuminator. Diffraction is minimized with a green light (546-nm wavelength) band-pass (5-nm bandwidth) filter that also reduces any photochemical damage to the RBC. The microscope is interfaced with a CCD camera (Pike, Allied Vision Technologies, PA). A digital image processor (model DSP-2000; Dage-MTI) is used to enhance the image. The signal also passes through a digital voltage multiplexer (model 401; Vista Electronics, Ramona, CA), which allows video integration and display of a timer on a screen. LabView allows integration of the camera recordings, as well as the piezocontroller with user interface on computer.

Each pipette can be coarsely manipulated by a mechanical drive mounted on the microscope (see Figure F.1, labeled as micropipette holder and manipulator) and finely positioned with a three-axis hydraulic micromanipulator (Model: M-461, Newport) on an air suspension vibration isolation table (Technical Manufacturing Corporation, MA) in order to avoid vibration of micropipettes during the experiment. The right micropipette is connected to a piezotranslator (E-665 Piezo Amplifier, PI, CA), which allows the micropipette to move in X-direction. Thus, the rigid micropipette (left) holding a test cell (RBC or MSC) come in contact with a RBC held by the moving (right) micropipette (Figure F.2). The contact time as well as the contact area can be

controlled by Labview commands of computer. A hydraulic line connects the micropipette holder to a fluid reservoir. We used a syringe to apply and maintain suction during the experiment.

F.2 Pulling micropipettes and microforging

Sutter Instrument, The P-97 Flaming/Brown type micropipette puller was used for fabricating micropipettes (Single-Barrel Standard Borosilicate Glass Tubes, World Precision Instruments, Sarasota, FL, USA) of the following specifications:

Item ID	Length	OD (mm)	ID (mm)
1B100F-4	4 in. (100mm)	1.0	0.58

Program number 55 (Type D Heat (Ramp+10), Pull (90), Vel (90), Time (175), Pressure (400), Loops (1)) was used to pull pipettes. Next, a house-built microforge (Micro Forge, MF-900, Narishige, Japan) was used to break the tip of the micropipette in order to achieve a flush tip with the desired diameter (in our case, ~3 μm for aspirating RBC and ~6 μm aspirating MSCs). The micropipette tips are held by a clamp while keeping it just over a platinum wire containing a glass bead (adapted from the laboratory of Robert M. Hochmuth, Duke University, Durham, NC). Then the platinum wire is heated up by passing electricity through it and once heated up (indicated by the orange glow of the glass bead) the micropipette tip, at the diameter desired to be cut, is lowered down to touch the bead and lifted up promptly so that it snaps and breaks. In order to make sure that the tip is not blocked, water/buffer is pushed through the pipette by using a syringe with copper needle. After that, the pipette is mounted on the pipette holder, directed on the stage of the microscope (Figure F.1).

F.3 Flow cytometry for quantification of cadherins

F.3.1 Data collection by LSR II Flow Cytometer and analysis of data

Flow cytometer allows analysis of multiple parameters (e.g. shape, size, number of target etc.) of individual cells in a heterogeneous population. This analysis is done by passing thousands of cells per second through a laser beam and capturing the light that emerges from each cells as it passes through. The data gathered can be analyzed statistically by flow cytometry software to report cellular characteristics such as size, complexity, phenotype and health.

The fluidic system allows samples pass into the interrogation point (the point at which the path becomes narrow, thus allowing hydrodynamic focusing in order to make sure that the particles or cells pass through the laser beam one at a time). The interrogation point is the heart of the system because this is where the laser beam and samples intersect, and also data are collected (Figure F.6). For determining N and E-cadherin densities expressed on MSCs, around $4x10^4$ cells were counted and suspended in 300 µl PBS solution and incubated with the appropriate primary and secondary antibody (each incubation duration was ~45 minutes at 4^o C). The solutions were transferred into flow cytometer tubes before running it into the system.

F.3.2 Standard calibration beads for Alexa 647

Quantum™ MESF (Molecules of Equivalent Soluble Fluorochrome) microsphere kits from Bangs Laboratories, Inc. was purchased for standardization of fluorescence intensity units for applications in quantitative fluorescence cytometry. The standard Alexa 647 beads were run on the same day using the same settings as stained cell samples to establish a calibration curve relating instrument channel values to standardized fluorescence intensity (MESF) units. Because Quantum™ MESF microspheres are surface labeled with the actual fluorochromes (in our case

Alexa 647) that are used to stain cells in flow cytometry, the standards are environmentally responsive (e.g. to pH, temperature etc.), and quantitative assignments are truly relevant.

Flow cytometry is a technique for determining fluorescently labeled species that are expressed on cells. For determining N and E-cadherin densities on MSCs as well as modified RBCs, LSR II by BD Biosciences (Figure F.7). The calibration curve is obtained by plotting the median intensity determined with five, standard fluorescent bead populations: 1 – Blank microsphere population and 4 – Microsphere populations surface labeled with increasing amounts of the specified fluorochrome. These populations are calibrated in MESF units. Using the excel sheet (Figure F.8) provided by the calibration bead company, Bangs Laboratories Inc, the molecules of equivalent soluble fluorochrome (MESF) values (approximately the number of antibodies), were converted into surface density (cadherins/area). This was done by dividing MESF by the estimated surface area of the cell or bead used for the analysis, which is 768 μm^2 for the MSCs and 168 μm^2 for RBCs.

F.4 Human blood purification

Human blood was collected from healthy volunteers by the trained phlebotomists at the Community Blood Services of Illinois (CBSI) in Champaign. Red blood cells were isolated from whole blood and purified according to the approved Institutional Review Board at the University of Illinois Urbana-Champaign (IRB protocol # 08669). The isolation and purification of human red blood cells protocol is based on protocol was published by Zarnitsyna and Zhu in 2011 and later modified by Langer et al., 2012 is given below:

First, after collection of the whole blood, it was stored and transported in Vacutainer vials (coated with EDTA to prevent coagulation). Inside a Biosafety Level II certified cell culture hood, 12 ml

of Histopaque 1119 (Sigma-Aldrich, St Louis, MO) and 8 ml human blood (in 7 ml of 0.9 w/v% NaCl) was measured out. The blood-saline solution was then slowly added to the tube containing Histopaque drop by drop. Once added, there are two distinct layers consisting of transparent Histopaque on the bottom and red blood on the top. Then the contents of the tube was centrifuged at 1200 g (rcf) for 20 minutes at room temperature in a benchtop centrifuge (Elmi Centrifuge, CM-75).

The supernatant was aspirated using a glass pipette inside cell culture hood into a flask containing bleach (20% by volume). The remaining cells, now consisting of mostly red blood cells were re-suspended in 6 ml of 0.9 % w/v NaCl, prior to the addition of 2 ml of 6 % w/v Dextran, to obtain a final concentration of 1.5% w/v. The cells were incubated at room temperature for 45 minutes, during which they settled to the bottom of the tube. After discarding the supernatant, the red blood cells (RBC) were washed twice at room temperature with 0.9 w/v% NaCl, centrifuged at 2000 RPM for 10 minutes and re-suspended in 12 ml EAS45 (2.0 mM Adenine, 110.0 mM Dextrose, 55.0 mM Mannitol, 50.0 mM NaCl, 10.0 mM glutamine and 20.0 mM Na_2HPO_4, at pH 8.0). The purified RBC suspension in EAS45 was stored at 4°C (Fig 2.2), and was used for up to 3 months, after which the RBC suspension was treated with 10% (by volume) bleach for 15 min and discarded. The figures in the following section were adapted from my Master's thesis (http://hdl.handle.net/2142/102855).

F.5 Figures

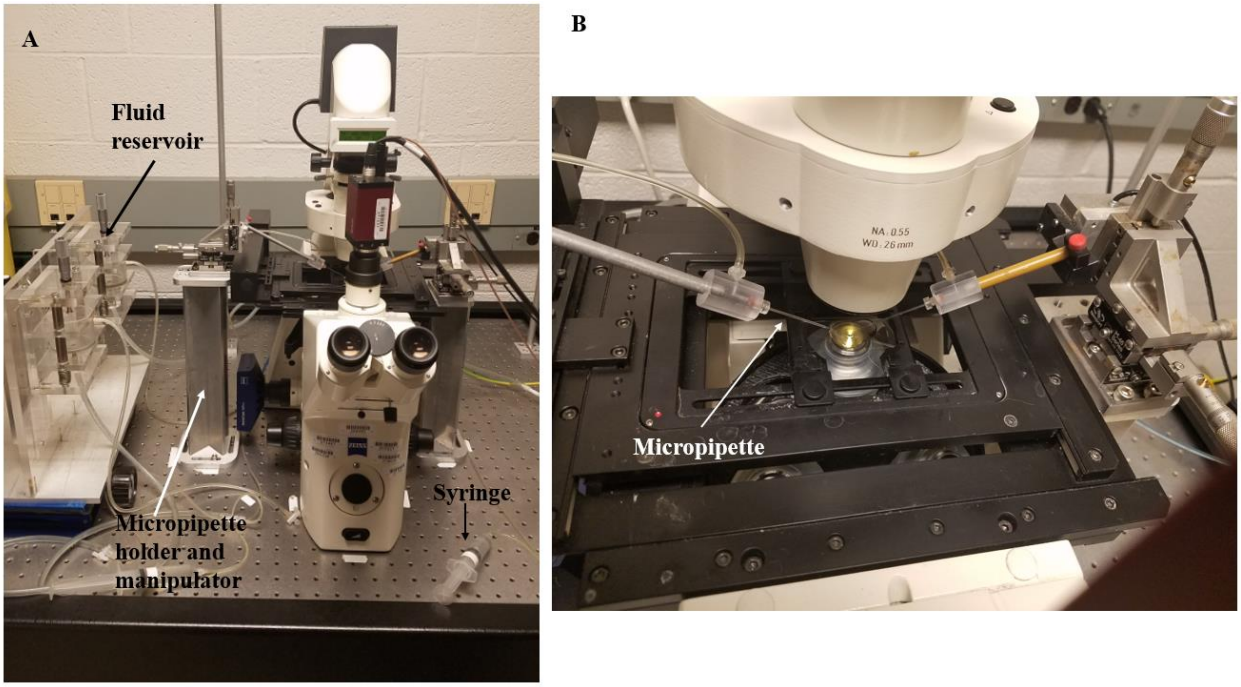

Figure F.1: (A) Micropipette Aspiration Assay setup and (B) a zoomed in view of two micropipettes focused on the microscope stage.

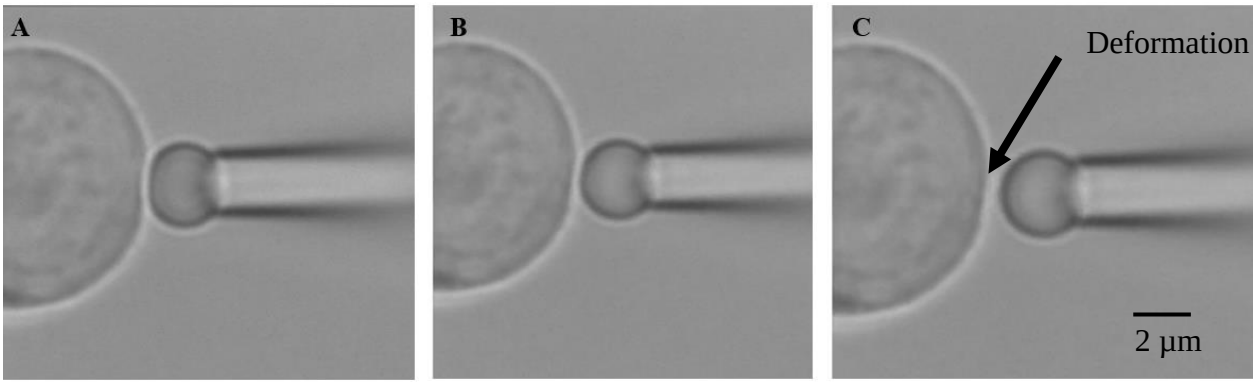

Figure F.2: Counting of adhesion binding events. (A) Cells are in contact (test cell on the left, here shown HaCat cell and red blood cells on right); (B) During detachment, the right pipette pulls away; (C) Deformation around the test cell (left) indicates binding event.

Figure F.3: Micropipette pulling instrument by Sutter Instrument Co.

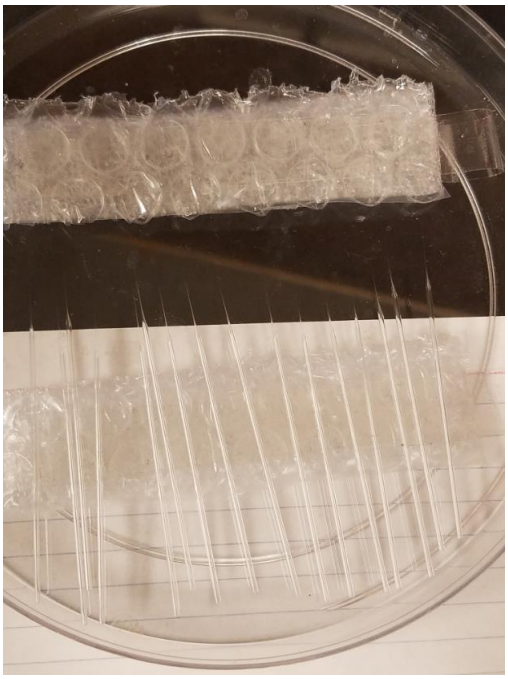

Figure F.4: Micropipettes of OD of 1 mm and ID 0.58 mm and the tip being ~3 µm for aspirating red blood cells and MSCs after microforging.

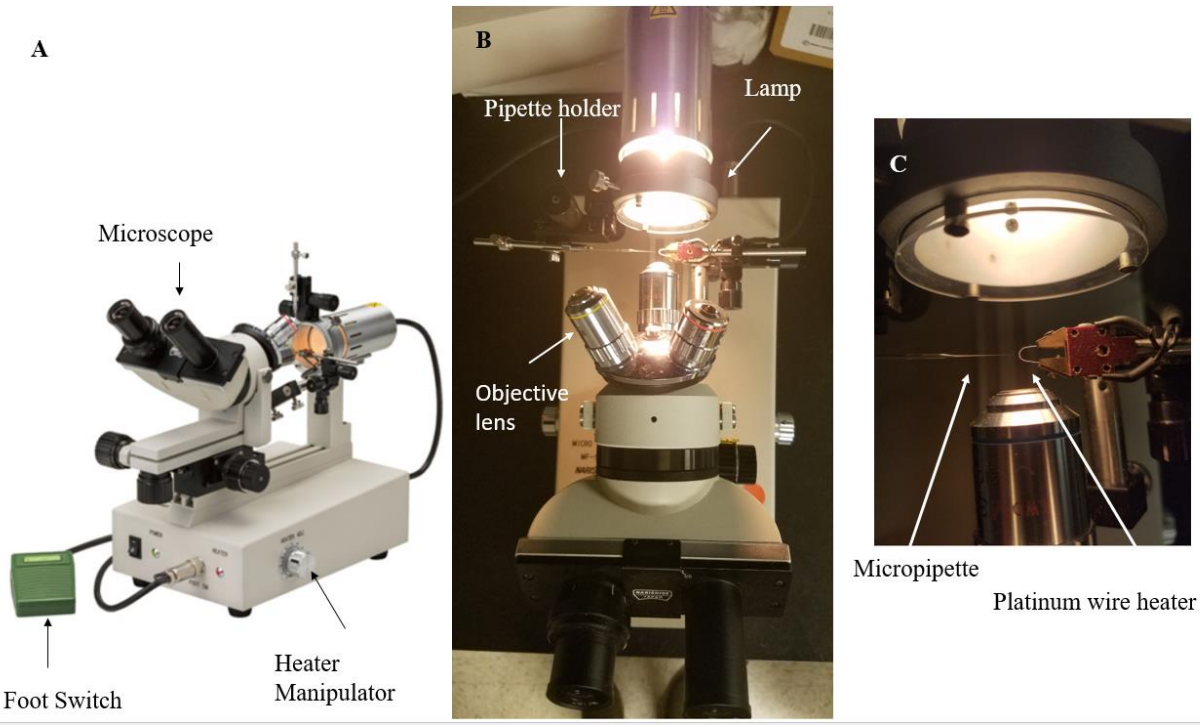

Figure F.5: Microforger for making micropipettes of desired diameters. (A) Different parts of MF-900 Microforger; (B) Micropipette to be cut is held over a heated glass bead on platinum wire; (C) Close up of image of the micropipette and the platinum wire heater.

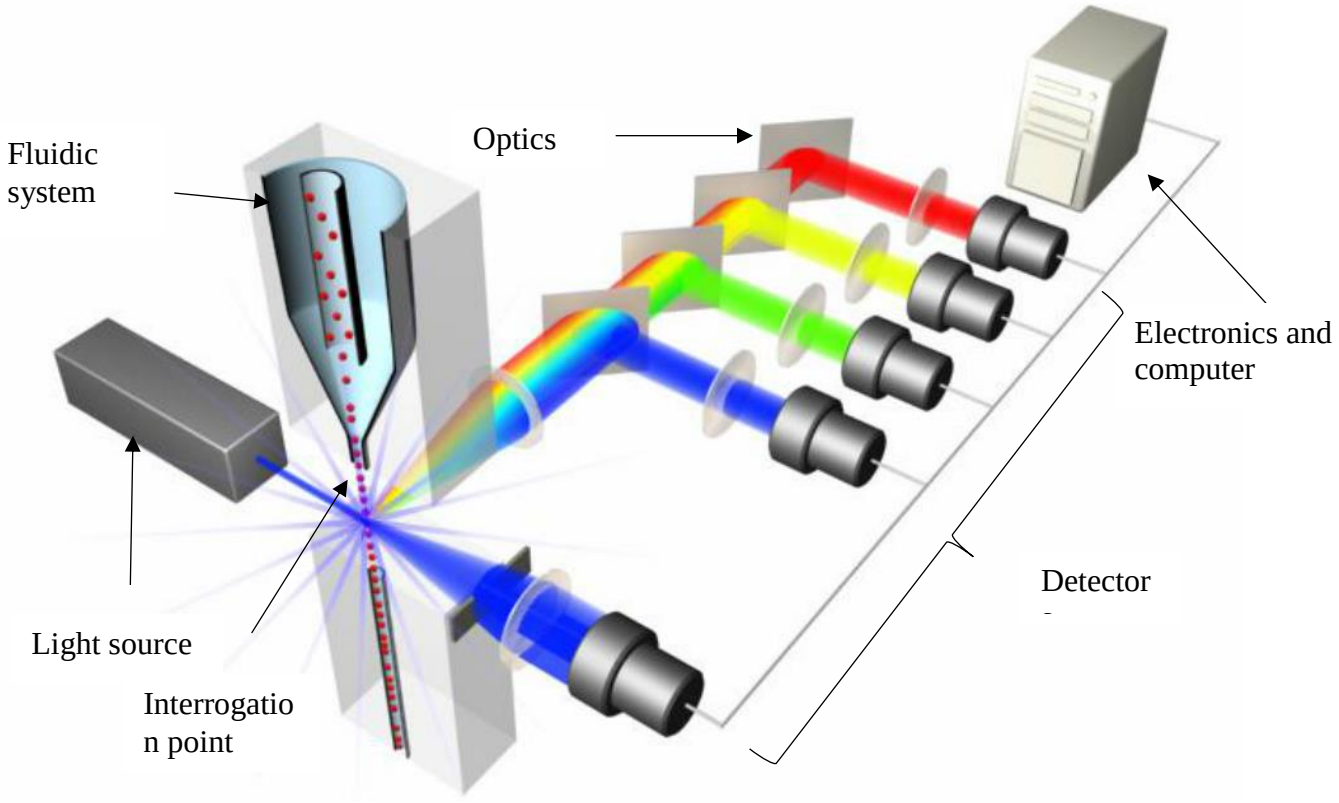

Figure F.6: Instrument overview (Photo courtesy: Invitrogen, BD)

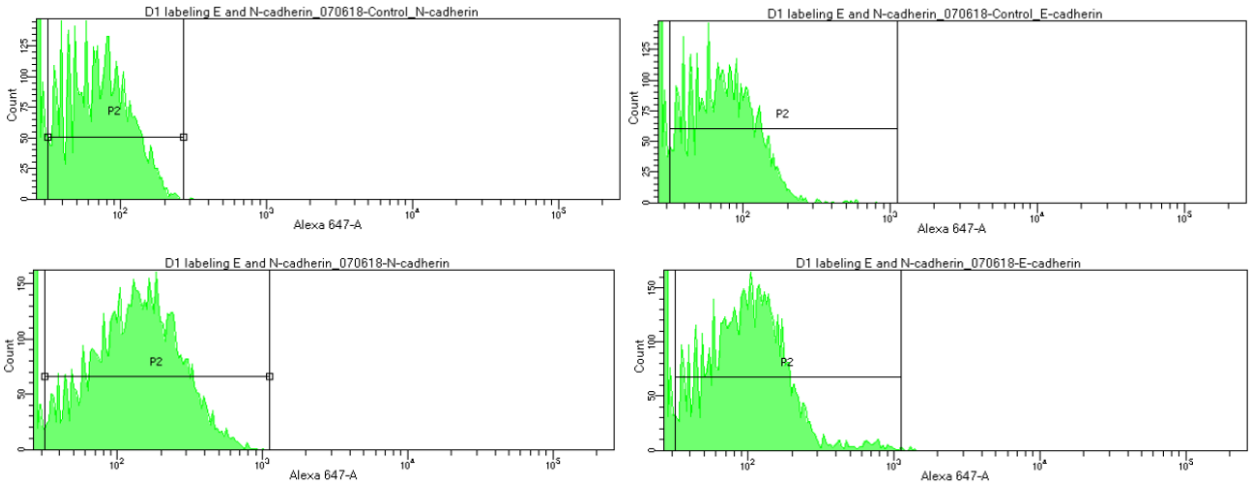

Experiment Name:	RBC Labeling_070218
Specimen Name:	D1 labeling E and N-cadherin_070618
Tube Name:	E-cadherin
Record Date:	Jul 6, 2018 7:25:14 PM
$OP:	Leckband
GUID:	536617af-384b-44c4-9681-2dc3e8b72cb6

Population	#Events	%Parent	FSC-A Mean	Alexa 647-A Median
All Events	10,000	####	22,103	71
P1	8,753	87.5	23,475	73
P2	6,273	71.7	23,837	100
P3	8,377	83.8	22,982	71

Figure F.7: Snapshot of median values calculated from MSCs labeled with Anti-N-cadherin antibody and DECMA-1 antibody to estimate N and E-cadherin density respectively.

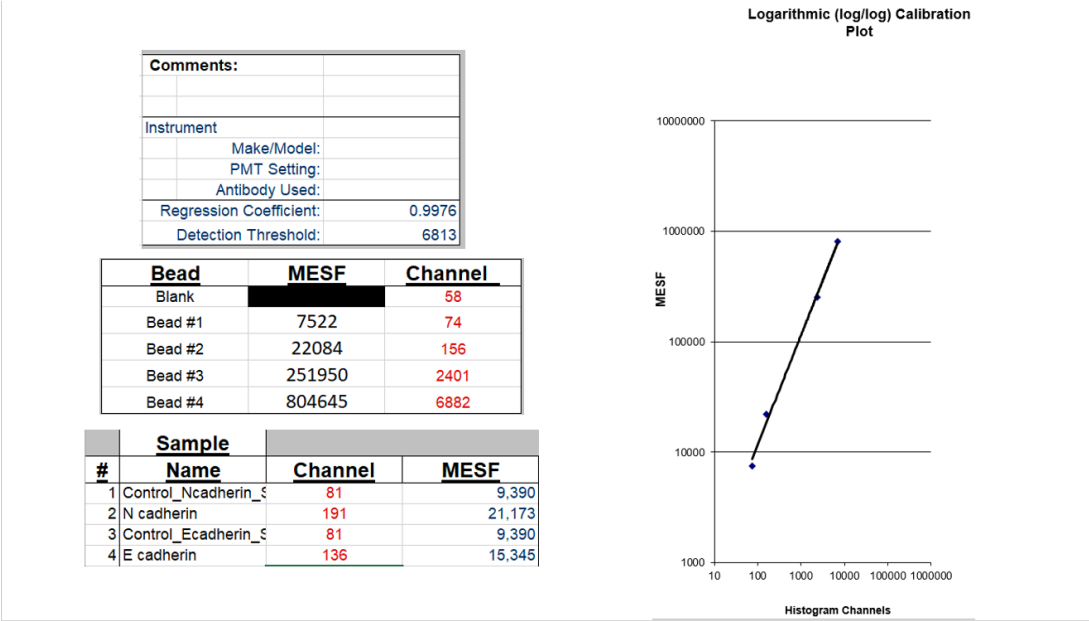

Comments:	
Instrument	
Make/Model:	
PMT Setting:	
Antibody Used:	
Regression Coefficient:	0.9976
Detection Threshold:	6813

Bead	MESF	Channel
Blank		58
Bead #1	7522	74
Bead #2	22084	156
Bead #3	251950	2401
Bead #4	804645	6882

	Sample		
#	Name	Channel	MESF
1	Control_Ncadherin_S	81	9,390
2	N cadherin	191	21,173
3	Control_Ecadherin_S	81	9,390
4	E cadherin	136	15,345

Figure F.8: Calibration of standard Alexa 647 beads by using data sheet provided by the manufacturer.

Figure F.9: (A) Benchtop centrifuge for isolating red blood cells from whole blood and (B) Red blood cells isolated (bottom) from whole blood (top) after centrifuging for 20 mins at 1200 g (rcf).

APPENDIX G: APPLICATIONS AND SYNTHESIS OF ZWITTERIONIC POLYMERS

G.1 Applications of zwitterionic polymers

Zwitterions have been utilized in a variety of forms in biological applications (Figure 1.2).[1] For example, zwitterionic polymers are used as protein chaperones and stabilizers,[50, 51] zwitterionic polymer-protein conjugates,[4, 5] zwitterion-coated surfaces,[20, 29, 43, 48] , zwitterion-modified membranes,[10–12] zwitterionic nanoparticles,[13–15] hydrogels,[16–19] and liposomes.[20] In the following subsections specific examples of use of zwitterionic polymers is discussed.

G.1.1 Use of zwitterionic polymers in preventing biofouling

In marine environment, the vicinity of a pristine surface cause charged proteins to adhere due to screening of electric double layer, which then facilitates attachment of microbes such as- (1) bacteria, e.g. *Escherichia coli*, *Straphylococcus epidermis*, *Streptococcus mutans*, and (2) marine organisms like-spores, diatoms, barnacles, tubeworms etc.[21] Zhang et al. showed using a polySBMA coated surface prevents a green marine algae *Ulva* spores from settling down. [12] Another study compared the biofilm formation by preventing the settling down of a Cyprus larva of barnacle called *Balanus amphitrite* onto the coated surfaces with polySBMA and polyCBMA. [22]

G.1.2 Applications in biomedical field

Biofilm formation on blood contacting surfaces is a serious problem. Fouling occurs in a hierarchical manner, with smaller proteins first adsorbing on the surface due to strong Van der Waals attraction (primary adsorption), triggering the immune response and resulting in deposition of thick collagenous capsule and subsequent rejection of the surface.[23]

Hydrogels consisting of polycaroboxybetaine methacrylate (pCBMA) were shown to be effective against formation of collagenous capsule deposition following subcutaneous implantation in mice for at least 3 months, in comparison with poly(2-hydroxyethyl methacrylate) (pHEMA). [24] Zwitterionic polymers based hydrogels with varied degree of crosslinking, and water content have been studied to develop hydrophilic and non-fouling material with desired mechanical properties.[25] Yang et al. reported a lightly crosslinked pCB hydrogel on glucose biosensors that allowed diffusion of proteins from 100% blood serum in and out of the hydrogel without entrapment, while maintaining the integrity of the hydrogel for ~20 days.[16] Wu et al. found that the drug loading capacity and diffusion rate from a hydrogel are dependent on the anti-biofouling molecules composing the hydrogel, with different combinations of PEG and pSB showing variations in diffusion rates and drug loading capacity *in vitro*.[26] These examples show the potential of using zwitterions to enhance the utility and biocompatibility of hydrogel structures.

G.1.3 Drug delivery and gene therapy

Hydrolyzable zwitterionic polymers like pCBs have great potential for use as gene or drug carrier because (1) in cationic form, pCB esters can form complex with DNA, protein and bacteria and (2) upon hydrolysis of the ester group they obtain zwitterionic form which is non-toxic and ultralow-fouling. The hydrolyzed pCB-ester-DNA complex is postulated to release the gene or protein without damaging it. [27]

G.1.4 Use of zwitterionic polymers as stabilizers and dispersants

Nanoparticles (NPs), are widely utilized in medicine as protein stabilizers, biocatalysts, imaging agents, and drug carriers.[28, 29] When unmodified, NPs are prone to aggregation and removal from the body, but conjugation with zwitterionic polymers has been shown to overcome these challenges.[30] The anti-aggregation effects exhibited by zwitterionic polymers are comparable to

those displayed by poly(ethylene glycol) (PEG).[31] The concurrent anionic and cationic properties of zwitterionic molecules can reduce NP aggregation by reducing the effective NP surface energy while also simultaneously increasing NP circulation time and cellular uptake in vivo.[30,32,33] These effects can be enhanced with the use of pH-sensitive zwitterionic moieties capable of adjusting the zeta-potential of NPs in response to the surrounding microenvironment.[30] Conjugation of NPs with polycarboxybetaines has been demonstrated to add further functionalities such as- attachment of antigens for antibody capture via EDC/NHS chemistry with the carboxylate ions on the betaine moieties. [13] Muro et al. used small and stable Sulfobetaine based ligand conjugated quantum dots for live-cell imaging. [34]

G.2 Synthesis routes: Atom Transfer Radical Polymerization (ATRP)

Atom Transfer Radical Polymerization or ATRP is the most commonly known Controlled Radical Polymerization (CRP) method which was developed by Matyajaszeweski group (Figure G.1). [19, 51–53] ATRP is well suited for polymerization on self-assembled monolayer (SAM) surfaces since the reaction can be carried out at room temperature, the reaction media can be water or other polar solvents, and the molecular weight of the polymer is controllable. In this reaction, an alkyl halide initiators or dormant species, RX or P_nX react with activators- usually a low oxidation state metal complexes, Mt^zL_m (Mt^z is the metal species in oxidation state z, L is a ligand) to reversibly form both propagating species R^o or P_n^o and deactivators-higher oxidation state metal complexes with coordinated halide ligands $XMt^{z+1}L_m$. Thus, the dormant species in this ATRP equilibrium can be polymer chains able to grow in one or many directions, or polymers attached to functional colloidal particles, surfaces, and biomolecules. ATRP permits the synthesis of copolymers with targeted composition, controlled molecular architecture, predetermined MW, and narrow polydispersity or

molecular weight distribution. It is also possible to incorporate a variety of functional groups into polymers via ATRP method in three different ways as described by Matyajaszeweski and Tsarevsky. [36] They are- (1) direct polymerization of functional monomers provides functional groups along the backbone (density and distribution can be regulated by monomer feeding, for example in gradient copolymers); (2) monofunctional ATRP initiators introduce functionality at the chain end; difunctional initiators generate functionality at the chain center; it is also possible to place functionality in any specific part of the chain; (3) chemical transformation of the alkyl halide chain end, using nucleophilic substitution, radical or electrophilic addition.

The polymerization rate, R_p is given by-

$$R_p = \frac{k_{act}}{k_{deact}} \; k_p \frac{[M][RX][Mt^z L_m]}{[XMt^{z+1}L_m]} = K_{ATRP}\, k_p \frac{[M][RX][Mt^z L_m]}{[XMt^{z+1}L_m]}$$

$$\frac{M_w}{M_n} = 1 + \left[\frac{k_p[RX]_0}{k_{deact}[XMt^{z+1}L_m]} \right] \left[\frac{2}{conv} - 1 \right]$$

These equations show that the polymerization rate, R_p and polydispersity index (M_W/M_n) depend on kinetic parameters and reagent concentrations. R_p depends on k_p, and the ratio of the k_{act} and k_{deact}, that is, the ATRP equilibrium constant ($K_{ATRP} = k_{act} / k_{deact}$), as well as on the concentrations of all reagents involved. Polydispersity is lower for polymerizations with faster deactivation (that is, for catalysts with a higher value of k_{deact} and/or at higher deactivator concentrations). The polydispersity decreases with the monomer conversion (designated as conv) and is lower for higher MW (lower initiator concentration, $[RX]_o$.

In all chapters of this thesis, it is described in details how ATRP method has been used for synthesis of homo and random copolymers in a 'graft-from' method.

G.3 Antifouling mechanisms of zwitterionic polymers

There has been an impressive number of studies that investigated the antifouling mechanisms of zwitterionic polymers, with no general consensus. Non fouling surfaces are generally hydrophilic. Thus, antifouling property of these materials are often attributed to their strong surface hydration. Surface hydration for the zwitterionic polymer surfaces take place through electrostatic-induced hydrogen bonding and at the nonionic PEG surfaces through hydrogen bonding between water molecules and ether oxygen atoms.[39–41] The tightly bound hydration layer is theorized to act as a physical and energy barrier against protein adsorption.

If a surface contains extensive water similar to bulk water, then free energy cannot be gained in replacing a protein/water interface with a protein/surface interface upon adsorption, resulting in repelling of proteins.[42] Kobayashi et al. measured low water-in-air contact angles on surfaces coated with MPC and SBMA brushes indicating such a low surface free energy.[43] Tanaka et al. classified interfacial waters into 3 categories- (1) non-freezing water (non-crystallize at -100^{o}C); (2) freezing bound water (crystallize at 0^{o}C) and (3) free water (crystallize at 0^{o}C) and demonstrated that freezing bound water around poly(2-methoxyethyl acrylate) (PMEA) prevent interactions with proteins.[44, 45] Molecular dynamics simulations estimated water coordination number around charged moieties of zwitterionic polymers and reported that about 7 water molecules around a sulfonate group and 19 water molecules around the quaternary ammonium in a sulfobetaine (SB) monomer, which is slightly more than for a similar carboxybetaine (CB). However, the water molecules around the negatively charged group of the carboxybetaine have a sharper spatial distribution, more preferential dipole orientation, and longer residence time.[46] In comparison, thermal analysis of the MPC polymer revealed about 23 water molecules per PC repeat unit.[47] Kitano et al. measured more water bound to surface of zwitterionic materials than

other hydrophilic or hydrophobic materials, which revealed the differences in the nature and strength of ion solvation and H-bonding.[48] These studies argued that the surface of zwitterionic polymers is super hydrophilic and provide a physical barrier against non-specific protein adsorption.

In contrast, experiments comparing PEG and zwitterionic polymer classes showed that surface hydration with PEG was perturbed upon contact with proteins, while no or little influence on water structuring could be seen around pSBMA brushes (Figure G.2).[88, 89] Kitano and coworkers also reported that there is no disruption of H-bonding of water around polyzwitterionic polymers more informatively by employing ATR-FTIR and Raman Spectroscopy.[51–53] Other studies reported that these polymers also show very little surface activity.[54] These studies suggest that despite being well-hydrated, there is minimal disruption of the water structure by the zwitterions. Therefore, there is neither any unusual water structuring nor any physical barrier of water molecules. However, there is energy barrier against protein adsorption.

Surfaces modified with grafted polymer chains show steric or osmotic repulsive forces on compression of such a dense film. When proteins approach a polymer coated surface it experiences superimposition of purely repulsive force because of insertion penalty into the brush layer and a purely attractive force between the underlying surface and the protein. Ternary adsorption is allowed when the protein size with respect to the brush height is small enough so that it can penetrate into the thin film and protein-zwitterionic polymer segment interactions overcome the repulsive osmotic forces.[55] Upon adsorption, protein loses translational entropy when it adsorbs, experiences a change in contact free energy on going from solvent to the surface, and possibly gains conformational entropy if it denatures[56] , but denaturing is not a requirement for adsorption.

G.4 Figures

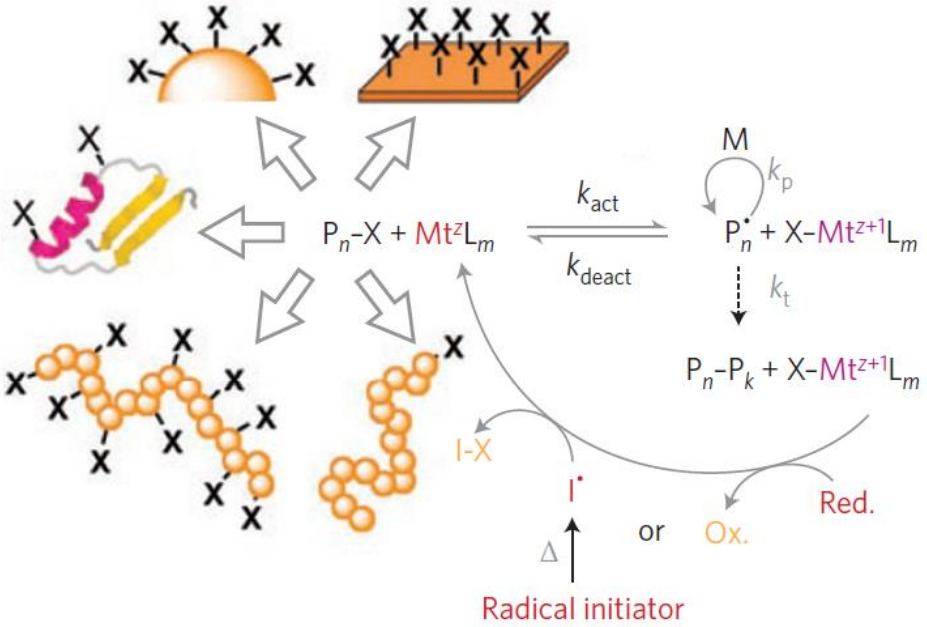

Figure G.1: The reaction scheme for ATRP method. [This figure is adapted from: Matyjaszewski and Tsarevsky, *Nat Chem* **2009,** 1, 276-288 with permission (Copyright 2009 Springer Nature)].

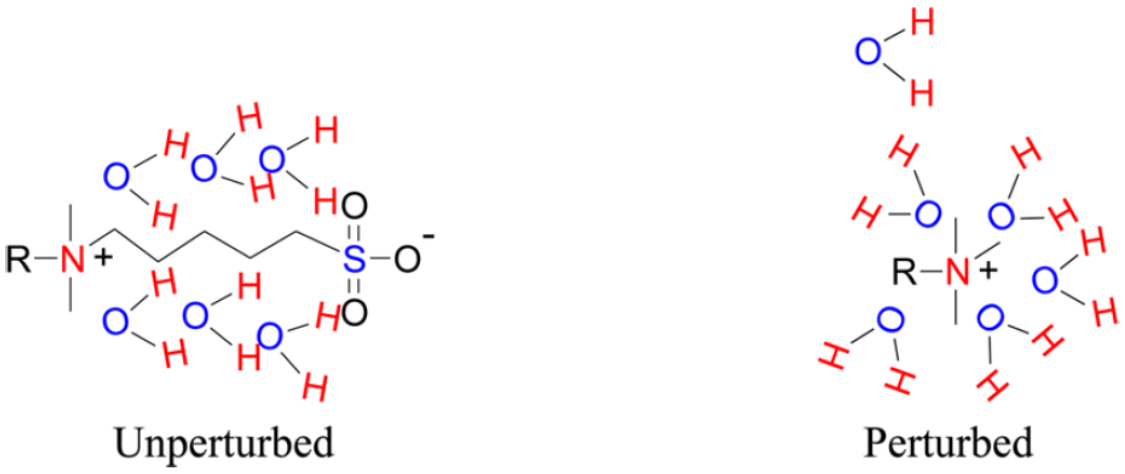

Figure G.2: Representation of differences in water molecule ordering around a zwitterion and a single positive charge. The zwitterion allows the H-bonding structure to remain unperturbed (with reference to bulk water), while the single charge reorients the waters to a more disordered and less H-bonded state (perturbed). [This figure is adapted from: Schlenoff J.B., *Langmuir* **2014**, 30, 9625−9636, https://doi.org/10.1021/la500057j with permission (copyright 2014 American Chemical Society].

References:

1. Erfani, A., Seaberg, J., Aichele, C. P. & Ramsey, J. D. Interactions between Biomolecules and Zwitterionic Moieties: A Review. *Biomacromolecules* **21**, 2557–2573 (2020).
2. Wangkanont, K., Forest, K. T. & Kiessling, L. L. The non-detergent sulfobetaine-201 acts as a pharmacological chaperone to promote folding and crystallization of the type II TGF-β receptor extracellular domain. *Protein Expr. Purif.* **115**, 19–25 (2015).
3. Ivanova, I. *et al.* Chaperone-Like Effect of Polyzwitterions on the Interaction of C1q with IgG. *Z. Naturforsch.* **64**, 149–154 (2009).
4. Liu, S. & Jiang, S. Zwitterionic polymer-protein conjugates reduce polymer-specific antibody response. *Nano Today* **11**, 285–291 (2016).
5. Liu, S. & Jiang, S. Chemical conjugation of zwitterionic polymers protects immunogenic enzyme and preserves bioactivity without polymer-specific antibody response. *Nano Today* **11**, 285–291 (2016).
6. Yang, W. *et al.* Film Thickness Dependence of Protein Adsorption from Blood Serum and Plasma onto Poly(sulfobetaine)-Grafted Surfaces. *Langmuir* **24**, 9211–9214 (2008).
7. Ladd, J., Zhang, Z., Chen, S., Hower, J. C. & Jiang, S. Zwitterionic Polymers Exhibiting High Resistance to Nonspecific Protein Adsorption from Human Serum and Plasma. *Biomacromolecules* **9**, 1357–1361 (2008).
8. Z. Zhang, Chao, T., Chen, S. F. & Jiang, S. Y. Superlow Fouling Sulfobetaine and Carboxybetaine Polymers on Glass Slides. *Langmuir* **22**, 10072–10077 (2006).
9. Li, G. *et al.* Ultralow fouling zwitterionic polymers grafted from surfaces covered with an initiator via an adhesive mussel mimetic linkage. *J. Phys. Chem. B* **112**, 15269–15274 (2008).

10. Lalani, R. & Liu, L. Electrospun zwitterionic poly(sulfobetaine methacrylate) for nonadherent, superabsorbent, and antimicrobial wound dressing applications. *Biomacromolecules* **13**, 1853–1863 (2012).

11. Liu, Q., Patel, A. A. & Liu, L. Superhydrophilic and underwater superoleophobic poly(sulfobetaine methacrylate)-grafted glass fiber filters for oil-water separation. *ACS Appl. Mater. Interfaces* **6**, 8996–9003 (2014).

12. Zhang, Z. *et al.* Polysulfobetaine-grafted surfaces as environmentally benign ultralow fouling marine coatings. *Langmuir* **25**, 13516–13521 (2009).

13. Yang, W., Zhang, L., Wang, S., White, A. D. & Jiang, S. Functionalizable and ultra stable nanoparticles coated with zwitterionic poly(carboxybetaine) in undiluted blood serum. *Biomaterials* **30**, 5617–5621 (2009).

14. Estephan, Z. G., Jaber, J. A. & Schlenoff, J. B. Zwitterion-stabilized silica nanoparticles: Toward nonstick nano. *Langmuir* **26**, 16884–16889 (2010).

15. Chen, Y. *et al.* Zwitterionic supramolecular prodrug nanoparticles based on host-guest interactions for intracellular drug delivery. *Polymer* **97**, 449–455 (2016).

16. Yang, W. *et al.* The effect of lightly crosslinked poly(carboxybetaine) hydrogel coating on the performance of sensors in whole blood. *Biomaterials* **33**, 7945–7951 (2012).

17. Kostina, N. Y., Rodriguez-Emmenegger, C., Houska, M., Brynda, E. & Michálek, J. Non-fouling hydrogels of 2-hydroxyethyl methacrylate and zwitterionic carboxybetaine (meth)acrylamides. *Biomacromolecules* **13**, 4164–4170 (2012).

18. Koc, J. *et al.* Low-Fouling Thin Hydrogel Coatings Made of Photo-Cross-Linked Polyzwitterions. *Langmuir* **35**, 1552–1562 (2019).

19. Zhang, L. *et al.* Zwitterionic hydrogels implanted in mice resist the foreign-body reaction.

Nat. Biotechnol. **31**, 553 (2013).

20. Huang, P. *et al.* Zwitterionic nanoparticles constructed from bioreducible RAFT–ROP double head agent for shell shedding triggered intracellular drug delivery. *Acta Biomater.* **40**, 263–272 (2016).
21. Cheng, G., Zhang, Z., Chen, S., Bryers, J. D. & Jiang, S. Inhibition of bacterial adhesion and biofilm formation on zwitterionic surfaces. *Biomaterials* **28**, 4192–4199 (2007).
22. Aldred, N., Li, G., Gao, Y., Clare, A. S. & Jiang, S. Modulation of barnacle (Balanus amphitrite Darwin) cyprid settlement behavior by sulfobetaine and carboxybetaine methacrylate polymer coatings. *Biofouling* **26**, 673–683 (2010).
23. Ward, W. K. A review of the foreign-body response to subcutaneously-implanted devices: the role of macrophages and cytokines in biofouling and fibrosis. *J. Diabetes Sci. Technol.* **2**, 768–777 (2008).
24. Zhang, L. *et al.* Zwitterionic hydrogels implanted in mice resist the foreign-body reaction. *Nat. Biotechnol.* **31**, 553–556 (2013).
25. Carr, L. R., Xue, H. & Jiang, S. Functionalizable and nonfouling zwitterionic carboxybetaine hydrogels with a carboxybetaine dimethacrylate crosslinker. *Biomaterials* **32**, 961–968 (2011).
26. Wu, J. *et al.* Protein diffusion characteristics in the hydrogels of poly(ethylene glycol) and zwitterionic poly(sulfobetaine methacrylate) (pSBMA). *Acta Biomater.* **40**, 172–181 (2016).
27. Zhang, Z. *et al.* The hydrolysis of cationic polycarboxybetaine esters to zwitterionic polycarboxybetaines with controlled properties. *Biomaterials* **29**, 4719–4725 (2008).
28. Langer, R. Perspectives and challenges in tissue engineering and regenerative medicine.

Adv. Mater. **21**, 3235–3236 (2009).

29. Ratner, B. D., Hoffman, A. S., Schoen, F. J. & Lemons, J. E. *An introduction to materials in medicine. Biomaterials Science* (Elsevier, Academic Press, 2004).

30. Yuan, Y. Y. *et al.* Surface charge switchable nanoparticles based on zwitterionic polymer for enhanced drug delivery to tumor. *Adv. Mater.* **24**, 5476–5480 (2012).

31. Estephan, Z. G., Schlenoff, P. S. & Schlenoff, J. B. Zwitteration as an alternative to PEGylation. *Langmuir* **27**, 6794–6800 (2011).

32. Ajmal, M., Demirci, S., Siddiq, M., Aktas, N. & Sahiner, N. Betaine microgel preparation from 2-(methacryloyloxy) ethyl] dimethyl (3-sulfopropyl) ammonium hydroxide and its use as a catalyst system. *Colloids Surf.* **486**, 29–37 (2015).

33. Song, J. *et al.* Encapsulation of AgNPs within Zwitterionic Hydrogels for Highly Efficient and Antifouling Catalysis in Biological Environments. *Langmuir* **35**, 1563–1570 (2019).

34. Muro, E. *et al.* Small and stable sulfobetaine zwitterionic quantum dots for functional live-cell imaging. *J. Am. Chem. Soc.* **132**, 4556–4557 (2010).

35. Wang, J.-S. & Matyjaszewski, K. Controlled/'living' radical polymerization. Atom transfer radical polymerization in the presence of transition-metal complexes. **117**, 5614–5615 (1995).

36. Matyjaszewski, K. & Tsarevsky, N. V. Nanostructured functional materials prepared by atom transfer radical polymerization. *Nat. Chem.* **1**, 276–288 (2009).

37. Matyjaszewski, K. & Xia, J. Atom transfer radical polymerization. *Chem. Rev.* **101**, 2921–2990 (2001).

38. Kamigaito, M., Ando, T. & Sawamoto, M. Metal-catalyzed living radical polymerization. *Chem. Rev. 101, 3689 (2001).* **101**, 3689 (2001).

39. Chen, S., Li, L., Zhao, C. & Zheng, J. Surface hydration: Principles and applications toward low-fouling/nonfouling biomaterials. *Polymer.* **51**, 5283–5293 (2010).

40. Leung, B. O., Yang, Z., Wu, S. S. H. & Chou, K. C. Role of Polyethylene, Interfacial Water on Protein Adsorption at Cross-Linked Oxide Interfaces. *Langmuir* **28**, 5724−5728 (2012).

41. Galvin, C. J., Dimitriou, M. D., Satija, S. K. & Genzer, J. Swelling of polyelectrolyte and polyzwitterion brushes by humid vapors. *J. Am. Chem. Soc.* **136**, 12737–12745 (2014).

42. Andrade, J. D. & Hlady, V. Protein Adsorption and Materials Adv., Biocompatibility - a Tutorial Review and Suggested Hypotheses. *Polym. Sci.* **79**, 1–63 (1986).

43. Kobayashi, M.; Terayama, Y.; Yamaguchi, H.; Terada, M.; Murakami, D.; Ishihara, K.; Takahara, A. Wettability and Antifouling Behavior on the Surfaces of Superhydrophilic Polymer Brushes. *Langmuir* **28**, 7212−7222 (2012).

44. Tanaka, M. *et al.* Cold crystallization of water in hydrated poly(2-methoxyethyl acrylate) (PMEA). *Polym. Int.* **49**, 1709–1713 (2000).

45. Tanaka M, S. E. N. Polymer-supported membranes as models of the cell surface. *Nature* **437**, 656–663 (2005).

46. Shao, Q., He, Y., White, A. D. & Jiang, S. Difference in hydration between carboxybetaine and sulfobetaine. *J. Phys. Chem. B* **114**, 16625–16631 (2010).

47. Morisaku, T., Watanabe, J., Konno, T., Takai, M. & Ishihara, K. Swollen, Hydration of Phosphorylcholine Groups Attached to Highly Polymer Hydrogels Studied by Thermal Analysis. *Polymer.* **49**, 4652–4657 (2008).

48. Kitano, H. *et al.* Structure of water incorporated in sulfobetaine polymer films as studied by ATR-FTIR. *Macromol. Biosci.* **5**, 314–321 (2005).

49. Leng, C. *et al.* Probing the Surface Hydration of Nonfouling Zwitterionic and PEG Materials in Contact with Proteins. *ACS Appl. Mater. Interfaces* **7**, 16881–16888 (2015).

50. Shao, Q., He, Y., White, A. D. & Jiang, S. Different effects of zwitterion and ethylene glycol on proteins. *J. Chem. Phys.* **136**, (2012).

51. Kitano, H.; Mori, T.; Takeuchi, Y.; Tada, S.; Gemmei-Ide, M.; Yokoyama, Y.; Tanaka, M. Structure of Water Incorporated in Sulfobetaine Polymer Films as Studied by ATR-FTIR. *Macromol. Biosci.* **5**, 314−321 (2005).

52. Kitano, H.; Imai, M.; Sudo, K.; Ide, M. Hydrogen-Bonded Network Structure of Water in Aqueous Solution of Sulfobetaine Polymers. *J. Phys. Chem. B* **106**, 11391−11396 (2002).

53. Kitano, H., Sudo, K., Ichikawa, K., Ide, M. & Ishihara, K. Raman Spectroscopic Study on the Structure of Water in Aqueous Polyelectrolyte Solutions. *J. Phys. Chem. B* **104**, 1425–11429 (2000).

54. Lowe, A. B., Billingham, N. C. & Armes, S. P. Synthesis and properties of low-polydispersity poly(sulfopropylbetaine)s and their block copolymers. *Macromolecules* **32**, 2141–2148 (1999).

55. Halperin, A., Fragneto, G., Schollier, A. & Sferrazza, M. Primary versus ternary adsorption of proteins onto PEG brushes. *Langmuir* **23**, 10603–10617 (2007).

56. Norde, W., MacRitchie, F., Nowicka, G. & Lyklema, J. Protein Adsorption at Solid-liquid Interfaces: Reversibility and Conformation Aspects. *J. Colloid Interface Sci.* **112**, 447–456 (1986).